NOVEL DIAPHRAGM FREE-PISTON STIRLING CRYOCOOLER

Alan Caughley, BE (Hons), ME

A thesis presented for the degree of Doctor of Philosophy

in

Mechanical Engineering

Department of Mechanical Engineering, University of Canterbury, Christchurch, New Zealand,

2015

CONTENTS

LIST OF FIGURES

LIST OF TABLES

ACKNOWLEDGEMENTS

This work would not have been possible without the continuing support of Industrial Research, Callaghan Innovation and MBIE; they have my gratitude.

I would also like to thank my supervisors, Drs Alan Tucker, Mathieu Sellier, Michael Gschwendtner and Robert Buckley whose guidance has been essential.

Last but not least, I would like to thank my wife Fiona and children John, Grace, James and Grant for their patience during the compilation of this thesis.

ABSTRACT

In 2004, the author of this thesis invented a novel metal-diaphragm based pressure wave generator (DPWG) for pulse tube and Stirling cryocoolers. The invention used a connected pair of metal diaphragms to seal the cryocooler's clean working gas from a conventionally lubricated drive mechanism at ambient pressure, and to balance the average gas forces on the working diaphragms so the drive only has to work against the pressure wave. The DPWG has since been developed and has proven to be effective and practical, driving pulse tube cryocoolers with up to 1200 W of refrigeration at 77 K. From early in the development of the DPWG, two questions have existed. The first is: Can the connected pair of diaphragms concept suspend the displacer in a free-piston Stirling cryocooler, removing displacer piston-to-cylinder sealing issues? And the second is: Can the large surface areas and radial flows offered by the diaphragms' flat geometry be used for heat exchange, thus reducing the need for costly heat exchangers? This thesis addresses those two questions. To address the first question, a proof-of-concept prototype was designed, constructed and tested. It did not perform as well as expected but did reach cryogenic temperatures. A second prototype with smaller displacer diaphragms was then designed and constructed. Its performance was significantly better than the first prototype; it achieved a low temperature of 56 K and produced 29 W of refrigeration at 77 K. The prototypes proved that the double diaphragm concept could be used to produce a free-piston Stirling cryocooler and perform refrigeration at cryogenic temperatures. To address the second question, two computer models of the second prototype were developed. The first was with a one-dimensional Stirling machine modeller called Sage; the second with ANSYS® CFX, a commercial Computational Fluid Dynamics (CFD) code. A series of validation exercises were performed to confirm the models' applicability to the oscillating flow and heat transfer typical of Stirling cryocooler gas spaces. The second prototype was modelled using Sage and CFX; both agreed with the macroscopic behaviour of the prototype and predicted the cooling power within an order of magnitude of the experiments. The CFD model confirmed the second question for the diaphragm on the cold side of the displacer, which was sufficient for heat exchange without a separate heat exchanger. However, it showed that the warm side of the machine needed extra area for heat rejection. The CFD model gave insights into why the second prototype was not performing as well as intended. A CFD model of a modified design, backed up with a Sage model, has predicted that it is possible to make a cryocooler with performance similar to a pulse tube with the same size pressure wave generator and with a higher efficiency.

NOMENCLATURE

a	Amplitude of the pressure wave generator movement	m
a_2	Amplitude of the displacer movement	m
A	Surface area	m^2
d	Characteristic dimension of a feature: diameter, thickness	m
D	Diameter of cylindrical object	m
D_h	Hydraulic diameter, the equivalent tube diameter of a non-cylindrical duct	m
F	Frequency	s^{-1}
h, h_f	Heat transfer coefficient	W m^{-2} K^{-1}
H	Enthalpy	J kg^{-1}
L_{nd}	Non-dimensional hysteresis loss in a cycle, defined by the adiabatic work done in a cycle over the adiabatic compression work done in the cycle	
Nu	Nusselt Number	
p	Pressure	N m^{-2}
pdV,	Work done in a time period (usually a cycle) by a surface on a gas	J
Pe	Peclet number based on average piston velocity	
Pe_w	Peclet number based on oscillation frequency	
pV	Work done by a surface on a gas, $work = \int pdV$ 'pV power' then refers to the acoustic power in a cycle as defined by pV power$= F \oint pdV$	J W
r	Radius from centre axis of machine or gas space	m
R	Specific Gas constant, 2078.6 for Helium	J kg^{-1} K^{-1}
Q	Energy flow	W
Re	Reynolds number	
S	Entropy	J kg^{-1} K^{-1}
t	time	s
T	Temperature	K
U	flow velocity	m s^{-1}

v	Velocity	m s^{-1}
V	Volume	m^3
W	Work	J
α	Thermal diffusivity	m^2 s^{-1}
γ	Polytropic exponent for adiabatic conditions, 1.667 for Helium	
κ	Thermal conductivity	W m^{-1} K^{-1}
μ	Dynamic viscosity	Pa s
ρ	density	kg m^{-3}
τ	shear stress in fluid	Pa
ø	phase angle, usually with respect to the crank angle of a machine	rad
ω	Rotational speed	rad s^{-1}

Vector quantities are represented in bold, for example $\boldsymbol{U}$ is a velocity vector.

1 INTRODUCTION

Cryogenics is derived from the Greek word *Kyros* which means 'freezing cold' and *genic* which means 'the production of '. There is no rigidly defined temperature below which conditions are considered cryogenic. Various definitions are used for cryogenic temperatures, such as below the reach of conventional vapour compression refrigerators, below CO_2 sublimation temperatures, below 120 K, below -150 °C, or below 93 K where the traditional permanent gases liquefy.

Cryogenic refrigeration is the process of removing heat from environments at cryogenic temperatures. It is now over one hundred years since Cailletet and Pictet first liquefied oxygen in 1877, followed by Wroblewski liquefying hydrogen in 1884, Dewar's invention of vacuum insulation in 1892, and the final climax of Onnes' liquefaction of helium in 1908. Early methods of cooling gases were very inefficient, using expansion valves to do the cooling and cascading down in temperature by expanding different gases in turn. Claude's invention of an expansion engine in 1902 initiated development of cycles which produced more efficient cooling and laid the foundations of modern liquefaction processes. Production of cryogenic liquids, such as liquid nitrogen, has been dominated by large liquefaction plants, with distillation towers, to separate oxygen from liquid air for use in steel making. Large multi-national companies such as Air Liquide, BOC, Linde, Air Products and Praxair have resulted from the substantial market for gases produced as a result of cryogenic air separation technologies.

Cryogenic refrigeration on the small scale is relatively recent. In the 1950s the Philips Stirling engine development programme discovered that, by turning the normally power-producing engine over with a motor, their machines could produce cryogenic refrigeration. The Philips Stirling technology is still producing cryocoolers as Stirling Cryogenics BV, long after the engine development programme was abandoned. In 1959, Gifford and McMahon invented a cryocooler [1] using a modified air conditioning compressor and valves to oscillate the pressure in a cold head and produce a cooling cycle. Later, Gifford explored the thermal effects of oscillating pressures in a blind tube, thereby inventing the basic pulse tube [2]. The pulse tube was finally made useful in 1983 with Mikulin's orifice phase shifter [3] to produce a cold head with no moving parts. Since then, development has improved power and efficiency, but pulse tubes are still not capable of achieving the same cooling power and efficiency of the original Philips Stirling system.

Stirling cryocoolers are based on a reversal of Robert Stirling's gas engine that was patented in 1816 and was used as a safe alternative to steam until good quality steel made boilers safer. The

gas engine was resurrected by Philips in the 1940s in an attempt to make a compact and safe external combustion engine for generators to power valve radios. The engine worked, although efficiency was mediocre and it was not able to be made cheaply enough for the developing countries that were its intended market. Development stopped when transistor radios, which ran on batteries, were invented. However reversing the Stirling engine produced a very efficient cryocooler. Development of the Stirling cycle for refrigeration has produced a range of cryocoolers from less than a watt of cooling power at 80 K for infra-red sensors, to helium liquefiers, coolers for spacecraft electronics, to multi-kilowatt nitrogen liquefiers. All Stirling coolers exhibit excellent efficiency but suffer from either a short lifetime (of a few thousand hours) or very high cost.

Applications that require cryogenics include superconductivity, biological storage, electronics, fuel and gas storage, gas separation and sensors. A recent application of cryogenics that has been growing over the last twenty years is High Temperature Superconductors (HTS). HTS refers to a class of ceramic materials that superconduct at 'high' temperatures relative to the superconductivity that occurs in most metals around liquid helium temperatures and below. HTS is attractive because the energy required to 'lift' a watt of heat from 80 K to ambient is orders of magnitude less than 'lifting' the same watt from 4 K, the temperature at which low temperature superconductors work. Of most interest for HTS materials are a class of doped copper oxides called BSSCO and YBCO which superconduct at 110 K and 90 K respectively. These two materials have been successfully made into wires and form the foundation of the HTS industry. The need to cool HTS applications developed at Industrial Research Ltd (IRL) was the original purpose of this work.

HTS technology has matured to the point where full scale demonstrations of power cables [4], motors [5], generators [6], transformers [7] and fault current limiters [8] are showing the benefits of the technology. Utility scale HTS power applications typically require 500 W - 5 kW of cryogenic refrigeration at temperatures between 30 and 70 K. The operating temperature range of the application is lower than the superconducting transition temperature because HTS materials can carry more current in higher magnetic fields at lower temperatures. This temperature and power range is not well served by currently available cryocooler technology, which has, in the past, been driven by space, military, and scientific applications or large scale gas liquefaction plants. Another application that requires similar cooling power and temperature is small scale gas liquefaction. Small scale liquefaction is economical for industry, hospitals or biological storage in areas that do not have ready access to the infrastructure for bulk cryogen supply.

The US Department of Energy published a report detailing the specifications required for cooling HTS systems [9] that forms the basis for the performance targets listed in Table 1-1.

Table 1-1: The DOE targeted performance criteria for HTS cryocoolers [9] and small liquefaction plants.

Characteristic	**Specification**
Temperature range	30-70 K
Refrigeration power	500-5 kW
Efficiency (% of Carnot COP at 77 K)	30%
Life (to major maintenance)	40,000 hours
Cost ($ W^{-1} at 77 K)	<US$100, ideally US$30

Table 1-2: Comparison of high power cryocoolers in the range of interest. Power and efficiency has been normalised to 77 K for direct comparison.

Manufacturer	**Model**	**Type**	**Cooling power [W at 77 K]**	**Efficiency % of Carnot COP**	**Hours to Major Maintenance**	**Cost**
Cryomech [10]	AL600	Gifford McMahon	600✓	11%	10,000hrs	Low✓
Praxair [11]		Pulse tube	1000✓	13%	40,000+ hrs✓	Pulse tube low, PWG high
Stirling Cryogenics [12]	SPC-1	Beta Stirling	1000✓	26%✓	6,000hrs	Low✓
Not commercially available	PuKyong Nat. University, Korea	Turbo Brayton	1000✓	12%	30,000+ hrs✓	Very high

Table 1-2 details a selection of current cryocoolers with cooling power in the range of Table 1-1. Each cryocooler in Table 1-2 exhibits some, but not all, of the desired characteristics; all of the incumbent technologies excelled in a few areas, but performed poorly in others. There is no all-rounder with the temperature and cooling power combination, and robustness for industrial applications. For example, Stirling cryocoolers achieve excellent efficiency but with a significant maintenance penalty. Gifford-McMahon (GM) coolers are a mature technology with low capital cost but have limited efficiency and insufficient life for continuous running. Turbo Brayton systems, being turbo-machinery, can achieve long lifetimes but with high cost due to very large heat exchangers. They are only economic with over 10 kW of refrigeration. Large pulse tube

refrigerators suffer from streaming problems which degrade performance and efficiency. Large pulse tubes also do not provide useful amounts of cooling below 50 K; for example Praxair's 1 kW pulse tube [11] has a no-load temperature of 60 K. Whilst pulse tubes themselves are simple and comparatively cheap, they require large linear pressure wave generators which are expensive and dominate their cost.

The author previously invented a novel metallic diaphragm pressure wave generator technology (DPWG) [13], [14], [15], [16] as a rugged alternative to linear drive pressure wave generators. DPWGs have been successfully coupled to many pulse tube refrigerators [17], [18], [19], [20], [21]. The DPWG uses a pair of metallic diaphragms to seal and suspend the driving piston in the pressure wave generator. Metallic diaphragms allow the cryocooler's clean working gas to be hermetically sealed from a conventionally lubricated motor-crank oscillating mechanism. The connected pair of diaphragms gives the DPWG a working diaphragm and a gas spring diaphragm that balances the considerable force from the average working gas pressure. In this manner the oscillating mechanism only experiences forces from the pressure wave. The DPWG, when combined with a pulse tube or Stirling expander, overcomes many of the shortcomings of current technology cryocoolers, such as cost, reliability, robustness and efficiency to provide an industrialised solution to cooling HTS power system applications.

Increasing the efficiency of a cryocooler is an effective way of reducing both capital and running costs. Moving from the 12% Carnot efficiency of a GM or large Pulse tube to the 26% of a Stirling cryocooler effectively halves the size and capital cost of a machine, in addition to the reduction in running cost from the greater efficiency. Moreover, running costs can be considerable for large cryocoolers that are required to operate continuously, such as for a power transformer. Depending on the electricity price, the cost of running a 20 kW motor for 10 years can easily exceed the capital cost of the cryocooler.

To achieve all of the desired characteristics in a single machine, two approaches can be made:

1. Take a cryocooler (pulse tube) that is inherently reliable and attempt to improve its thermodynamics to achieve the desired temperature and efficiency. This approach has been taken by many researchers around the world. When the state of the art from 20 years' development is only 50% of the desired efficiency, there is a high risk that fundamental thermodynamic limits have already been reached.
2. Take a machine that can deliver the desired performance (Stirling) and improve its reliability and longevity. The Philips Stirling has been refined over the past 50 years and still only achieves 5000 hours between major maintenance. The space industry has solved the longevity issue with clearance gap pistons (which do not touch the cylinder

bores) to produce highly efficient long life Stirling coolers for spacecraft, but at a very high cost.

This work takes the latter approach by replacing the pistons and cylinders in a free-piston Stirling cryocooler with metallic diaphragms to achieve a clean, oil-free movement. Thus the Stirling's high efficiency and cooling power should be retained with the addition of long life and low cost.

The aim of this work is to develop a free-piston Stirling expander technology, based on the diaphragm pressure wave generator, a thorough analysis of the corresponding thermo-fluid dynamics present in the radial flows, and unique geometry of the diaphragm system. The result will provide significant benefits to the cryogenic refrigeration industry by combining the longevity of diaphragms with the efficiency and power density offered by Stirling refrigerators.

1.1 Hypotheses

The diaphragm Stirling cryocooler concept has been motivated by two key questions.

The first question is: Can a practical Stirling cryocooler be made using the concepts developed in the author's previous invention and embodied in IRL's metallic diaphragm pressure wave generator? Stirling cold heads have practical limitations revolving around the need for a moving expander or displacer piston in the cold region of the machine. The difficulties stem from a stringent need for a clean working gas, free from volatile components such as lubricants which accumulate and freeze in cold heat exchangers and the regenerator. Some manufacturers use conventional piston seals and accept short lifespans [12]; others achieve long life through suspending the pistons so they never touch their cylinders [22] and accept the associated high costs. Hence the question: Can the diaphragm's flexible membrane be used to provide a cheap, long-life moving seal for suspending the displacer in a free-piston Stirling machine?

The second question is: If such a cryocooler can be made, are there thermodynamic advantages to be gained from the radial flows and large surface areas inherent in the diaphragms' geometry? The key difference in geometry between pistons and diaphragms is the aspect ratio. Piston-in-cylinder geometry typically has a diameter similar in size to the stroke, with most of the fluid velocity being axial and the surface-area to volume ratio close to its minimum. Metallic diaphragms have a very short working stroke because they rely on the flexing of the metal membrane which has a high modulus of elasticity (as opposed to rubber for example). Therefore, metallic diaphragm geometry has a diameter that is approximately 100 times the stroke, leading to a large area-to-volume-ratio with significant radial flows. Heat exchangers are one of the high cost items in a cryocooler. For regenerative cryocoolers that depend on an oscillating cycle, heat has to be exchanged between the working gas and the heat exchange surfaces very rapidly. Common forms of heat exchanger are wire mesh, shell and tube, or slots. Mesh heat exchangers are effective for small coolers but lose effectiveness as the cooler size increases due to the long radial conduction paths down wires to the heat sink. Shell and tube heat exchangers can be effective but are labour intensive in their construction, consisting of many small pipes. Slotted heat exchangers are very effective for larger coolers and can offer good surface areas, conduction paths and high velocities. The cost of slotted heat exchangers rises with cooling power as the surface area needed is proportional to the heat to be transferred and is also proportional to the slot cutting time. Hence it would be very desirable in a cryocooler to utilise other features available to reduce the amount of heat exchanger area required, and hence manufacturing cost.

The two questions then lead to the two hypotheses that will be tested in this work.

The first hypothesis is: That a practical Stirling cryocooler can be made using the metallic diaphragm concepts embodied in the diaphragm pressure wave generator.

The second hypothesis is: That the large surface area and radial flows of diaphragm systems have the potential for enhanced heat transfer, thus reducing the need for, and therefore cost of, large heat exchangers.

1.2 Methodology

This thesis addresses the two hypotheses (i.e. the viability of the concept and the usefulness of the area and radial flows produced by the diaphragm); then combines the answers into an improved cryocooler design.

1.2.1 PROOF OF CONCEPT PROTOTYPE FREE-PISTON EXPANDER.

Chapter 3 addresses the first hypothesis, which concerns the question of the viability of the diaphragm free-piston Stirling cryocooler concept, via a model and experimental proof-of-concept prototype followed by a second-iteration prototype.

Free-piston Stirling engines and cryocoolers have been made successfully for many years [23], [24], [25], [26], [27], [28], [29]. The use of diaphragms poses challenges as the proportions, forces, spring rates and displacements are significantly different from the piston-based designs traditionally used. The dynamics of split free-piston Stirling machines with conventional pistons are well known [30], and these dynamics had to be modified to achieve the correct dynamics of a free-piston system with a displacer suspended and sealed by diaphragms .

The first step was the construction of a thermodynamic model of the proposed system within the one-dimensional modelling software Sage [31]. The model was used to optimise the proportions of the proof-of-concept prototype and produced a configuration that predicted good cooling power and efficiency.

The next step was a machine design that embodied the thermodynamic aspects of the model. The displacer was supported by a pair of diaphragms that acted as both seals and flexure bearings. Hence the effects of the bounce space, compression space and expansion space were achieved with flexing parts and no rubbing. A number of dimensional changes were required at the design stage to make sure the parts all physically fitted together and able to withstand the gas pressure and thermal stresses from operation. Once the design was completed, the Sage model and performance predictions were updated with the as-designed dimensions.

A prototype was then constructed and tested at IRL's cryogenics laboratory. The prototype was instrumented to measure the dynamic behaviour of the displacer and to track the temperature of the cold parts. As with any new proof-of-concept prototype, there were the inevitable reliability (something broken), thermodynamic (something overheated), and instrumentation (something needed better measuring) issues which required rectification after the first few runs. A set of characterisation experiments was performed to confirm the displacer movement and cooling effect. Finally the original Sage model was adjusted to reflect the as-built prototype and compared with the experimental results.

The first proof-of-concept prototype's testing highlighted that the design could be improved upon for better performance. A second prototype was designed, constructed and tested. The Sage model was further improved and compared with the experimental results.

1.2.2 MODELLING OF OSCILLATING RADIAL FLOWS

Chapters 4 and 5 of this thesis address the second hypothesis which concerns the question of whether the diaphragms' large surface areas and radial flows can provide sufficient heat transfer to eliminate, or significantly reduce, the need for expensive heat exchangers.

Computational Fluid Dynamic (CFD) modelling was the principal tool used to study the flow and heat transfer in the free-piston diaphragm Stirling cryocooler. Modelling a diaphragm Stirling cryocooler presented a number of challenges. In particular, the expansion and compression spaces were complex three-dimensional flow fields, where the gas flow alternately changed direction between oscillating parallel plates. The gas pressure, walls and flows all oscillated out of phase with each other. To complicate matters further, the gas oscillated between ambient and cryogenic temperatures giving rise to gas properties, such as density, that varied with time and position throughout the machine.

In Chapter 4 a CFD model of the cryocooler was developed. The CFD modelling technique, using ANSYS® CFX, needed validation. Validation consisted of comparing the CFD modelling of gas spring dynamics with well-known analytical solutions and experimental work. The first validation modelled oscillating compression in a simple cylinder, comparing results with Kornhauser and Smith's experimental work [32]. The model was progressively modified; firstly to a flat geometry characteristic of the cold gas space in the prototype and secondly Kornhauser and Smith's compression piston was added to the flat geometry to simulate compression into a radial space. The final validation included the prototype's DPWG diaphragm compressing through a tube into the flat geometry, a configuration that was experimentally validated.

In Chapter 5 the validated gas spring model was modified to form a full model of the second cryocooler prototype described in Chapter 3 to test the second hypothesis. The full CFD model was run with the walls at 200 K and compared with the Sage model and characterisation experiments of Chapter 3. The model was then run with the cold walls at 77 K to simulate the cryocooler prototype in operation when liquefying nitrogen. Calculation of the heat transfer potential of the diaphragm spaces confirmed the hypothesis.

1.2.3 IMPROVED DIAPHRAGM STIRLING CRYOCOOLER.

Chapter 6, combined the results from the previous two objectives into an improved design for a free-piston Stirling cryocooler. The final design used both Sage and CFD modelling to direct changes to the design and predict the magnitude of the performance improvements. It involved using Sage for initial optimisation of the system, CFD for detailed 3D design of the heat exchange, and practical design experience from the proof-of-concept prototypes. The result was a cryocooler design that was predicted to provide cryogenic refrigeration with a competitive cooling power and efficiency when compared to currently available technologies.

1.3 Background Theory

1.3.1 GAS REFRIGERATION CYCLES

Gas cycles form the core of today's refrigeration technology whether it be air-conditioning, domestic refrigerators or freezers, cool stores or air liquefaction plants. All refrigeration gas cycles rely upon rejecting heat from gas warmed by compression, and absorbing heat from gas cooled by expansion. When the compression happens at ambient and the expansion elsewhere at a cooler temperature, then heat can be moved from one place to another against its natural flow from warm to cold.

In his 1824 book [33], Sadi Carnot proposed an ideal gas cycle using reversible processes throughout. Carnot's cycle, shown in Figure 1-1 in the refrigeration mode, consisted of:

- 1 -> 2, isentropic compression;
- 2 -> 3, isothermal heat rejection;
- 3 -> 4, isentropic expansion;
- 4 -> 1, isothermal heat rejection.

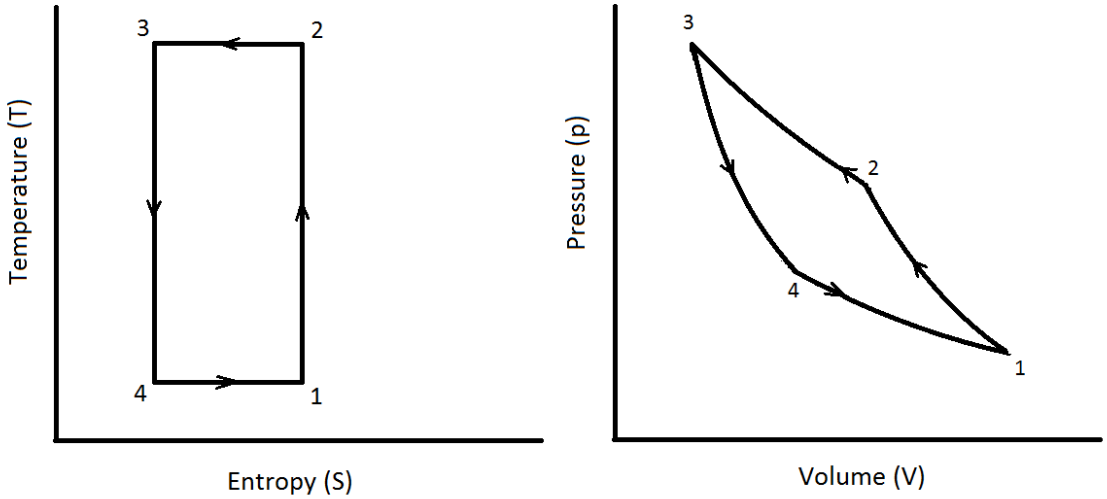

Figure 1-1: T-S and p-V diagrams for the Carnot Cycle

Through analysis of his cycle, Carnot showed that is not possible to make an engine that converts heat completely to work, meaning that heat always needs to be rejected. The refrigeration equivalent is that heat cannot be moved from a cold reservoir to a warm one without work being done. The amount of heat or work required to be expended has formed the base of the second law of thermodynamics. Carnot determined that the maximum possible efficiency of an engine is,

$$\eta_{carnot} = 1 - \frac{T_c}{T_h}, \quad 1\text{-}1$$

and the maximum possible coefficient of performance (COP) of a refrigerator is,

$$COP_{carnot} = \frac{T_c}{T_h - T_c}. \quad 1\text{-}2$$

Where T_c is the cold reservoir temperature and T_h is the warm reservoir temperature.

Equation 1-2 shows that for a refrigerator operating with T_h at ambient (around 300 K), the COP_{carnot} is very dependent on T_c and the colder T_c is the more pronounced its effect on the COP_{carnot}. For this reason, cryogenic refrigerators are commonly compared via the concept of efficiency as a percentage of the COP_{carnot}, thus giving a good indication of the actual performance of the refrigerator relative to the maximum possible performance at a given temperature.

The Carnot cycle is now the standard reference cycle, an ideal that cannot be improved upon. Due to its total reversibility, the Carnot cycle can be used as either an engine or a refrigerator. Unfortunately, the combination of reversible processes that Sadi Carnot chose for his ideal cycle means that it is an impractical machine to build. Other, more practical, cycles have been developed over the following centuries, some with the potential for ideal efficiency, such as the Stirling cycle.

Near-ambient refrigeration, typically down to -40 ^{0}C, or 233 K, is commonly performed by vapour-compression cycles. Vapour-compression cycles are non-ideal cycles which fall short of the ideal performance due to the use of an expansion valve, which is a non-reversible process. However, due to the latent heats involved in the condensation and evaporation phases of the vapour compression cycle, heat exchange is close to isothermal and thus very effective; meaning that, over small temperature ranges, vapour-compression cycles are the most efficient, economical and practical cycles for near ambient refrigeration [34]. Cascaded vapour-compression cycles, ones that use several stages using working fluids with different boiling points, can achieve temperatures down to around -100 C, or 173 K. Below 173 K, multi-staging

becomes uneconomic and different types of gas cycles are required to achieve practical, cryogenic refrigeration.

The five gas cycles commonly used in small scale cryogenic refrigeration today are described by Radebaugh [29] as the Joule-Thompson, Brayton, Stirling, Gifford–McMahon (GM) and the pulse tube. All the cycles use heat exchangers to cool the gas going from the ambient compressor to the cryogenically cold expander, and warm it on its return journey. The Joule-Thompson and Brayton are referred to as recuperative cycles, as they use counter-flow heat exchangers to cool a continuous flow of gas between the warm and cold parts of the cycle, recovering the heat on the return journey. Stirling, GM, and pulse tube are referred to as regenerative cycles as they oscillate the working gas between warm and cold, using heat exchangers that store heat in a solid while cooling the gas, and returning the heat to the gas on its return.

The Joule-Thompson (JT) cycle, Figure 1-2, relies on the Joule-Thompson effect where real-gas properties drop the gas temperature during isentropic expansion, typically through an orifice. The cycle consists of, with reference to Figure 1-2:

- 1->2, isobaric cooling in the recuperative heat exchanger,
- 2->3, isenthalpic expansion in the JT expansion valve,
- 3->4, isobaric warming in the recuperative heat exchanger,
- 4->1, adiabatic compression in a rotary or piston compressor.

Since the JT expansion valve is a non-reversible processes, the maximum possible performance is lower than the ideal Carnot cycle. In practice, JT cryocoolers do have lower COP's than other cryocoolers, but simplicity and lack of moving parts mean they are cheap cryocoolers [35] and can be readily miniaturised [36], [37] .

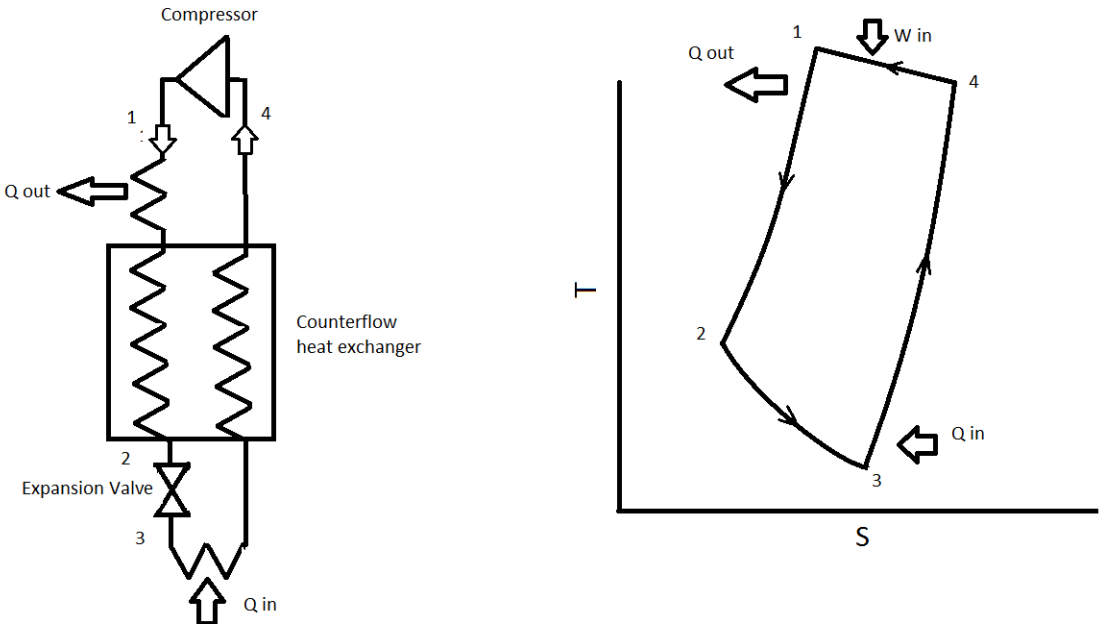

Figure 1-2: Schematic and *T-S* diagram of JT cycle.

The Brayton cycle, Figure 1-3, is an improvement on the JT cycle that uses an expansion engine instead of the JT orifice. The work done in expansion can then be returned to the compressor, increasing efficiency. Variations of the Brayton cycle, especially those that use turbo compressors and expanders, now form the core of gas liquefaction cycles at large scales. The Claude cycle, used for liquefiers, is a Brayton machine with a JT orifice for the last part of the expansion stage, when liquefying, to avoid mixed phase flow in the expansion turbine. The inefficiencies of the JT valve are minor as the expansion engine takes most of the work out of the gas.

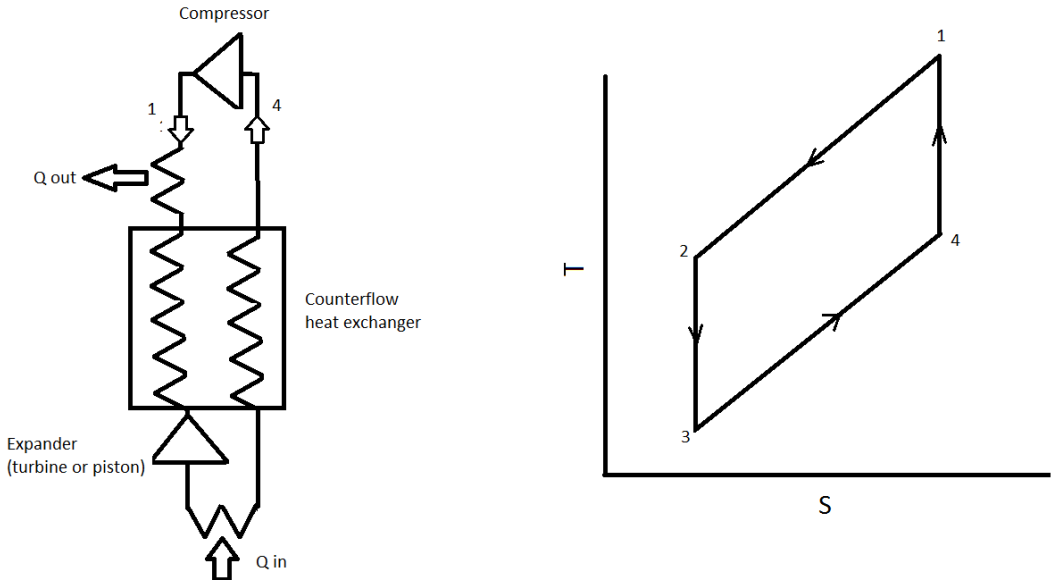

Figure 1-3: Schematic and ideal *T-S* diagram of a Brayton cycle

The GM cryocooler, invented by W Gifford and H McMahon [1] , is a regenerative cycle which stores heat in a regenerator matrix, thus separating the cold and warm gas spaces, and has similarities to the Stirling and Ericsson cycles. The GM cycle incorporates a variant of an industrial air-conditioning compressor and cleans the gas, post compression, with an activated carbon adsorber. The compressor fills a high pressure tank from a low pressure tank. A set of valves alternately connects the cold head to the low and high pressures, producing a pressure oscillation. The GM cycle can thus achieve a low frequency cycle, approximately 1 Hz, with the equivalent of a very large swept volume compression piston from a cheap mass produced compressor. The GM cycle has the following steps, referring to Figure 1-4:

- 1->2 isochoric cooling. With the pressure high and valves closed, the displacer/regenerator moves from the cold end to the warm end, cooling the gas and filling the cold end.
- 2->3 isothermal expansion (via valves). The low pressure valve opens, discharging gas and lowering the pressure. Heat is absorbed from the surroundings.
- 3->4 isochoric heating. The low pressure valve closes and the displacer moves from warm to cold. The gas is warmed as it moves through the regenerator to the warm end.
- 4->1 isothermal compression (via compressor and valves). The high pressure valve opens, pressurising the cold head for the next cycle.

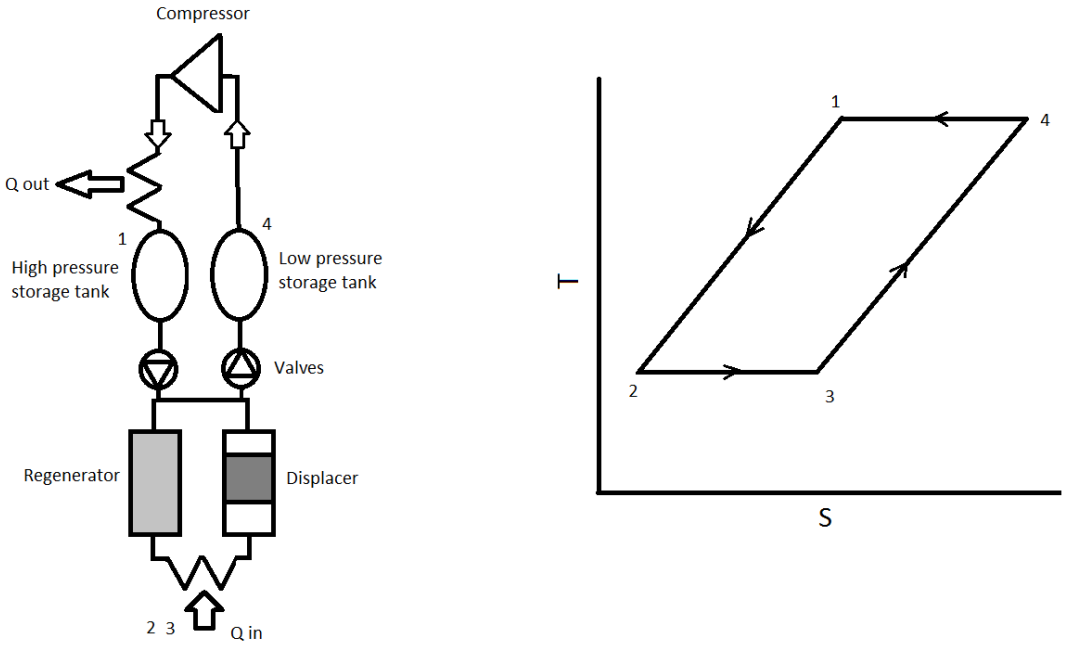

Figure 1-4: Schematic and *T-S* diagram of a GM cryocooler.

The Stirling cryocooler, which is the subject of this thesis, is described in more detail in the next section of this chapter. At this point it is sufficient to note that the Stirling cycle is a regenerative cycle like the GM, the difference being that a Stirling cycle (Figure 1-5) does not have a compressor and valves, but directly works with the pressure wave created by a compression/expansion piston. Hence Stirling machines typically operate faster (30-50 Hz) to achieve usable powers with practically sized pistons.

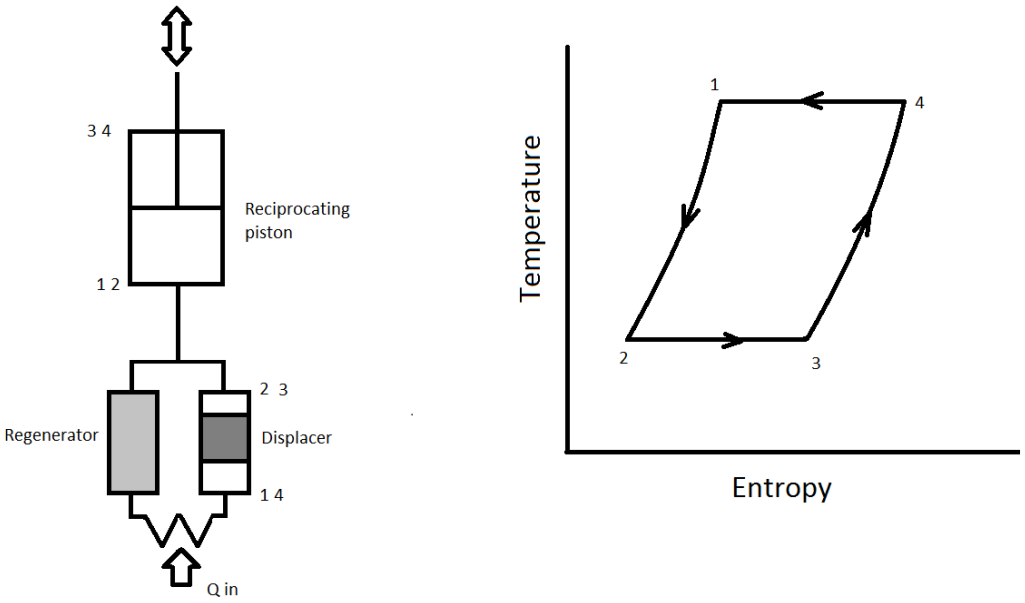

Figure 1-5: Schematic diagram of a Stirling refrigerator

The pulse tube, Figure 1-6, was initially invented in its basic form in 1959 by Gifford and Longsworth [2]; then in the 1980's Mikulin [3] added an orifice phase shifter to create a useful cryocooler. The pulse tube cryocooler is a variation of a Stirling machine where the expansion piston is replaced by a plug of gas in the pulse tube, acting as a virtual piston. A second thermodynamic cycle occurs inside the pulse tube to cause a heat pumping effect that conveniently forces a temperature gradient in the pulse tube and rejects heat at the 'warm end' of the pulse tube. Pulse tube thermodynamics has been a subject of study by Radebaugh [38], Kittel [39], Boer [40] and others, and the reader is directed to these authors if detailed study of pulse tube thermodynamics is desired. A *T-S* diagram is not shown in Figure 1-6 as, in a pulse tube, the gas does not undergo a single cycle, but indeed there are several cycles occurring simultaneously. Kittel [41] and Tucker [42] argue that *T-S* and *p-V* diagrams have limited value for regenerative cycles in general due to the fact that in a real cryocooler, any particle of gas will only partake in part of a cycle, and not the whole cycle.

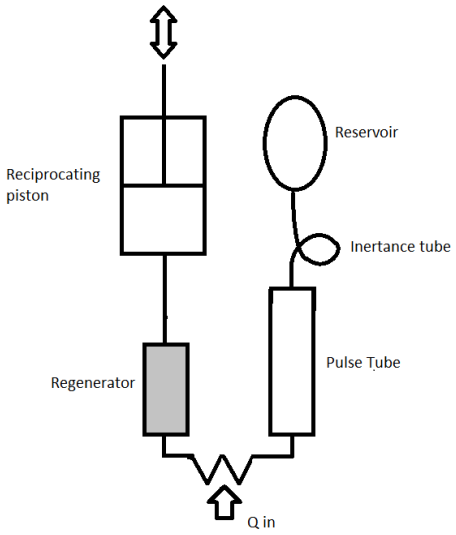

Figure 1-6: Schematic diagram of a pulse tube cryocooler

1.3.2 STIRLING CYCLE DESCRIPTION

The ideal Stirling cycle refers to a closed thermodynamic gas cycle where the working gas undergoes four processes. For a heat pump, the processes, referring to Figure 1-7, are:

- 1->2, isochoric heat transfer,
- 2->3, isothermal compression,
- 3->4, isochoric heat transfer,
- 4->1, isothermal expansion.

Whether it is an engine (net work out) or a refrigerator (net work in), the expansion process absorbs heat and performs work, and the compression process absorbs work and releases heat. In an engine, heat addition occurs at a higher temperature than during heat rejection, and the net work transfer is outwards (which is regarded as positive in the Engineering Thermodynamics sign convention but negative in the Acquisitive sign convention). In a refrigerator the heat addition occurs at a lower temperature than during heat rejection, and the net work transfer is inwards (which is regarded as negative in the Engineering Thermodynamics sign convention but positive in the Acquisitive sign convention).

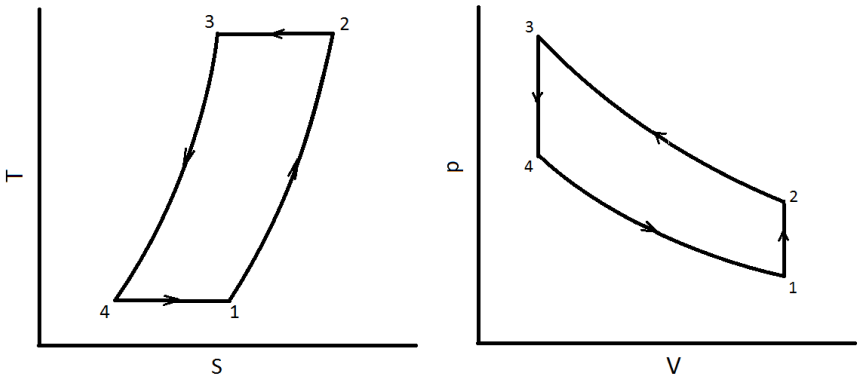

Figure 1-7: *T-S* and *p-V* diagrams for the Stirling cycle in refrigerator mode.

In a real reciprocating machine, the instantaneous accelerations of the piston and displacer that would be required to achieve the sharp corners of the ideal *p-V* diagram are not possible. Instead, the motor-crank or resonant drives used by real machines produce sinusoidal movements. The effect is a rounding of the corners as shown in Figure 1-8.

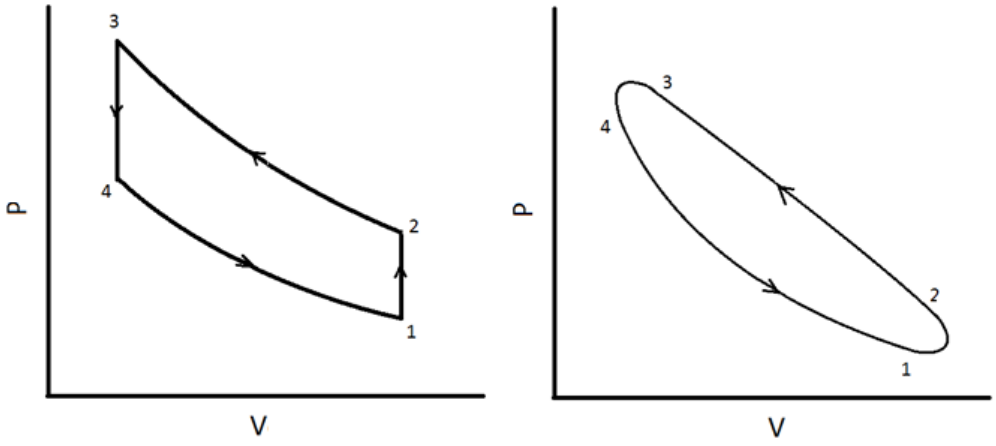

Figure 1-8: *p-V* diagram for the Stirling cycle in heat pump mode. The ideal cycle is on the left and representation of a cycle typically achieved by a real cryocooler is on the right.

1.3.3 CONFIGURATIONS OF STIRLING MACHINES

The three most common embodiments of the Stirling cycle are known as the alpha, beta and gamma configurations:

The alpha configuration, Figure 1-9, has a compression piston and an expansion piston that are separated by a regenerator. Alpha Stirling cryocoolers are not common as they require cold expansion pistons, which are difficult to make. The pulse tube refrigerator is close to an alpha Stirling cooler as it uses a plug of gas in the pulse tube as a virtual expansion piston. (The pulse tube has an additional heat pumping cycle in the pulse tube gas [40]).

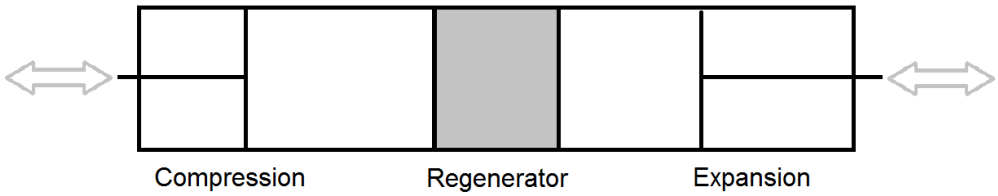

Figure 1-9: Schematic diagram of an alpha Stirling configuration.

The beta configuration, Figure 1-10, uses a single driven piston to perform both compression and expansion of the working gas. A moving displacer (sharing the same volume as the working piston) pushes the gas through the regenerator so that the majority of gas is warm during compression and cold during expansion. The regenerator can be external, as in the figure, or integrated into the displacer. The Philips Stirling cryocooler is a beta configuration driven by cranks. Sunpower's Stirling cryocooler [43] is a free-piston beta configuration with a linear motor driving the compression piston.

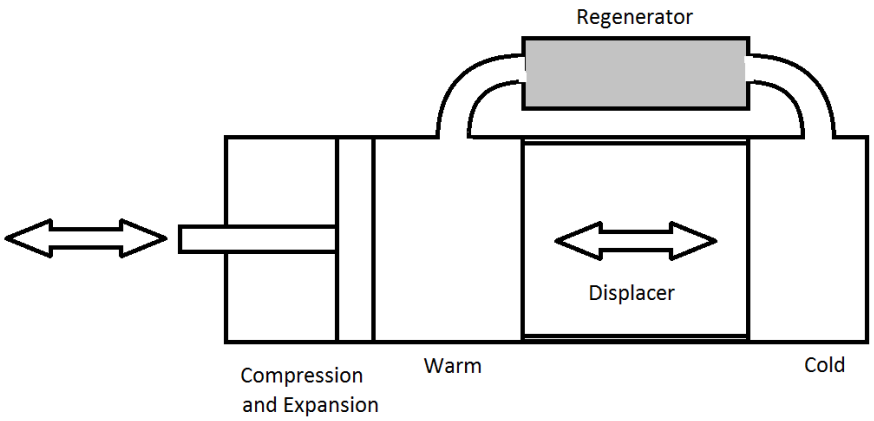

Figure 1-10: Schematic Diagram of a beta Stirling configuration.

The gamma configuration, Figure 1-11, works the same as the beta configuration except that the compression piston and displacer work in separate volumes that are connected by a transfer passage. Most tactical and space coolers [44] are beta configuration.

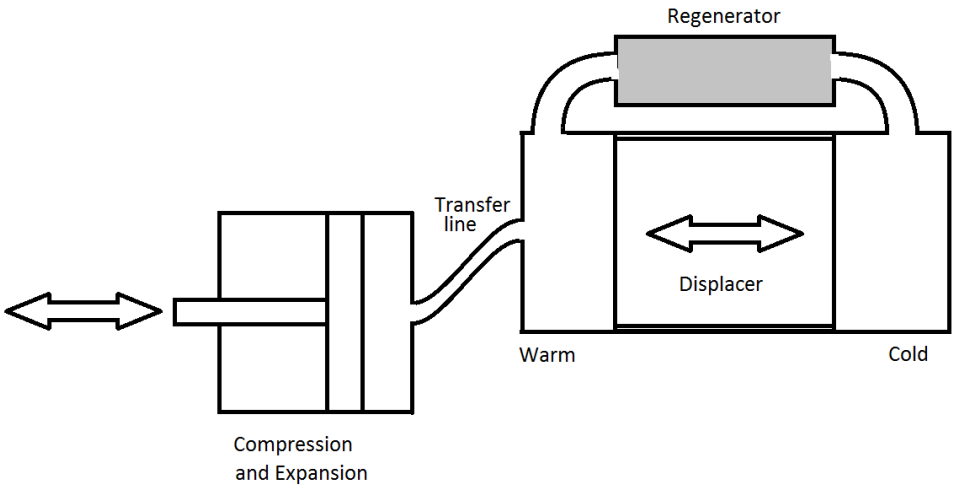

Figure 1-11: Schematic diagram of a gamma Stirling configuration.

In practical Stirling machines, the discrete movements of the ideal cycle degrade to sinusoids by the crank or inertial effects of a resonance driven movement of the pressure wave generator. The sinusoidal movement still allows a good approximation of the ideal case as velocities are low at top and bottom dead centres and fastest mid-stroke. The best approximation to the ideal occurs when the displacer movement leads the pressure wave generator piston by 90°. Inertial effects near resonance shift the displacer's phase angle and amplify its movement, so each machine will have an optimal operating frequency for efficiency and another for output power. One advantage of the beta and gamma Stirling arrangements is that the expansion work is recovered by the driving piston and is easily captured for the next compression by inertia in the pressure wave generator. The displacer does no real work other than overcoming flow losses in the regenerator.

1.3.4 FREE-PISTON STIRLING SYSTEMS

The type of Stirling machine studied in this thesis is known as a free-piston Stirling cryocooler. A free-piston Stirling machine is a beta or gamma configuration Stirling machine that does not have an actuator to move the displacer, but relies on the oscillating gas pressure across its two ends to achieve movement. The displacer is a spring-mass system with a resonant frequency and the pressure differential across it provides an exciting force. In its simplest form the pressure drop across the regenerator provides the exciting force. An improvement uses a guide rod whose shaft protrudes into a 'bounce space' that is at a constant average pressure. The area

of the guide rod shaft produces an imbalance in the pressure force between the ends of the displacer and hence an oscillating force with a better phase relationship to the driving pressure wave.

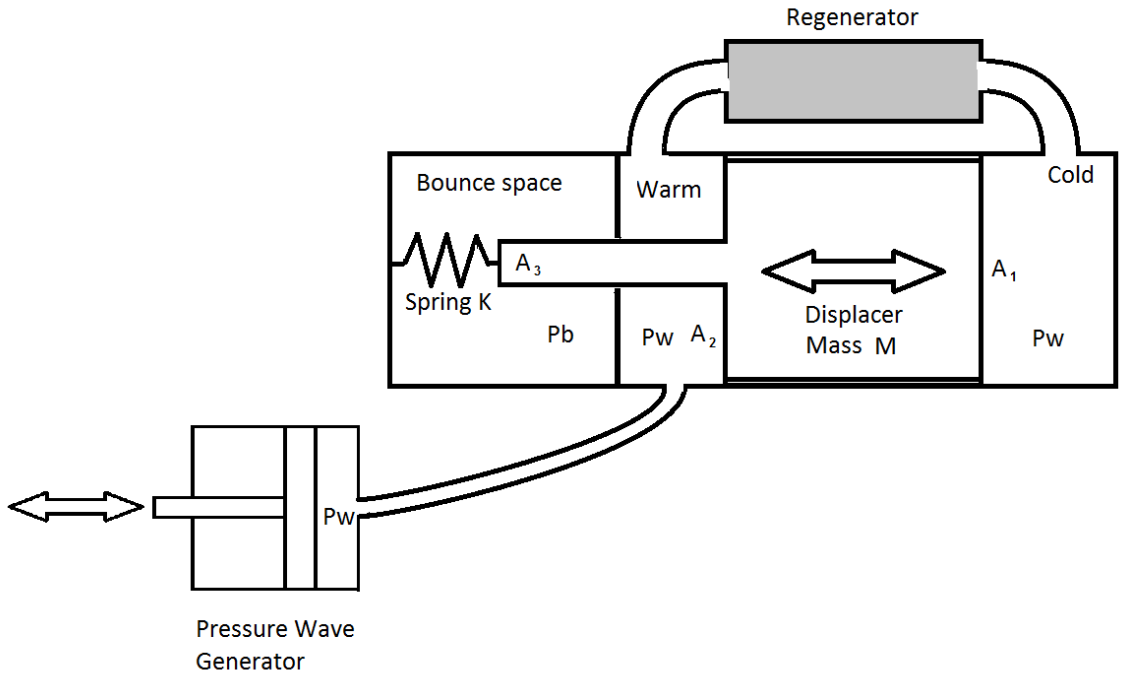

Figure 1-12: Typical free-piston Stirling layout.

Figure 1-12 shows a typical free-piston Stirling system. An oscillating piston in the pressure wave generator produces a pressure wave. The pressure wave, $p_w(t)$, is transferred to the warm side of the cooler via a transfer line, and then to the cold side via the regenerator. For simplicity it can be assumed that there are no pressure gradients due to flow and, since the time to transfer gas throughout the machine is negligible, p_w is uniform throughout. The displacer is supported by a shaft which protrudes into the bounce space. The fit of the shaft in its guiding cylinder is good but not perfect so the bounce space pressure, p_b, is close to the average pressure of the system. The area of the cold side of the displacer is A_1 and the warm side of the displacer is A_2, which is A_1 minus the shaft area A_3.

Figure 1-13 shows the phase angles and typical movement of a free-piston Stirling refrigerator. Movement of the displacer is driven by the difference between the pressure wave, $p_w(t)$, and the bounce space pressure p_b with the force on the displacer being

$$F(t)=A3\ (p_w(t)-p_b) \qquad 1\text{-}3$$

The imbalanced force is 180° out of phase with the compression piston. The displacer has a mass M and spring with stiffness K, so it has a resonant frequency,

$$\omega = \sqrt{\frac{K}{m}} \qquad 1\text{-}4$$

At resonance, the phase response of the displacer position lags the forcing function by 90° [45]. Added to the 180° phase angle of the forcing function, the displacer movement then lags the compression piston by 270°, which is the same as leading by 90°, the ideal for gamma Stirling refrigerators. In reality, gas takes time and pressure to get from place to place and there is damping in the machine so the optimal phase angle is not 90° but nearer 50° or 60°. It is possible to tune a free-piston system by varying the resonant and operating frequencies, and damping of the displacer.

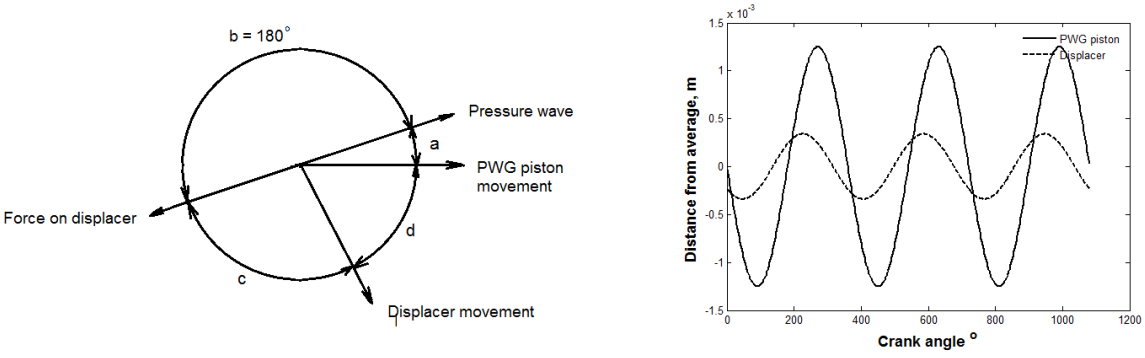

Figure 1-13: Left, Phase angles for a free-piston Stirling refrigerator. Angle a is the phase between the pressure wave and PWG piston that gives the work input in the cycle. Angle b represents the effect of area A3 which makes the force on the displacer 180 degrees out of phase with the pressure wave. Angle c is the phase angle of the displacer's dynamic response. Angle d is the phase difference between the PWG piston movement and the displacer movement. Right, a typical PWG piston and displacer relative movements for the diaphragm free piston concept.

1.4 Description of Modelling tools

Several modelling tools were used to analyse flows and heat transfer in this work. Each had its own advantages and limitations. The main tools were Sage and ANSYS® CFX:

1.4.1 SAGE

Sage [31] is a software tool developed and supported by David Gedeon of David Gedeon Associates, Athens, Ohio. Gedeon, a contemporary expert in Stirling cycle modelling, used Sage to design Sunpower's range of products [43]. Sage has since become an industry standard modelling system for oscillating thermodynamic systems including Stirling and pulse tube cryocoolers.

Sage is a one-dimensional frequency domain modeller designed for modelling oscillating thermodynamic systems. It presents an object-oriented approach to solving dynamic problems where standard objects, such as volumes and heat exchangers, are connected together using mass-flow, heat-flow, force or displacement connections. Sage then solves the simultaneous equations of motion and heat transfer for the objects in the frequency domain at a given frequency. The outputs are in the form of amplitudes, phase angles and cycle-averaged quantities. Objects can be solid, such as masses, springs, or conductors; or fluid, such as cylinders and channels, or mixes of both such as a regenerator matrix with both gas and solid properties. Interactions between solid and fluid can be in the form of pressure force, heat transfer or fluid flow pressure loss.

Sage was developed to analyse Stirling engine and cryocooler systems. A later addition to Sage has been the compliance tube object to model the pulse tube cryocooler and its engine equivalent, the thermo-acoustic Stirling pressure wave generator. The origins of Sage in Stirling machines mean it has been optimised for standard piston-cylinder based geometry where the cylinder bore and piston stroke are of similar magnitude. This may provide a limitation for the concept to be explored in this thesis as, with diaphragm systems, the stroke is two orders of magnitude less than the cylinder diameter. Moreover, diaphragm systems have a relatively small hydraulic diameter – being equivalent to closely spaced flat plates - and exhibit significant radial flows.

In spite of its limitations for radial flow, Sage is a fast solver and provides sufficiently accurate results for optimisation of cryocooler geometry in the first part of the design process. Many cryocooler developers [46] use Sage for the first part of the design, then use CFD to refine critical areas and finally use experimental optimisation to reach the final cryocooler design.

1.4.1.1 Governing equations

Sage's governing equations start with the Navier-Stokes equations in integral form, with specific conditions for the types of problems that Sage has been designed to model. Body forces are neglected and the control volume *v* is not fixed. The inlet and exit boundaries are fixed and side boundaries are allowed to move. A rubber tube with space and time varying cross section is a useful image of the general control volume in Sage. The general forms of the governing equations, in Sage's nomenclature, are:

Continuity, the time rate of change in mass in the volume equals the rate that the mass leaves through its surface boundaries,

$$\frac{d}{dt}\int_v \rho dv + \int_s \rho \boldsymbol{n}\cdot\boldsymbol{V}_r ds = 0 \qquad 1\text{-}5$$

Momentum, the net force acting on the surfaces equals the change of momentum of the control volume less the momentum leaving through its surface boundaries,

$$\frac{d}{dt}\int_v \rho \boldsymbol{V} dv + \int_s [(\boldsymbol{n}\cdot\boldsymbol{V}_r)\rho\boldsymbol{V} - \boldsymbol{n}\boldsymbol{\sigma}] ds = 0 \qquad 1\text{-}6$$

Energy, the rate of change of internal plus kinetic energy, less the energy leaving the boundaries equals the net heat flux plus the mechanical work done on the boundaries,

$$\frac{d}{dt}\int_v \rho e dv + \int_s n\cdot(\rho e\boldsymbol{V}_r - \boldsymbol{\sigma}\boldsymbol{V} - \boldsymbol{q}) ds = 0 \qquad 1\text{-}7$$

Where

v = control volume
s = surface of volume *v*
e = mass-specific total gas energy, $\varepsilon+u^2/2$
ε = mass-specific internal gas energy
$\boldsymbol{n}$ = unit normal of surface *s*
$\boldsymbol{q}$ = heat flux vector
t = time
$\boldsymbol{V}$ = flow velocity vector in Netwonian-frame
$\boldsymbol{V}_r$ =flow velocity vector , boundary-relative
ρ = gas density
$\boldsymbol{\sigma}$ = stress tensor

The general equations are then converted into one-dimensional differential equations in the conservative form. In the equations, dv is replaced by *Adx* where *A* is the flow area and *x* the flow direction, the limit *Δx->dx* is taken and then divided by *dx*. For example, $\frac{d}{dt}\int_v \rho dv$ becomes $\frac{\partial}{\partial t}(\rho A)$. The reader is directed to the Sage manual for more details of the derivation if desired. The equations then become:

continuity

$$\frac{\partial \rho A}{\partial t} + \frac{\partial \rho u A}{\partial x} = 0 \qquad 1\text{-}8$$

momentum

$$\frac{\partial \rho u A}{\partial t} + \frac{\partial u \rho u A}{\partial x} + \frac{\partial P}{\partial x} A - FA = 0 \qquad 1\text{-}9$$

gas energy

$$\frac{\partial \rho u e A}{\partial t} + P\frac{\partial A}{\partial t} + \frac{\partial}{\partial x}(u\rho e A + uPA + q) - Q_w = 0 \qquad 1\text{-}10$$

The three implicit solutions variables are ρ, ρuA and ρe. Terms F, Q_w and q are empirical terms with separate definitions for each of the kinds of objects provided by Sage.

For example in a heat exchanger object of hydraulic diameter d_h and length L, the viscous pressure gradient F is formulated in terms of the Darcy friction factor f and a local loss coefficient K as

$$F = -\left(\frac{f}{d_h} + \frac{K}{L}\right)\frac{\rho u|u|}{2} \qquad 1\text{-}11$$

and the heat transfer in the energy equation is in the form of

$$Q_w = hS_x(T_w - T_g) = N_u\left(\frac{k}{d_h}\right)S_x(T_w - T_g) \qquad 1\text{-}12$$

where k is conductivity, S_x the wetted perimeter, $(T_w\text{-}T_g)$ the temperature difference between the wall and the section average gas temperature, and N_u is the Nusselt Number.

Sage makes extensive use of complex formulations for the Nusselt number and other variables to account for phase differences in the oscillating flow it models. The reader is directed to the Sage manual's extensive theory section if more detail is required.

1.4.2 CFD ANALYSIS WITH ANSYS® CFX

ANSYS® CFX is the commercial CFD code used to model flow and heat transfer in the diaphragm Stirling cryocooler that is the subject of this thesis. This section is not a complete description of the CFD method but a summary intended to give a reader new to the CFD methodology sufficient understanding to be able to follow the use of CFD as a tool in this thesis. A brief description of the method and underlying model will be given; if the reader wishes further description of the derivation of the code then they are referred to texts such as Veersteg and Malalasekera [47], which provides an excellent description of the finite volume method, or to the ANSYS® CFX documentation. This section introduces what CFD is, the underlying equations of the finite volume method and the method of use.

1.4.2.1 What is CFD?

CFD is a computational technique whose development has benefited from the exponential growth of computing power over the last four to five decades. It is now a tool available on high-end engineering workstations and, with the graphics developed for computer aided design (CAD), has had its user interface made much more usable. Integration of CFD into CAD packages has further increased usability as geometry can be taken straight from the design. However, skill and understanding are still required to use CFD properly if results with any form of accuracy and correct interpretation are required for design decisions.

CFD uses the same overall premise as the now common Finite Element method for structural analysis. This is that a complex geometry can be analysed by breaking it up into many small discrete blocks, called elements. The equations for each element are solvable, and the elements are all inter-connected. The solution for the whole is therefore a simultaneous set of equations that can be solved numerically to find an approximate solution. If the elements are small enough then the approximate solution is very close to the real solution, certainly close enough for engineering purposes.

CFD is however more complex than structural finite element analysis as it involves transport phenomena, such as mass and enthalpy flow and, by definition, is dynamic with the time domain involved. There are four common CFD solution methods in use: finite element, which solves for the degrees of freedom at the nodes (corners or control points on the element edges) and uses simple piecewise (linear or quadratic) functions in-between; finite difference, which again solves for the nodes but uses derivatives at each point approximated by finite differences to create the equations for solution; spectral methods, which approximate unknowns with truncated Fourier series or Chebyshev polynomials, solving for the coefficients; and finally the finite volume method which solves for the unknowns at the centre of each volume element. The

finite volume method is the method used by ANSYS® CFX and the majority of commercial codes and is discussed in more depth in the following section.

1.4.2.2 The Finite volume method

The Finite volume method assumes that each element is a small finite volume, Figure 1-14, that can be described by the conditions, and gradients, at the centre of the element. Each face is a distance of *½ δx* from the centre point, therefore properties for each face can be calculated using the value at the centre and the gradient. So, for example, the pressures on the faces normal to the *x* axis are,

$$p - \frac{\partial p}{\partial x}\frac{1}{2}\delta x \quad \text{and} \quad p + \frac{\partial p}{\partial x}\frac{1}{2}\delta x. \qquad 1\text{-}13$$

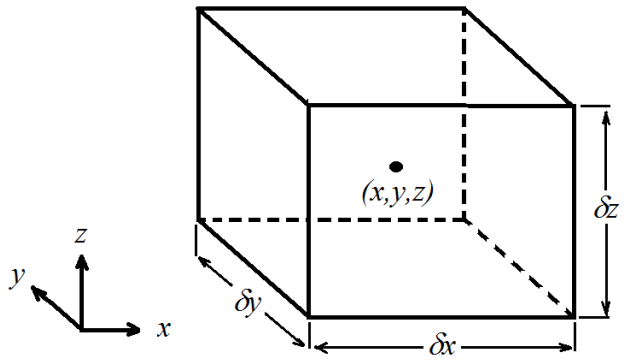

B

Figure 1-14: A finite volume element

An important approximation of the finite volume method is that the gradient inside the element is linear. If in the results of an analysis, the gradient of a property lies entirely inside one element, then what is observed is the gradient of the element, not the real situation. To be confident that the results reflect a physical situation, the gradient should be over several elements. For example, if the temperature of the gas next to a wall goes from the bulk gas temperature to the wall temperature in one element, then the conduction of heat through the element to the wall will be calculated for a linear gradient over the size of the element, and will likely be less than the real situation being modelled. If the element size is reduced, then the gradient will be over a smaller distance, until the element size is small enough to achieve a gradient over several elements and then the conduction result can be trusted.

1.4.2.3 Governing equations

The finite volume method is based on satisfying four conditions for each element: mass conservation, momentum conservation, energy conservation and the equations of state. Veersteg and Malalasekera [47] present a derivation of the equations if the reader is interested.

The first condition is mass conservation, which states that the rate of increase of mass inside the element equals the net rate of mass flow into the element. For a unit volume this can be expressed as,

$$\frac{\partial \rho}{\partial t} + \nabla \cdot (\rho \boldsymbol{U}) = 0 \qquad 1\text{-}14$$

where $\boldsymbol{U}$ is the velocity, ρ the density, and t is the time.

The second condition is momentum conservation, which is Newton's second law and states that the rate of increase of momentum equals the sum of the forces on the particle, or

$$\frac{\partial (\rho \boldsymbol{U})}{\partial t} + \nabla \cdot (\rho \boldsymbol{U} \otimes \boldsymbol{U}) = -\nabla p + \nabla \cdot \tau + \boldsymbol{S}_M \qquad 1\text{-}15$$

where the stress tensor, τ, is related to the strain rate by

$$\tau = \mu \left(\nabla \boldsymbol{U} + (\nabla \boldsymbol{U})^T - \frac{2}{3} \delta \nabla \cdot \boldsymbol{U} \right) \qquad 1\text{-}16$$

$\boldsymbol{S}_M$ represents body forces on the particle, such as gravity. The dyadic operator, $\otimes$, is used to multiply the momentum by the velocity and achieve a vector form so

$$\nabla \cdot (\rho \boldsymbol{U} \otimes \boldsymbol{U}) = \begin{bmatrix} \frac{d}{dx}(\rho U_x U_x) + \frac{d}{dy}(\rho U_y U_x) + \frac{d}{dz}(\rho U_z U_x) \\ \frac{d}{dx}(\rho U_x U_y) + \frac{d}{dy}(\rho U_y U_y) + \frac{d}{dz}(\rho U_z U_y) \\ \frac{d}{dx}(\rho U_x U_z) + \frac{d}{dy}(\rho U_y U_z) + \frac{d}{dz}(\rho U_z U_z) \end{bmatrix} \qquad 1\text{-}17$$

The third condition is the conservation of energy, which is the first law of thermodynamics, and states that the rate of increase of the internal energy of the element equals the net inflow of energy, or,

$$\frac{\partial (\rho h_{tot})}{\partial t} - \frac{\partial p}{\partial t} + \nabla \cdot (\rho \, \boldsymbol{U} \, h_{tot}) = \nabla \cdot (\kappa \nabla \boldsymbol{T}) + \nabla \cdot (\boldsymbol{U} \cdot \tau) + \boldsymbol{U} \cdot \boldsymbol{S}_M + \boldsymbol{S}_E \qquad 1\text{-}18$$

where h_{tot} is the total enthalpy, includes kinetic energy and is related to the static enthalpy $h(p,T)$ by

$$h_{tot} = h + \frac{1}{2} \boldsymbol{U}^2; \qquad 1\text{-}19$$

κ is the thermal conductivity; S_M represents momentum sources (such as work done on the gas); and S_E energy sources (such as combustion). Or, in words, the rate of increase in the total enthalpy minus the rate of change in pressure energy, plus the energy flow due to convection of mass into the element equals the energy inflow due to thermal diffusion plus work done by viscous stress (damping), energy from a change in momentum and energy from other sources (for example reactions).

And finally, the equations of state need to be satisfied. Equations of state can be for incompressibility, ideal gases, Redlich Quong gas model, Peng Robinson model or real gas behaviour. In this analysis ideal gas behaviour is sufficient. Conjugate heat transfer is available where heat transfer can be calculated for solid domains without flow. Effects such as buoyancy, multi-component flow and rotational forces can be modelled by CFX but are not important to this analysis. For the purposes of this work, helium is assumed to be an ideal gas. The Ideal gas equations of state are:

$$\rho = \frac{p}{RT} \qquad 1\text{-}20$$

where p is the absolute pressure, R is the specific gas constant T temperature.

$$dH = C_p dT \qquad 1\text{-}21$$

where H is enthalpy, C_p is the heat capacity at constant pressure.

$$C_p = C_p(T) \qquad 1\text{-}22$$

which states that C_p is a function of temperature, defined for the gas in a table.

1.4.2.4 Method of use

The CFD method involves three stages: pre-processing, solving and post-processing.

Pre-processing includes definition of the geometry and computational domains, definition of the mesh of elements (finite volumes), fluid and material properties definition, set up of the physical phenomena to be modelled, and set up boundary conditions.

The geometry is usually defined in a 3D CAD package; such as Solidworks which was used for this work. The CAD geometry is then exported through an intermediate format, STEP for example, and imported into the CFD software for meshing.

Meshing involves taking the CAD generated 3D model and breaking it up into elements. The process is largely automated although user input is required to produce a sensible mesh with

elements that are neither too large nor too small. Avoidance of highly distorted elements (where one dimension is more than an order of magnitude different from the others) is essential for stable analysis and accurate results. Figure 1-15, left, shows a section of geometry that has been meshed with hexahedral elements to provide a structured mesh, and on the right an unstructured mesh with tetrahedral elements, which allow complex geometry changes to be modelled.

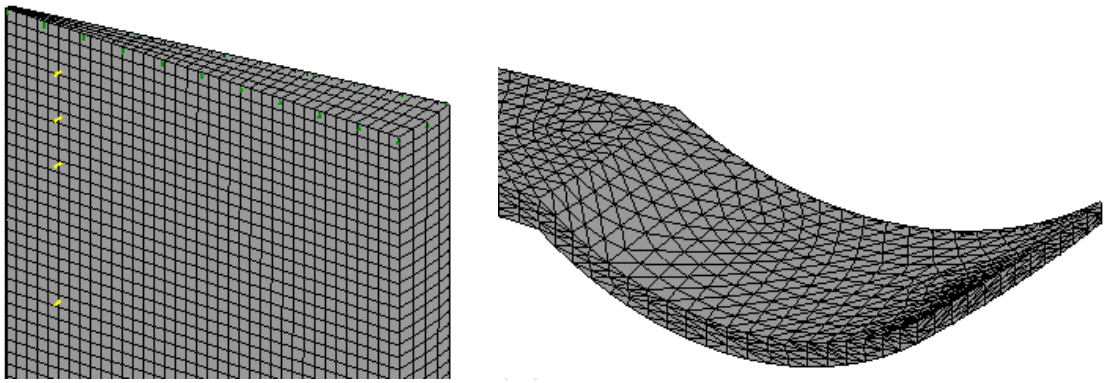

Figure 1-15: Two types of mesh: Left a hexahedral mesh, and right a tetrahedral mesh.

Once the mesh has been defined, the pre-processor is used to define fluid properties and boundary conditions for surfaces in the model. Boundary conditions define how the fluid interacts with the walls, or define inlet or outlet conditions of mass flow and pressure. In this work, the analyses are for completely closed volumes so inlet/outlet conditions are not used. Wall conditions, however, are important, with the three main wall boundary conditions being: adiabatic walls, with no heat transfer; isothermal walls, which have set temperatures and allow heat to transfer to the fluid; and symmetry walls, which assume no heat or mass flow across the boundary and no resistance along the boundary. Symmetry conditions are used on the edges of repeating sections.

Once the pre-processor has been used to define the model for solving, the simultaneous equations previously mentioned are solved using a 'Solver' program. The solver is separate from the pre- and post- processors as the solution can take a long time; separate pre- and post-processors allow the operator to look at previous runs and set up new runs while the solver is working in the background, or on another machine. For more information about different solution methods, the reader is referred to the ANSYS® CFX solver manual.

The final step in a CFD analysis is analysing the results produced by the solver. For these purposes, ANSYS provides a post-processor program that reads the copious solver outputs and produces graphical representations of the flow field with plots such as streamlines, as shown in Figure 1-16, velocity vectors and contour plots.

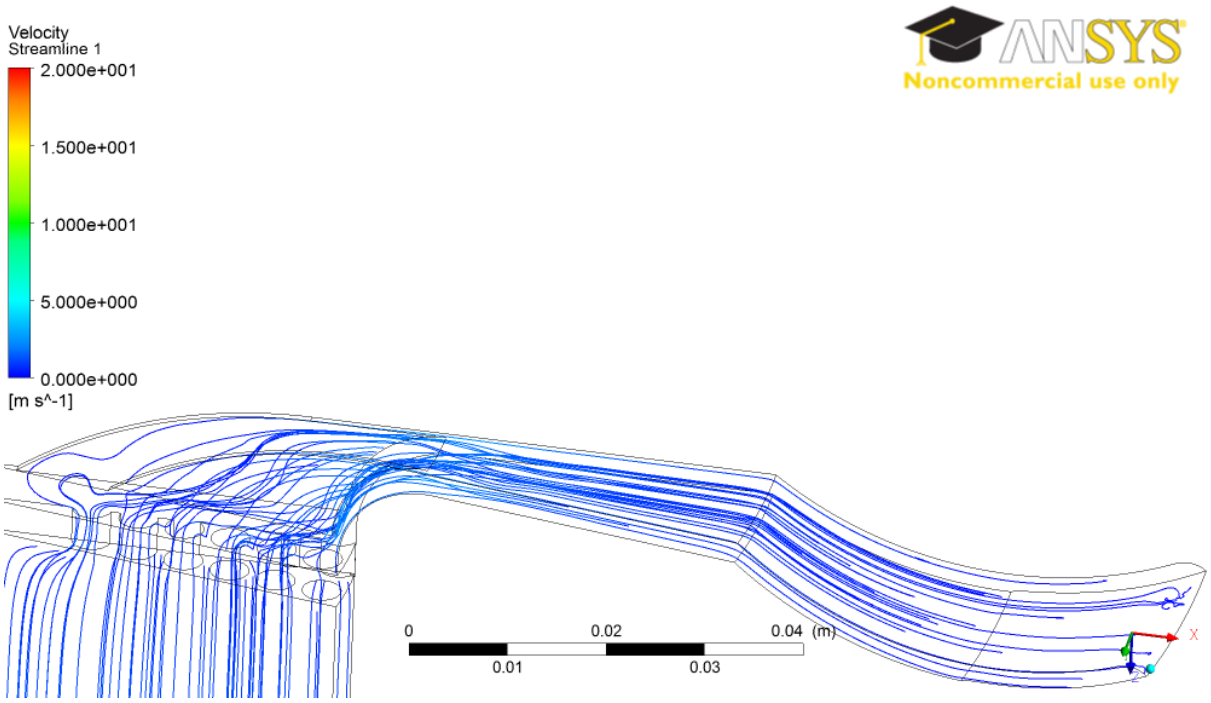

Figure 1-16: Example of a streamline plot from a post processor

1.4.2.5 Turbulence

At low Reynolds numbers ($Re = \frac{\rho U t}{\mu}$), fluid flow is orderly and dominated by viscosity; this is called laminar flow. Laminar flow can be analysed using continuity and the Navier-Stokes equations. As *Re* increases, instabilities (often from geometry changes) cause vortices and eddies to form in the flow, transferring momentum and enthalpy on a macroscopic scale. At high *Re*, shear and momentum forces are high enough to overcome viscous stress and the instabilities cause mixing in the flow across a whole range of scales; the flow is called turbulent. For each type of flow, there is a *Re* below which the flow is principally laminar and a *Re* where the flow is fully turbulent. In-between is a transition region where the flow is typically chaotic and vortices and eddies dominate.

CFD techniques can solve for laminar flow with the equations for continuity listed in equations 1-14 to 1-22. For turbulent flow, modifications to the governing equations and boundary conditions are required to account for the extra momentum and enthalpy transport due to the transverse mixing in the turbulence. Most engineering flow problems occur at high *Re* and require turbulent solutions so a number of turbulent flow models have been developed for CFD; the most commonly used by commercial CFD is the *k-ε* model. The reader is directed to texts such as Versteeg and Malalasekera or the ANSYS® CFX solver manual for a full description of the *k-ε* and other turbulent flow models.

Unlike most engineering flows, the flows encountered in this work are oscillating flows, which stop and reverse direction every cycle. The flow can thus transition between laminar and turbulent flow twice during each cycle. Barreno et al [51] and Simon [50] studied flows in Stirling machine heat exhcangers and observed that the accelerating parts of flow exhibited laminar flow and that the deceleration parts exhibited turbulent flow characteristics. A key factor was the time required to establish turbulence. The ANSYS® CFX solver requires the whole model to be either laminar or turbulent, so a choice has to be made by the user as to which is more appropriate for the situation. The diaphragm Stirling concept in this study has oscillating flows in its heat exchangers but different hydraulic diameters and flow velocities to the Stirling machines studied by Barreno and Simon. Moreover, this work concerns a cryogenic refrigerator and not an engine, so the fluid properties will differ as a very hot heat exchanger is swapped for a very cold one. The choice and merits of laminar or turbulent flow models will have to be made during the validation and analysis phases of the work.

1.4.2.6 Porous media

The regenerator in a Stirling cryocooler is a fine matrix of material with a very high surface area whose purpose is to transfer heat to and from the gas during the cycle. The hydraulic diameter of the flow passages in a typical regenerator matrix is in the order of 30 to 60 microns. Directly modelling such structures, containing many thousands of passages, would be prohibitively expensive (computationally). CFD methods have been developed to model porous structures, such as regenerators, with average properties. The ANSYS® CFX porous media model is a generalisation of the Navier-Stokes equations and Darcy's law as commonly used for porous regions. The use of the porous media model in CFX requires the input of five parameters: the volume porosity ratio γ, the interfacial area ratio A_r, the heat transfer coefficient h_f, Darcy resistance loss coefficient R, and the diffusivity Γ.

The volume porosity ratio, γ, is defined as the ratio of the void volume, V', to the total volume, V, of the domain, or,

$$V'=\gamma V \qquad 1\text{-}23$$

which, for an isotropic porous medium, implies a flow area defined by the area porosity tensor $\boldsymbol{K}$. In ANSYS CFX, $\boldsymbol{K}$ is isotropic so $\boldsymbol{K}^{ij}=\gamma\delta^{ij}$ (δ is the identity matrix). The flow area $\boldsymbol{A'}$ is therefore

$$\boldsymbol{A'}=\boldsymbol{K}\cdot\boldsymbol{A} \qquad 1\text{-}24$$

The conservation and momentum equations become,

$$\frac{\partial}{\partial t}\gamma\rho+\nabla\cdot(\rho\boldsymbol{K}\cdot\boldsymbol{U})=0 \qquad 1\text{-}25$$

and,

$$\frac{\partial(\gamma\rho\boldsymbol{U})}{\partial t}+\nabla\cdot(\rho(\boldsymbol{K}\cdot\boldsymbol{U})\otimes\boldsymbol{U})-\nabla.\left(\mu_e\boldsymbol{K}\cdot\left(\nabla\boldsymbol{U}+(\nabla\boldsymbol{U})^T-\frac{2}{3}\delta\nabla\cdot\boldsymbol{U}\right)\right)$$

$$=-\gamma\nabla p+\gamma S_M \qquad 1\text{-}26$$

where $\boldsymbol{U}$ is the true velocity, μ_e the effective viscostity, and S_M a momentum source which can be written as $-\boldsymbol{R}\cdot\boldsymbol{U}$ (where $\boldsymbol{R}=(R^{ij})$ and represents the resistance to flow in the porous medium). In the limit of large resistance, S_M, a large adverse pressure gradient, ∇p, has to be set up to balance the resistance; the terms on the left become small compared to S_M and ∇p , and equation 1-26 reduces to

$$\boldsymbol{U}=-\boldsymbol{R}^{-1}\cdot\nabla p \qquad 1\text{-}27$$

which is a version of Darcy's law, noting that $\boldsymbol{U}$ is the actual fluid velocity through the porous media. The Darcy resistance coefficient $\boldsymbol{R}$ determines the pressure and momentum losses through the media.

Heat transfer in the gas can be modelled by,

$$\frac{\partial}{\partial t}(\gamma\rho h) + \nabla\cdot(\rho\boldsymbol{K}\cdot\boldsymbol{U}H) - \nabla\cdot(\Gamma_e\boldsymbol{K}\cdot\nabla H) = \gamma S_k^h + Q_{fs} \qquad 1\text{-}28$$

where H is the gas specific enthalpy, Γ_e is an effective thermal diffusivity, S_k^h is a heat source or sink, and Q_{fs} is heat transfer between the gas and the solid phase of the porous medium. Similarly heat transfer in the solid phase of the porous media is

$$\frac{\partial}{\partial t}(\gamma_s\rho_s C_s T_s) + \nabla\cdot(\rho\boldsymbol{K_s}\cdot\boldsymbol{U}C_s T_s) - \nabla\cdot(\lambda\boldsymbol{K}\cdot\nabla T_s) = \gamma_s S_s^T + Q_{sf} \qquad 1\text{-}29$$

where $\gamma_s = 1-\gamma$ and the interfacial heat transfer between the fluid and solid, S_s^T is a heat source for the solid. In this thesis, the component that is to be modelled with the porous media model (the regenerator) has no heat source or sink, so S_s^T and S_k^h are zero and can be ignored. Q_{fs} is calculated using an overall heat transfer coefficient h_f using

$$Q_{fs} = -Q_{sf} = h_f A_s\left(T_{matrix} - T_{gas}\right) \qquad 1\text{-}30$$

The heat transfer coefficient is an input parameter to CFX so has to be empirically determined. The interfacial area A_s is calculated from the volume and interfacial area ratio, A_r, as

$$A_s = A_r\, V. \qquad 1\text{-}31$$

A_r, is defined as the ratio of the matrix surface area to the domain volume and is directly calculable from the geometry of the porous medium.

.

1.5 Novel aspects of the work

The work described here is unique as it is the first to use the metallic diaphragm pressure wave generator (DPWG) technology, previously invented by the author [50], in a free-piston Stirling cryocooler. The concept to be investigated involves using diaphragms as flexure bearings and seals for the displacer in a free-piston Stirling arrangement. Two diaphragms will be used to support the displacer and balance out the average gas pressure across it. A third membrane is used to achieve the bounce space necessary for correct phasing of the pneumatically driven displacer (refer to Section 1.3.4 for the function of the bounce space in free-piston Stirling dynamics). The DPWG will be used to generate the pressure wave and act as the compression piston. In this way a Stirling cryocooler will be made with the inherent efficiency of Stirling machines and without the disadvantage of oil seals (as in Philips Stirling machines), expensive tight clearances required by flexure bearings, or 3D flow problems found in large pulse tube cryocoolers.

This arrangement is unique and developing it into a useful technology presents some significant challenges, such as:

- Analysing the heat transfer in the radial expansion and compression spaces. The expansion space of a diaphragm system is a radial oscillating flow field between plates with a varying gap. Cooke-Yarborough [51], Kornhauser and Smith [32], [52] and Gedeon [53] all investigated different aspects of heat transfer in oscillating flows. Cooke-Yarborough's work was the most relevant to this case as he analysed the flow between parallel plates whilst the others analysed heat transfer in cylindrical containers. Cooke-Yarborough was constrained by the comparatively limited computing power available at the time.
- The expansion diaphragm will be cryogenically cold. Fatigue strength data for materials at cryogenic temperatures is not as extensive as at room temperature due to the time taken for such testing. Data that exists suggests that the fatigue strength of many metals increases with decreasing temperature[54]. The brittle transition temperature is however important.
- The free-piston system is a dynamic system and the diaphragm's short movement and large area have considerably different proportions to a standard free-piston system. Areas, masses, movement amplitudes and spring rates are all different from free-piston Stirling systems analysed to date.

- Expansion heat transfer will be performed at cryogenic temperatures where heat capacity, density, sonic speed, and heat conduction properties differ from those at ambient temperature. This will add complexity to the analysis.

2 LITERATURE

2.1 Stirling cycle

2.1.1 HISTORY

In 1816 Robert Stirling invented and patented a practical gas engine that used a regenerator, or economizer as he named it. The regenerator's task was to alternately warm and cool the working gas as it shuffled back and forwards between the hot expansion and cold compression cylinders in his engine. Stirling's engines were used in the 1800s as a safe alternative to steam as the quality of the wrought iron used for boilers was variable. Internal combustion engine development and eventual domination as a prime mover in the early 1900s relegated Stirling's invention into obscurity until the 1940s when a development team at Philips saw it as a solution to fuel issues in the third world.

2.1.2 PHILIPS STIRLING

Philips started development of an external combustion engine in the 1940s to power generators for valve radio equipment in third world countries and for military situations where very quiet generator operation might be important. Philips' developed an engine based on Stirling's cycle. Philips' engine produced 200 W of electrical power but could not be manufactured at a competitive cost. The advent of the transistor with its low power consumption removed the engine's purpose and development stopped. During the engine development programme, the Philips team showed that the cycle could be reversed and used very effectively as a cryogenic refrigerator. Today the Philips Stirling cryocooler is made by Stirling Cryogenics BV and is currently the most successful commercial application of Stirling technology. Its main market is small helium, nitrogen and oxygen liquefiers. They are efficient, cheap and provide cooling in the range of 500 W to 5 kW at 77 K, a range not served well by other technologies. They use a conventionally lubricated motor-crank drive that resides in the cryocooler's working gas circuit. The oil seals on the pistons eventually leak oil vapour which gradually blocks the regenerator. Maintenance intervals are short with only 6000 hours operation between major maintenance.

2.1.3 WORK OF BEALE

W T Beale worked on a configuration of a Stirling engine [23] that moved the displacer using gas pressure instead of the crank used by the Philips Stirling engine. Beale named his engine a free-piston Stirling engine and he devised many different ways to make it work for generating electricity or pump water [24]. Beale's work in the 1960s led to the formation of the Sunpower Company [25], which currently sells small free-piston Stirling and pulse tube cryocoolers. Beale's focus was originally on free-piston Stirling engines to perform a variety of tasks using

biofuel or concentrated sunlight (hence Sunpower) as a heat source. As with the Philips Stirling, Sunpower found commercial success with cryocoolers rather than engines. Sunpower makes a range of free-piston Stirling cryocoolers [43] in the range of 1-35 W cooling power at 77 K. Sunpower's machines use a single linear-motor driven piston, gas bearings to support the small piston and displacer, and dynamic vibration absorbers. Sunpower coolers are very efficient and are used in applications such as cooling electronics for cellular base towers. Recently Sunpower (under the Global cooling name) have started making and selling near-ambient coolers through LG of Korea.

2.1.4 WORK OF COOKE-YARBOROUGH

Cooke-Yarborough started work in the 1960s on a diaphragm-based free-piston Stirling generator with the aim of providing power for light houses [26], [27], [55]. Cooke-Yarborough's machine used a diaphragm as the power piston, and had a sprung displacer that resonated with the diaphragm's movement. The gap between the displacer and the cylinder wall acted as a regenerator. Power was generated by a variable gap reluctance linear generator. The whole machine was hermetically sealed and self-started when a sufficient temperature difference was achieved between the ends of the displacer. Cooke-Yarborough's machines achieved approximately 10% thermal efficiency and demonstrated exceptional longevity. His commercial mistake was that he used radio-isotope decay as his heat source just when nuclear power was becoming unpopular. He did, however, make a prototype that ran continuously at 110 Hz for 12 years, demonstrating the longevity of the diaphragm concept.

Cooke-Yarborough came close to proposing a free-piston displacer similar to the concept explored in this thesis using diaphragms with a sketch in one of his patents [56]. Figure 2-1 shows Cooke-Yarborough's patent drawings and how he proposed using diaphragms in a free-piston Stirling heat engine, as opposed to a refrigerator. The top illustration, labelled 'Fig 2', in the patent drawing comes close to the proposed concept, but does not have the required area difference between the displacer ends to drive movement. The bottom illustration, labelled 'Fig 3', of the patent has differently sized diaphragms but does not account for imbalance caused by the difference in pressure force on each end. His system would have worked in ambient air, but not with a pressurized working gas or vacuum insulation around the displacer as required by a cryocooler. He did not progress these concepts but opted to develop a different concept with a single diaphragm and a clearance gap regenerator. Cooke-Yarborough's patent has not stopped the author from patenting the invention in this thesis in four jurisdictions (US, Europe, Japan and Korea).

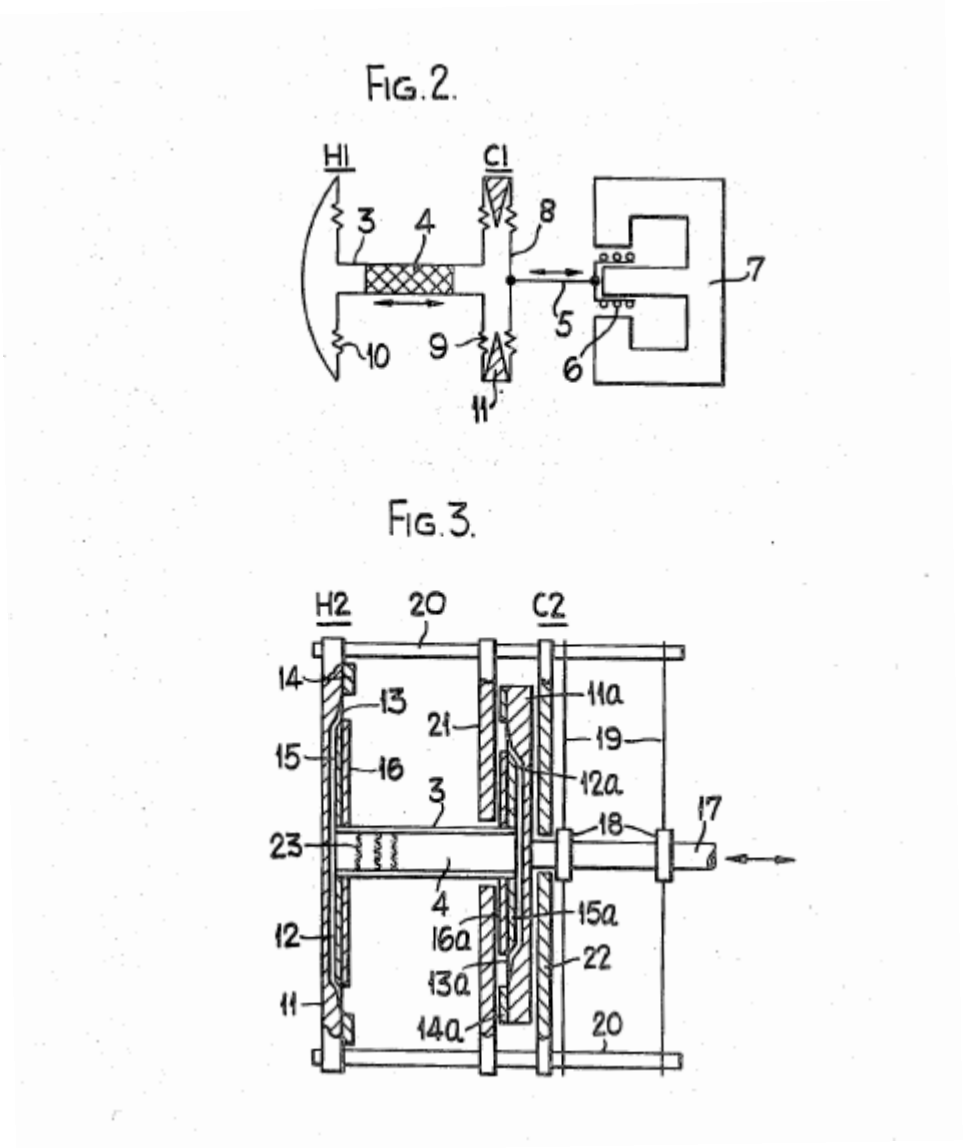

Figure 2-1: Images from Cooke-Yarborough's patent US3548589 'Heat Engines'.

More recently, Boukhanouf et al [57] explored the concept of a diaphragm Stirling engine. Boukhanouf's engine was very similar to Cooke-Yarborough's although a rubber diaphragm was used.

2.1.5 PULSE TUBE CRYOGENIC REFRIGERATORS

Pulse tubes, sometimes known as acoustic Stirling coolers, are a variant of the Stirling cycle that use a plug of gas in the 'pulse tube' to act as an expansion piston, thus eliminating moving parts in the cold region of a cryocooler. Gifford and Longsworth invented the Pulse Tube cooler in the 1960s [2]. Gifford and Longsworth's original invention, known as the basic pulse tube, was not a Stirling cooler, but worked on heat shuffling between the oscillating gas and the tube walls. It was not very effective and development stopped until the 1980s when Mikulin [3] added an orifice phase shifter to the pulse tube and made an efficient cryocooler. Mikulin's pulse tube

started to behave like a Stirling machine with the pulse tube acting as an expansion piston. Subsequent development has further increased pulse tube performance with improved phase shifters such as the inertance tube. The 'pulse tube' is not a pure Stirling machine as it has a secondary gas cycle within the pulse tube that performs heat pumping and forces a temperature gradient along the pulse tube's length. Two distinct types of pulse tube cryocooler exist. The first, as made by Gifford, uses a pressured helium supply and valve bank from a Gifford-McMahon (GM) cooler [1] to provide the pressure oscillations to drive the pulse tube. Operating frequencies for these machines are low, approximately 1 Hz, and efficiency is also low. Such machines thrive because the low frequency and lack of moving parts allow low vibration cooling at very low temperatures (<2 K). The second type of pulse tube uses a pressure oscillator (usually piston-based) and operates at higher frequencies (30 - 60 Hz). These machines are more efficient than the GM variant though not as good as a piston-based Stirling cooler. Swift [58], Radebaugh [59], and Kittel [39] have analysed the pulse tube cycle in depth, showing that it has a fundamentally lower efficiency, although this is of academic interest only as the best of cryocoolers still only achieve a third of the ideal Carnot performance. Pulse tubes work best when closely coupled to their pressure wave generator (PWG) to reduce dead volume, but this limits utility. Whilst transmission of the pressure wave is possible via a transfer line, friction losses are inevitable from the gas oscillating in the line. The size and expense of linear pressure wave generators limit the commercial viability of pulse tube cryocoolers to those with less than 20 W of cooling power at 77 K. Whilst multi-staging is possible and temperatures below 4 K have been reached [60], [61], [62], non-GM single-stage pulse tubes cannot produce useful amounts of cooling below 50 K as most have no-load temperatures above 40 K. Large pulse tubes (>500 W at 77 K) are difficult to make as they suffer from three-dimensional streaming in the pulse tube and the regenerator [46], [11]. However, inherent low vibration and reliability have made small pulse tubes popular for cooling sensors and as a research subject.

2.1.6 THE IRL DIAPHRAGM PRESSURE WAVE GENERATORS

Industrial Research Ltd (IRL) started working with cryogenic refrigerators in 2003 as part of its High Temperature Superconductor programme. The initial focus was to produce an industrialised PWG for pulse tube refrigerators. The key invention [50] from that work was a method of utilising diaphragms in the pressure wave generator to provide a hermetic, non-rubbing seal between the cryocooler's clean working gas and a conventionally lubricated reciprocating mechanism. The resulting diaphragm pressure wave generator (DPWG) was presented to the industry at the Cryogenic Engineering Conference/ International Cryogenic Materials Conference (CEC/ICMC) in 2007 [13]. It was coupled to a pulse tube refrigerator that was made by Cryomech which had achieved 108 W of cooling at 77 K [17]. The DPWG is

currently being commercialised and has been patented in four jurisdictions: USA, Japan, Korea and Europe. The first units were sold in 2008 and were coupled to pulse tube refrigerators by Air Liquide [21]. Cooling power was 600 W at 120 K per machine. During the DPWG development work, it became apparent that the same diaphragm design concepts could be used to produce a Stirling cryocooler without the attendant rubbing, clearance gap seals or gas bearings that trouble current Stirling machines. The Stirling concept explored in this thesis was included as a part of the original DPWG patent. An objective to explore the concept of a diaphragm-based Stirling refrigerator was written into a successful research proposal. The work in this thesis is the major component for meeting that objective.

2.2 Radial oscillating flow literature review

The diaphragm free-piston Stirling concept incorporates three diaphragms that have short strokes and large areas. There is a potential for using the natural geometry of the diaphragms for heat transfer. This means an understanding of the heat transfer in a radial, oscillating gas flow between two flat plates with an oscillating gap is required.

2.2.1 HEAT TRANSFER IN OSCILLATING FLOWS

Kornhauser and Smith conducted heat transfer experiments [32], [63] in piston spaces. Lee [64] produced a basic analytical model of heat transfer between two parallel walls that oscillated in the transverse direction to each other, thus providing a variable gap and compression. Lee's model predicted the power loss due to cyclic heat transfer. Cooke-Yarborough [51] analysed heat transfer between plates for his 'near isothermal' Stirling machine. Kornhauser and Smith compared Cooke-Yarborough's and Lee's models with their experimental results.

Gedeon [53] and Kornhauser [52] worked on the concept of a complex Nusselt number to explain heat transfer in oscillating flows, principally within the compression and expansion cylinders of Stirling machines. At high Peclet numbers, it was observed that the real and imaginary components of the Nusselt number were equal, with a phase angle of 45°.

An alternative approach to heat transfer and flow between oscillating plates has been the analysis of squeeze film bearings such as that done by Mahajan [65]. However, the squeeze film bearing effect relies on flow through a gap several orders of magnitude smaller than those found in the machine in this study, that is 90 microns as opposed to the 1-2 mm of the DPWG.

2.2.2 KORNHAUSER AND SMITH'S GAS SPRING EXPERIMENTS

Kornhauser & Smith's experiments involved fitting a piston and cylinder to the top of an existing compressor mechanism with a stroke of 3" (76 mm) as shown in Figure 2-2. The piston was hollow and long, and had its seal at the bottom to negate seal heating effects on the cylinder walls. The cylinder was made of micata, a fibre impregnated phenolic resin, which was an interesting choice as initially one thinks of resins as insulators. The experimental procedure however, ran the experiment for a very short time using the heat capacity of the wall material as an isothermal reservoir, a technique which meant that the wall material became unimportant as the heat capacity and conductivity of solids are significantly higher than those of gases. Piston position and pressure were measured, with the work done by the piston on the gas in a cycle being the integration of pressure and volume change.

The experiments were conducted at speeds between 0.038 Hz and 15.8 Hz and at pressures from 100 to 2500 KPa, conditions typical of Stirling machines.

Kornhauser & Smith chose the cyclic average Peclet number as their non-dimensional number for data analysis. For these experiments they defined the Peclet number as

$$Pe = \frac{v_p D}{\alpha}, \qquad 2\text{-}1$$

where v_p is the average piston velocity cycle over the compression (or expansion) half of a cycle, D the piston diameter and α the thermal diffusivity. Kornhauser normalised the hysteresis loss by dividing a single cycle's loss by the adiabatic work required for compressing the gas over the pressure ratio. Thus it was possible to compare losses with different pressure ratios, gases and charge pressures. The non-dimensional loss was defined as

$$L_{nd} = \frac{\oint p dV}{W_{adiab}}, \qquad 2\text{-}2$$

where

$$W_{adiab} = \frac{1}{\gamma - 1}\left(p_{\max} V_{\min} - p_{\min} V_{\max}\right) \qquad 2\text{-}3$$

and p is pressure , V is volume, and γ the adiabatic compression exponent as defined by

$$\frac{p_2}{p_1} = \left(\frac{V_1}{V_2}\right)^{\gamma} \qquad 2\text{-}4$$

Equation 2-4 states that when adiabatically compressing (or expanding) an ideal gas from V_1 to V_2, the pressure changes by the inverse of the volume ratio to the power of γ. For most diatomic gases, γ is very close to 1.4, and 1.67 for most monatomic gases.

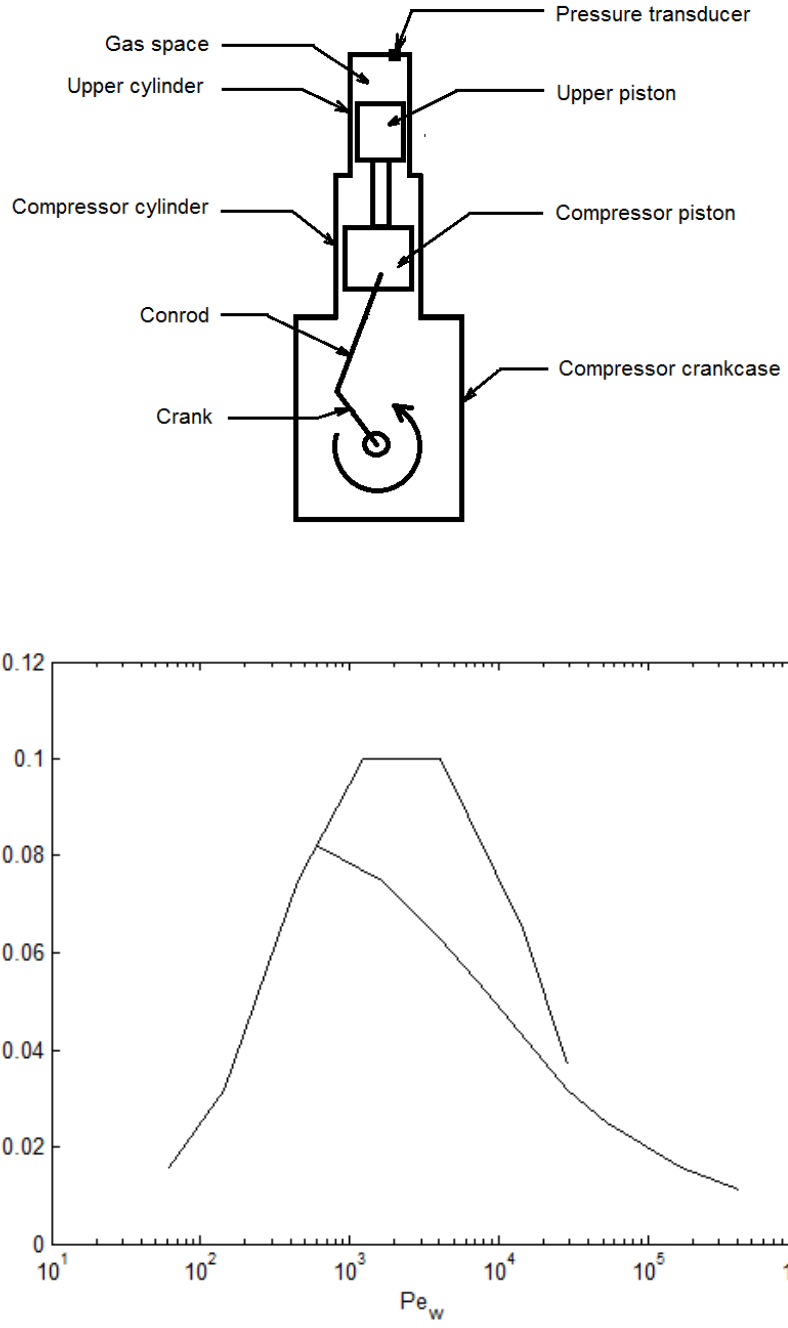

Figure 2-2: Kornhauser's experimental rig and results, from [32]. The two curves represent sets of results at different pressures, which could produce the same Peclet numbers at different speeds.

Kornhauser and Smith showed that hysteresis losses were low at low Peclet numbers where conditions were near isothermal, and at high Peclet numbers where conditions were near-adiabatic. Hysteresis losses were high in the region of *Pe* = 5 to 10,000. In the high loss region, it was hypothesised that there was significant entropy generation from non-reversible heat exchange between the gas and walls. Kornhauser successfully used analytical expressions by Lee and Cooke-Yarborough to predict the losses.

Of the expressions that Kornhauser and Smith evaluated, the best correlation achieved was by combining expressions by Cooke-Yarborough [51] and Lee [64]. Cooke- Yarborough's analytical expressions, Equations 2-5 and 2-6, agreed well with the experimental results at high and low Pe_ω as shown in Figure 2-3. The analytical expression had two cases, one assuming isothermal compression polytropic exponent (1) and the other assuming an adiabatic polytropic exponent (γ). The unknown region in the middle was not dealt with well. If an experimentally determined polytropic exponent is inserted, as Kornhauser and Smith did, then the gap in the centre approximates the experimental work.

The combined Lee and Cooke-Yarborough equations[32] were

$$L_{nd} = \frac{P_o V_o}{W_{adiab}} \frac{\pi}{2} \left(\frac{P_a}{P_o}\right)^2 \frac{(\gamma - 1)}{\gamma} \frac{1}{y} \left(\frac{\cosh y \sinh y - \sin y \cos y}{\cosh^2 y - \sin^2 y}\right) \quad 2\text{-}5$$

where

$$y = D_h \left(\frac{\omega}{32\alpha_o}\right)^{\frac{1}{2}}. \quad 2\text{-}6$$

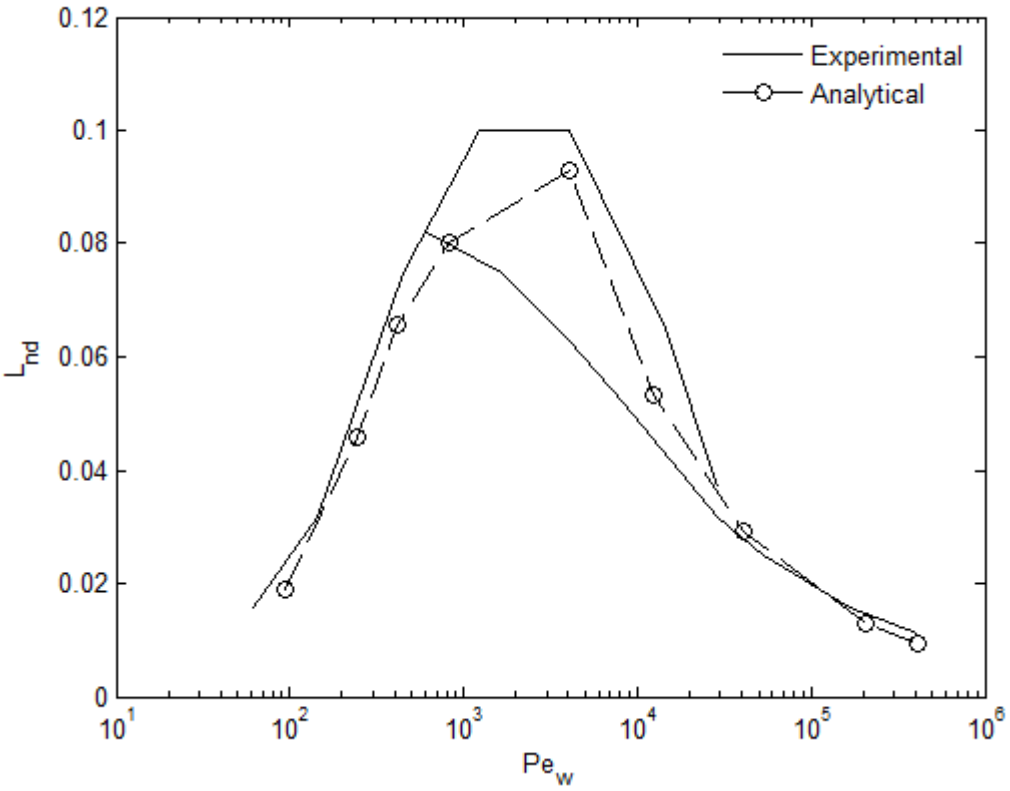

Figure 2-3: Comparison of Lee and Cooke-Yarborough combined expressions with Kornhauser and Smith's experiments, from [32].

Kornhauser and Smith extended their experiment to include an annular space with a much smaller hydraulic diameter than the compression piston [63]. This two-space experimental apparatus is shown in Figure 2-4.

Kornhauser and Smith's two-space experiment measured the complex Nusselt number at different places along the annular space. The annular heat exchanger is similar to this work's radial experiment with the exception that the radial space gets larger with the distance down the heat exchanger (moving radially) whilst Kornhauser's system keeps constant dimensions along the heat exchanger (moving axially instead). The two-space experiments redefined the Peclet number, this time based on the oscillating speed as the piston speed became irrelevant for the heat exchanger geometry, as

$$Pe_{\omega} = \frac{\omega D_h}{\alpha}, \qquad 2\text{-}7$$

where ω is the oscillating speed in rad s^{-1}. Significant phase differences between heat flux and bulk gas temperature were observed. The Pe_{ω} defined in this way proved to be a useful non-dimensional number of relevance in interpreting the experimental data.

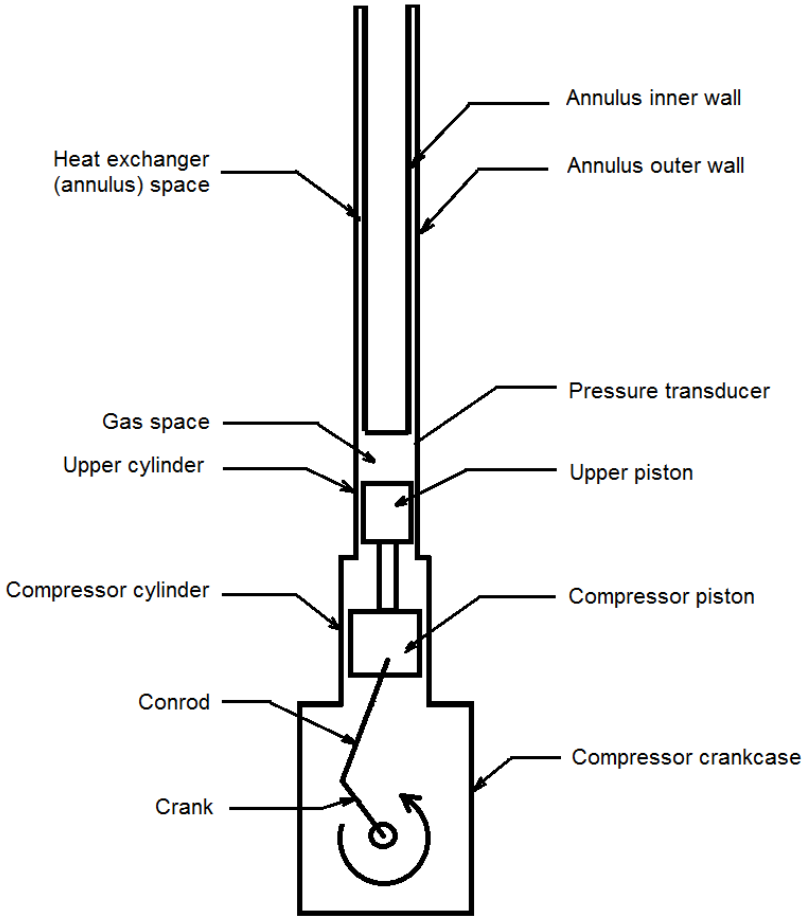

Figure 2-4: Kornhauser's two-space apparatus, from [63].

2.2.3 *HUANG'S MODEL OF FLOW IN A DIAPHRAGM PRESSURE WAVE GENERATOR*

Huang, used ANSYS® CFX in an attempt to model radial flow in a DPWG [66], then used his results to compare with Sage [67]. The author's contribution to the work was provision of the DPWG and project management. The CFX model looked at compression into a variety of volumes and, like Kornhauser, used gas spring hysteresis as the comparison tool. The focus of the study was the interaction of the flat DPWG geometry with the cylindrical geometry of a conventional cold head (pulse tube or Stirling). Huang used a laminar flow model and found that CFX provided a good correlation with Kornhauser's work and his own experiments. Huang's comparison of Sage with CFX and his experiments showed that Sage did not model the DPWG well and was inconclusive about its correlation with reality in those situations.

2.3 Modelling porous regenerator screens

Modelling the porous regenerator matrix is a difficult task. Some, like Gheisari [68] concentrated on analytical regenerator models, whereas Sage has its own models for regenerator matrices based on Gedeon's experimental work [69].

CFD codes such as ANSYS® CFX describe regenerators as uniform porous media with a set of parameters; the parameters 'volume porosity' and 'interfacial area' are directly calculable from the matrix geometry. Likewise, the material properties of the matrix are defined in the ANSYS® material library. Determining the Darcy flow loss coefficient, permeability and heat transfer coefficient for a particular matrix is more difficult. Cha [70], [71] completed his PhD thesis using a flow bench and the CFD code Fluent to measure the hydrodynamic parameters for regenerator matrices. Cha produced a set of parameters for 400 mesh screens, typical of Stirling and pulse tube regenerators, which could be used. The Fluent parameters had equivalents in CFX which is not surprising as ANSYS® has now taken ownership of both codes.

Venkata [72] used CFX to model a section of mesh, comparing it to empirical data from Perry's handbook [73] for mesh flow losses and achieved a good correlation for incompressible types of flow but divergence of up to 50% when compressibility was high. The usefulness of Venkata's result resides in the confidence of using Perry's data to check flow loss figures.

3 DIAPHRAGM FREE PISTON STIRLING CRYOCOOLER CONCEPT

This chapter explores the first hypothesis in this thesis, that diaphragms can be used to suspend and seal the displacer in a free-piston Stirling expander, thus producing a practical cryocooler with no rubbing parts in the cold section. Throughout this section Sage is used as the thermodynamic design tool. The design process was iterated between Sage, the mechanical design and prototype experimentation.

3.1 The Concept

The DPWG previously invented by the author uses a pair of metallic diaphragms as shown in Figure 3-1. One diaphragm is used to produce a pressure wave and the other works against a larger volume that functions as a gas spring. A kinematic drive mechanism is located between the diaphragms to provide oscillation. The two opposed diaphragms are rigidly connected so they move in tandem along the same axis. The gas spaces of the two diaphragms are connected via a bleed line that sets the gas spring pressure to the average of the pressure wave side at all times. The effect of the gas spring is to balance out the average pressure force on the pressure wave side which, with a typical 25 bar gas pressure, is considerable. Hence the drive mechanism only works against the pressure wave. The metallic diaphragms seal in the helium working gas; furthermore, they seal out the lubricating oil from the drive which is essential for long life. This diaphragm pressure wave generator has proved itself as a viable alternative to linear motor drives for pulse tube cryocoolers.

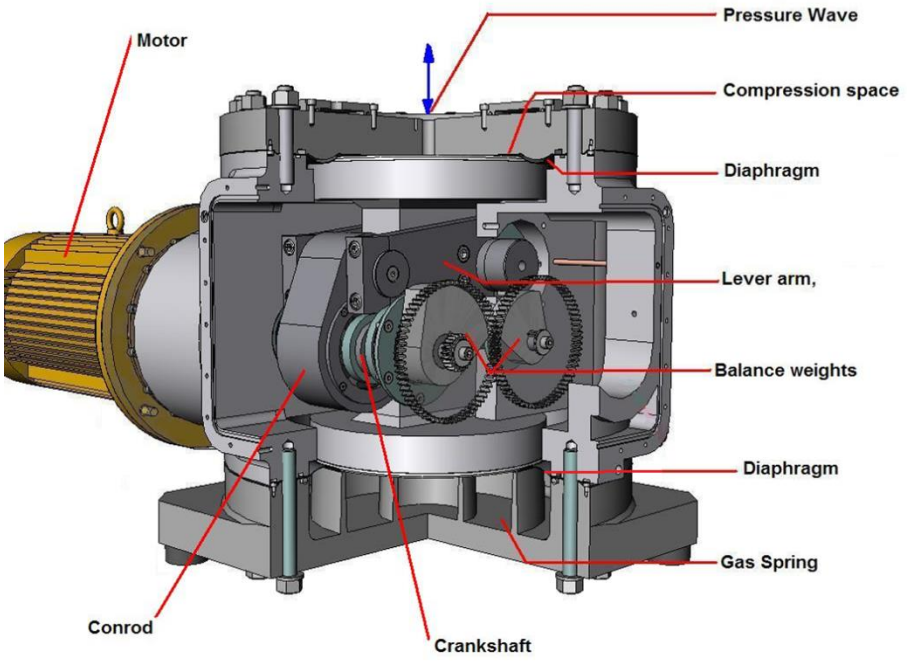

Figure 3-1: The diaphragm pressure wave generator.

The concept to be tested in this section is to use a pair of metallic diaphragms to suspend the displacer of a gamma-configuration Stirling refrigerator as shown in Figure 3-2. The diaphragms perform the multiple purposes of acting as: flexure bearings to guide the movement of the displacer; seals to seal the displacer from the housing and ambient conditions; and springs to centre the displacer. The shaft and bounce space effects of a free-piston system can be achieved by a smaller diameter diaphragm, which seals off a section of the gas volume on the warm side of the displacer, thus reducing the area of the warm side of the displacer that is subject to the pressure wave. The bounce space is maintained at the average gas pressure by a restricted gas connection, most conveniently achieved by not using a proper seal between the two gas spaces.

Referring to Figure 3-2: The pressure wave is generated in (c) by the reciprocating movement of the pressure wave generator diaphragm (a). The gas moves through to the warm side of the displacer (d). There is a diaphragm separating the bounce space (f) from the warm side of the displacer. The regenerator (g) is housed within the displacer (b) and the cold side of the displacer (e).

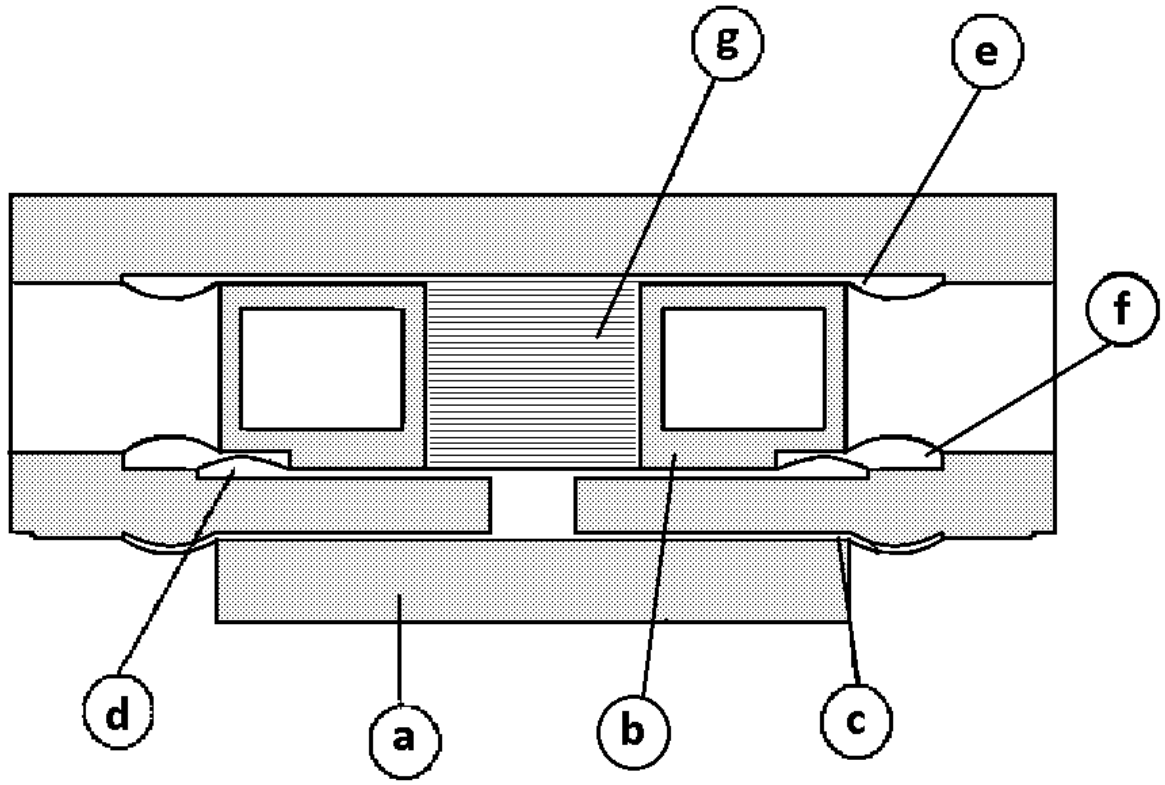

Figure 3-2: A cross-section of the diaphragm version of the free-piston system concept: a) Pressure wave generator driving piston, b) displacer, c) pressure wave generator compression space, d) warm side of displacer, e) cold expansion space, f) bounce space, g) regenerator.

Figure 3-3 shows the expander concept on a 200 ml swept volume pressure wave generator (CHC200). The free-piston expander bolts directly on to the top of a CHC200 pressure wave generator, replacing the top plate and uses identical diaphragms to the pressure wave generator.

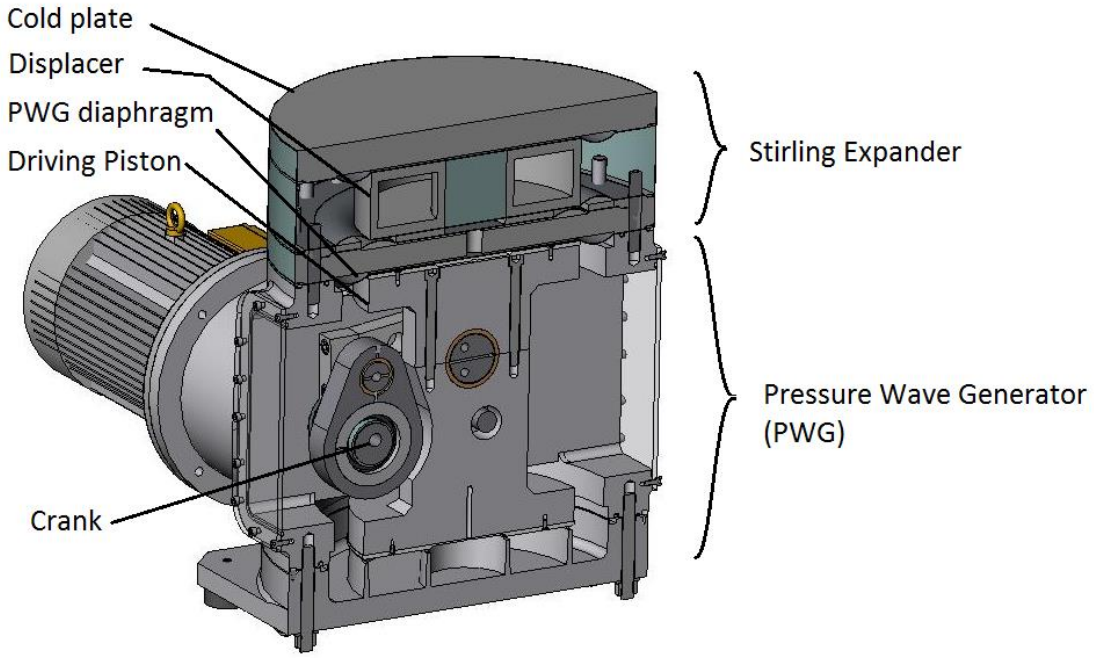

Figure 3-3: Diaphragm Free-Piston Stirling concept shown on a CHC200 pressure wave generator

3.2 Modelling

The design of the diaphragm Stirling expander started with a one-dimensional model using the Sage software by Gedeon Associates [31]. Sage is described in Section 1.4.1 of this thesis. The Sage model, shown in Figure 3-4, contains objects that represent the key parts of the pressure wave generator and expander.

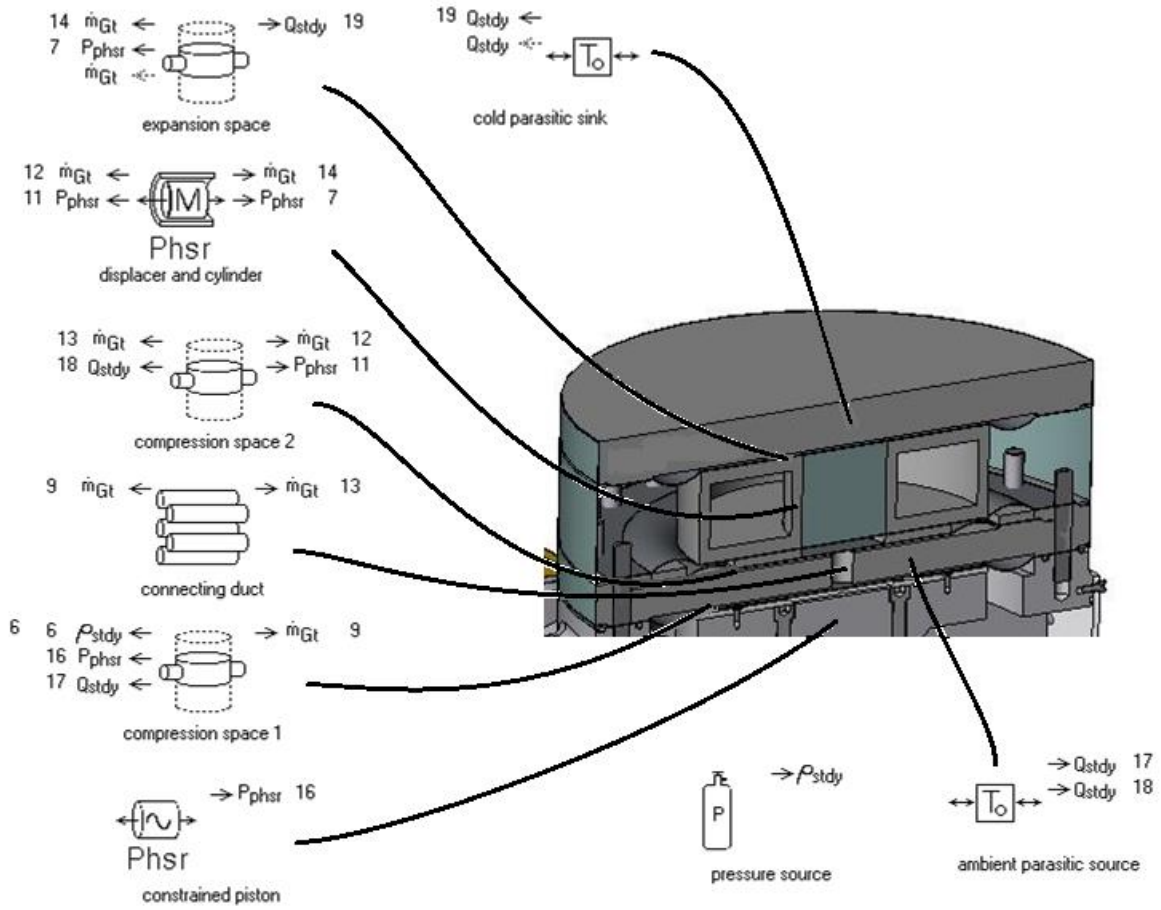

Figure 3-4: SAGE model schematic of the free-piston system showing the objects used and connections.

Figure 3-4 is a schematic of the objects used in Sage to model the free-piston expander. Starting from the bottom, the '*constrained piston*' object represents the pressure wave generator's drive mechanism, a motor crank system producing a sinusoidal movement with 1.25 mm amplitude and phasing of zero degrees. The movement is transferred to the next object by the position connection called 'P_{phsr} *16'*. '*Compression space 1'* represents the compression volume of the CHC200 pressure wave generator with an average volume of 235 ml. P_{phsr} *16* moves the diaphragm area of 0.08042 m^2 resulting in a sinusoidal volume change of 100 ml amplitude about the average volume. The '*pressure source'* object is connected to *compression space 1* via '*6* ρ_{stdy}*'* and defines the system's average pressure. A heat flow connection, '*17* Q_{stdy}*'*, connects the

compression space 1 walls to '*ambient parasitic source*' which is a heat sink at 300 K. *Compression space 1* is connected to the '*connecting duct*' object via mass flow connection 'm_{Gt} *9,*' which transfers gas between the two objects. The *connecting duct* object represents the hole connecting the pressure wave generator to the warm side of the displacer and is modelled as a tube bundle (in this case with only one tube) which connects to '*compression space 2'* via mass flow 'm_{Gt} *13'*. *Compression space 2* represents the variable volume on the warm side of the displacer. It has an area movement dictated by 'P_{phsr} *11'* and heat transfer to its walls which are connected to the ambient parasitic source via '*18* Q_{stdy}'. 'm_{Gt} *12'* connects to the '*displacer and cylinder'* object**.**

The *displacer and cylinder* object is a complex collection of sub-objects that come as a standard set with Sage. The standard displacer and cylinder object assumes that the displacer is a regenerator matrix mounted inside a piston which moves inside a cylinder and takes into account the conduction down the walls, the regenerator matrix heat transfer and flow loss, mass, spring, forcing function from gas pressure on ends and leakage between piston and cylinder. In the diaphragm case the diaphragms effectively seal the displacer piston to the cylinder, so Sage's standard gap-leakage sub-object was removed. The spring is provided by the stiffness of the diaphragms, derived from the Finite Element stress analysis used to design the diaphragm. The displacer piston walls represent the displacer walls, and the cylinder walls represent the walls of the cold head housing. Sage calculates the displacer movement based on a forcing function from the gas forces on either end of the displacer and the dynamic response of the displacer as a spring-mass-damper system.

The cold side of the displacer is connected to variable volume '*expansion space'* via mass flow connection 'm_{Gt} *14'* and moving area 'P_{phsr} *7'*. The *expansion space* walls are connected via 'Q_{stdy} *19'* to the '*cold parasitic sink'* which is set to 77 K. The heat flow Q_{stdy} *19* is considered to be the refrigeration power of the cryocooler.

The displacer's warm and cold diaphragms were to be the same as the CHC200 pressure wave generator as these were the only diaphragms available at the time, thus dictating the diaphragm area, movement limits and spring rate. Ranges of values for the regenerator size, intermediate diaphragm area and displacer mass were mapped and optimised using Sage to get the best performance at 77 K. Table 3-1 details the Sage input parameters for the optimised Sage model, and Figure 3-5 shows the equivalent dimensions in the concept design.

Table 3-1: Input parameters for the optimised Sage model.

Item	Value	Note
PWG		
Volume, m^3	2.354×10^{-4}	Average 2.25 mm height
Wetted area, m^2	2.093×10^{-1}	
Piston effective area, m^2	8.042×10^{-2}	
Stroke, m	1.250×10^{-3}	
Transfer port		
Diameter, m	2×10^{-2}	
Length, m	2.5×10^{-2}	
Displacer warm end		
Volume, m^3	1.569×10^{-4}	Average 1.5 mm height
Wetted area, m^2	2.093×10^{-1}	
Moving area, m^2	4.988×10^{-2}	As a result of optimisation
Regenerator		
Length, m	8.0×10^{-2}	
Diameter, m	8.6×10^{-2}	Diameter includes shell thickness, mesh has diameter of 80 mm
Porosity (void volume/total volume)	6.9×10^{-1}	
Matrix material	316 Stainless Steel	
Wire diameter, m	3.0×10^{-5}	400 mesh screens
Displacer shell wall, mm	6.1	Calculates axial heat loss
Displacer mass, kg	7.21	
Spring constant, N m^{-1}	2.2×10^6	From FE model
Displacer cold end		
Volume, m^3	1.569×10^{-4}	
Wetted area, m^2	2.0926×10^{-1}	
Moving area, m^2	8.04×10^{-2}	
Bounce Space		
Moving area, m^2	1.11×10^{-2}	Difference between displacer cold end and warm end moving areas
General		
Gas pressure, bar gauge	25	
Warm heat sink, K	300	
Cold heat sink, K	20 - 100	Target performance is 77 K
Frequency, Hz	50	

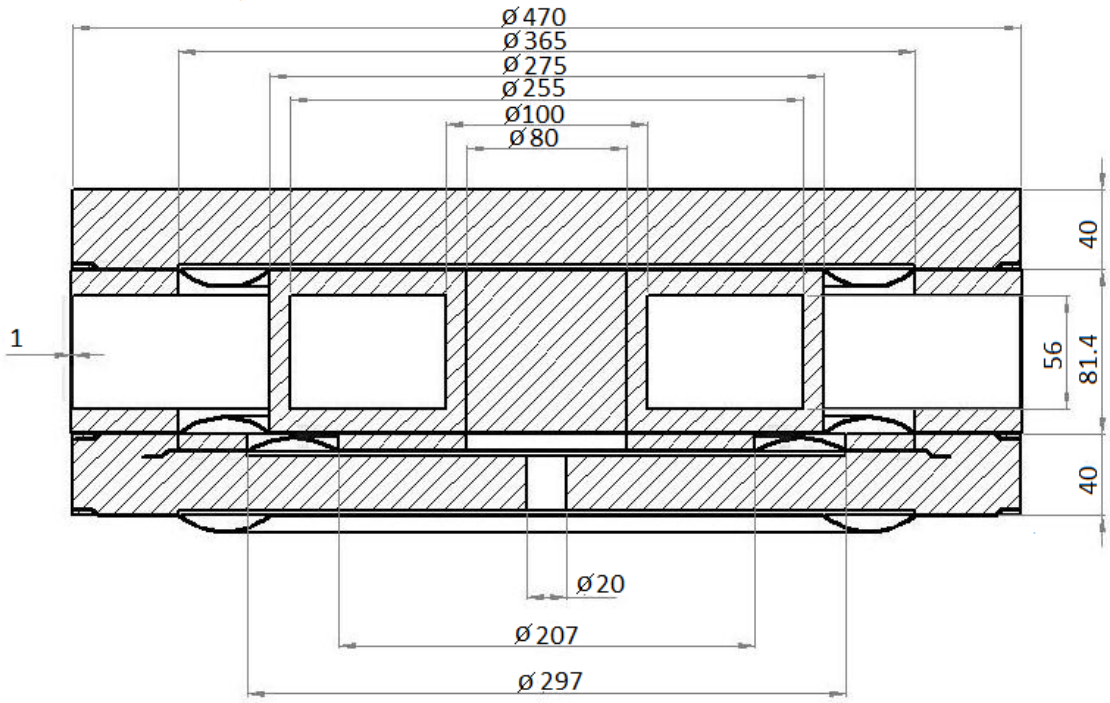

Figure 3-5: Dimensions of the Expander as summarised in Table 3.

3.2.1 *PERFORMANCE PREDICTION, & CHARACTERISTICS*

The optimised Sage model predicts a refrigeration effect that is dependent on the temperature of the cold reservoir as shown in Figure 3-6. The no-load temperature, where the net refrigeration is zero, is predicted to be just over 20 K. The refrigeration effect is predicted to rise linearly with temperature; there is however a small knee in the curve at 30 K which could be due to a significant drop-off in the heat capacity of the regenerator at low temperatures in the Sage material data [74]. A gross refrigeration effect of 462 W is predicted at 80 K, approximately the temperature for nitrogen liquefaction, for an input acoustic power at the DPWG diaphragm face (referred to as *pV* power to differentiate it from motor power), of 4410 W which gives an efficiency that is 30.3% of the ideal Carnot COP at that temperature. The model predicted 243 W at 50 K which is 15% of the ideal Carnot COP. This is similar to the performance of other cooling technologies such as Gifford McMahon [10] or pulse tube cryocoolers [75], and ideal for HTS applications as outlined in reports such as the 2001 US Department Of Energy HTS Cryogenic roadmap [9] which sets an efficiency goal of 30% of Carnot COP at 77 K.

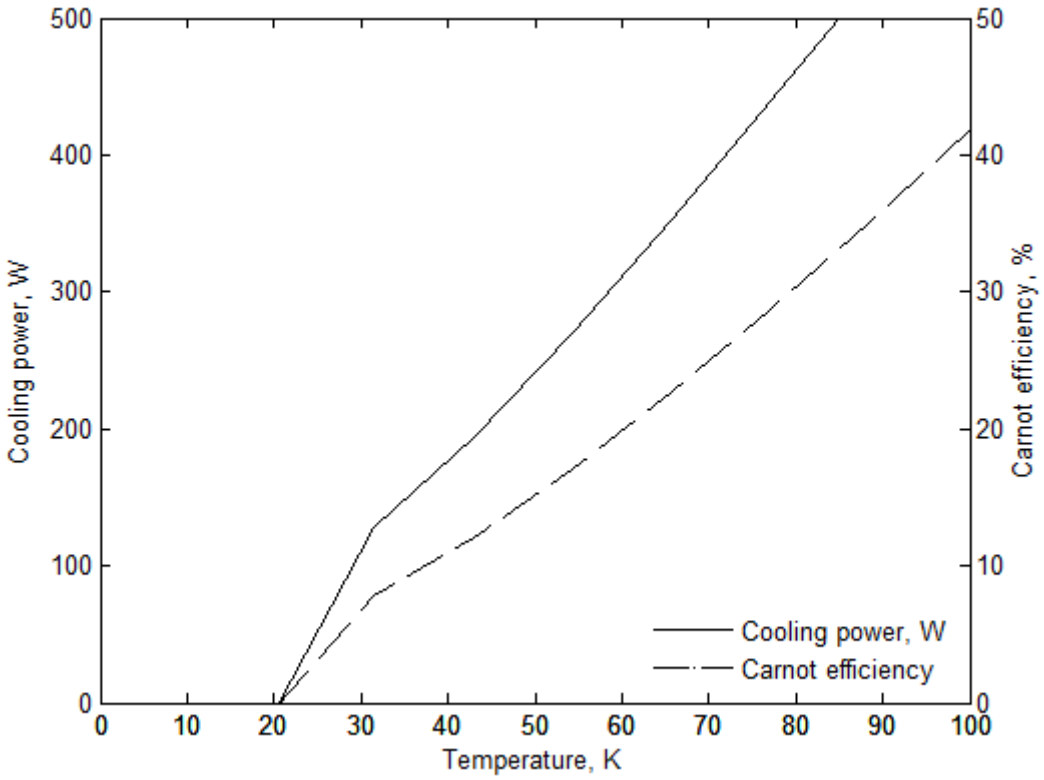

Figure 3-6: Predicted performance of initial Sage model at 80 K:
30.3% Carnot efficiency and 462 W of cooling from 4410 W *pV* input.

3.2.2 *FREQUENCY AND COOLING POWER*

Figure 3-7 shows the relationship between frequency and cooling power at 77 K. Of significance is a relatively constant efficiency over a wide range of frequencies. Maintaining efficiency over a wide frequency range is very useful for managing heat loads. A cryocooler with these characteristics can be made to work hard at high speed for a fast cool-down or when the cooling load is high (for example when a HTS transformer or cable is operating at its maximum capacity), and then set to a lower speed, producing less cooling but operating at a high efficiency to maintain temperature when the load is less (for example when a transformer is idle).

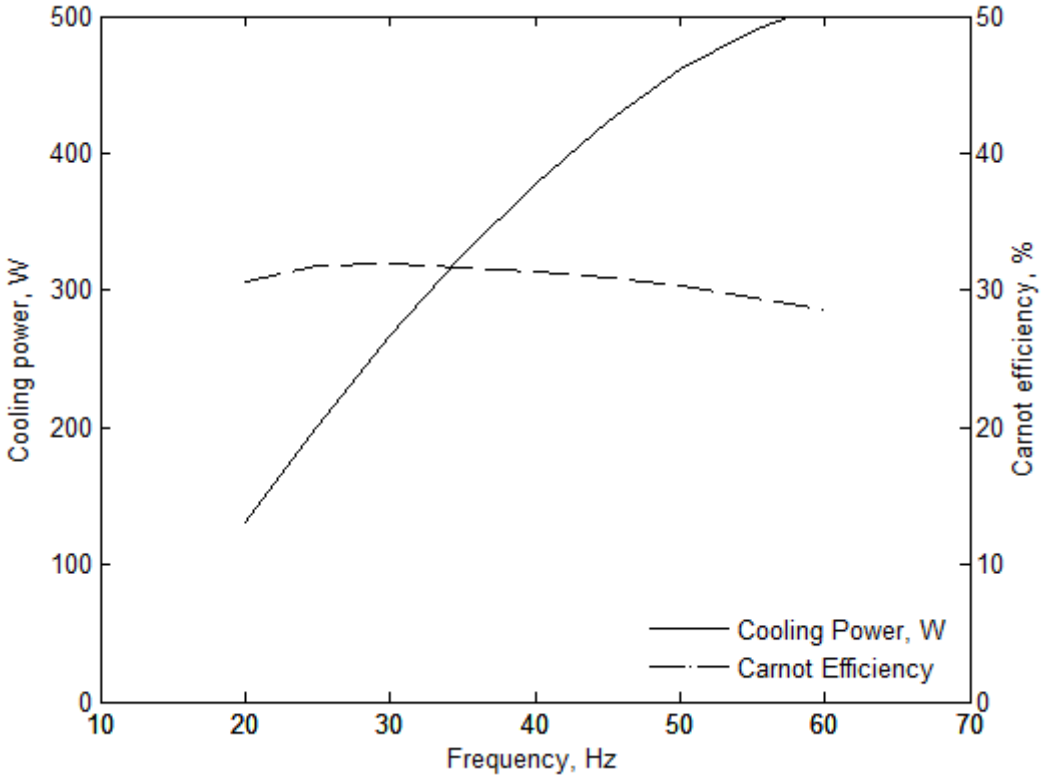

Figure 3-7: Frequency vs Cooling power and Carnot efficiency at 77 K

3.2.3 *Model sensitivities*

Knowing the design sensitivity allows the designer to make educated compromises during the design process; trading efficiency for power or cost vs performance.

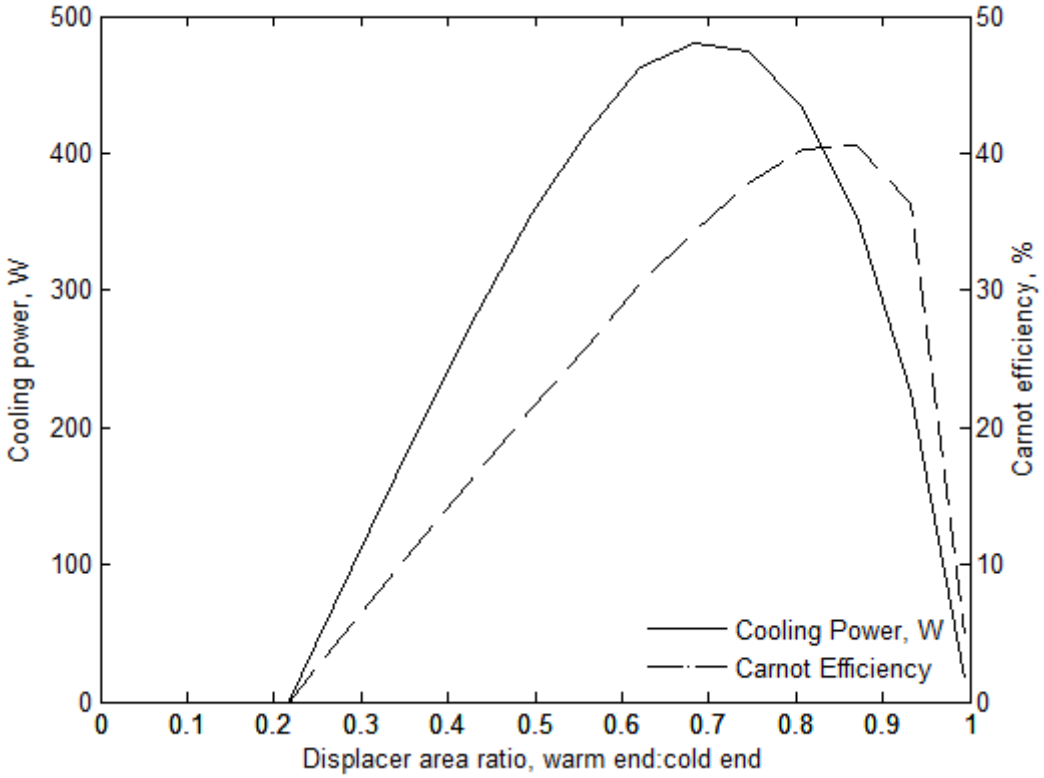

Figure 3-8: Sensitivity of the system to the ratio of the areas between the warm and cold sides of the displacer.

The ratio of the areas of each end of the displacer determines the magnitude of the exciting force that moves the displacer back and forwards. Figure 3-8 shows that a maximum cooling of 481 W at 80 K is achieved with an area ratio of 0.68. However, efficiency reaches 40% of the Carnot COP at an area ratio of 0.88 but at a lesser cooling power of 400 W. The peak in efficiency might be well worth the reduction in cooling power as, for a large cooler, the savings in electricity could outweigh the capital cost of a larger machine over its lifetime.

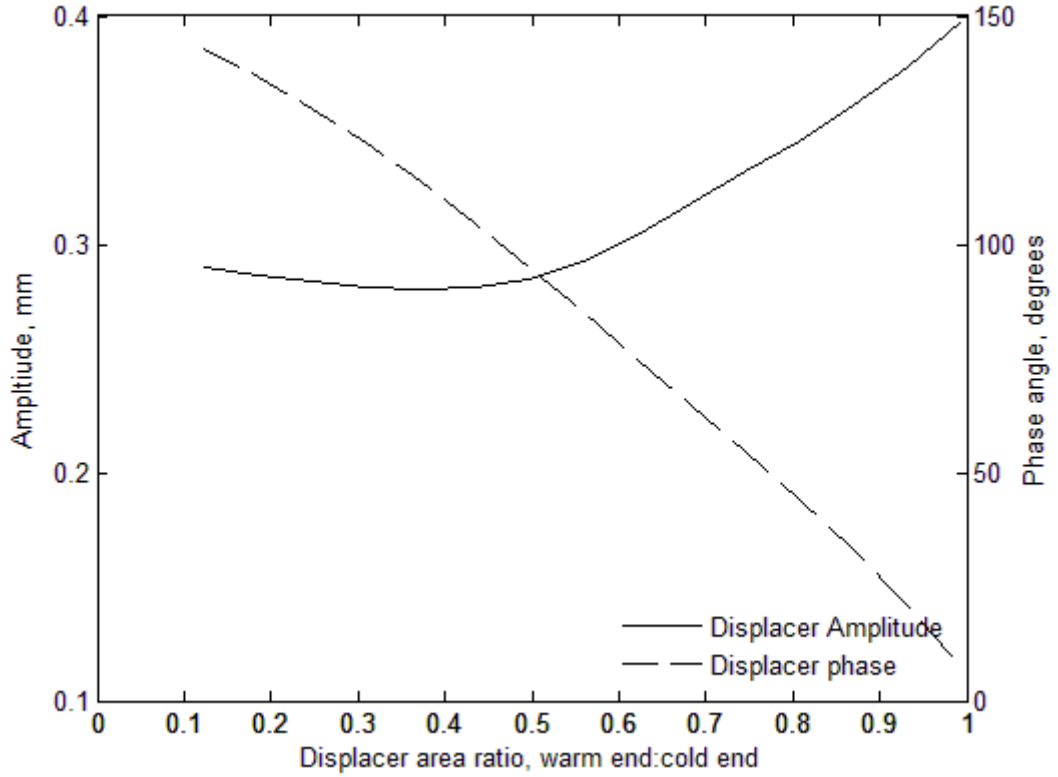

Figure 3-9: Displacer phase and amplitude as function of area ratios.

Figure 3-9 shows the displacer response to its area ratio. At a low area ratio, where the displacer's warm end experiences only the average gas pressure from the bounce space, the driving force for the displacer is created by the pressure at the cold end. The displacer movement will closely follow its forcing function, with a time lag for fluid flow through the regenerator. When the pressure is low (bottom of pressure wave generator stroke) the displacer will be high, and when the pressure is high (top of pressure wave generator stroke) the displacer will be low, hence the displacer will be near to 180^0 out of phase with the pressure wave generator piston, which is not desirable for refrigeration as the same amount of gas will be in the cold side for both the compression and expansion strokes. The dynamic response of the displacer's spring mass system will give a phase lag, the magnitude of which is dependent on how close the operating frequency is to resonance. Damping of the displacer is high as the out-of-phase movement forces more gas through the regenerator. A high damping will reduce the displacer amplitude and absorb more pV power. At the other extreme, an area ratio of one means that the force driving the displacer movement is due to the pressure drop from the flow through the regenerator. This will produce a force in phase with the mass flow through the regenerator which will then lead the pressure wave generator piston position by up to 90°. The dynamic response and the time it takes for the gas to move through the regenerator will cause a

phase lag that will reduce the displacer's phase angle, bringing it nearer to zero. Low damping means that although the magnitude of the forcing function may be low, the displacer movement can be large, especially if operating near its resonant frequency.

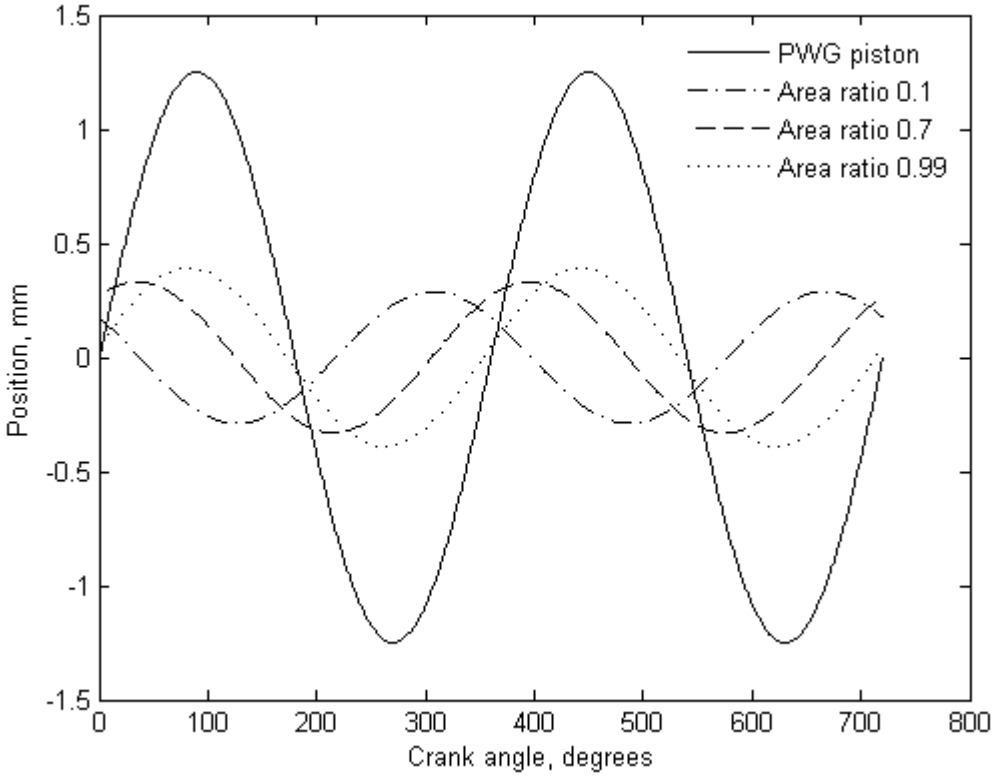

Figure 3-10: The effect of area ratio on the displacer movement showing displacer movements vs crank angle for low area ratio (0.1), optimal area ratio (0.7) and high area ratio (0.99).

As described in section 1.3.4, the ideal Stirling cycle phase angle is when the displacer leads the compression piston by 90°. When work is done by the compression piston via a pressure-volume phase angle of around 30°-40°(pressure lagging piston position) the optimal displacer lead becomes 50°-60°. In the Sage model of this system, Figure 3-8, the maximum performance occurred with area ratios between 0.65 and 0.75 which corresponds in Figure 3-9 to a phase angle of 50°-60° as expected. Figure 3-10 shows PWG piston and displacer movements calculated by the Sage model for three cases: a low area ratio of 0.1, an optimal area ratio of 0.7 and a high ratio of 0.99. As described above, the low area ratio displacer movement is close to 180° out of phase from the PWG movement; the optimal area ratio has the displacer movement leading the PWG (the displacer highest point occurs before the PWG highest point) by 55°; and the high area ratio is close to being in phase with the PWG.

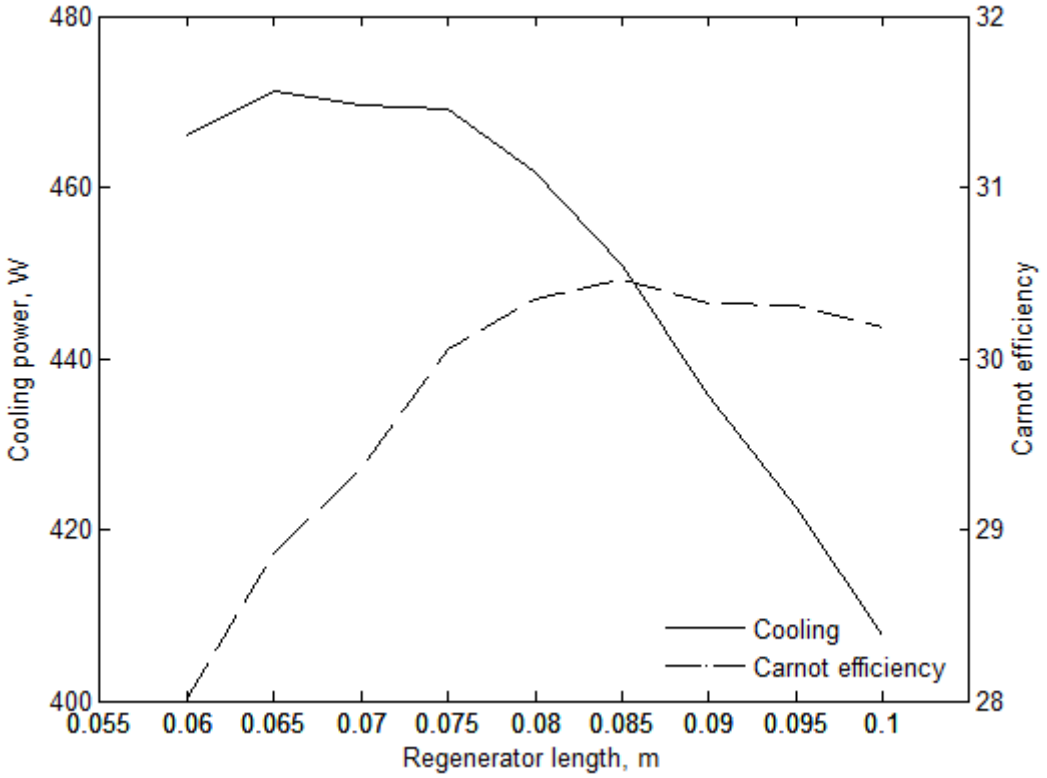

Figure 3-11: The effect of regenerator length on the cooling power at 77 K.

Figure 3-11 shows the effect of different regenerator lengths. The shorter regenerator produces more power at 77 K, with a peak at 65 mm in length and drops off steadily after 80 mm. However, peak efficiency is achieved with an 85 mm long regenerator; efficiency starts to drop steadily below 75 mm in length. The power and efficiency changes between 65 mm and 85 mm in length are in the order of 5% so a compromise length of 80 mm was chosen as it is at the start of the efficiency plateau and power drop-off. It is recognised that the final regenerator length can be shorter if required by the design; the trade-off would be more power for less efficiency.

Intuitively, lengthening the regenerator will increase the pressure drop across the regenerator and increase its dead volume, leading to reduced refrigeration power. However, lengthening the regenerator will reduce the temperature gradient from warm to cold and so decrease the amount of heat that needs to be transferred to and from each layer in the mesh stack; and require a lower temperature difference between gas and metal on each mesh layer, decreasing entropy generation. These are consistent with the results which show that as the regenerator is lengthened, efficiency increases (less heat to transfer for each mesh layer) and refrigeration power decreases (more dead volume and pressure drop).

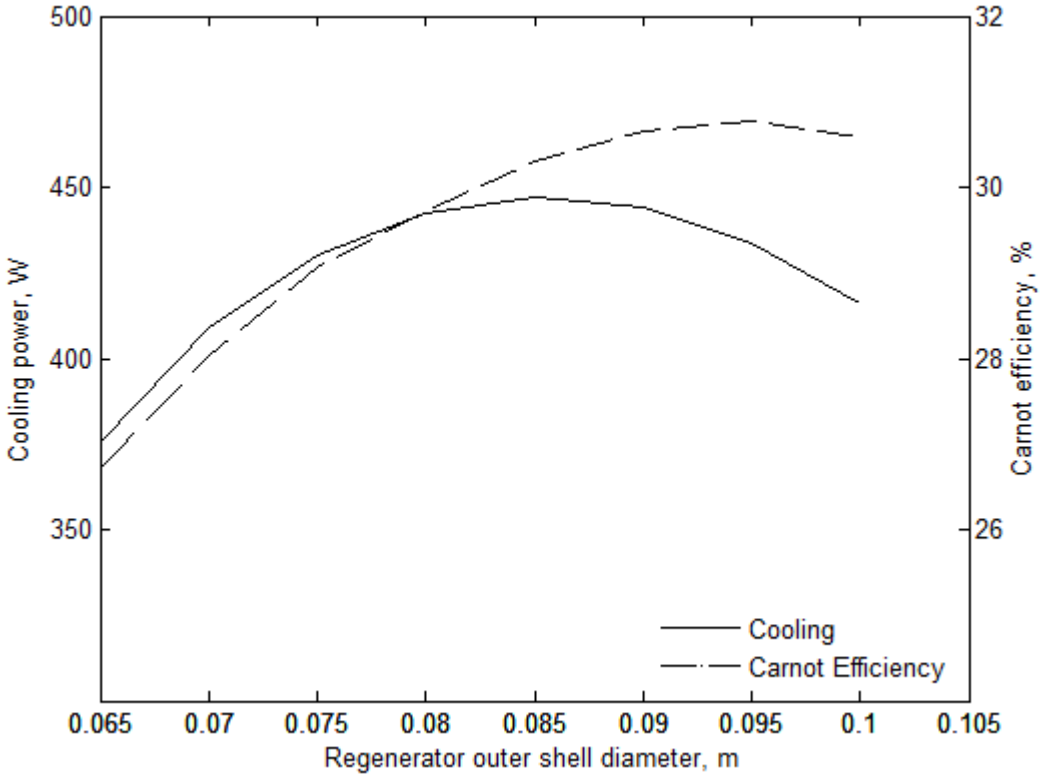

Figure 3-12: The effect of the regenerator outer shell diameter for a length of 80 mm; maximum cooling power is at 0.085 m and maximum efficiency is at 0.095 m.

Increasing the regenerator diameter increases the heat transfer area and heat capacity of each layer in the mesh stack, allowing the regenerator to process more gas more efficiently and increases the cooling power. However an increase in dead volume in the regenerator leads to more dead volume which lowers the pressure wave amplitude and gas spring hysteresis losses. Figure 3-12 predicts the maximum cooling power for a regenerator outer shell diameter of 0.085 m and maximum efficiency at a diameter of 0.095 m. Again a compromise is needed; this time a mesh diameter of 80 mm was chosen. The model had a shell wall thickness of 6.1 mm, leading to an outer shell diameter of 0.092 m which was close to the maximum efficiency in Figure 3-12.

3.2.4 PARASITIC LOSSES NOT INCLUDED IN THE SAGE MODEL

The Sage model did not take into account axial conduction losses in the displacer system. In the proof-of-concept prototype system the displacer was intended to be made of G10 fibreglass for its low thermal conductivity and good compressive strength. The tension from the gas on the expansion space was taken by a thin stainless steel cylinder having the circumference of the cold head. Stainless steel was chosen because of its proven cryogenic performance, low thermal conductivity for a metal and high strength. Additionally, constructing the tension cylinder from the same grade of stainless steel as the cold head ensured that its thermal contraction from 200 K of cooling was the same as the cold head, thus reducing stresses from thermal contraction.

An estimate of the conduction heat leak down the displacer walls was performed. The conductivity of G10 fibreglass changes with temperature. NIST publishes conduction integrals on their cryogenic website [76]. G10 fibreglass from 300 K to 77 K has an average conductivity of k = 0.37 W m^{-1} K^{-1}. The displacer consisted of two cylinders, inner cylinder 80 mm ID, 100 mm OD and outer cylinder 255 mm ID, 275 mm OD. The combined conduction area was 0.0111 m^2 and the conduction length 60 mm, a typical value from the concept design. The total heat conduction calculated using Fourier's Law from 300 K to 77 K was then 15.5 W.

The compressive gas force on the displacer needs a reactive force to hold the cold end in place. This tensile force is taken up with a thin stainless steel cylinder of 470 mm diameter and 1 mm thick. The gas pressure load is 314 kN which results in a tensile stress of 212 MPa. Again, using the NIST integrated values for conduction of 304 SS from 300 K to 77 K, k = 11.16 W m^{-1} K^{-1}. The conduction area was 0.00148 m^2 and conduction length 70 mm. The heat conduction from 300 to 77 K was therefore 52.6 W.

Combining the two heat conduction components above, the total parasitic conduction loss was 68 W. This parasitic loss reduces the expected cooling power of the system from the Sage prediction of 462 W to 394 W and the Carnot efficiency from 30.3% to 26%, which is still acceptable.

3.2.5 *PRESSURE WAVE GENERATOR EFFICIENCY*

The pressure wave generator converts electrical energy to acoustic energy. The Sage model does not include the pressure wave generator as it starts its analysis at the diaphragm face. The pressure wave generator efficiency takes into account all the electrical losses in its motor, friction losses in its bearings, windage of moving parts inside it and the peripheral power consumption of items such as the lubricating oil pumps. The DPWG efficiency results in extra electricity consumed by the motor and does not affect the cooling power. Accounting for the CHC200 DPWG's measured efficiency [17] of 72%, the cryocooler's Carnot efficiency at 77 K reduces to 18.6% which is still significantly better than most cryocoolers [29].

3.2.6 *CONCLUSIONS*

The initial Sage model has shown that a potentially viable cryocooler can be made using diaphragms in a free-piston Stirling configuration. Moreover, the Sage model has predicted very good performance for the cooler, even when parasitic and pressure wave generator losses are considered. A refrigeration power of 394 W was predicted at 77 K with a Carnot efficiency of 18.6%. The cooler's predicted performance at 30-50 K is good enough for HTS applications. The cooler retains efficiency over a wide range of operating speeds which gives it desirable characteristics for cooling variable loads, such as when cooling HTS applications.

3.3 Proof-of-concept prototype

3.3.1 DESIGN

A proof-of-concept prototype was designed and manufactured using the parameters from the Sage model. Figure 3-13 shows the 3D model of the design mounted on the CHC200 DPWG. The practicalities of design and manufacture introduced a number of deviations from the initial Sage model. The first and most significant was the stiffness of the intermediate diaphragm. Once designed for stress and deflection, the prototype's intermediate diaphragm was an order of magnitude stiffer than assumed in the original Sage model. The stiff diaphragm reduced the displacer movement, resulting in less gas movement through the regenerator and less gas participating in the cooling cycle. More gas therefore remained on each side of the displacer, compressing and expanding without performing any useful function. The second and almost equally significant deviation was the introduction of extra dead volume at the outer radii of the diaphragms. This was to accommodate a method of sealing the cold gas by welding a sheet metal plate to the diaphragm, effectively forming a sealed metal bladder. The result sealed well but added extra volume, therefore reducing the compression ratio, which translated to less input power into the gas and a lower pressure wave for moving the displacer; all reducing the cooling power.

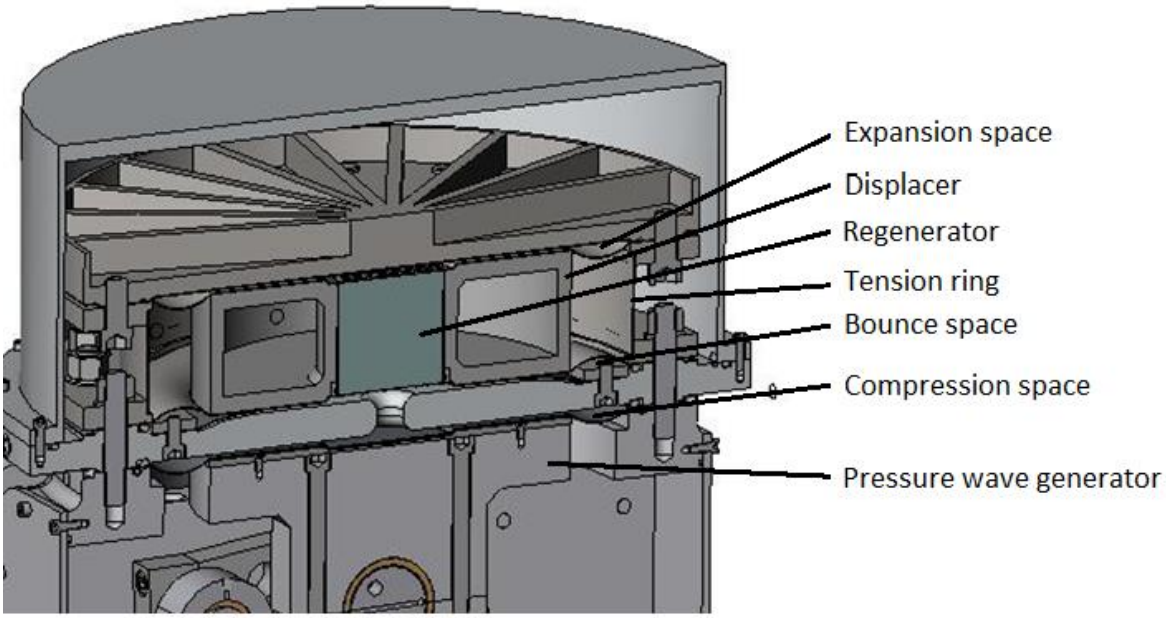

Figure 3-13: A 3D model of the final design showing the layout of the components.

3.3.2 *Material Considerations*

Material choices were based on the consideration that the cold end of the cryocooler was to experience cryogenic temperatures. Moreover, the tension ring, whose diameter was approximately 360 mm, would have a 200 K temperature gradient along its 70 mm length. All cold parts should be of the same material or have very similar thermal contraction coefficients to avoid adding stresses due to differential thermal contraction. As discussed earlier, the displacer material was chosen to be G10 fibreglass for its low thermal conduction and good compressive strength.

The 300-series austenitic stainless steels (SS) are the 'workhorses' of cryogenic applications. These materials do not experience brittle transitions at low temperatures like carbon steels. Therefore, 316 SS was chosen for the expander as it was readily available and had good strength. Additionally, the yield and fatigue strengths of 316 SS increase with decreasing temperature [54]. No data was found for the low temperature properties for the 430 SS diaphragm. The pressure wave generator diaphragms are made of 430 SS (a ferritic grade). The intention of using the same diaphragms as the pressure wave generator could be a problem when running at cryogenic temperatures. Should the use of 430 grade prove to be an issue at low temperatures then the option of making the expansion diaphragm from 304 SS or 316 SS would remain. The displacer's predicted deflection was less than 0.4 mm, which is significantly less than the DPWG diaphragm's deflection of 1.25 mm. Stresses in the cold diaphragm will be less than the DPWG and the lower endurance limit of the austenitic stainless steels may be acceptable.

3.3.3 *Revised Sage Model*

The design modifications, such as the dead volumes of the expansion and compression spaces and the final spring stiffness from the diaphragms, were incorporated into the Sage model after construction of the prototype. Figure 3-14 shows the revised cooling power prediction. The changes significantly reduced the predicted cooling power from 394 W at 77 K to 13 W at 80 K with 1.6 kW of input power. The model indicated that cryogenic temperatures would still be attainable, although 80 K would be unattainable as parasitic losses not included in the model were expected to be 68 W, well in excess of the 13 W of refrigeration available.

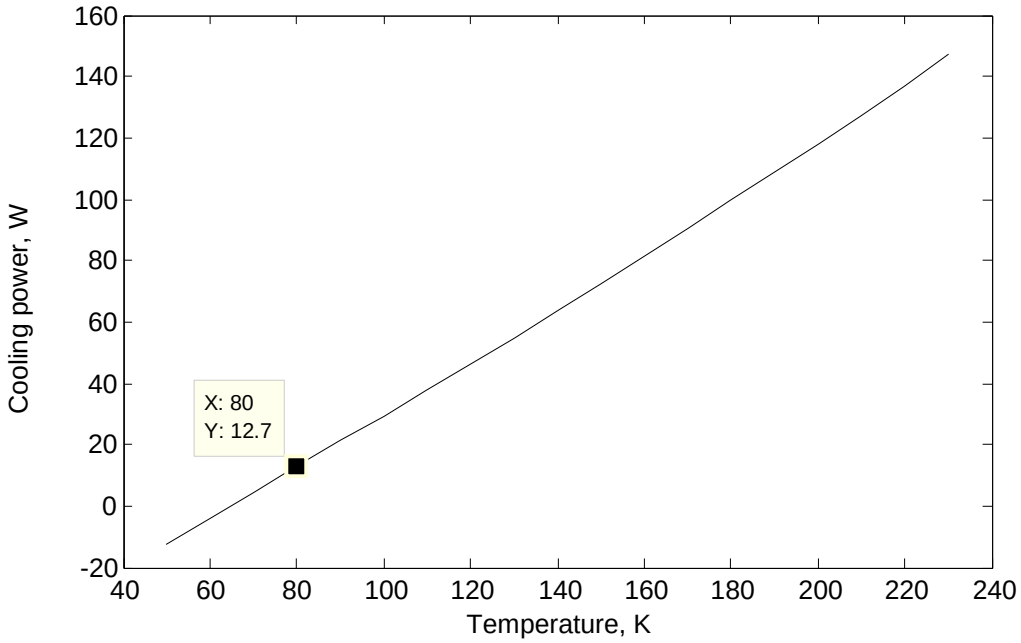

Figure 3-14: Revised model prediction of the as-built prototype at 50 Hz and 20 bar charge pressure.

3.3.4 INITIAL TESTING AND MODIFICATIONS

On the first run, refrigeration was apparent. The greatest amount of cooling occurred at the centre of the cold plate as shown in Figure 3-15 which shows frost forming on the cold plate.

A considerable temperature gradient between the centre and outside of the plate was observed. This was hypothesized to be a combination of: most of gas participating in the Stirling cycle being at the centre of the expansion space; the highest velocities (and therefore best convective heat transfer) at the centre; and the cold plate's large thermal mass combined with stainless steel's low conductivity maintaining a thermal gradient.

The first run highlighted problems with the weld connecting the intermediate diaphragm to the warm displacer diaphragm and the weld connecting the tube that houses and seals the regenerator to the cold diaphragm. The welded seams were brittle and quickly cracked. The rapid cooling of the centre of the cold plate indicated that a heat conductive material (copper) would be appropriate at that place. Likewise, the welded joint between the intermediate diaphragm and the warm displacer diaphragm cracked quickly. The warm side of the composite displacer showed signs of being overheated, with the gas pressure producing a permanent deformation.

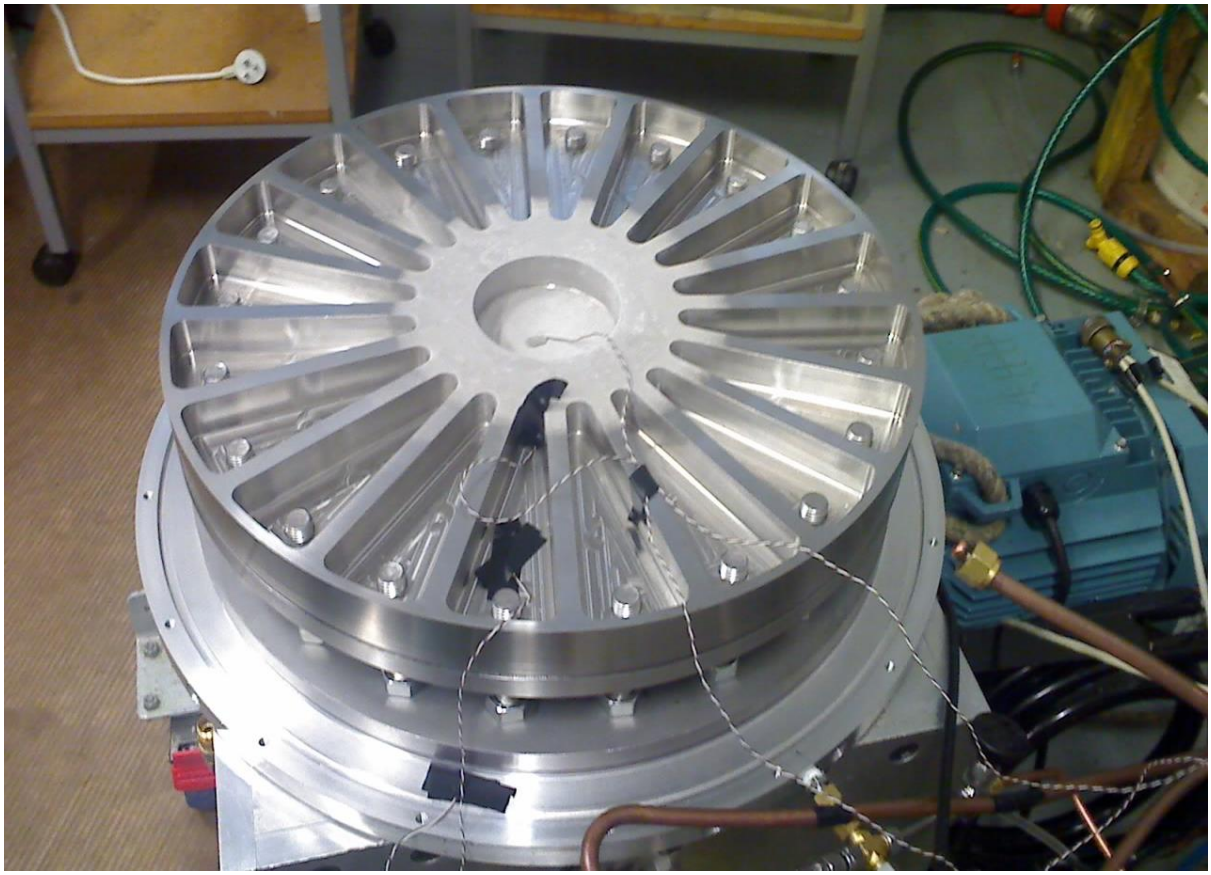

Figure 3-15: Frost forming on the cold plate showing cooling in the centre.

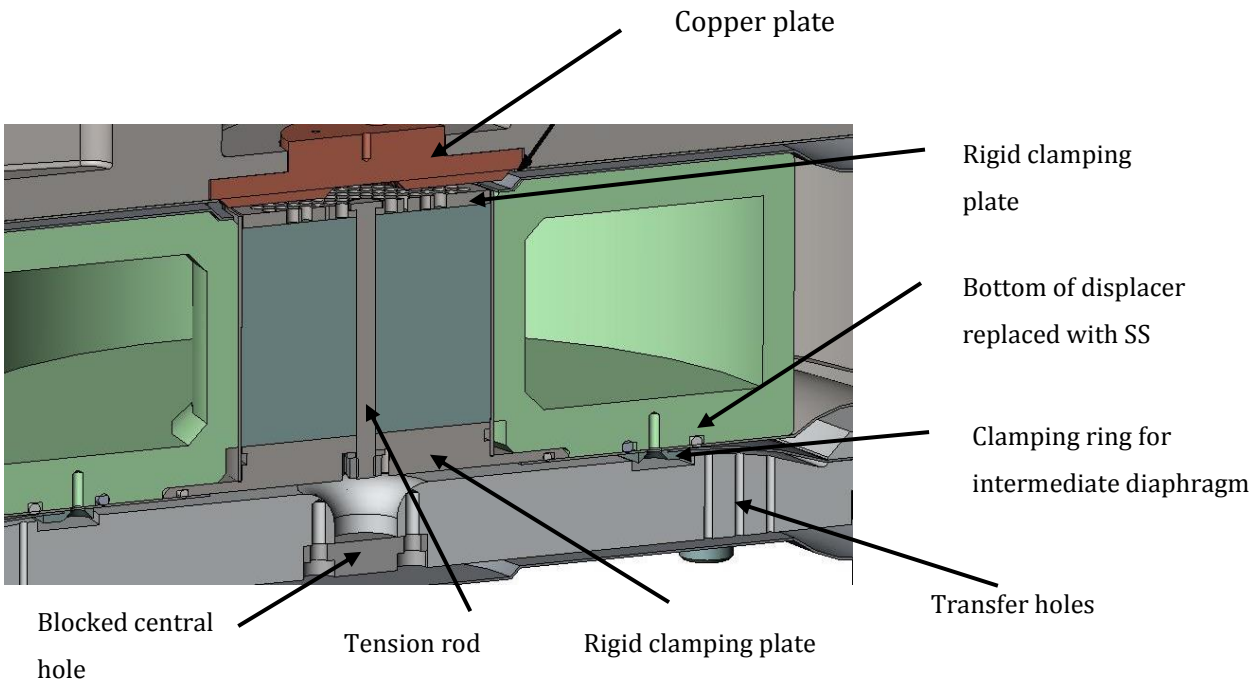

Figure 3-16: Modifications to the prototype. The clamping ring seals and retains the intermediate diaphragm. The regenerator is clamped between two perforated rigid clamping plates with the tension rod. A copper plate was added to enhance heat transfer at the coldest part of the machine.

A new regenerator design and intermediate diaphragm retention system was implemented as shown in Figure 3-16. The regenerator was more securely clamped with a bolted assembly incorporating a tie rod and perforated end caps. The intermediate diaphragm was bolted to the displacer with a clamping ring. A copper plate was added to the centre of the cold plate to aid conduction. The deformed warm end of the composite displacer was replaced with a stainless steel disc. A further addition was a set of holes at the outer periphery of the intermediate diaphragm to encourage radial flow on the warm side of the displacer; the central transfer hole was blocked accordingly.

3.3.5 TEMPERATURE TRANSIENTS

With the majority of the cooling happening in the centre of the cold plate; a steady state was eventually reached with a constant temperature difference between the centre and outside. The temperature gradient is a function of the heat capacity of the top plate, the conductivity of the stainless steel, and the heat flux distribution due to the gas cycle favoring cooling at the centre. The temperature difference between the middle of the cold plate and its outer edge was observed to be up to 100 K. Such a temperature distribution had the potential to induce significant thermal stresses due to contraction of the material in the cold centre. To ensure that transient thermal stresses did not pose a dangerous situation when superimposed on the pressure stress of the cold plate, a finite element analysis was performed with heat removal of 100 W at the centre and holding the outer edge at 300 K. The analysis was performed in two steps, firstly an analysis of the plate with the circumference held at 300 K and -100 W heating applied to the centre. A temperature distribution was predicted which produced a thermal strain distribution. The second step imposed the strain from the thermal distribution on the plate to calculate resultant stresses. The thermally induced stresses thus calculated were superimposed on the stress due to 30 bar of gas pressure to get the final stress on the plate.

The temperature distribution calculated in the first step is shown in Figure 3-17. A 105 K temperature difference between the centre and outside edge is predicted which is close to the maximum temperature difference observed on the prototype. Figure 3-18 shows the stresses induced from thermal contraction of the plate centre superimposed on the stress from the internal gas pressure. The resulting stress is at a maximum of 356 MPa in the centre. This is close to yield but well under the 580 MPa ultimate tensile stress for 316 SS. Some local yielding may occur depending on the temper of the stock material, which was unknown. The stress in the rest of the plate is below 90 MPa which is well under the yield stress of annealed 316 SS. Additional confidence is gained from strength data for 316 SS showing an increase in yield stress with decreasing temperature [54].

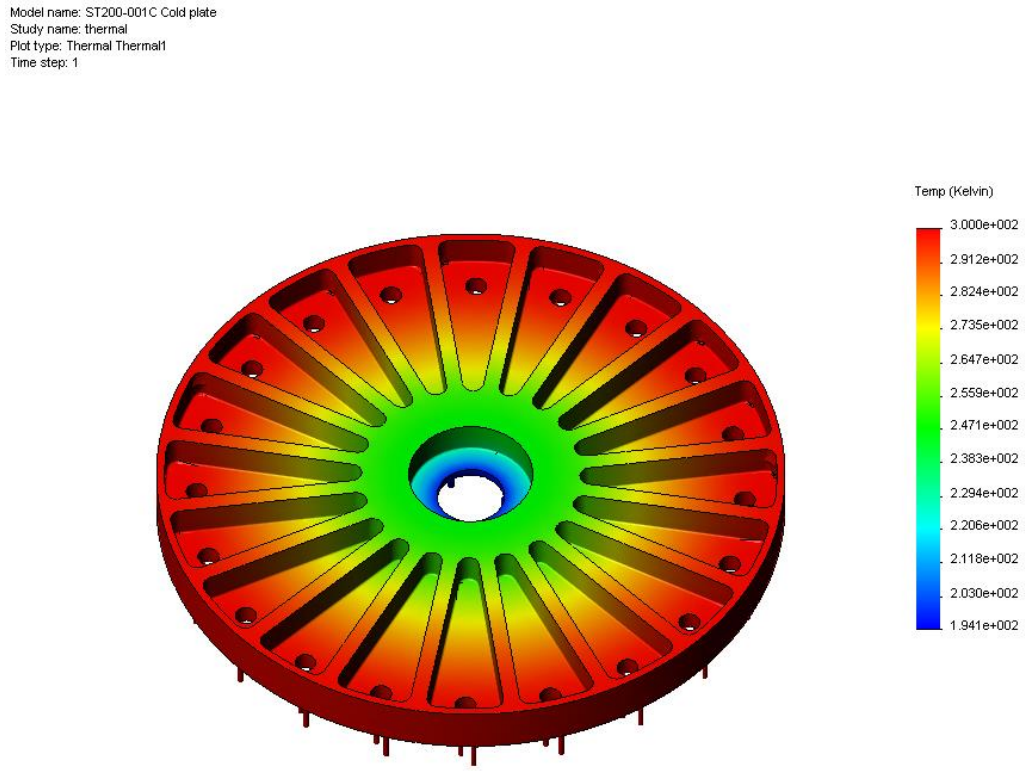

Figure 3-17: Finite element analysis of the temperature distribution in the cold plate, calculated from applying 100 W of cooling to the centre recess and holding the outer circumference at 300 K.

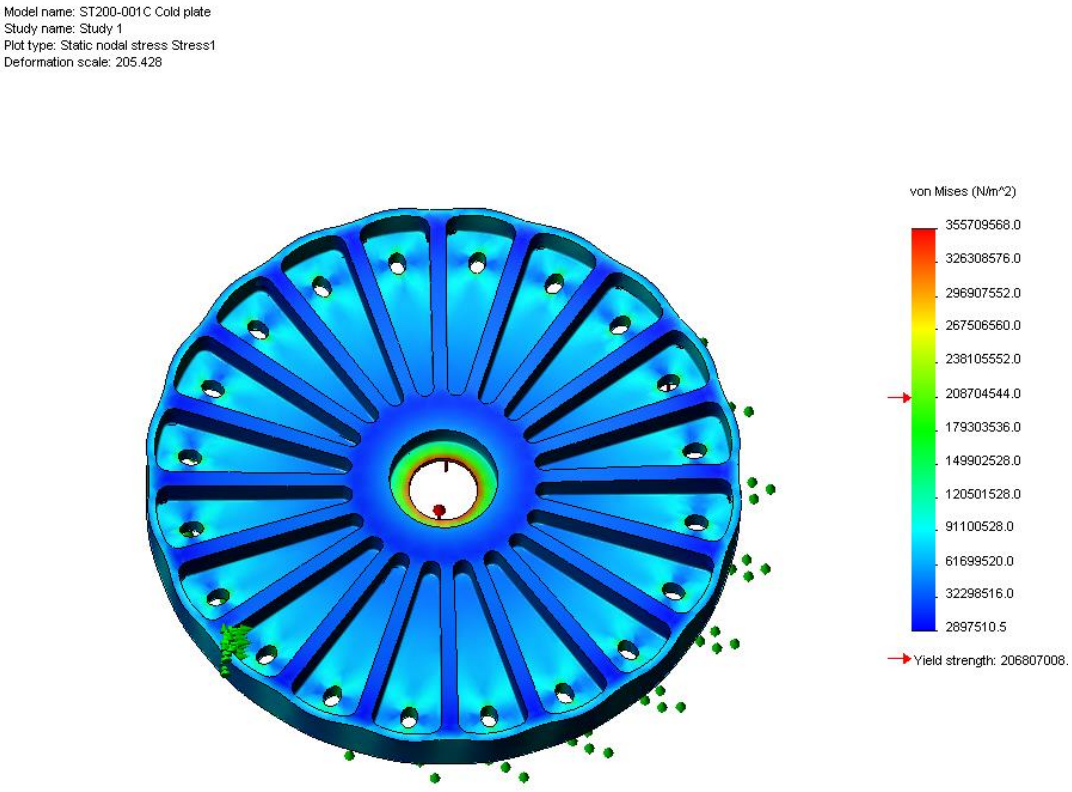

Figure 3-18: Thermally induced stresses superimposed on the gas pressure stress.

3.3.6 CHARACTERISATION AND VERIFICATION EXPERIMENT

A characterisation experiment was performed to determine the dynamic and cooling behaviour of the prototype and verify the Sage model of the cryocooler.

The experiments were conducted without insulation at the cold head to give access to the displacer position sensor. Hence they were conducted around the temperature of 200 K, a temperature readily achieved without a cryostat for insulation. The charge gas was helium at a pressure of 20 bar. The pressure wave's amplitude and phase, and the displacer's movement, amplitude and phase were measured for comparison with the Sage model. Phase angles were relative to the pressure wave generator's driving piston.

The driving piston and displacer movements were measured using Keyence LB72 laser transducers, which allowed non-contact direct position measurement. Experiments were conducted over a range of frequencies from 20 to 60 Hz. The pressure was measured adjacent to the DPWG's diaphragm. The temperature was measured in the centre of the cold plate with a PT100 transducer.

Two cases were considered: the first was as designed and the second with the intermediate diaphragm removed, which removed the bounce space and hence changed the exciting force. Hence, the two cases are called 'bounce' and 'no bounce' respectively. The effects of removing the intermediate diaphragm were: a significant reduction in the spring constant of the displacer; the dead volume on the warm side of the displacer was increased by the volume of the bounce space; and the movement of the displacer was driven solely by the pressure drop across the regenerator. A modified Sage model was produced to simulate the effect of the second case which predicted reduced cooling power with a no-load temperature of 100 K.

Figure 3-19 shows the pressure wave amplitude and *pV*-powers experimentally measured as compared with the Sage model for the two cases: 'bounce' and 'no bounce'. The correlation of the macroscopic parameters of pressure wave amplitude and *pV*-power shows that the Sage model provides a reasonable prediction of gas compression and heat transfer inside the machine. Removal of the bounce space in the Sage model involved making the moving areas of the ends of the displacer the same and adding the volume of the bounce space to the variable volume object 'compression space 2'.

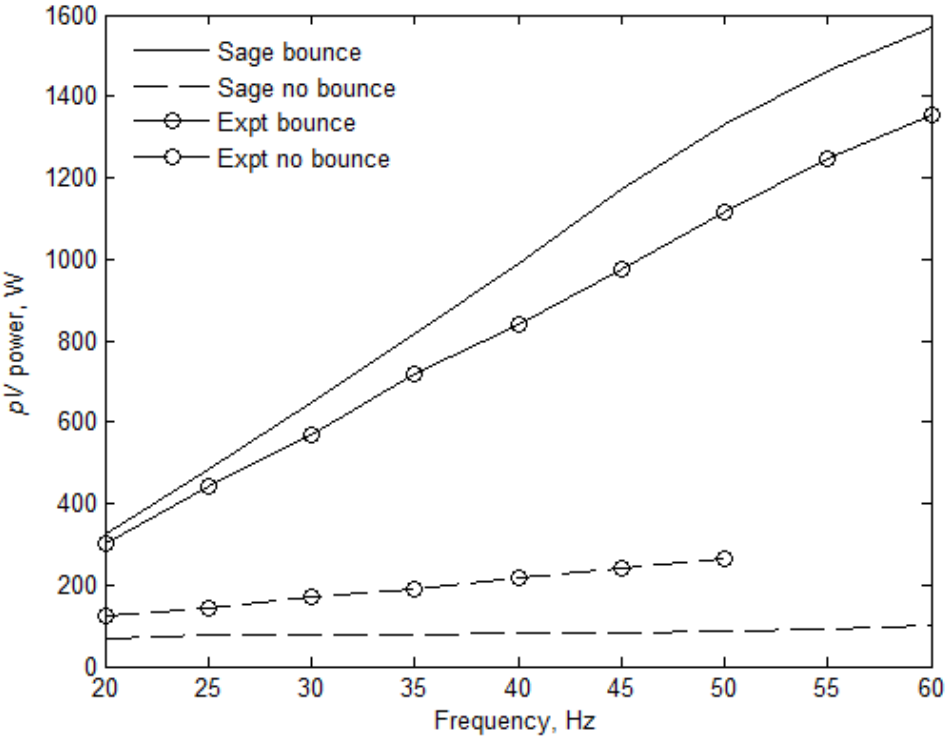

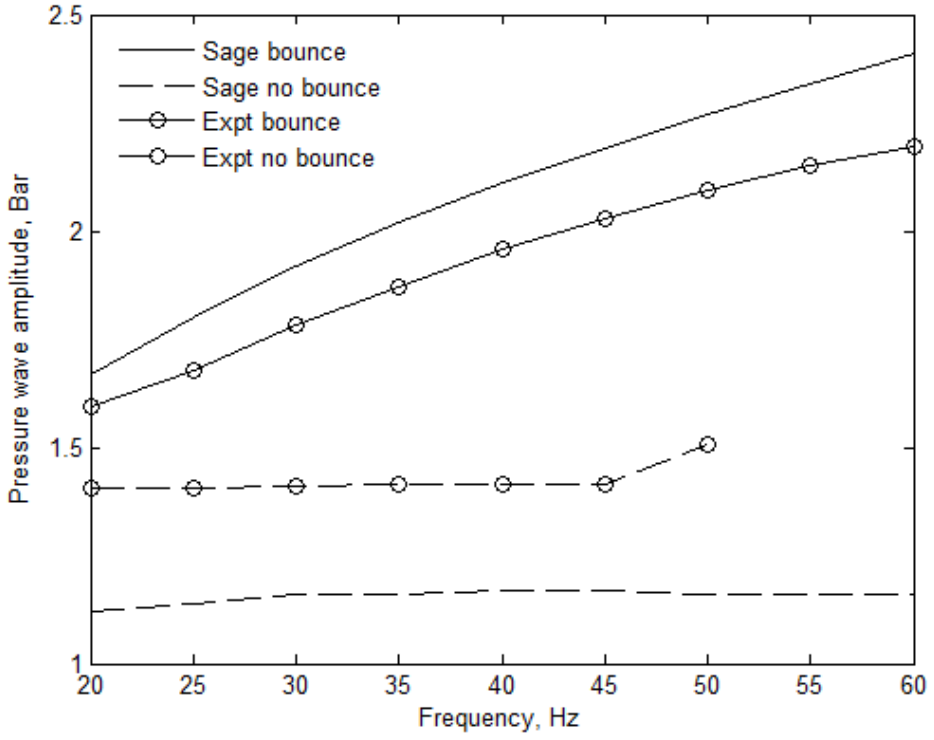

Figure 3-19: Comparison of Sage model and experimental pressure wave amplitude and pV-power for proof-of-concept prototype characterisation runs.

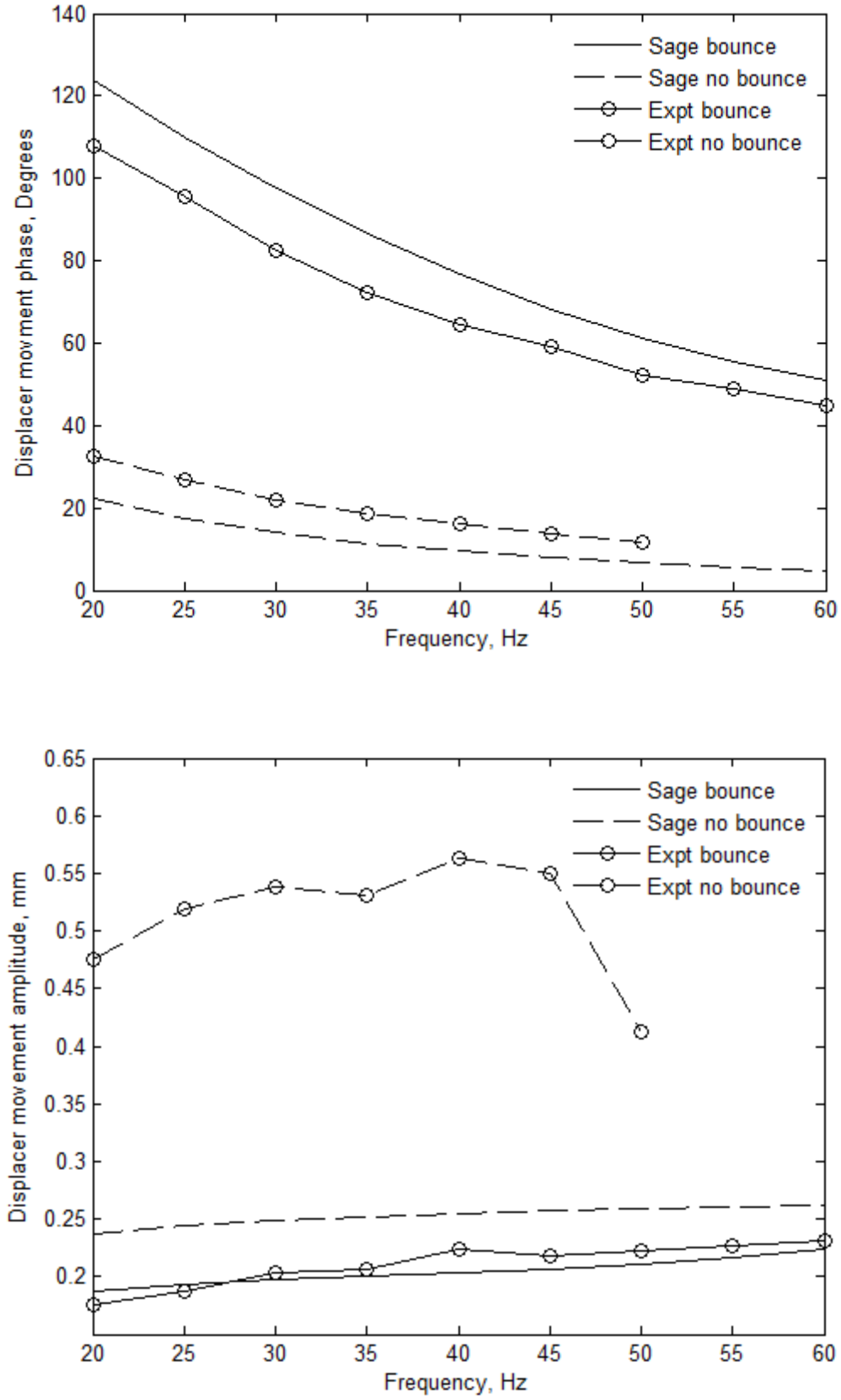

Figure 3-20: Comparison of Sage model and experimental prototype displacer movement for proof-of-concept characterisation runs.

Figure 3-20 shows the displacer movement over a range of frequencies. The experiment agreed well with the Sage prediction for displacer amplitude for the case with the bounce space. However, with the bounce space removed, the experimental displacer amplitude was higher than predicted. There are a number of possible reasons for the prototype's increasing amplitude such as the displacer, once freed from the intermediate diaphragm, was close to resonance; or that vibration of the pressure wave generator could have excited the displacer; or that Sage over-predicted the damping in the regenerator, leading to a low amplitude prediction.

The as-measured displacer phase angle compared well with the Sage predictions. In the case with the bounce space, the prototype's phase angle was less than predicted which would lead to poorer cooling of the prototype than Sage's prediction. However, when the bounce space was removed, the phase angle was larger than predicted, leading to increased cooling, especially when added to the increased amplitude.

3.3.7 COOL-DOWN TEST

The cool down rate was dominated by the thermal mass of the 29.5 kg stainless steel top on the cold head. An initial fast cooling rate was observed while temperature gradients in the plate became established, and then a long slow descent was observed while it steadily cooled the outer parts of the plate. The lowest temperature recorded for the standard design, with bounce space, was 148 K. This was much poorer than expected. Without the bounce space, the prototype achieved a much slower cool-down, indicating a lower cooling power but cooled to a lower temperature, implying lower losses.

During the experiment the prototype suffered from an elusive slow leak into the cryostat, limiting the vacuum in the cryostat to an unsatisfactory 1 mbar and resulting in poor insulation throughout the tests. The heat load from the cryostat leak was significant, limiting the ultimate cold temperature and made cooling power measurements impractical.

Figure 3-21 shows the cooling of the prototype without the bounce space. The initial running speed of the machine was 45 Hz, a speed that appeared to work well at higher temperatures, and cooled it to 107 K in 8 hours. The DPWG frequency was then increased to 60 Hz, which cooled it down to 100.5 K in a further 15 minutes.

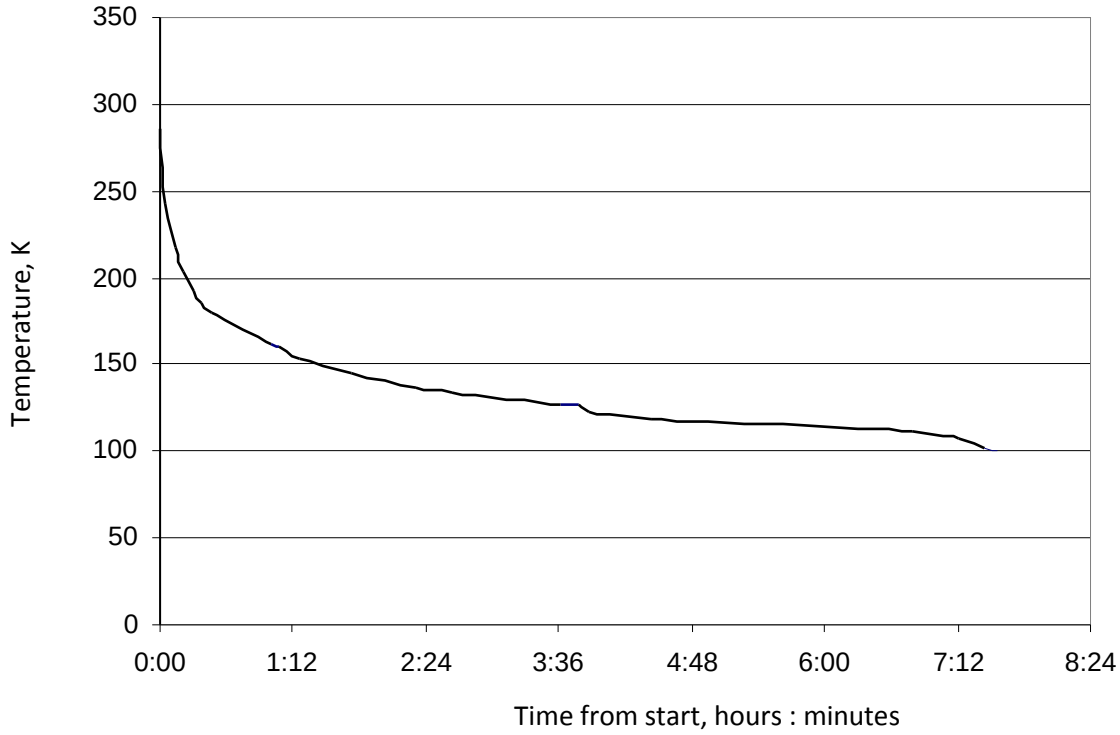

Figure 3-21: Cool-down curve of the prototype without the bounce space. The prototype was run at 45 Hz for most of the run. The dip at the end of the run was from an increase in frequency to 60 Hz.

3.3.8 DISCUSSION / CONCLUSIONS

A proof-of-concept prototype of the diaphragm free-piston Stirling cryocooler based on the initial Sage model has been manufactured and tested. The prototype incorporated a number of design compromises that reduced its measured performance to less than that predicted by the modelling. In particular the intermediate diaphragm was stiffer than originally anticipated and the dead volumes in the compression and expansion spaces were larger.

The concept of using twin opposed diaphragms to support and seal the displacer of a free-piston Stirling cryocooler has been tested and appears feasible according to a Sage model of the system and a proof-of-concept prototype. The coldest temperature reached by the proof-of-concept prototype was 100.5 K. This was achieved without the bounce space, indicating that the benefits from a softer displacer spring outweighed the loss in displacer phase angle and extra dead volume experienced when the intermediate diaphragm was removed.

The Sage model was able to predict the prototype's macroscopic thermodynamic and dynamic behaviour, such as the pressure wave magnitude, pressure wave phase, and displacer

movement. The Sage predictions correlated reasonably well with the prototype's behaviour both with and without the bounce space and intermediate diaphragm.

Sage is a one-dimensional modeler and hence was not able to account for the radial gas flows encountered in the design. Section 21.6 (Gas Domain Theory) of the Sage manual describes the gas domains: " A rubber tube with space- and time-variable cross section is a useful thought picture. The principle flow axis is the tube axis". Of particular importance is the flow in the expansion space where large temperature differences were present, the centre being 100 degrees colder than the perimeter. Possible hypotheses why Sage over-estimated heat transfer are based around Sage's well-verified modeling of cylinder compression where heat transfer is heavily influenced by inlet/outlet turbulence experienced by conventional pistons. The assumed turbulence enhanced by a greater wall-to-volume ratio of the diaphragm geometry is suspected to produce an over-estimation of the heat transfer in the cylinder spaces. Additionally, the piston in a normal cylinder sweeps up and down the walls (a distance of the same order of magnitude as the cylinder diameter), whereas in the diaphragm case there is no sweeping (only a slight flex) and the 'piston' movement is two orders of magnitude smaller than the outer diameter. One might argue that the piston movement is in the order of the hydraulic diameter, which is true, but in that case the area is much larger than an equivalent piston.

The Sage model indicated a number of areas for improvement of the prototype. A smaller diaphragm for the displacer would be an advantage as it would use more of the diaphragms' potential stroke; reduce dead volumes; and reduce diaphragm area and hence requiring thinner walls to hold the gas pressure resulting in reduced conduction losses.

3.4 Second Prototype

3.4.1 INTRODUCTION

The proof-of-concept prototype experimentation and modelling highlighted a number of areas that could improve performance. The outer annulus of the cold diaphragm introduced a significant dead volume of gas that did not contribute to the cooling cycle. The presence of a dead volume reduces the volume ratio (the swept volume being fixed) which reduces the pressure wave amplitude for no positive benefit to performance. Moreover, a dead volume in the cold space increases the mass flow through the regenerator which increases the pressure drop through the regenerator (converting pressure energy to heat) and reduces performance. Shaping of the cold plate to match the diaphragm membrane shape would remove the extra dead volume. The cold diaphragm's swept volume was ideally 37 ml, which under-utilised the CHC200 diaphragm's potential swept volume of 200 ml. A smaller diameter diaphragm would achieve the same swept volume with less area and hence dead volume due to clearance. The smaller area would mean that the tension ring would have to hold a reduced gas force and therefore need thinner walls and reduce heat leakage to the cold areas. Additionally, a smaller diameter would reduce the size of the cold plate and hence the mass of steel to cool down. During the time of testing the first prototype, IRL developed a new 60 ml swept volume pressure wave generator with a 255 mm diameter diaphragm that had the potential to address the above issues.

The intermediate diaphragm added a large amount of stiffness to the displacer suspension which reduced the displacer movement and hence the amount of gas transferring to and from the cold region. An alternative to a metal intermediate diaphragm to seal off the bounce space, such as a clearance-gap piston in a cylinder (dashpot) or rubber diaphragm, would achieve the required forcing function with less spring stiffness. Another aid to achieving better displacer movement would be to add more moving mass to the displacer. The displacer could conceivably be made out of solid steel in two sections, the warm and cold ends, connected by a tube of sufficient wall section to withstand the compressive forces on it but thin enough to limit heat leakage. A heavy displacer would lower its resonant frequency bringing it nearer the operating frequency of the cooler and increase the amplitude of its movement.

The Sage model was updated to include the small displacer diaphragm diameters, heavy displacer and the intermediate diaphragm's spring stiffness removed (the effect of the dashpot). As with the first prototype, the model was optimised by mapping the dashpot area (A3) and regenerator length, keeping the same regenerator diameter as the mesh discs were an expensive item.

3.4.2 *PROTOTYPE DESCRIPTION*

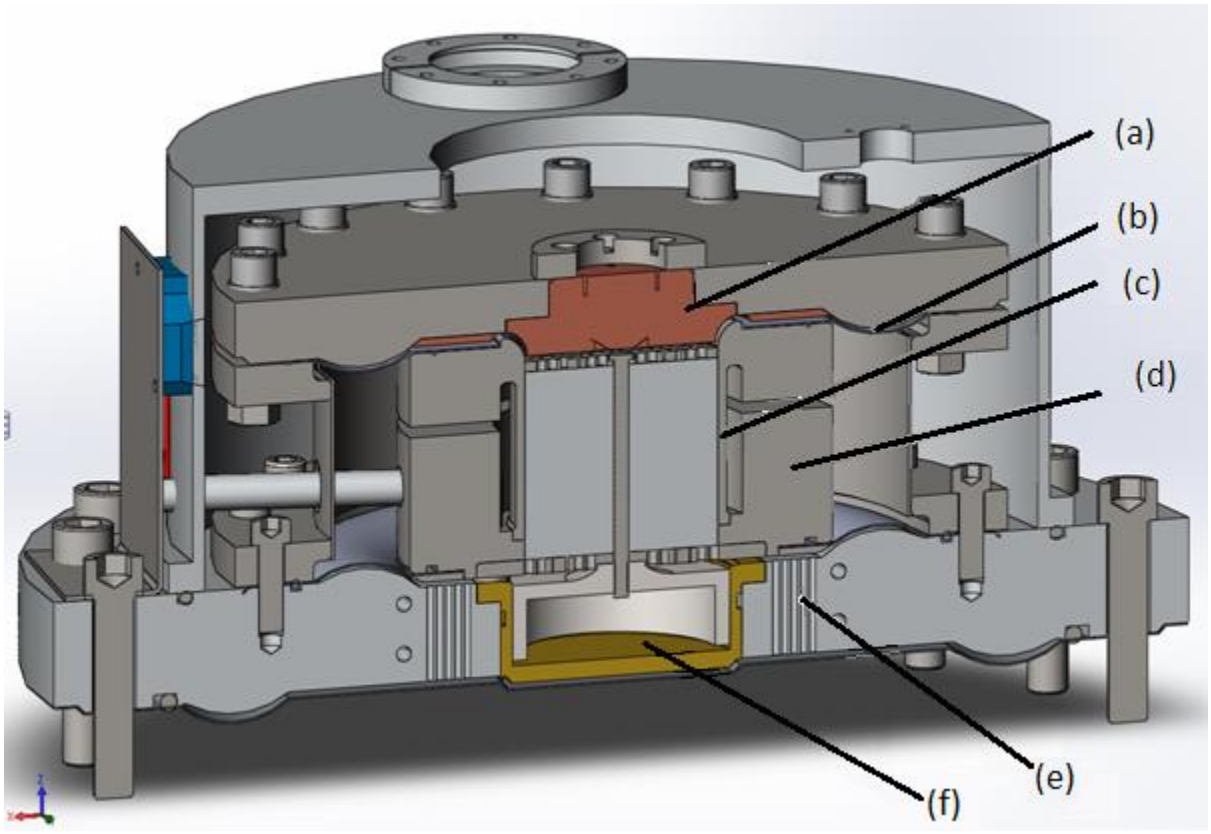

Figure 3-22: CAD cross-section of second iteration prototype.

Figure 3-22 shows the second iteration prototype design with the smaller displacer diaphragm and dashpot. The design incorporates: a copper finned heat exchanger at the centre near the regenerator (a); the annulus of the cold diaphragm filled in (b); a regenerator tube taking the compressive load (c) and a solid displacer with warm and cold sides separated (d); small diameter transfer holes from the pressure wave generator to the warm side of the displacer (e); and a dashpot (f), which was eventually replaced with a rubber diaphragm (Figure 3-23).

The regenerator tube's wall needed to be as thin and long as possible to reduce heat conduction from the warm end to the cold end. However, the regenerator tube also needs to be designed to safely support the compressive loads from the gas on the displacer ends without buckling. Finite Element modelling was used for the analysis and showed that minimising flexure of the cold end of the displacer was critical for achieving a high compressive strength in the regenerator tube. Any flexing of the cold end of the displacer transferred a bending moment to the regenerator tube, reducing its compressive strength. The final design, shown in Figure 3-22, is a compromise between a thick section to give rigidity and a minimised cold mass to reduce cool-down time.

3.4.3 *SAGE MODEL*

Figure 3-23 shows the revised Sage model objects linked to features in the design. Table 3-2 details the values of significant parameters in the Sage model for the second iteration prototype.

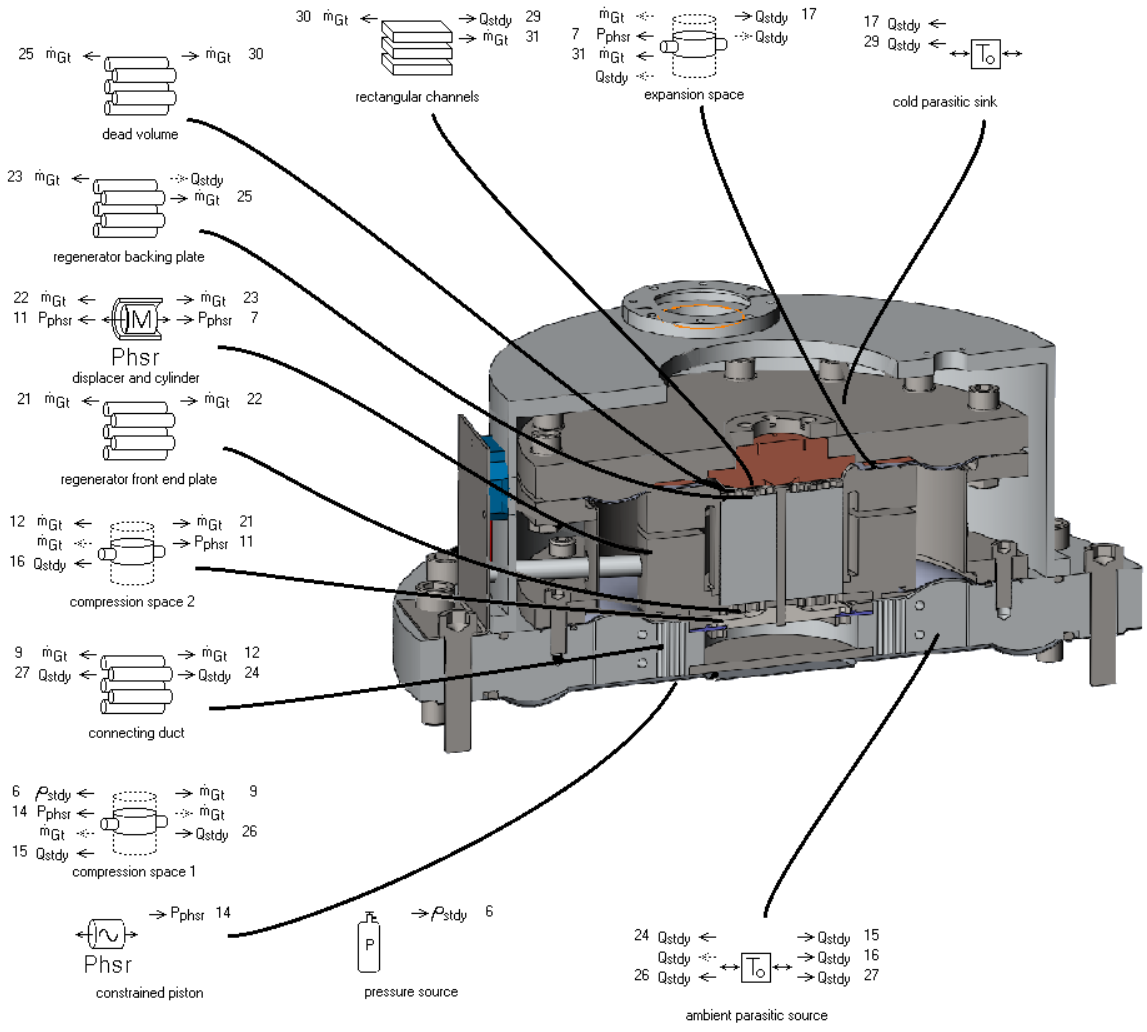

Figure 3-23: Sage model of the second iteration prototype.

Table 3-2: Sage input parameters.

Component	**Parameter**	**Value**
Compression space 1, PWG diaphragm	Effective piston diameter, m	0.31
	Piston area, m^2	0.0755
	Piston stroke (amplitude), m	0.00125
	Wetted surface Area, m^2	2.39×10^{-1}
	Average volume, m^3	3.13×10^{-4}
	H multiplier (manually modifies the heat transfer coefficient)	0.5
Transfer holes	Diameter, m	0.0025
	Length, m	0.04075
	Number	80
	H multiplier (commented on later)	1
Compression space 2, warm side of displacer	Effective piston diameter, m	0.215
	Wetted surface area, m^2	4.5×10^{-2}
	Average volume, m^3	1.68×10^{-4}
	Dashpot diameter, m	0.090
	H multiplier	1
Displacer/reciprocator	Positive facing area, m^2	3.63×10^{-2}
	Negative facing area, m^2	2.99×10^{-2}
	Mass, kg	10
	Spring rate (measured), N m^{-1}	8×10^{6}
Regenerator	Diameter, m	0.0797
	Length, m	0.075
	Wire diameter, m	3×10^{-5}
	Porosity(void volume/total volume)	0.64
Expansion space, cold end	Wetted area, m^2	5.1×10^{-2}
	Mean volume, m^3	1.68×10^{-4}
	H multiplier	1
	Slotted copper heat exchanger (rectangular channels	Width 34 mm Height 1.6 mm Length 10 mm
System	Average pressure, bar	20
	Running frequency, Hz	45
	Warm heat sink, K	300
	Cold heat sink, K	200

A significant addition to the Sage model was a rectangular channel heat exchanger object to model the slotted copper heat exchanger that was inserted into the cold plate. This item recognised the role that the centre of the cold plate played in interacting with the cold gas coming out of the regenerator. The 1.6 mm wide slots were intended to keep typical channel sizes of similar hydraulic diameter to the cold space and give more heat exchange area where needed the most. The values of the rectangular channel object inputs corresponded to the geometric values of the channels, recognising that the 90° turn and significant radial flow in the channels would not be accounted for by Sage. The Sage object is modelled as a set of 36 rectangular 34 mm x 1.6 mm channels, 10 mm long to match the prototype's 36 radial slots, 34 mm long, 10 mm deep and 1.6 mm wide. The Sage model does not take into account that the flow in the slots starts on the 34 mm x 1.6 mm opening but exits perpendicular on the 10 mm x 1.6 mm side. Section 5 of this thesis uses CFD modelling to show the flow in the slots more precisely. Adding the central heat exchanger object brought the cooling power and performance much more in line with the prototype performance.

There are two ways in which the compression spaces can be modelled in Sage. The choice arises because the surface of the aluminium top plate is cooled while the stainless steel diaphragms are not. The aluminium top plate surfaces behave isothermally, with their temperature set by the cooling water and hence can transfer heat in or out of the system. The diaphragm surfaces, in the sub-cycle timescale, act as isothermal surfaces that are at the average gas temperature as the heat capacity of the diaphragm material (0.7mm thick stainless steel) is sufficient to absorb or provide the amount of energy required during the cycle. In the long timescale, the cycle-average heat transfer is zero as the diaphragms are not connected to heat sinks and have no ability to continually transfer heat in or out of the system, so the surfaces behave adiabatically on the long time scale and will follow the average gas temperature. Sage cannot model a gas space with two types of surface in it. Care has to be taken with regards to the assumptions made when modelling the compression spaces as they do not match exactly with Sage's input parameters. A similar situation exists for the expansion space where the cold plate is the heat source and the cold side of the displacer and diaphragm float with the gas temperature (ignoring the small amount of heat conduction down the displacer walls).

The first way of modelling a volume where only half the wall area is available for heat exchange is to enter the volume and assume half the surface area, as an isothermal surface. This causes problems with the hydraulic diameter which is calculated from the area and volume. The hydraulic diameter is used to calculate the Reynolds number, Nusselt number and therefore heat transfer in a fluid flow situation. For a tube, it is the diameter of the tube (hence its name), for non-circular sections it is calculated as four times the area divided by the perimeter, which

for infinite parallel plates reduces to twice the distance between the plates. In the case of the prototype, the mean distance between the walls of the compression spaces is 2 mm, which gives a hydraulic diameter of 4 mm. If only half the walls was used for the wetted area to simulate having half the active heat transfer, then Sage would calculate a hydraulic diameter of 8 mm and would calculate incorrect velocities and convection.

The second method of modelling a volume in Sage where only half the surface area was available for heat transfer is to use the full area of the chambers, thus letting Sage calculate the correct hydraulic diameter for the bulk of the gas, and then halve the heat transfer coefficient to reflect the halved area available for the heat transfer to move heat away from the walls. Sage allows for this to happen with its 'Hmult multiplier' parameter [Sage manual Section 21], which applies a scaling factor to the heat transfer coefficient. This second method was chosen for the modelling.

The Sage model of the second iteration prototype predicts 250 W of cooling at 200 K (at 50 Hz), and 75 W at 77 K as shown in Figure 3-24 and Figure 3-25. Figure 3-26 predicts that at 200 K and 50 Hz, the displacer amplitude would be 0.39 mm at a phase angle of 52°.

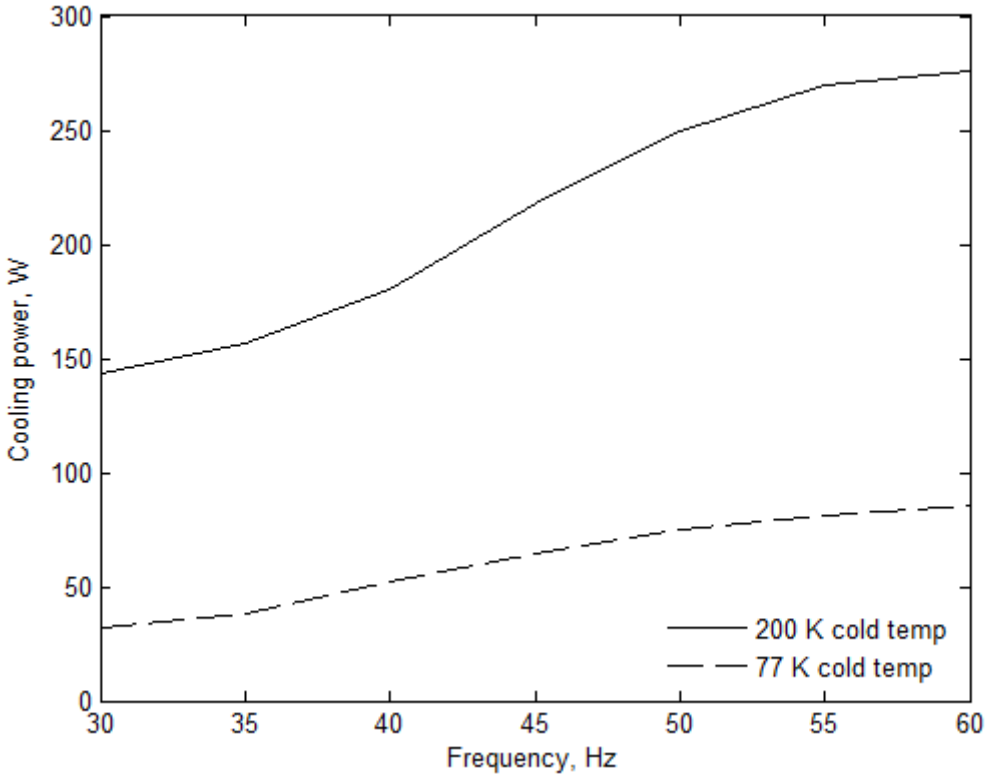

Figure 3-24: Sage predicted cooling power with varying frequency at 200 K and 77 K cold temperatures.

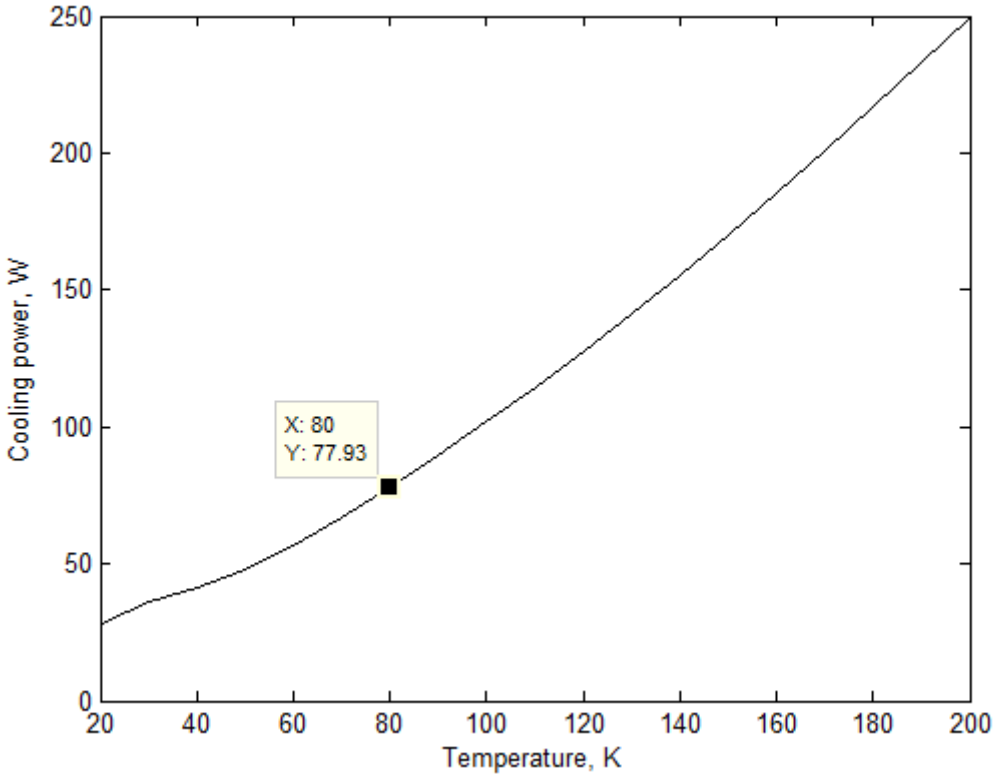

Figure 3-25: Sage prediction of cooling performance of second iteration prototype running at 50 Hz

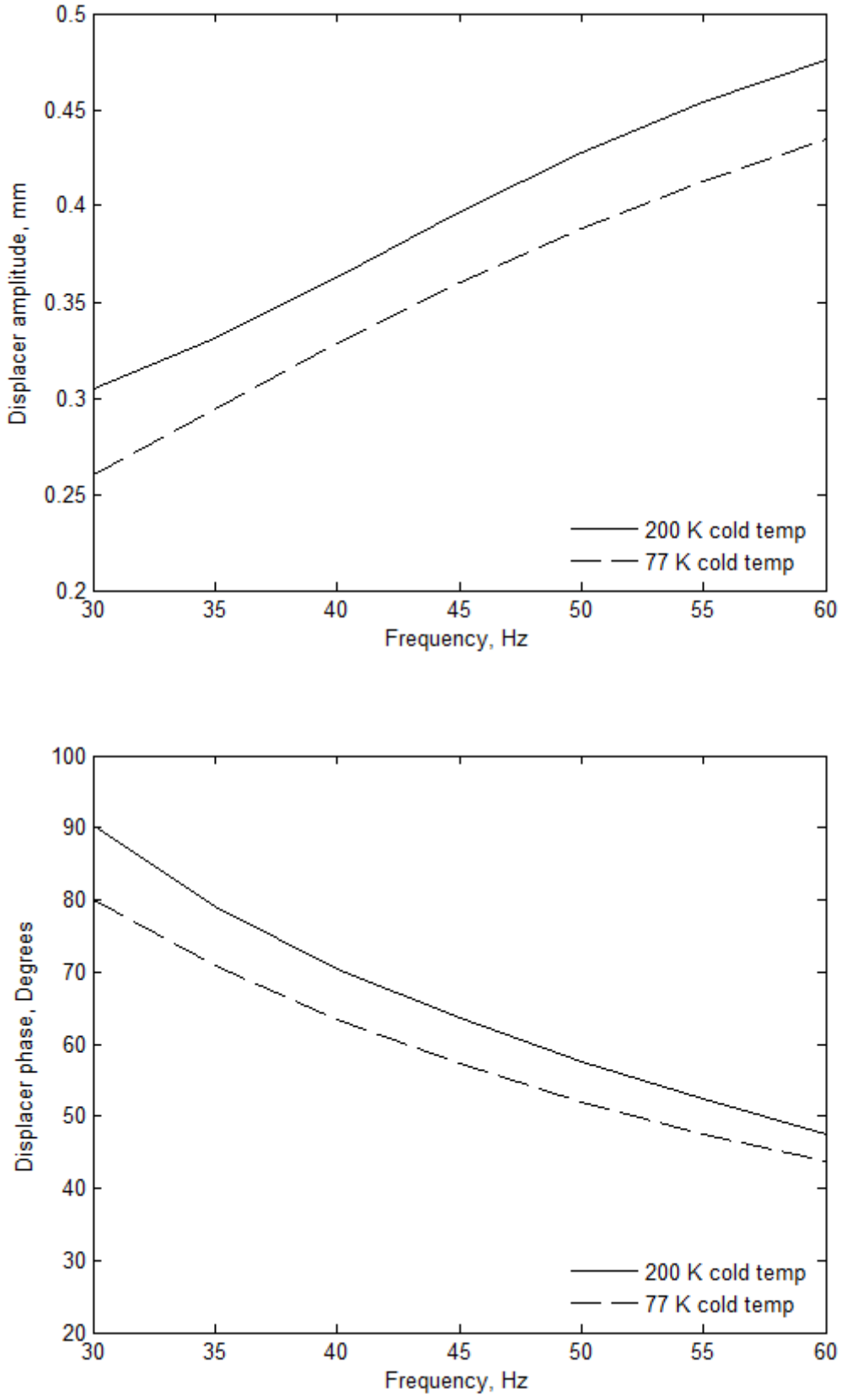

Figure 3-26: Predicted movement of second iteration prototype's displacer at 200 K and 77 K

The sensitivity of Sage to a number of parameters was checked. These parameters were those not directly related to a well-defined physical property, such as the volume of an area or length of a tube. Parameters checked were:

- Ncells – The Ncells parameter was the number of cells that a single component would be broken up into for the solution, somewhat similar to the number of elements in a Finite Element or CFD model. The Ncells parameter was checked for the compression volume, warm and cold sides of the displacer and the connecting ducts. Increasing the number of Ncells from the default values had little effect on the model results.
- Mean Flow Length – The mean flow length is a flow parameter in the cylinder object that corresponds to the swept distance of the piston. The mean flow length parameter had very little effect on the model for the compression volume and warm side of the displacer. It did, however, have a large effect on the cooling power when applied to the cold side of the displacer, with cooling predictions ranging from 400 W to 0 W over the range of values open to interpretation. Sage [74] uses the mean flow length to calculate the cross- sectional area of the generic cylinder element when regarding the cylinder as a passage. The cross-sectional area is used to calculate flow losses and wall conduction losses. Thus a small value, the same as the hydraulic diameter, was used.
- Hmult – Hmult is a multiplier for the heat transfer coefficient, having a default value of 1. In this case, it was assumed that Hmult was 0.5 as previously discussed. Increasing Hmult to 2 decreased the useful refrigeration effect by 10% and decreasing Hmult to 0.25 had less than a 1% effect on the refrigeration, The pV power and displacer movement were minimally affected (all less than 5% over an order of magnitude) Hence it can be argued that the calculated value of Hmult of 0.5 is reasonable and that the model is not very sensitive to this parameter.

3.4.4 Experimental Performance

The spring stiffness of the displacer diaphragms was initially calculated from the Finite Element Analysis used to design the diaphragm of the DPWG. The initial Sage modelling did not predict the displacer movement well, with the modelling suggesting a higher stiffness. To verify the stiffness value used in modelling, an experiment was performed where a pressure tapping was put into the dashpot. The whole cooler was pressurised and the displacer position was recorded simultaneously with the pressure in the dashpot and the rest of the cooler. Initially the pressure in the system would be higher than in the dashpot and, as the gas leaked into the dashpot, the pressures equalised producing a slowly varying force (known from the dashpot area) on the displacer. The slope of the pressure/position line, shown in Figure 3-27, provides the spring constant. The experiment showed where the dashpot reached the end of its travel, indicating

that an adjustment was required to ensure free movement. The measured spring constant was 7.8 x 10^6 N m^{-1}.

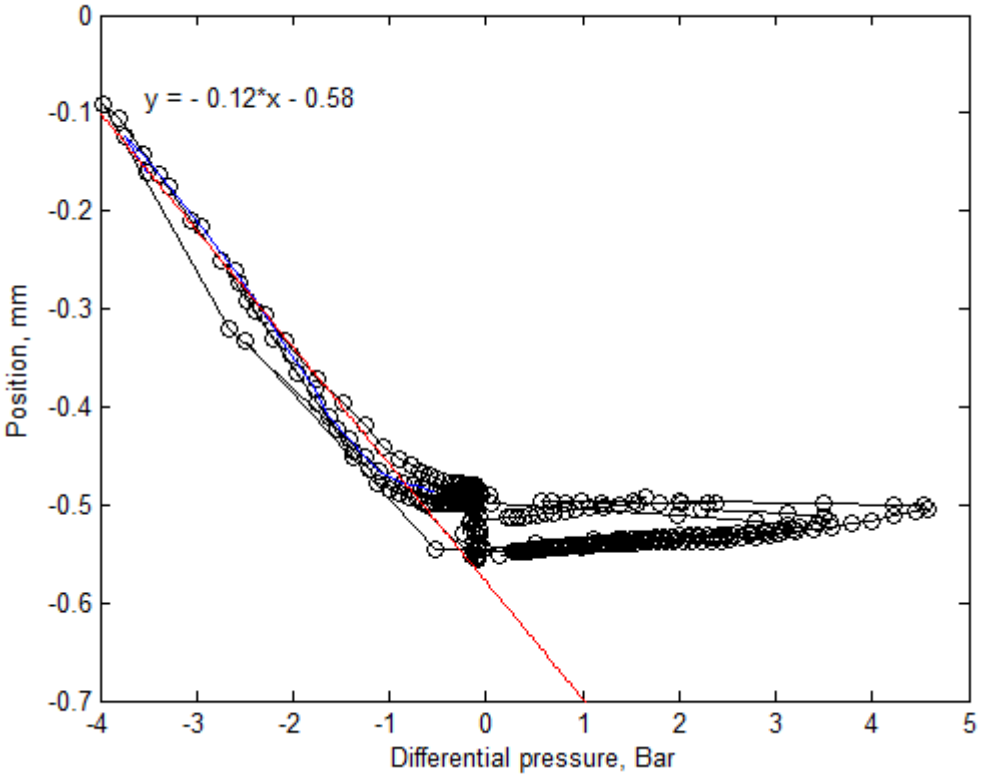

Figure 3-27: Differential pressure vs position for pressurising the dashpot and measuring its effect on the displacer position. The dashpot was bottomed out at 0 bar pressure. The force vs displacement slope for the free section corresponds to a spring rate of 7.8 x 10^6 N m^{-1}

Initial testing was frustrated by unreliable indium cold seals on the displacer diaphragm, both the inner and outer seals. Indium sealed well up to approximately 15 bar gas pressure then consistently started leaking at higher pressures. The seal stopped leaking when the pressure dropped below 15 bar. This was thought to be due to small deflections in the diaphragm as the pressure was increased. A Finite Element analysis was performed to investigate and indicated deflections of close to 10 microns were possible between the flange bolts. The final solution was to weld the diaphragm to the displacer and the cold plate, which produced an effective seal over a wide pressure range.

The prototype, with the cold diaphragm welded for sealing, was run for a characterisation test without the cryostat in place to allow fitment of a position sensor to the displacer.

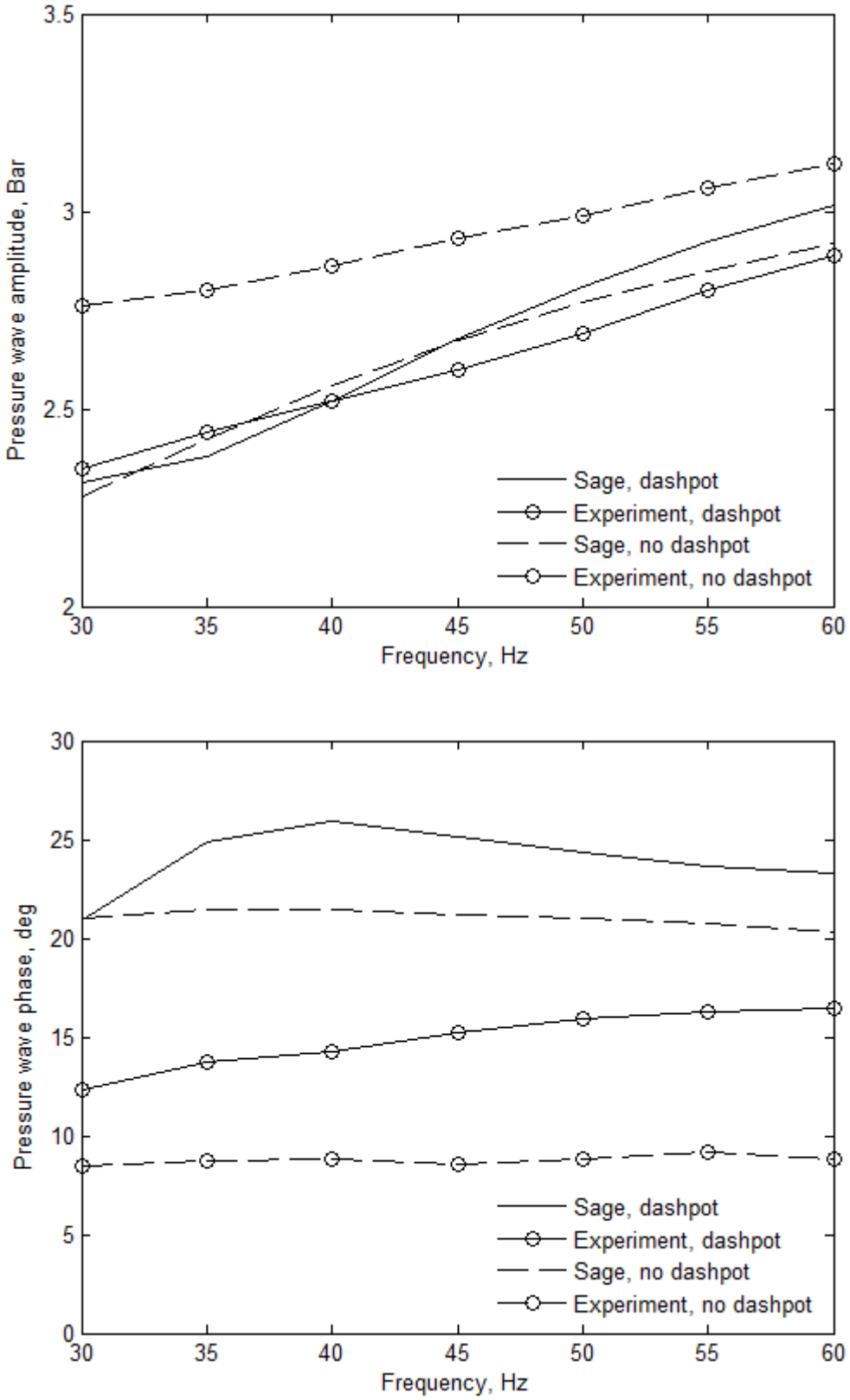

Figure 3-28: Phase and amplitude of the pressure wave at 200 K

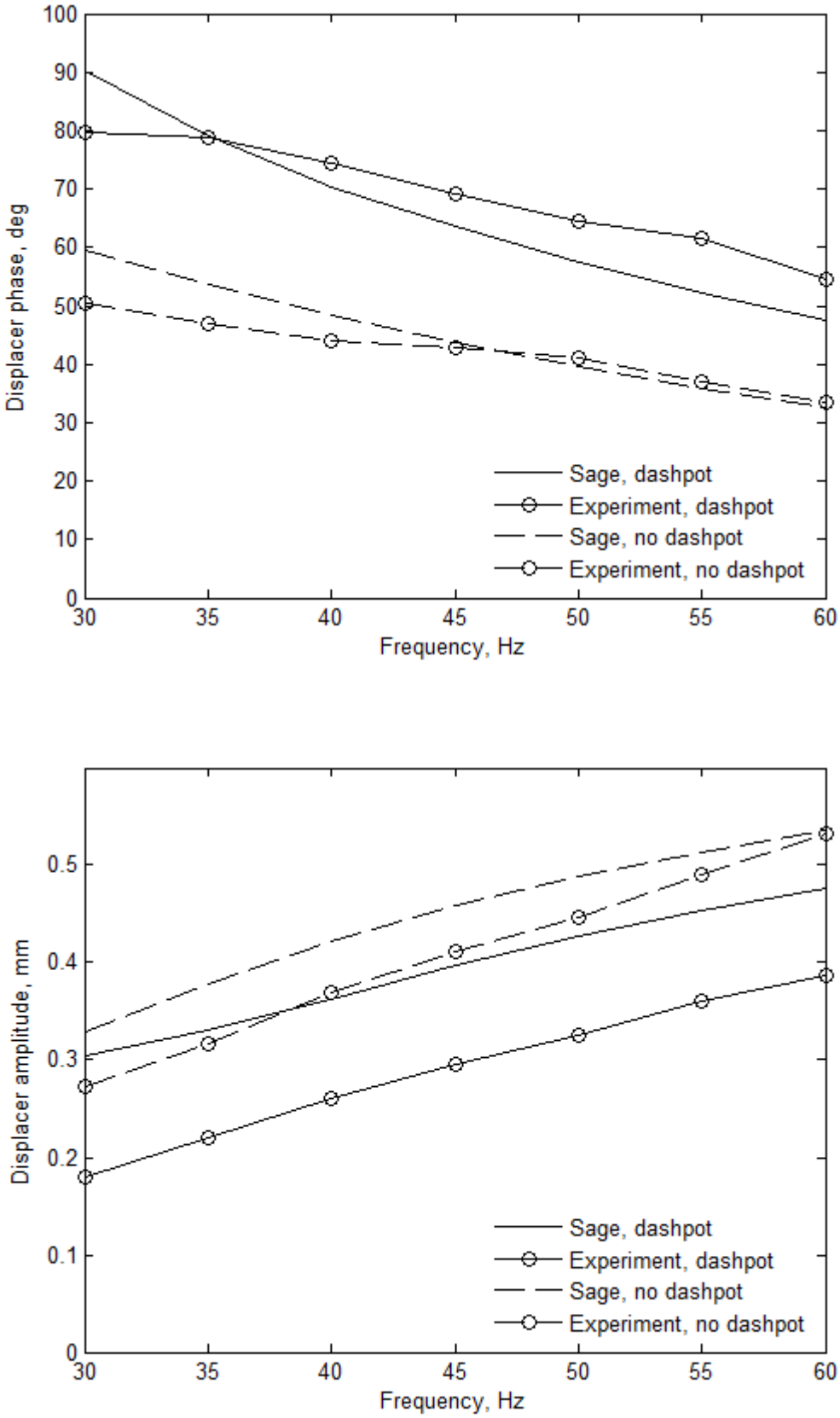

Figure 3-29: Phase and amplitude of the displacer movement at 200 K

Figure 3-28 shows good correlation for the pressure wave amplitude when using the dashpot but the experiment had a lower-than-predicted amplitude for the no-dashpot case. The pressure wave phase angle was smaller than predicted, which followed on to a lower than predicted pV power.

Figure 3-29 shows good correlations between the experiment and predictions for the displacer phase amplitude for the no-dashpot case but the dashpot case measured lower than predicted.

3.4.5 PARAMETERS FOR SUBSEQUENT MODELLING

The characterisation runs above provided a set of results that were used for validation of the CFD modelling performed in Chapter 5 and are shown in Table 3-3 below.

Table 3-3: Parameters from experiments to be used in the CFD modelling in Section 5.

Parameter	**Value**
Frequency	50 Hz for 200 K 60 Hz for 77 K
Displacer amplitude	0.32 mm for 200 K (experiment numbers, Sage was 0.43 mm), 0.34 mm for 77 K (Sage numbers, adjusted by 0.1mm as per 200 K difference between Sage and expt)
Displacer phase (w.r.t PWG diaphragm)	65° for 200 K (experiment numbers, Sage was 57°), 44.3° for 77 K (Sage numbers)
Mean pressure	20 bar for 200 K, 22 bar for 77 K
Pressure wave amplitude	Expect 2.8 bar for 200 K, 3.36 bar at 77 K
Pressure wave phase angle (w.r.t PWG diaphragm)	Expect 15° at 200 K , 19.6° at 77 K
PV power	924 W measured for 200 K (Sage was 1715 W) 2280 W measured, (2960 W from Sage) for 77 K
Warm end wall temperature	CFD to be 300 K
Cold end wall temperature	CFD to be 200 K or 77 K
Pressure wave generator, diaphragm amplitude	1.25 mm. This is what was measured during the time of testing.

3.4.6 *COOL-DOWN EXPERIMENTS*

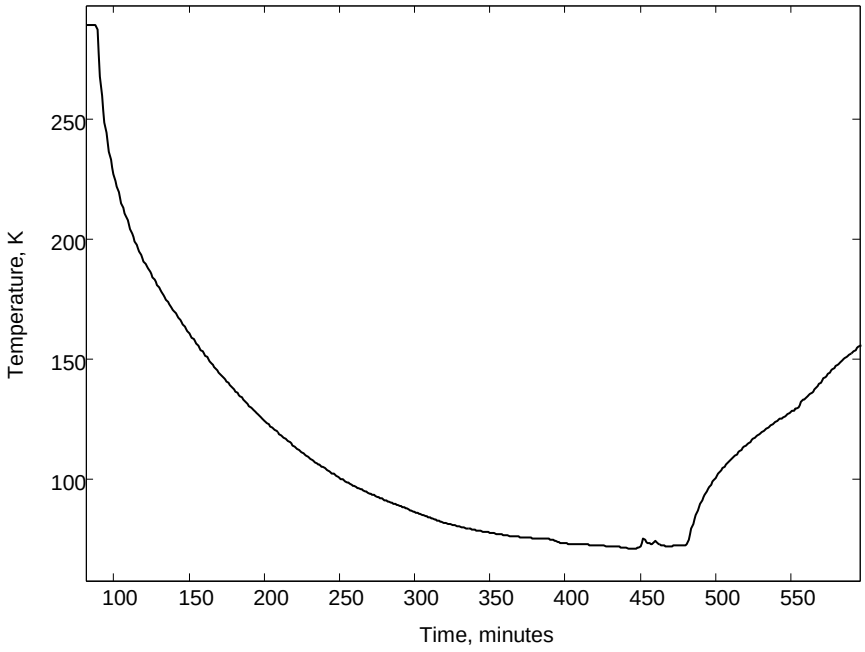

Figure 3-30: The first cool-down and warm-up curves for the second iteration prototype.

Figure 3-30 shows the first cool-down and warm-up curve for the second iteration prototype with a cryostat fitted. It took approximately 5 hours (300 minutes) to cool to 71 K. The slope perturbations at the low temperature were from changes in frequency (to find the best frequency for the low temperature). A kink can be observed in the warm-up curve, where the cold diaphragm cracked, breaking the gas seal during warm-up. Further investigation of literature [77] found references to 430 SS having a brittle transition temperature around -40°C which explains the sudden failure observed. Inspection of the crack was consistent with a brittle failure that propagated from a weld.

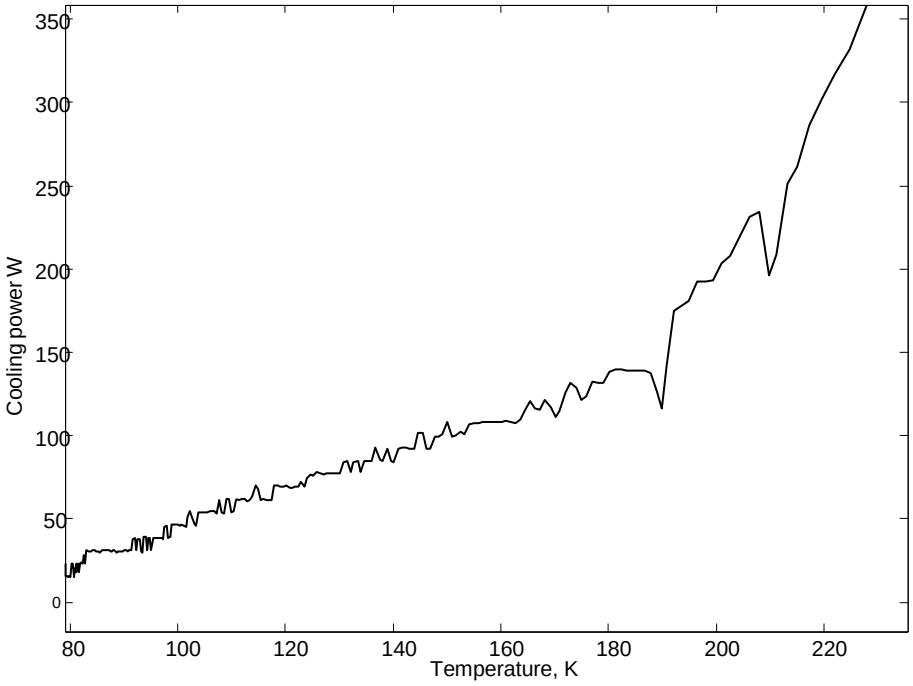

Figure 3-31: Cooling power for the first cool-down experiment, calculated using the cool-down rate and the heat capacity of the cold mass in the cooler.

Figure 3-31 shows the cooling power based on the heat capacity of the cold mass in the cooler. The heat capacity used was for stainless steel at 200 K was 334 J kg^{-1} K^{-1}. The cold mass totalled 22.6 kg of which 14.6 kg was the cold plate, 4.2 kg the cold side of the displacer and 3.9 kg the clamping ring. The displacer consisted of two thick flanges connected with a tube. The tube was sized to minimise heat conduction between warm and cold. The mass of the cold flange only was used in the calculation as the mass of the tube with the temperature gradient was minimal. The slope of the graph is changing down to approximately 180 K, below which it is roughly linear. This suggests that temperature gradients were still being established in the cold mass above approximately 180 K. Extrapolating the linear section to 200 K implies a cooling power of 150 W at 200 K, which is considerably less than the 250 W predicted by Sage, Figure 3-25. Cooling at 77 K was approximately 20 W, as compared to the Sage model prediction of 75 W. Noting that not all of the heat leaks were included in the Sage model this is also a reasonable prediction.

The 430 SS cold diaphragm that cracked on warm-up was replaced with a 316 SS diaphragm. 316 SS is known to be both weldable and not brittle at cryogenic temperatures. Moreover, keeping the diaphragm material the same as the displacer and the cold plate would reduce stresses from differential thermal contraction rates.

The dashpot sealing had proved unreliable, so a rubber membrane was clamped in place to seal the dashpot. The small movement of the displacer and the pressure wave over the small area of the rubber membrane put little stress on the rubber. The rubber provided a seal but did not add significant spring stiffness to the displacer. Finally, as the rubber was not required to provide a hermetic seal for the full helium pressure (as the other metal diaphragms were), diffusion of helium through the rubber was not an issue.

A further set of cool-down experiments was performed. In the first test, shown in Figure 3-32, the cryocooler was run at 50 Hz for a day and night. It had reached 62 K by the morning and was running smoothly. The pressure wave generator frequency was increased to 60 Hz which provided another decrease in temperature. The gas pressure had dropped to 18 bar overnight so it was topped back up to 20 bar, with another increase in cooling. The gas pressure was increased to 22 bar later in the day, at approximately 3200 minutes, provided more cooling and a final low temperature of 55.6 K was reached.

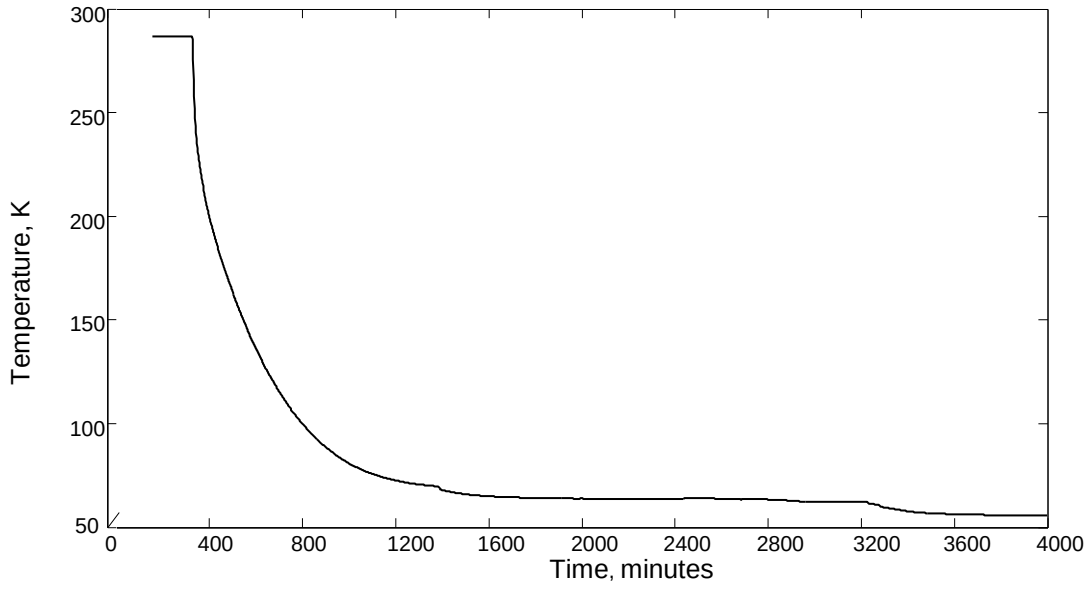

Figure 3-32: Cooling curve with the final low temperature of 55.6 K

A second cooling run was performed starting at 60 Hz with a gas pressure of 22 bar. The cooling power calculated from the cooling rate of the cold mass is shown in Figure 3-33. A refrigeration power of 29 W was achieved at 77 K.

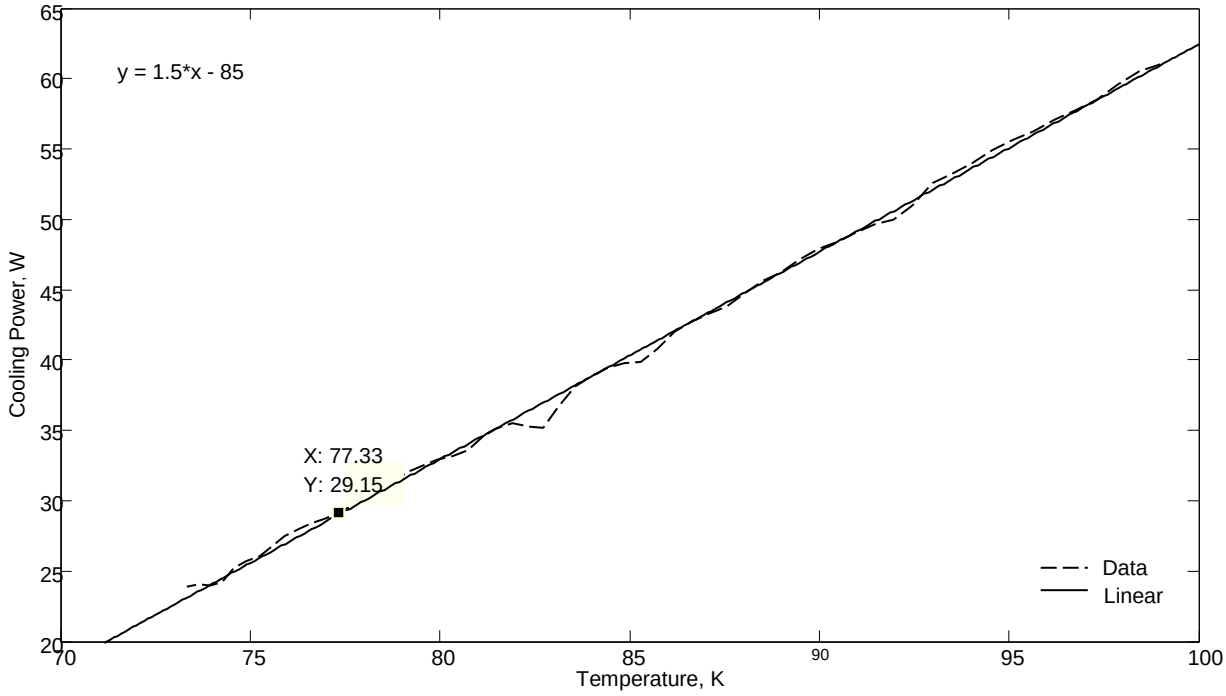

Figure 3-33: Net cooling power of the ST 200 cryocooler at 60 Hz based on cooling rate of the cold mass.

The parasitic heat leak can be estimated by measuring the steady state warm-up rate of the cryocooler when cooled down and then stopped. The warm-up rate is a function of the heat flow from ambient into the cold mass via its connections to the warm side of the cryocooler. This heat flow is regarded as an undesirable energy gain as it detracts from the net refrigeration power of the cooler. The net refrigeration power is the difference between the gross refrigeration performed by the gas and the heat flowing into the cold mass via connections such as the regenerator walls. Radiation and conduction with the cryostat walls were calculated to be minimal due to a vacuum of 10^{-4} mbar and multi-layer radiation shielding.

The temperature distribution changes when the cooling heat flow is removed. After a period of time the transient passes and a steady temperature distribution is established and the measured warm-up rate is a function of the cold mass heat capacity and heat inflow to the cold mass. In the experiment, steady state warming was established when the centre temperature sensor reached 140 K. Figure 3-34 shows the steady state warming section of the warm-up power curve. A linear fit to the warm-up curve predicts 61 W of heat leak at 77 K. Adding the 61 W to the measured 29 W of cooling at 77 K gives a gross refrigeration effect of 90 W at 77K, which is close to the Sage model's predicted 75 W.

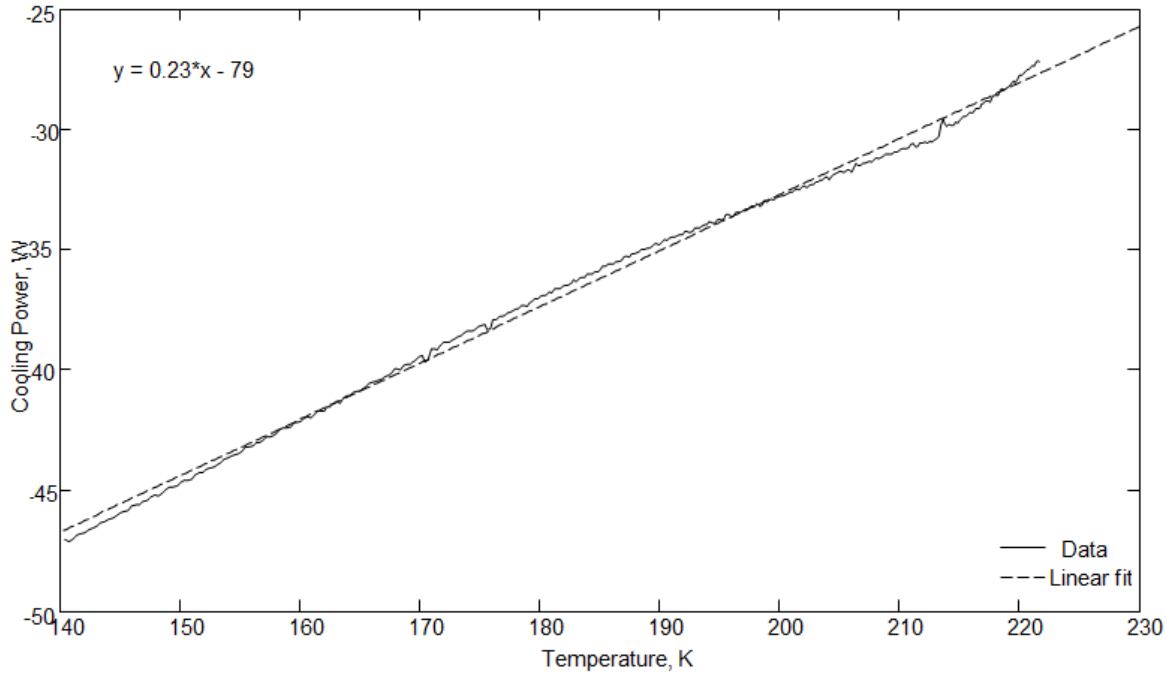

Figure 3-34: Linear section of warm-up power curve for cryocooler when not running.

The characterisation and cool-down tests were repeated with similar results; the lowest temperature reached was 56 K and 12 W of cooling power at 77 K running at 50 Hz. Parasitic heat leak was deduced to be 80 W using the warm-up curve as earlier. The vacuum level, at 10^{-3} mbar, was not as good as the earlier test and would have contributed to more heat leakage. The gross refrigeration of 92 W is similar to the earlier tests. In the later experiments, a second temperature probe was mounted on the cold plate, near the bolt pattern. This probe consistently read a 30 K higher temperature than the cold centre. The temperature difference, when imposed on a Finite Element heat conduction model similar to Figure 3-17, indicated a heat flow of 43 W from outside to centre. This corresponds well with 30.4 W (calculated by CryoComp software [78]) heat leakage down the tension ring walls, which form a physical connection from the cold plate to the warm part of the cryocooler.

3.4.7 CONCLUSION

The two proof-of-concept prototypes showed that it is possible to make a free-piston Stirling cryocooler using diaphragms to suspend the displacer. The sealing and movement of the displacers enabled the manufacture of a free-piston Stirling cold head without the accurate alignment needed for non-rubbing clearance gap seals, confirming the first hypotheses in this thesis, that it is possible to make a free-piston Stirling cryocooler with metal diaphragms. Moreover, the two prototypes both reached cryogenic temperatures, with the second prototype reaching a cold temperature of 56 K. The second prototype produced a small amount of usable cooling power at 77 K, the temperature of liquid nitrogen. For proof-of-concept prototypes this is an encouraging result.

The prototypes both demonstrated more cooling at the centre of the cold plate than at the edges. This indicates a heat flux from the circumference to the centre of the cold plate where the maximum cooling occurs. The gradient corresponded to the heat leak down the tension ring walls.

The diaphragms provided a much stiffer movement than desired, reducing the displacer movement and consequently the performance. This was countered partially by having a heavy displacer. The positive aspect of a heavy displacer is that the mass of the regenerator does not detract from performance, as can be the case with piston displacers which commonly have the regenerator mounted outside the cylinder. Additionally a heavy displacer can provide ample material to support the gas force from the diaphragm area. The negative aspect of a heavy displacer is that there is a significant mass of metal to cool down to cryogenic temperatures, increasing the cool-down time for the cooler.

Sage is a useful modelling tool, providing approximate displacer movement prediction and cooling power. However, it did not give any insight into the heat exchange in the radial flow spaces adjacent to the diaphragms. A separate heat exchanger object was needed in the centre of the expansion space to make the model correlate with the experimental work. A modelling tool such as Sage influences the thought processes of a designer towards the use of heat exchangers and geometries that are included in Sage's library. A circular process arises as Sage is based on current Stirling design practices and, since Sage is the dominant design tool, current design practices become limited to Sage's toolbox. Another, more detailed, thermo-fluid analysis tool, such as CFD, is required to understand and design a better cryocooler that utilises the geometries, and radial flows that are inherent to metallic diaphragms. This is the subject of the forthcoming chapter.

4 CFD MODELLING OF OSCILLATING RADIAL FLOWS

4.1 Introduction

The diaphragm Stirling cryocooler includes three large flat gas spaces containing significant radial flow conditions. The radial flow gas spaces are adjacent to the pressure wave generator and the two displacer diaphragms. Fluid flow and heat transfer in the radial gas spaces resemble the conditions of flow between flat plates, as opposed to the flow-in-a-cylinder found in the equivalent parts of conventional Stirling machines.

One-dimensional analysis techniques, such as Sage, have been developed to model duct and piston-in-cylinder configurations commonly found in Stirling machines where the piston stroke is of the same order of magnitude as the diameter of the cylinder. The diaphragm compression and expansion spaces of interest in this study have strokes typically two orders of magnitude less than the diameter and contain significant radial flow components. Such conditions are not accounted for in a modelling tool such as Sage. Accurate modelling of the diaphragm Stirling system requires a two or three-dimensional modelling approach. Computational Fluid Dynamics (CFD) is a method of analysing complex two or three-dimensional situations by approximating the complex geometry with a collection of simple inter-connected fluid volumes (elements). In ANSYS® CFX, the CFD code used, the time-oscillating conditions in a cryocooler are modelled by using a first or second order backward Euler time stepping method [79], where time is broken up into discrete steps, each step dependent on the conditions calculated for in the preceding step (or steps). Section 1.4.2 details the theory behind ANSYS® CFX.

Whilst ANSYS® CFX's theory has been well verified, the accuracy of a particular model is dependent on the appropriateness of the boundary conditions, mesh, and material properties applied to the model. Hence a key part of CFD technique is validation to ensure appropriateness of the model, mesh and boundary condition assumptions for the situation to be analysed. In the case of the Stirling cryocooler with its volume oscillation and heat exchangers, the assumptions most in question are: the gas model; heat transfer between the gas and walls; the appropriateness of the wall boundary conditions; the time-step transient method for modelling the oscillations; and the mesh density for modelling the thermal and fluid boundary layers in the gas.

Validation of the model can be either against well-known analytical solutions, or accurate physical measurements in experiments. The choice of parameters to validate is important as some parameters are easily calculated in the model but difficult to physically measure in an experiment. For instance, high speed oscillating gas systems have rapidly varying temperatures

that are difficult to measure due to the heat capacity of real sensors. However, parameters such as pressure and volume can be readily measured at speed with commonly available sensors that are able to respond much faster than the 50 Hz running speed of typical cryocoolers.

There are three time-scales to consider in the CFD modelling of the oscillating systems in this thesis.

The first time-scale is each time-step in the transient analysis. The conditions in each time-step must satisfy the CFD model's governing equations (momentum, mass and energy conservation) to an accuracy that is better than the residual error set at the start of the calculations (in this case 10^{-4}).

The second time-scale is the cycle length. In the models in this thesis, there are between 180 and 400 time-steps per cycle and each cycle represents approximately 0.02 seconds (running at 50 Hz). Energy may be transferred in and out of the system during a cycle, mass may move around the system. The internal energy of the system can change through a change in pressure or temperature as energy is added or removed. Energy, mass and momentum need to be conserved. Steady behaviour on the second time-scale is when the gas in each part of the model is substantially the same at any time during the cycle as at the same time in the next cycle. In this way two cycles would look almost identical.

The third time-scale is the long time scale, over many cycles and involves movement of the average conditions during the cycle. Steady-state has been reached when the cycle-average conditions in the cycle are the same from one cycle to the next.

The differentiation between the second and third time scales is important in this thesis because of the large difference in heat capacity between a cryocooler's gas and the solid regenerator matrix. A model may achieve steady behaviour on the second time scale in a few cycles but, because of the magnitude of the cycle-average heat transfers compared with the heat capacity of the regenerator, may take thousands of cycles to reach steady-state in the third time-scale.

Based on Kornhauser's work, gas compression always occurs somewhere between the extremes of isothermal and adiabatic compression. A fast moving cycle with a low surface area-to-volume ratio does not have time to exchange all the heat generated in the gas with the walls, so will tend towards adiabatic behaviour. A very slow cycle, or one with a very large surface area-to-volume ratio, will tend towards isothermal behaviour. In between the two extremes, there is a condition where significant heat transfer takes place with a high temperature difference between the walls and gas, a condition that produces entropy, inefficient compression, and therefore more work done by the piston. Hence, gas spring hysteresis provides a measurable quantity for

verifying compression of gas in a cylinder models. For an analytical expression or computer model (CFD) to calculate the hysteresis loop experienced by the driving cylinder correctly, it has to take into account the physics of the compressed gas and the heat transfer between the gas and the walls.

Isothermal compression requires all the heating from compression to be instantaneously transferred out of the gas during compression; the pressure change is inversely proportional to volume change according to the ideal gas state equations for constant temperature. Adiabatic compression keeps all the energy in the gas, with no transfer to the surroundings, the heat of compression increasing the temperature and hence pressure. The pressure ratio is therefore a function of the heat transfer between the gas and walls and can be used to validate gas spring compression models. The polytropic index, *n,* is defined as

$$\frac{p_2}{p_1} = \left(\frac{V_1}{V_2}\right)^n \qquad 4\text{-}1$$

and is the exponent that describes the relationship between the pressure ratio and the volume ratio. A polytropic index of 1 occurs with isothermal compression and 1.67 for adiabatic compression of monatomic gases.

In this work, validation of the CFD modelling technique was performed in four stages as illustrated in Figure 4-1. Firstly a simple well known model was validated, then the complexity of the model was increased until it became similar to the final cryocooler geometry of interest.

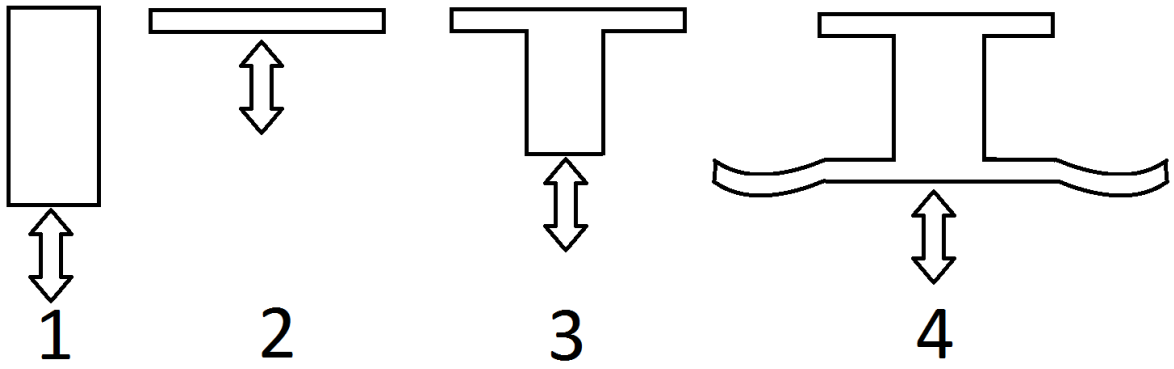

Figure 4-1: The four validation stages: 1) Kornhauser's piston-in-cylinder, 2) Flat cylinder, 3) T cylinder, 4) validation experiment with diaphragm pressure wave generator (not to scale).

The first CFD validation step is a model of the fundamental gas spring hysteresis experiments performed by Kornhauser and Smith [32]. Kornhauser and Smith's experiments spanned a range of conditions from near-isothermal to near-adiabatic compression in a cylinder with a two-to-one compression ratio, typical of many Stirling machines. Kornhauser and Smith measured the pressure and volume of their system to calculate the work done in a cycle. They related the work done in a cycle to the work done during adiabatic compression for the same conditions to produce a characteristic non-dimensional loss that showed the transition from isothermal to adiabatic compression.

The second validation stage modified Kornhauser's cylinder to be typical in size and proportion to the diaphragm expansion or compression spaces of interest, whilst keeping the same volume and compression ratio used in Kornhauser's work. Of key interest in this stage was to observe the effect of hydraulic diameter and flat geometry on the magnitude and position of maximum hysteresis. Also of interest was whether Sage could accurately model the validation experiment.

The third stage introduced a radial flow component by the means of splitting the compression volume into a cylinder space consistent with Kornhauser's experiments, plus a flat radial section to compress into. The flat radial section introduced radial flows into the model. The volume and compression ratio of the Kornhauser's model was maintained.

The fourth stage validated the CFD with an experiment. The validation experiment used a modification of the second iteration prototype from Section 3-2, where the regenerator and moving displacer were removed to produce a simpler situation to model. The regenerator is a component with a very high surface area and heat capacity that has the effect of pushing compression towards isothermal. The validation experiment retained the prototype's average internal volume. The hypothesis of the validation was that for the CFD model to predict the experiments' polytropic index over a range of conditions from isothermal to adiabatic, it would have to accurately model the gas flow and heat transfer with the walls throughout the cycle.

Sage, in spite of its one-dimensional assumption, is a very useful design tool, and defining the limitations of Sage, with reference to diaphragm geometry, is essential for its proper application to the design of diaphragm Stirling cryocoolers. Throughout the validation process, Sage was compared to the CFD model and with the experiments. The expectation was that Sage will model the standard piston-in-cylinder cases better than those with flat geometry or radial flows. In addition, the comparisons will provide a level of confidence with which Sage could be used in the initial design stages for diaphragm systems.

4.2 Key Assumptions

There are two fundamental assumptions that are used in the modelling in this work. They are that the working gas, helium, behaves as an ideal gas and that the walls of the cryocooler are isothermal. These assumptions make the modelling much simpler.

The validity of the first assumption that helium behaves as an ideal gas was tested using the RefProp code by NIST [80] for real helium gas properties. The overall range of conditions tested were typical of Stirling or pulse tube cryocoolers using DPWGs, that is between temperatures of 50 to 350 K and pressures between 0.1 to 2.0 MPa gas pressure. Ambient conditions of 293 K (20°C) and 0.1 MPa (atmospheric) pressure were the reference point. From Table 4-1, the ideal gas assumption for helium is within +/- 0.5% in the near-ambient range and can therefore proceed with confidence with the helium ideal gas model for validation experiments that occur around ambient temperatures. Even when extending to higher pressures and very low temperatures, the ideal gas model is accurate to within 7% of the real gas properties between 300 K and 50 K. At 200 K and 2.0 MPa, conditions used for the prototype characterisation tests, the error from the ideal gas is in the order of 1%.

Table 4-1: Comparison of helium real gas and ideal gas behaviour.

Pressure (Bar-absolute)	**Temperature (K)**	**RefProp volume for 1 kg of gas (m^3)**	**Ideal gas calculation of volume for 1 kg of gas (m^3)**	**Error (%)**
1	293	6.0891	6.0891	Reference for ideal gas calculations
3	300	2.080083	2.0782	-0.45%
1	250	5.195885	5.1955	-0.01%
6	250	0.866701	0.86591	-0.01%
1	350	7.273256	7.27367	+0.01%
6	350	1.214506	1.21228	0.18%
20	300	0.31443	0.31173	0.8%
20	200	0.21071	0.20782	1.01%
20	100	0.10689	0.10391	2.87%
20	50	0.054503	0.50195	7.3%

The second assumption is that the heat exchanger walls are isothermal. The CFD models conducted on compression of gas in a cylinder and the validation model of the pressure wave generator plus radial flow/compression space all assume isothermal wall conditions. The assumption of isothermal walls is only valid if the temperature change of the wall is very small compared with the temperature oscillations in the gas. To test the assumption a finite difference (Euler) model was created using Matlab to calculate the transient conduction behaviour of an aluminium wall in contact with helium gas. Two cases were considered:

1. A layer of helium gas in contact with the aluminium. The boundary of the helium has an oscillating temperature imposed on it. Initial conditions are that the temperature is uniform and equal to 300 K at the start. Figure 4-2 shows the model.
2. An oscillating heat flux is imposed on the aluminium wall. The amplitude of the heat flux is typical of the maximum values from the CFD modelling. Figure 4-3 shows the model.

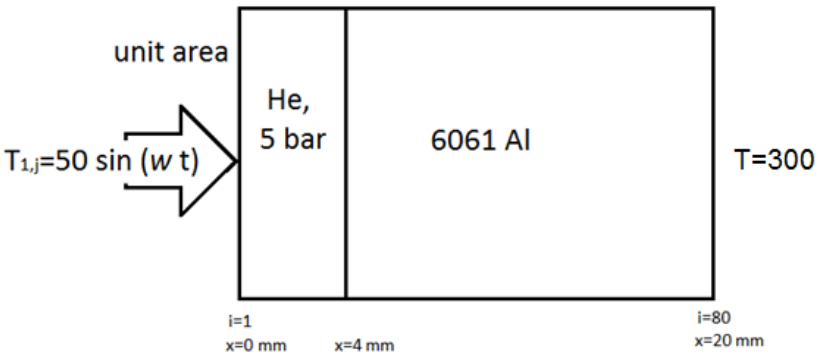

Figure 4-2: Schematic of Case 1 where the gas temperature is oscillating 4 mm from the wall.

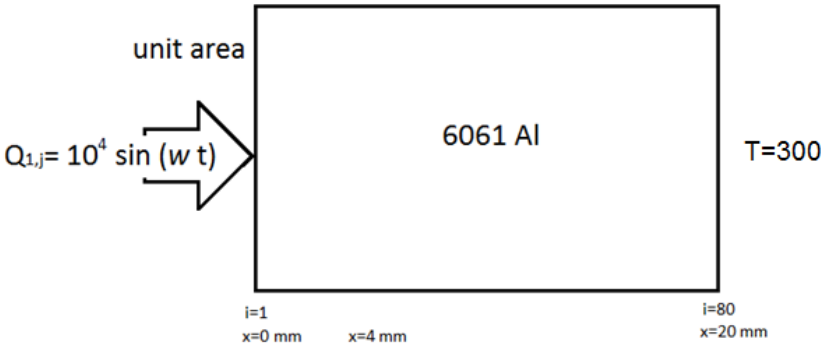

Figure 4-3: Schematic of Case 2 where an oscillating heat flux is applied to the wall.

Each model was broken up into 80 elements. Each element, Figure 4-4, was assumed to have unit surface area, constant mass and constant volume. Thus $\dot{Q}$, the heat flow into the element also had the units of heat flux (heat flow per unit area). Material properties for the gas and aluminium are detailed in Table 4-2.

Each element had the same governing equations as below:

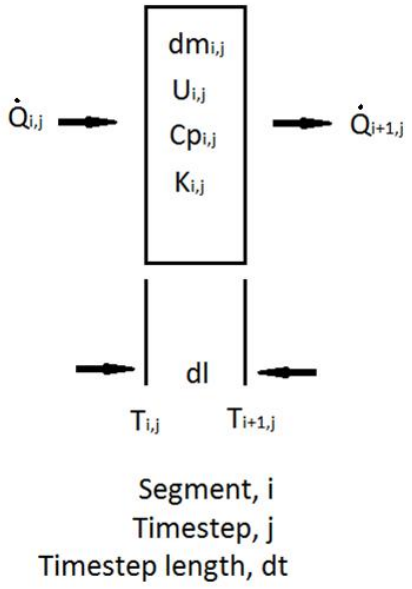

Figure 4-4: The calculation element.

The governing equations for each element, *i* and time step *j* were:

$$\dot{Q}_{i,j} = \frac{\kappa_{i,j}(T_{i-1,j-1} - T_{i,j-1})}{dl_i} \quad 4\text{-}2$$

$$dU_{i,j} = (\dot{Q}_{i,j} - \dot{Q}_{i+1,j})dt \quad 4\text{-}3$$

$$dT_{i,j} = \frac{dU_{i,j}}{Cp_i dm_i} \quad 4\text{-}4$$

$$T_{i,j} = T_{i,j-1} + dT \quad 4\text{-}5$$

where $\dot{Q}$ is the heat flow rate, κ conductivity, U internal energy, l length, t time and T temperature. The boundary between helium and aluminium in Case 1 was modelled by setting

the material properties to those of helium for elements where i< 16 and the remainder to those of aluminium.

Table 4-2. Material properties for the isothermal wall assumption test

Parameter	**Helium at 5 bar**	**6061 aluminium**	**Unit**
Density	0.8005	2700	Kg m^{-3}
Heat capacity	C_v=3117	C_p=896	J kg^{-1} K^{-1}
Conductivity	0.1563	167	W m^{-1} K^{-1}

The Matlab analysis progressed through the elements and time steps. The overall thickness was assumed to be 20 mm, with 4 mm of the thickness to be helium gas for the first case. The element length, *dl*, was adjusted to show good resolution, and the time step, *dt*, was set to achieve stability. Much finer time steps were necessary to achieve stability for the helium elements than for the aluminium elements as the helium elements did not have as much heat capacity and thus experienced a much larger temperature swing for a given change in internal energy.

Figure 4-5 shows the time vs temperature results for Case 1, with 4 mm of helium gas in contact with aluminium wall and an oscillating temperature with an amplitude of 50 K imposed on helium boundary. The blue curve with the largest amplitude is at the boundary with the oscillating temperature and each subsequent trace, green, then red and so on, represents the temperature of the next element. The black trace is the last gas element. The oscillating temperature gradient in the gas can easily be seen in the gas with a phase lag in the gas next to the wall as would be expected as the gas in each element is warmed or cooled by its adjacent elements. The temperature oscillations in the aluminium are very small, appearing as a straight line at the scale shown in Figure 4-5. Figure 4-6 plots the same information with temperature versus position instead. Each coloured line represents the temperature profile at a given time. It is very apparent that the gas temperature oscillations are much larger than those of the aluminium. The assumption of the isothermal aluminium wall holds well for the conditions in this work.

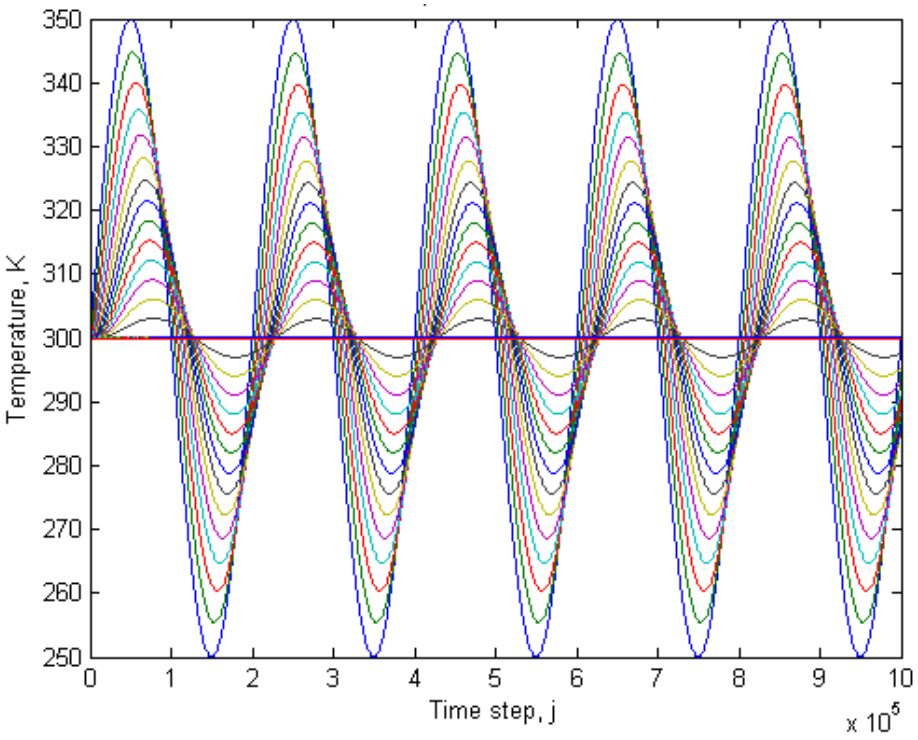

Figure 4-5: Case 1 temperature vs time with temperature input. Each curve represents a position at segment *i;* the largest amplitude is at *i*=1.

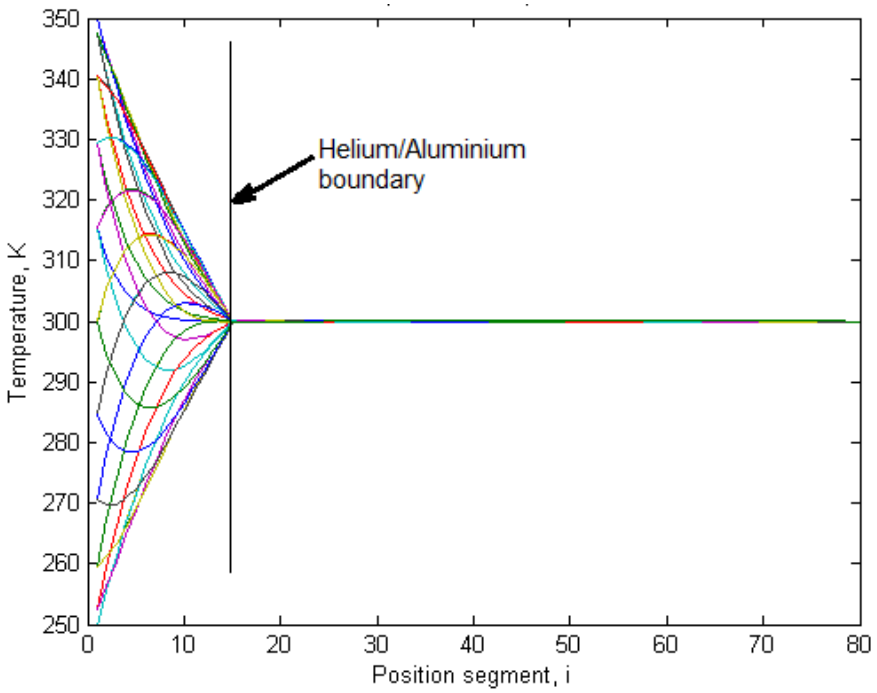

Figure 4-6: Case 1, temperature vs position trace for case 1. Each curve represents a time step *j*.

For Case 2 where an oscillating heat flux with an amplitude of 10^4 W m^{-2} was applied directly to the aluminium (with no gas present), the magnitude of the temperature oscillations in the aluminium can be calculated. Like Case 1, Figure 4-7 shows temperature vs time with each line representing the trace for a position, and Figure 4-8 shows temperature vs position with each line representing the temperature at a time. The plots show the heat being dissipated into the aluminium block, with the overall temperature rising slowly as the block is heated. Importantly, the maximum amplitude of the oscillations at the wall is in the order of 0.15 K which is much smaller than the gas temperature amplitude, therefore the isothermal wall assumption is supported.

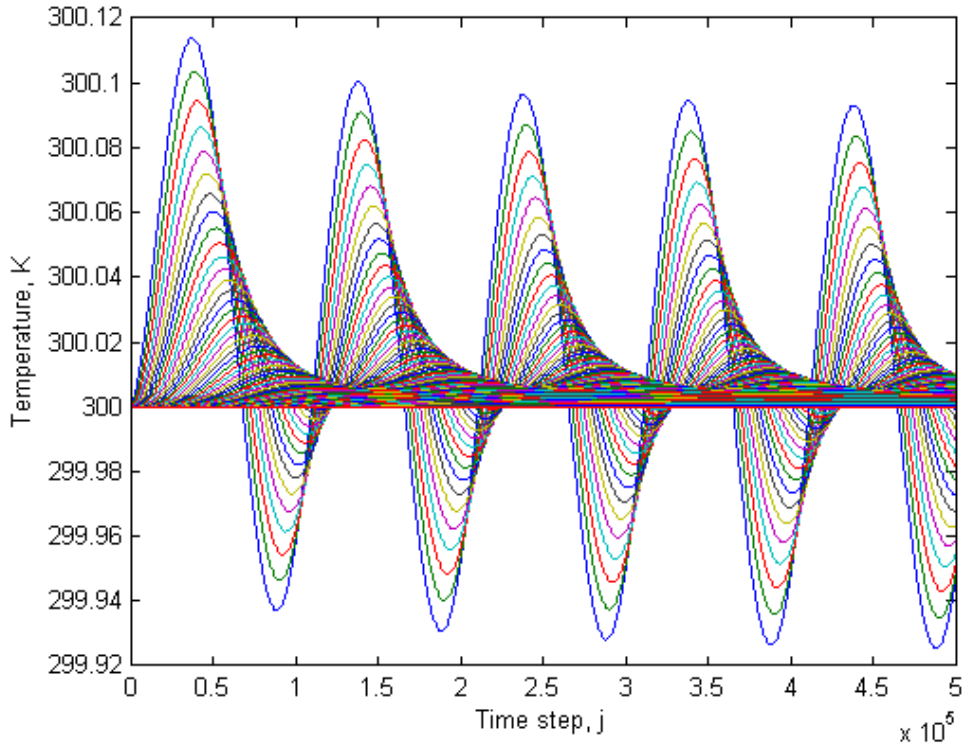

Figure 4-7: Case 2, temperature vs time within the wall for a flux input. Each curve represents a position segment, *i*.

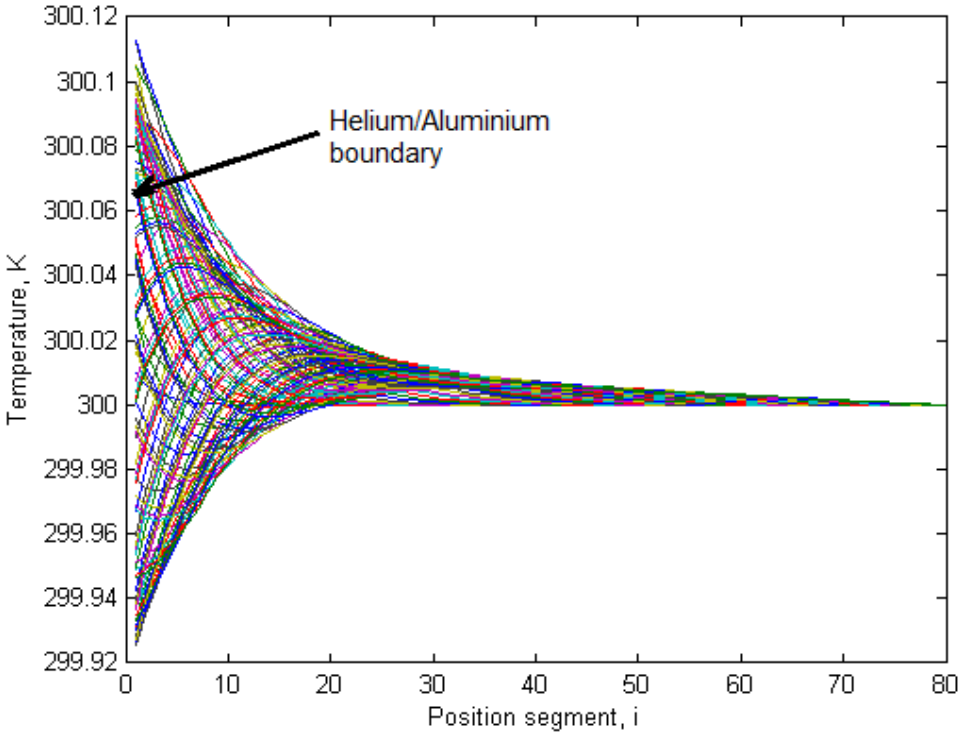

Figure 4-8: Case 2, temperature vs position within the wall for a flux input. Each curve represents a time step *j*.

Case 1 shows that the heat capacity and conduction of the aluminium totally dominates the helium gas, the temperature changes in the aluminium are insignificant and dampen the adjacent helium temperature fluctuations to an almost zero level. This confirms the isothermal wall assumption for the experiments and the CFD analysis.

Case 2 shows that the heat fluxes produce minimal temperature fluctuations in the aluminium, again confirming the isothermal wall condition. Case 2 also predicts a warming of the aluminium. This, as shown by Figure 4-8, is a transient effect from the first cycle and cyclical steady-state gradient is reached after ~15 cycles.

Another indication that the walls behave isothermally might be obtained from a comparison of thermal diffusivity. Thermal diffusivity, α, is defined as:

$$\alpha = \frac{\kappa}{\rho C_p} \qquad 4\text{-}6$$

where κ is thermal conductivity, ρ density and C_p heat capacity. One would initially think that the differences in thermal diffusivity as defined by Equation 4-6, between the two materials would be a good indicator of the validity of the isothermal wall assumption.

In this case, however, for helium at 5 bar α is 3.76 x 10^{-5} and for aluminium α is 6.9 x 10^{-5}. The ratio of these values is only 1.8, which does not indicate a dominance of one over the other.

Finally, the dimensionless Biot number could be used as an indicator of whether the walls are behaving isothermally. The Biot number is the ratio of the convective resistances to the conductive resistances at an interface and is often used for calculating transient penetration of heat into cooling fins. It is defined as

$$Bi = \frac{hL_{char}}{\kappa} \quad , \qquad 4\text{-}7$$

where the heat transfer coefficient h = ~500 W m^{-2} K^{-1} (see Section 5.4.6), characteristic length L_{char} = 0.01 m (typical thickness) and conductivity κ =167 W m^{-1} K^{-1} gives a Bi of 0.03, indicating that the conduction resistance is 1/33 of the convective resistance, and that the walls will quickly conduct any thermal transient away; therefore, to the gas, the walls appear to be isothermal to the gas.

4.3 Modelling Kornhauser & Smith's experiment

The first stage of validation was to model and predict the results of Kornhauser's experiments. It was known that the ANSYS® CFX software could model this case well as Huang [66] had carried out a similar exercise with CFX. The purpose of repeating Huang's work was to verify the construction of the model for this thesis in preparation for further study. The validation will be described here in detail as it introduces important concepts for the subsequent validations and the final model.

Kornhauser's single-space experiment [32], discussed in Section 2.2.2, used a Peclet number that was based on piston velocity. Again this becomes invalid when comparing different geometries as the piston velocity becomes insignificant for flat geometries. Later Kornhauser performed experiments with two sections of different hydraulic diameters [52] and based his Peclet number on the angular velocity of the volume oscillations; which allows for wider comparisons so will be used for the analysis in this section.

4.3.1 MODEL

Kornhauser's single-space experiment involved a simple cylinder of diameter 50.8 mm (2"), piston stroke 76.2 mm (3") and a volume ratio of two. As shown in Figure 4-9, the cylinder was modelled in CFX as a 5° segment with symmetry conditions on the flat sides. The piston was modelled by moving a wall in a sinusoidal motion equivalent to the piston motion of the experiment. The ANSYS® mesh deformation routine smoothly compressed the mesh to fit the new shape for each step. The walls were assumed to be isothermal (no temperature change in the gas molecules directly in contact with the walls) which was consistent with Kornhauser's assumption of isothermal walls. Kornhauser reasoned that if his experiment was performed over a short enough time (a few cycles) then the heat capacity of the cylinder walls would be sufficient to create a quasi-steady-state isothermal wall condition, one where the wall temperature variation between adjacent cycles was very small and that conduction inside the walls could keep the surface isothermal.

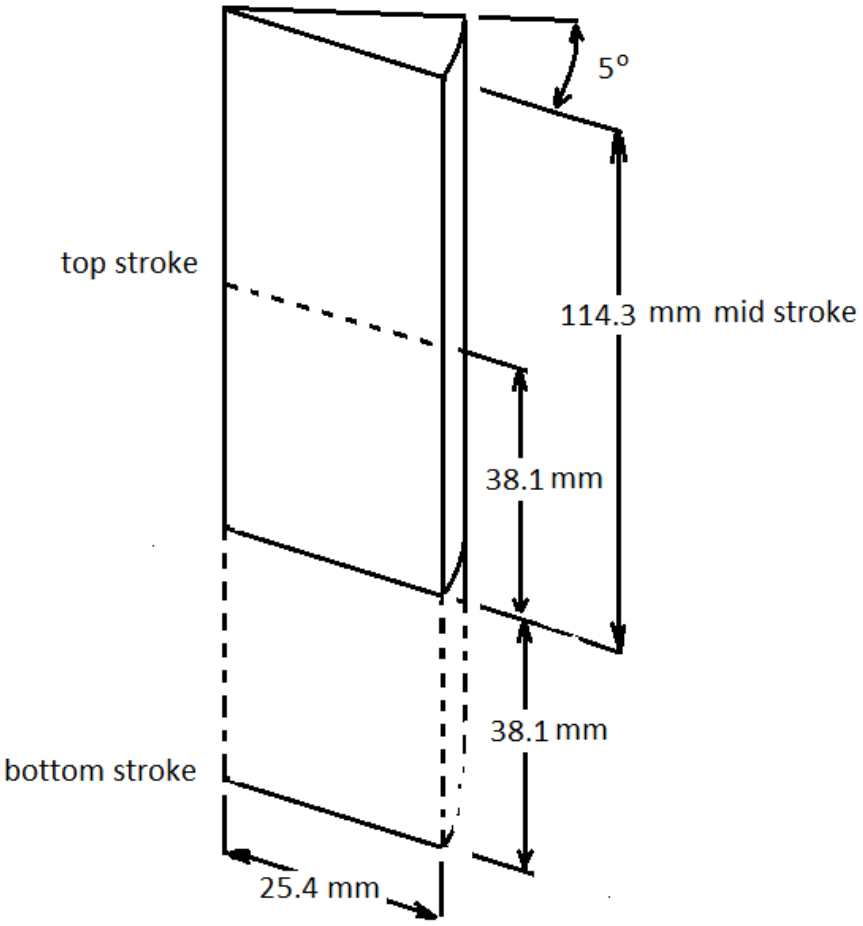

Figure 4-9: Geometry of CFD model of Kornhauser's experiment.

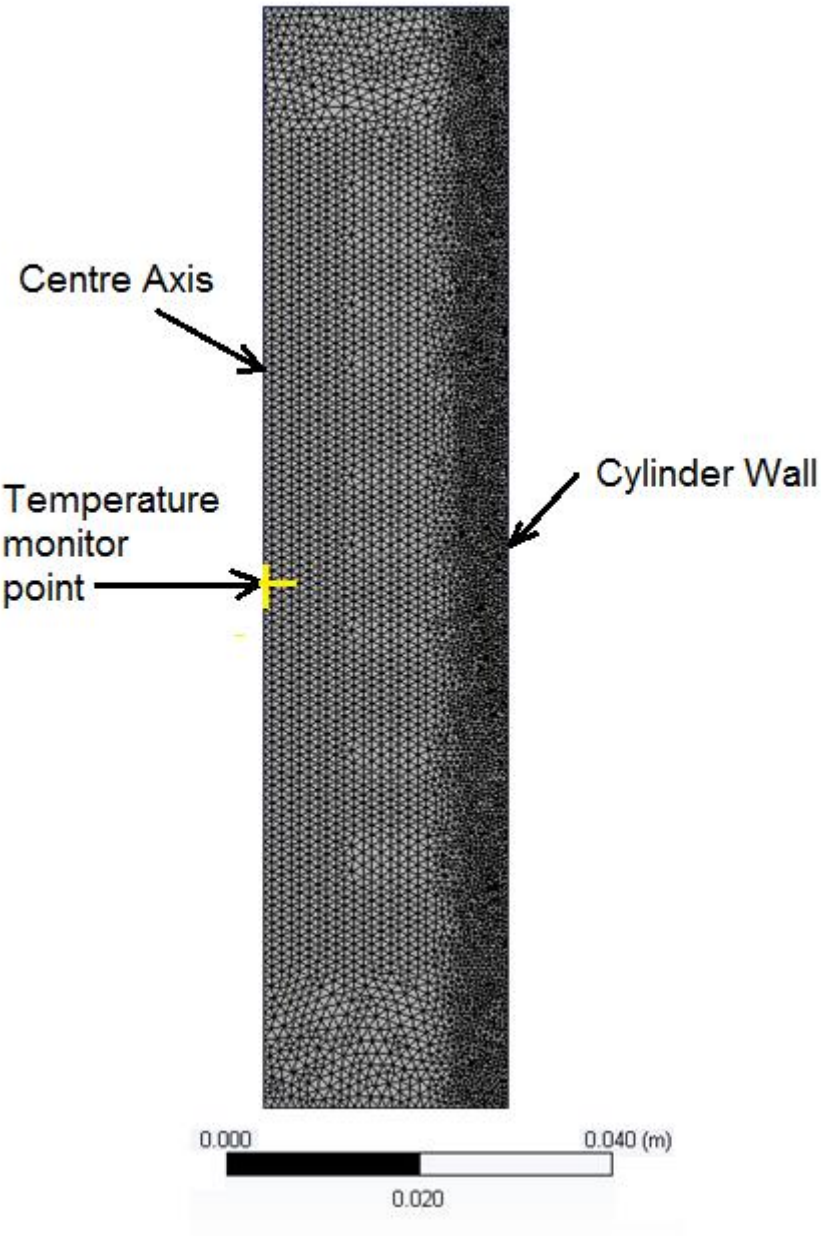

Figure 4-10: The final mesh used for validation of CFX with Kornhauser's experiment. The mesh has 355516 tetrahedral elements.

The determination of the optimal running conditions for the model was an iterative process. CFX's automatic tetrahedral meshing routine was used to generate the mesh. Firstly a coarse mesh and time step was used to get the mechanics of the model and analysis of the output running properly. Run times were only a few minutes. The results for low Peclet numbers agreed well with Kornhauser's experiment. A higher Peclet number was chosen and it was found that more time steps were necessary to get agreement between the model and experiment. Run time increased to approximately 20 minutes per analysis. A sweep of Peclet numbers identified that a finer mesh was required for high Peclet numbers. A coarse mesh with a k-epsilon turbulence model, as opposed to the original laminar model, had good agreement at

high Peclet numbers but it was found that the k-epsilon model did not work well at low Peclet numbers. The fine meshes, with 750,000 elements, took a very long time to run and consumed a lot of hard disc space (>100 Giga bytes per run). The best results were obtained with a laminar gas model, coarse mesh in the centre of the cylinder (left hand side of the segment shown) and a fine mesh next to the walls, to ensure that temperature gradients occur over several mesh elements. The final model is shown in Figure 4-10. The mesh had 355516 elements; each cycle was broken up into 150 time steps and run for four cycles (enough to get steady state) which took approximately 8 hours.

4.3.2 *Results from the model replicating Kornhauser and Smith's experiments*

The absolute gas pressure and the position of the piston face were monitored during each run. The monitored variables can be considered the computational equivalent of transducers in an experimental rig. Figure 4-11 shows a typical output graph of the monitored variables in a run. The first cycle's pressure amplitude was lower than the others, showing that steady-state was being established in the first few cycles. In this numerical experiment, quasi-steady-state conditions are considered to be reached when flow, temperature and pressure fluctuations are the same from one cycle to the next. Quasi is used to describe the steady-state reached as the cycle-average temperature and pressure gradually increase from cycle to cycle due to the small amount of energy fed into the system via entropy generation. The increases are small as the energy input per cycle is small compared to the gas' heat capacity.

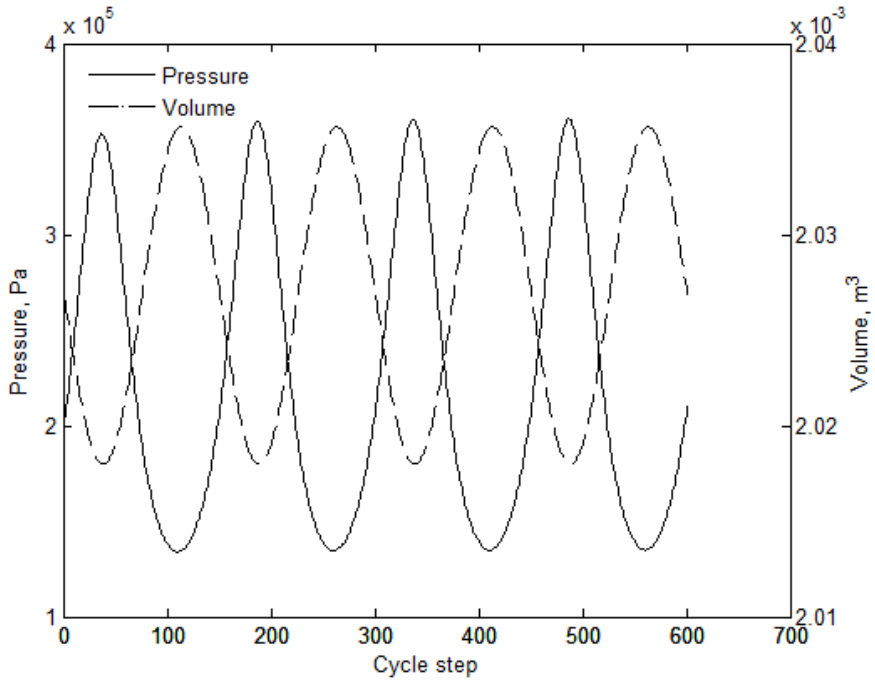

Figure 4-11: Typical output of solution run plotting pressure and volume, at a Peclet number of 82.

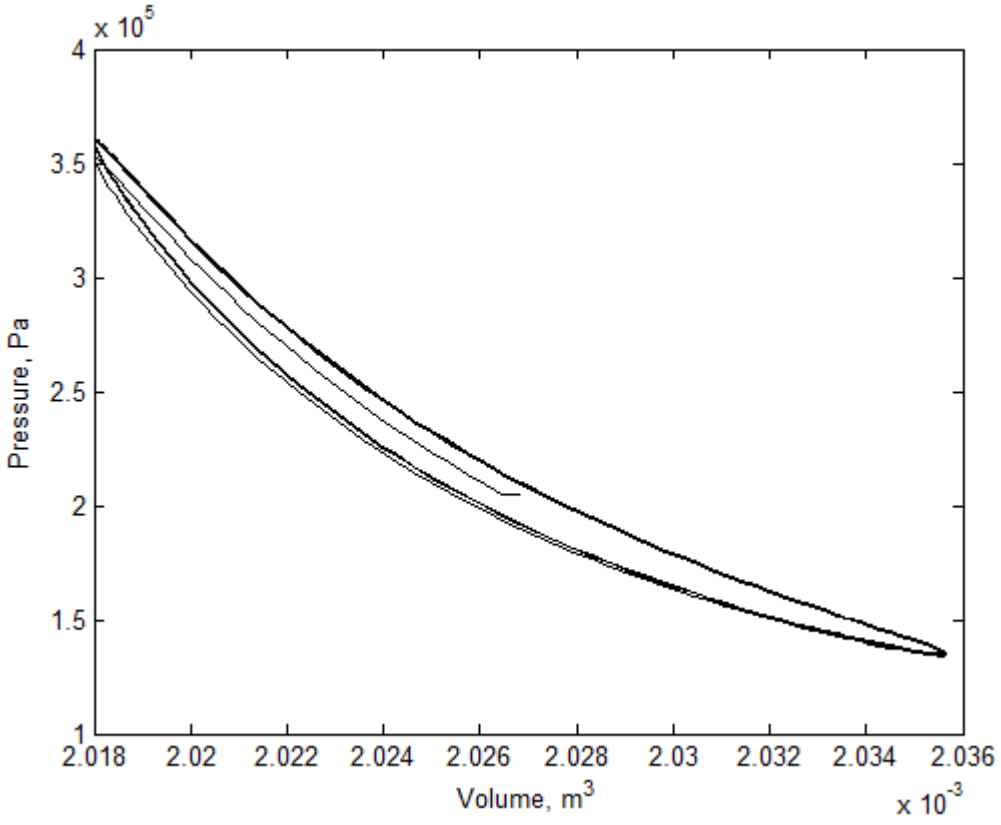

Figure 4-12: A typical pressure-volume hysteresis loop calculated by the CFD model. The Peclet number of 82 indicates near-isothermal conditions. The area inside the loop represents the work done by the hysteresis loss in the cycle.

Plotting pressure against volume, Figure 4-12, shows the hysteresis created by the entropy generated from a finite temperature difference between the gas and walls, required for heat transfer. The area inside the *p*-*V* loop represents the work done in a cycle and equals the hysteresis loss in the cycle. This energy is added to the gas internal energy and increases the gas temperature, until a sufficient temperature difference is set up between the average gas and wall temperatures to transfer all the work energy to the walls.

The start of the run can be seen at the centre of the loop and shows that it takes three quarters of a cycle to establish quasi steady-state. The subsequent four cycles lie on top of each other, indicating that quasi steady-state has been reached and that the change between cycles is very small compared with the fluctuations within the cycle.

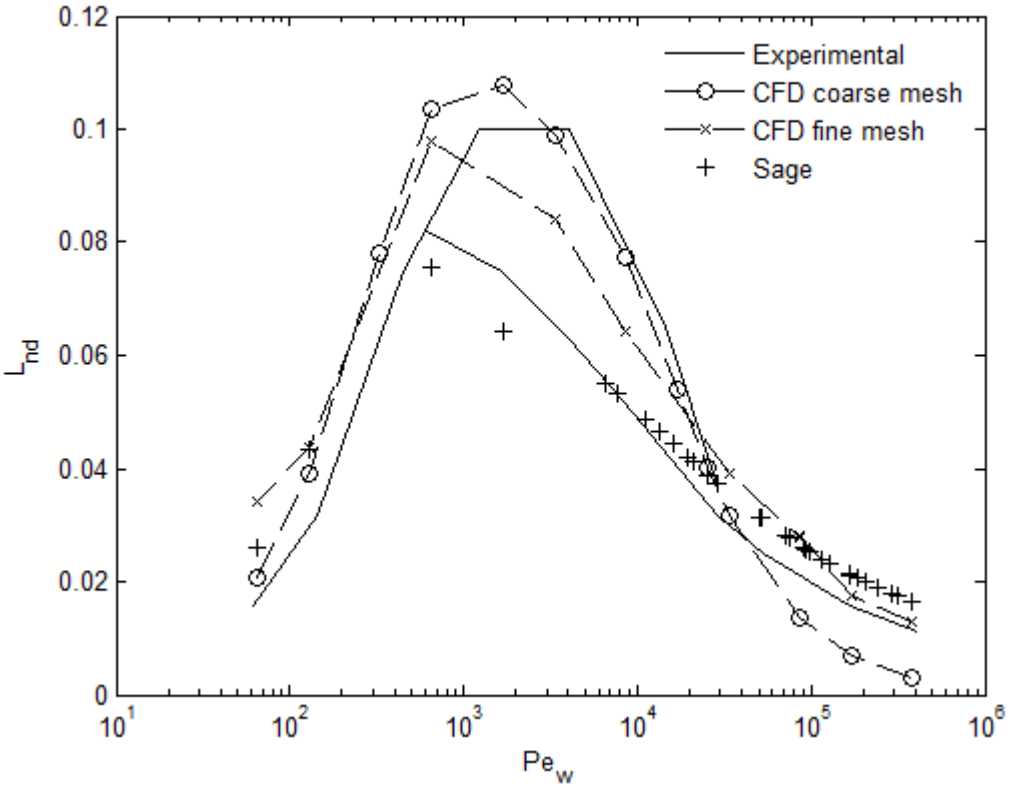

Figure 4-13: CFD and Sage hysteresis loss predictions compared to the experimental results of Kornhauser and Smith. The hysteresis loss is normalised by dividing the loss per cycle by the theoretical adiabatic work done by the volume change in the cycle.

Figure 4-13 plots the non-dimensional work done in a cycle for a range of Peclet numbers. The non-dimensional work, defined in Section 2.2.2, is the ratio of the hysteresis work done in the cycle to the adiabatic compression work done for the volume change. Kornhauser's experimental results (the solid line in the figure) had two branches in the high-L_{nd} region, indicating that there may be some other factor in the experiments that affects the magnitude of the loss and is not included in the Peclet number. The CFX model varied the Peclet number by changing the cycle frequency and gas pressure to match Kornhauser's experiments. The coarse mesh CFX model predicted the low Peclet number conditions best and the fine mesh predicted the high Peclet number conditions best. Sage's prediction of the gas spring hysteresis losses for the same range of conditions are also plotted for comparison and, as expected, provide good agreement with the experiment.

CFX's prediction of gas spring hysteresis agreed with Kornauser's experimental results over a wide range of Peclet numbers, from near isothermal to near adiabatic conditions. The maximum error for the fine mesh prediction was within 0.01 of the experimental L_{nd}, which is 1% of the adiabatic work done in a cycle. The high entropy condition is predicted well, both in magnitude and position in the Peclet number range.

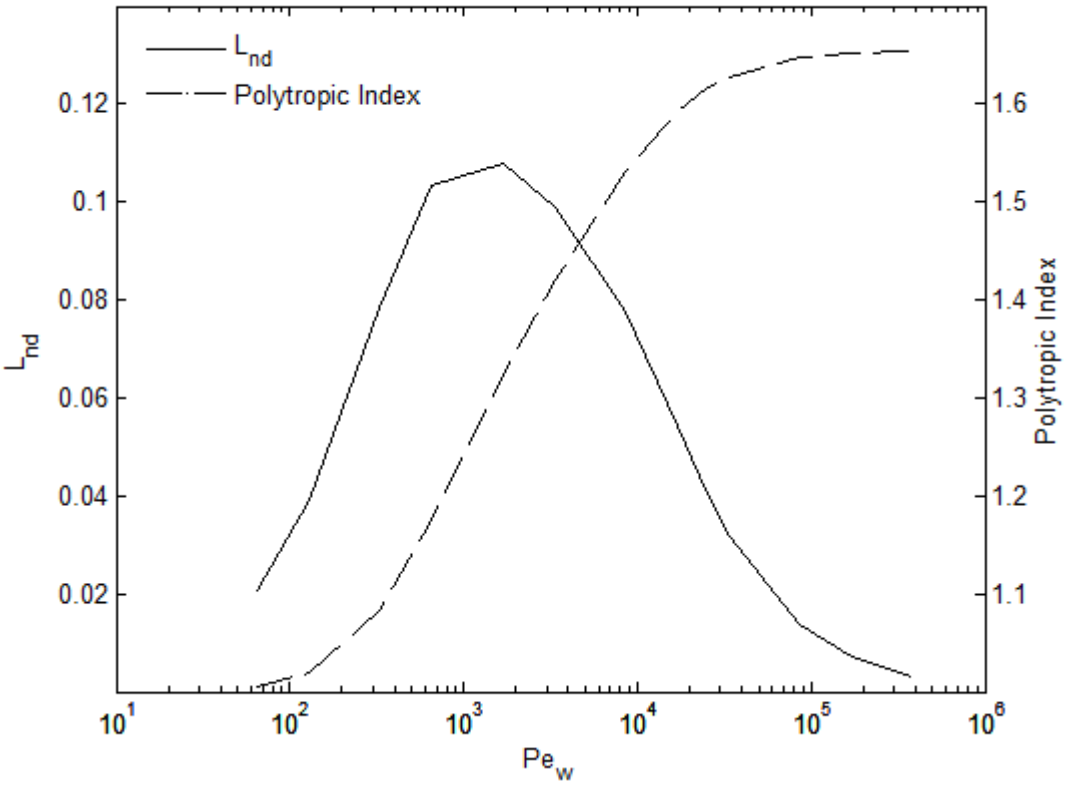

Figure 4-14: Polytropic index comparison with hysteresis loss as calculated by the fine mesh CFD model.

Figure 4-14 compares the polytropic index with the hysteresis loss. It shows that the conditions for rapid changes ($10^2 < Pe_w < 10^5$) in polytropic index occur when the hysteresis losses are high. This confirms the hypothesis that the polytropic index is also an indicator of the gas spring hysteresis loss. Differentiating the polytropic index with respect to Peclet number, as shown in Figure 4-15, replicates the shape of the hysteresis loss graph. The similarities of the hysteresis loss and differentiated polytropic index curves further confirm the importance of the polytropic index for validation exercises.

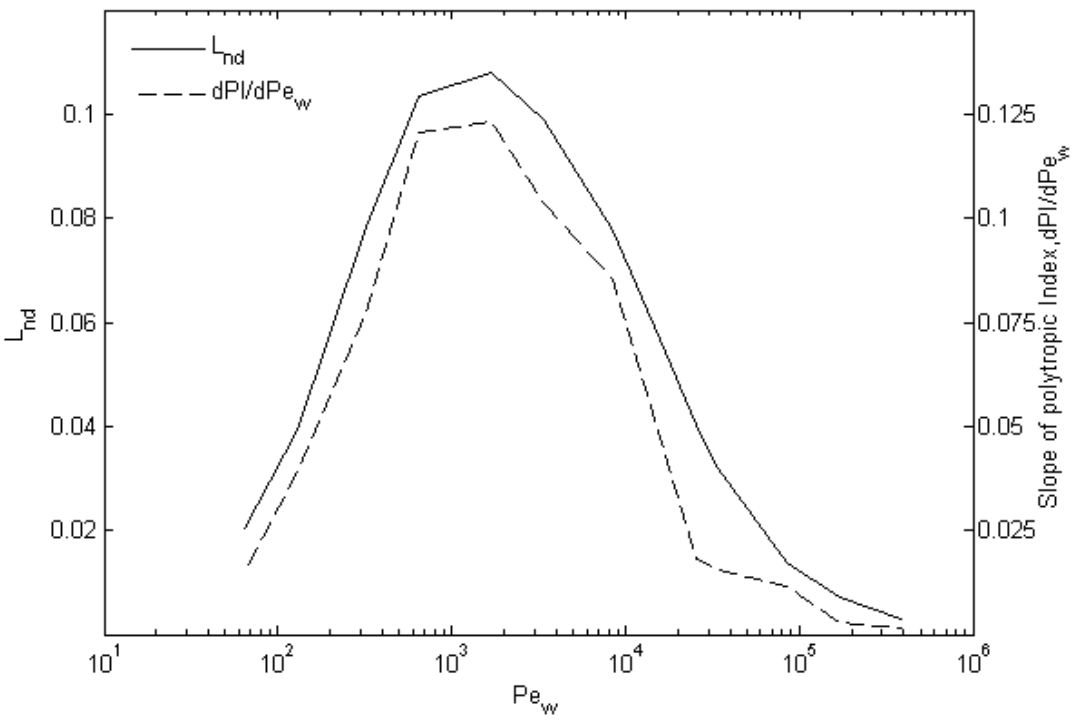

Figure 4-15: Comparison of the slope of the polytropic index graph with the hysteresis loss.

CFX can provide visual displays of flow and temperature profiles. Figure 4-16 shows temperature profiles for the gas near the top of the stroke and Figure 4-17 near the bottom of the stroke. The top plots are for a Peclet number of 3390 which is the middle of the high loss conditions and the bottom plots are for a high Peclet number of 384,000. When the Peclet number is in the high loss condition, the temperature profiles show that a large amount of the gas core is at a high temperature (top of stroke) or low temperature (bottom of stroke) depending on compression or expansion respectively. Of interest is a well-defined temperature gradient across the gas, showing that heat transfer is occurring through the gas and affecting most of the bulk of the gas. For high Peclet number conditions, the thermal gradients are over a small distance very close to the walls with the bulk of the gas at a uniform temperature, indicating that compression is well into the adiabatic regime. The thin thermal boundary layer implies a higher heat flux to and from the walls, but since the bulk of the gas is unaffected by the heat flux, the net result is a more efficient gas spring.

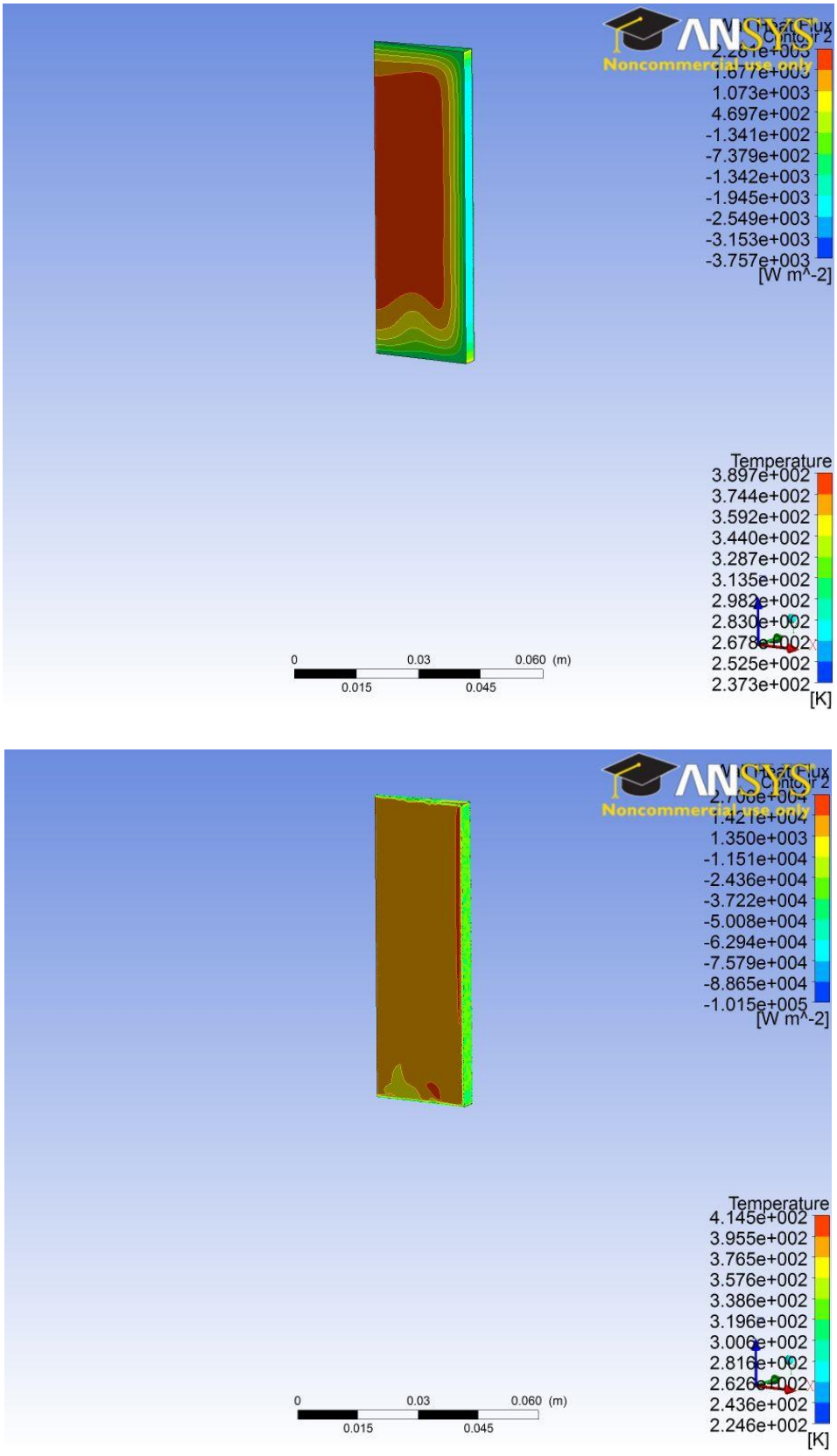

Figure 4-16: Temperature (on the wedge face) and heat flux (on the cylindrical surface) profiles in the cylinder near the top of the stroke while compressing. Peclet numbers of 3390 (upper) and 384,400 (lower). Note that the temperature and heat flux scales are different.

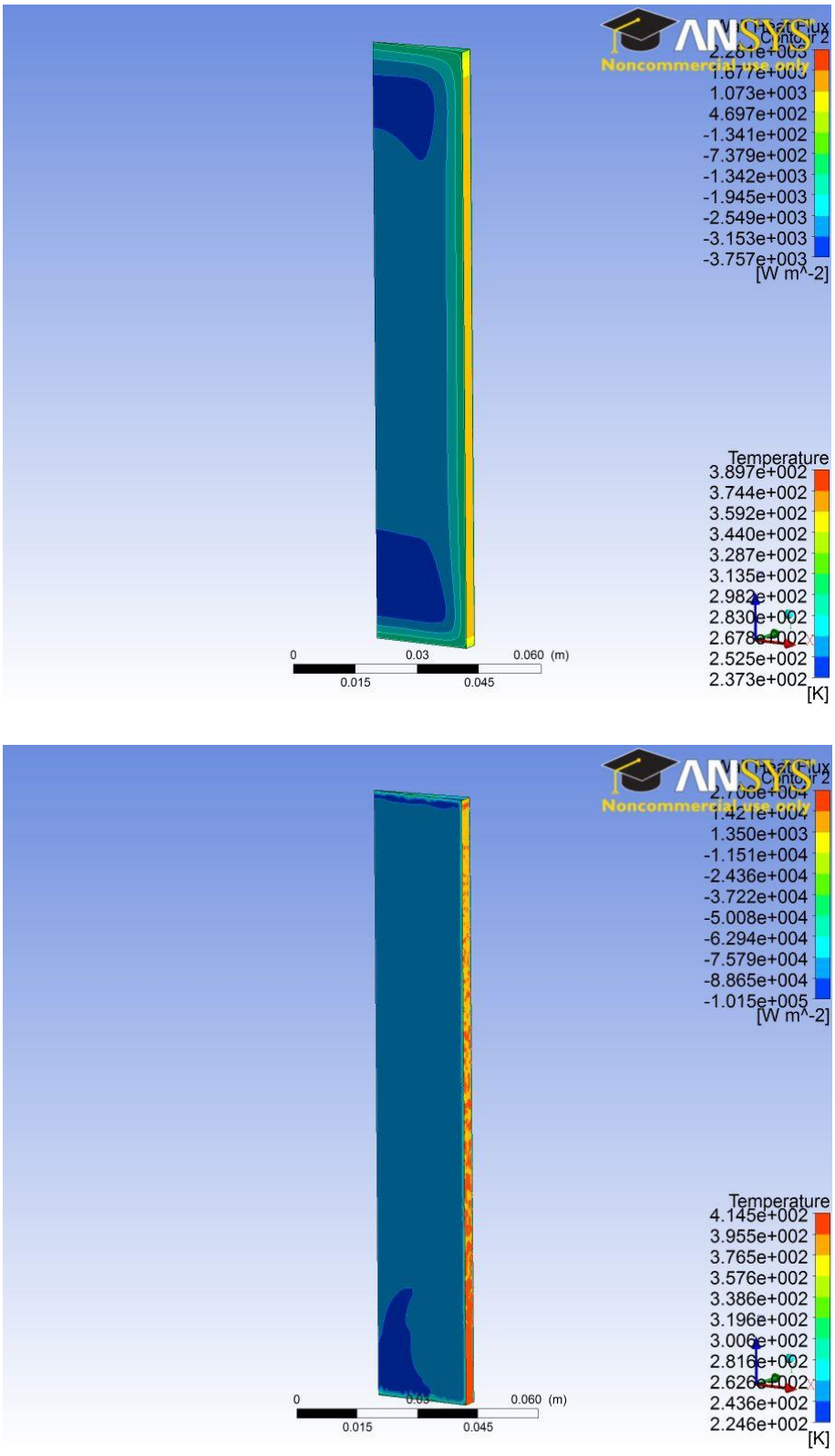

Figure 4-17: Temperature and heat flux profiles in the cylinder near the bottom of the stroke while expanding. Peclet numbers of 3390 (upper) and 384,400 (lower)

Instantaneous heat flux is very difficult, if not impossible, to measure experimentally so highlights the value of a CFD analysis. Table 4-3 compares the maximum wall heat fluxes as predicted by the CFD analysis.

The peak instantaneous heat flux on the wall was an order of magnitude higher for the high Peclet number run as compared with the lower Peclet number run (~10^4 W m^{-2} for high Peclet number and 3.5 x 10^3 W m^{-2} for the low Peclet number). However, the higher cycle speed of the high Peclet number run reduced the time available for heat transfer per cycle. The net result was that a similar amount of heat was dissipated per cycle for both the high and low Peclet number cases, 2.89 J $cycle^{-1}$ and 2.99 J $cycle^{-1}$ respectively. However, the adiabatic work done in the high Peclet number case was 257 J $cycle^{-1}$ as compared to 34 J $cycle^{-1}$ for the low Peclet number case. The net result was that the non-dimensional loss for the high Peclet number case was much lower, indicating a more efficient spring.

Table 4-3: Comparison of heat fluxes and gas hysteresis for high, mid and low Pe runs.

Peclet number	**Frequency Hz**	**Position**	**Temperature in centre, K**	**Maximum Heat flux W m^{-2} (positive is energy into gas)**	**Hysteresis work per J $cycle^{-1}$**	**Adiabatic work J $cycle^{-1}$**
384,400	15	Near top of stroke	395	-2.4 x 10^4	2.99	257
		Near bottom of stroke	240	1.4 x 10^4		
3390	1	Near top of stroke	390	-2.3 x 10^3	2.89	34
		Near bottom of stroke	250	2.0 x 10^3		

4.3.3 DISCUSSION OF RESULTS FROM THIS MODEL

The CFX model was able to predict Kornhauser and Smith's experimental results for gas spring hysteresis loss. The predictions were accurate to within 0.01 of the experimental L_{nd} , or 1% of the adiabatic work done in the cycle, over a wide range of conditions from near isothermal to near adiabatic compression. This shows that CFX can model compression of gas in a confined space, including adiabatic compression heating and heat transfer to the walls. Confidence has been gained in the construction of the CFD model from this exercise and the next step can be taken.

Sage provided a good prediction of gas spring hysteresis over a large range of conditions. Sage's accuracy was expected as the geometry and conditions of the experiments were consistent with the piston-in-cylinder situations that Sage was developed to analyse. The results give confidence for using Sage as a modelling tool for Stirling systems.

The Peclet number has been shown to be useful for characterising the conditions in a gas spring. The Peclet number is the ratio between the parameters that keep energy in the gas and those that dissipate energy to the walls. Increased hydraulic diameter and cycle speed keep the energy in the gas and move the behaviour towards adiabatic, whereas increased thermal diffusivity enables dissipation of energy and move behaviour towards isothermal. Thermal diffusivity is a function of conductivity and heat capacity which in turn are functions of density and therefore pressure and temperature. Experiments at different speeds, diameters and pressures can have equal Peclet numbers and should produce the same gas spring hysteresis behaviour.

The Sage results support the Peclet number as a characteristic number for gas spring compression. The plot of the Sage results in Figure 4-13 is the result of a square mapping of speed and pressure, where different combinations of pressure and speed can produce the same Peclet number (refer to Equation 2-7). All the hysteresis loss points fitted onto a single, smooth, curve. Kornhauser and Smith's experiments used a range of pressures and speeds to achieve a large range of Peclet number values with the limited range of operating conditions imposed by their rig. It should be noted that Kornhauser's results had two lines in the high loss section that corresponded to different pressures, whilst the CFX and Sage results produced single lines traversing the same range of conditions. This could be a function of their rig and experimental technique, or an effect not modelled by CFX and Sage.

Figure 4-16 , the high-L_{nd} case, shows the temperature gradient in the gas stretching from the centre of the cylinder to the wall. For the near-adiabatic case, Figure 4-17, the temperature gradient is very close to the walls. A gradient that traverses the bulk gas corresponds to a significant heat flux driven by a real temperature difference affecting the bulk of gas with irreversible heat transfer. In the near-adiabatic condition there is not enough time to form the temperature gradients in the bulk gas so relatively little heat is transferred per cycle and the energy added from compression is retained in the gas for expansion (when work is done by the gas). The bulk of the gas therefore experiences a near-reversible process. For near-isothermal compression and expansion, there is sufficient time to transfer the heat through the gas to the walls with a small gradient, with an associated small hysteresis loss and therefore efficient compression and expansion.

It was observed that the net hysteresis loss per cycle was the same for high and mid-range Peclet numbers. However, at high Peclet number conditions the adiabatic work of the cycle is also high; hence the non-dimensional loss is low. This corresponds to near adiabatic compression where most of the energy of compression stays in the gas and is returned to the compression piston on the expansion stroke.

Table 4-3 shows that the hysteresis loss per cycle is similar for low and high Pe_w cases. The average power absorbed however is higher for the high Pe_w case as the higher frequency means more cycles per second.

The polytropic index provides a good indication of whereabouts in the isothermal-to-adiabatic range a gas spring is operating. Differentiating the polytropic index with respect to Pe_w produces a very similar curve to the hysteresis loss curve (Figure 4-15). This is a very useful result for validating a model with respect to an experiment, as only one high speed transducer is needed to determine the Peclet number for maximum L_{nd}, which reduces error by eliminating the need for high precision timing required to measure the small phase angle between pressure and volume when measuring the work input in a cycle. The polytropic index can be used for experiments at different average pressures as it compares pressure and volume ratios, not just the average values or absolute oscillation amplitudes.

The Peclet number of the diaphragm Stirling cryocooler under typical operating conditions of 25 bar gas pressure and 50 Hz speed with a 2 mm typical gap between the walls of the diaphragm spaces is approximately 170,000, which is well into the near-adiabatic region. The CFX model with the fine mesh is the most appropriate. Moreover, variations in the geometry, such as reducing the gap between upper and lower walls to 1 mm by moving the diaphragm, will not move the compression away from near-adiabatic.

The regenerator matrix on the cryocooler has a hydraulic diameter two orders of magnitude smaller (0.03 mm between wires in a 400 mesh regenerator), giving a Peclet number of 1700, which indicates conditions of high heat transfer and also entropy generation. Regenerator design is a compromise between achieving high heat transfer rates, minimising dead volume and minimising losses (due to viscous flow and entropy).

4.4 Flat cylinder model

The second step in validation was to modify the model of Kornhauser's experiment to a flat geometry, typical of a diaphragm compression or expansion space.

4.4.1 MODEL OF THE FLAT CYLINDER

The second iteration prototype's average gas space height of 2 mm was chosen for the compression space. A disc of 288 mm diameter was chosen because it allows the overall volume in the T-cylinder model (the next step in the validation) to equal that of Kornhauser's cylinder. Additionally, it is similar to the diameter of the second iteration prototype's displacer diaphragms (255 mm). In the flat cylinder model, the base of the flat disc was moved in a sinusoidal manner to give a volume ratio of two, the same as Kornhauser's experiment. To calculate the Peclet number for analysis, the generalised formula for hydraulic diameter, D_h, as defined by

$$D_h = \frac{4\ x\ Cross{-}sectional\ area}{Perimeter} \tag{4-8}$$

is used. For the flat cylinder the top and bottom surfaces of the cylinder approximate two infinitely large plates. For a rectangular cross section width *l*, height *d*,

$$D_h = \frac{4\ ld}{2l + 2d}$$

When $l >> d$ (approaching infinity), the $2d$ term becomes insignificant, $4l/2l=2$ and then D_h then equates to

$$D_h = 2d \tag{4-9}$$

where *d* is the distance between the plates. The model thus had an average hydraulic diameter of 4 mm, which is an order of magnitude smaller than Kornhauser's 50.8 mm.

As with Kornhauser's experiment, the flat cylinder was modelled as a segment with symmetry conditions on the wedge sides. Initially a tetrahedral mesh similar to the piston model was used for calculation (Figure 4-18). Later this was converted to an extruded 2D mesh (Figure 4-19) which proved to be more computationally efficient and produced the same results. It was found that the number of elements in the axial direction was the most critical for accuracy. It was important to have several elements across the thermal boundary layer gradient to model heat flow well. The results were not sensitive to the mesh density in the circumferential direction.

It was hypothesised that if the Peclet number is a true indication of polytropic compression, then the hysteresis curve for the flat cylinder should have its maximum at the same Peclet number as Kornhauser's cylinder.

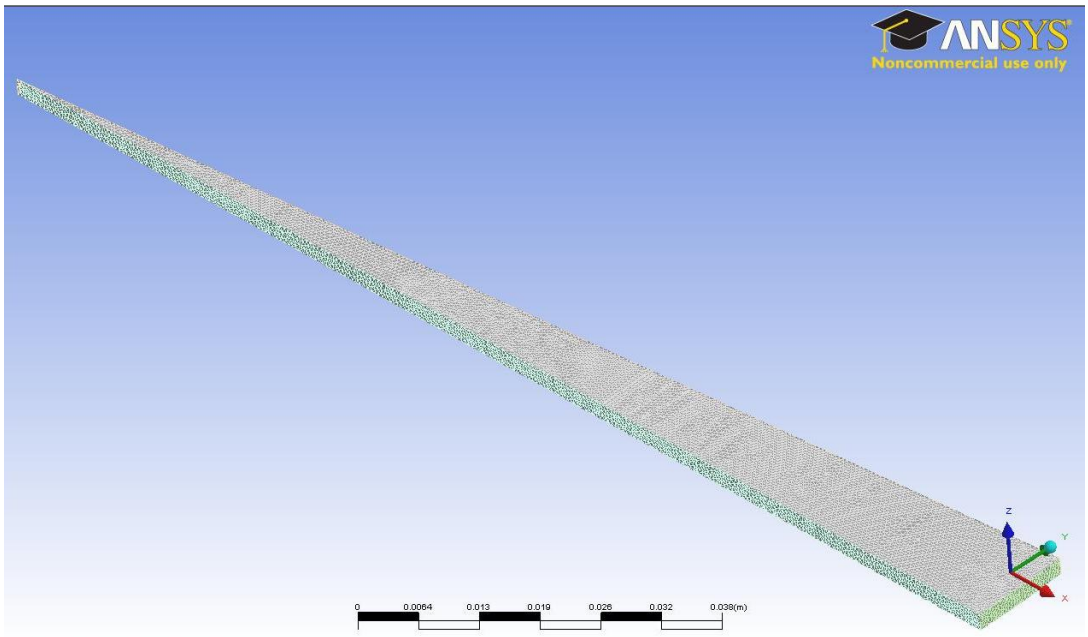

Figure 4-18: Tetrahedral mesh of flat model

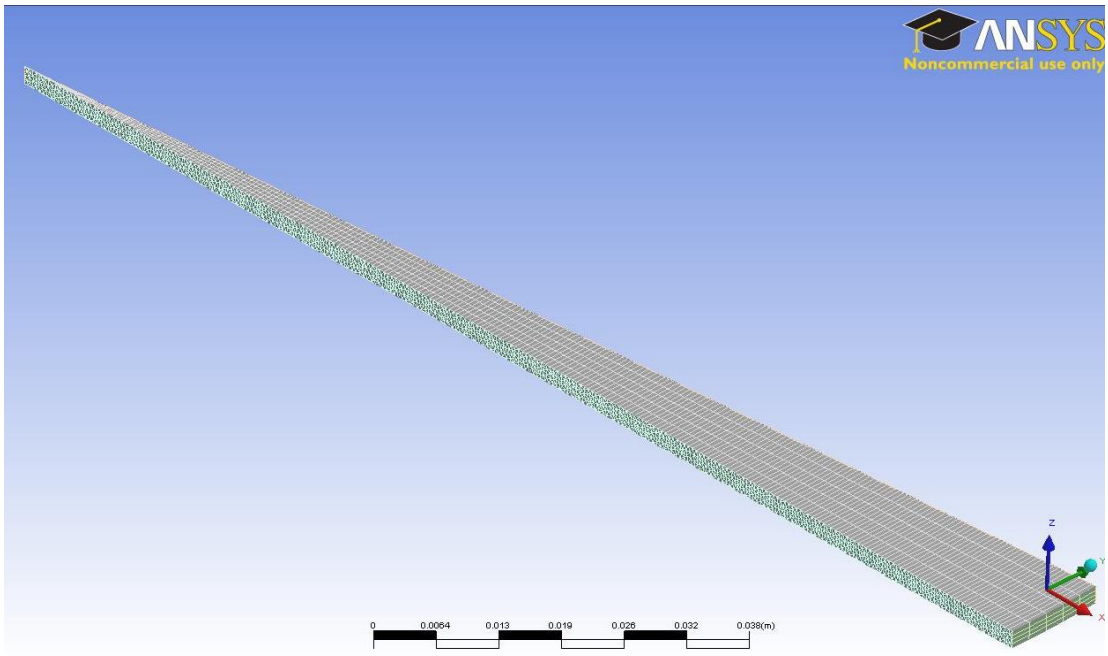

Figure 4-19: Extruded 2D mesh of flat model

4.4.2 *RESULTS FROM THE FLAT CYLINDER MODEL*

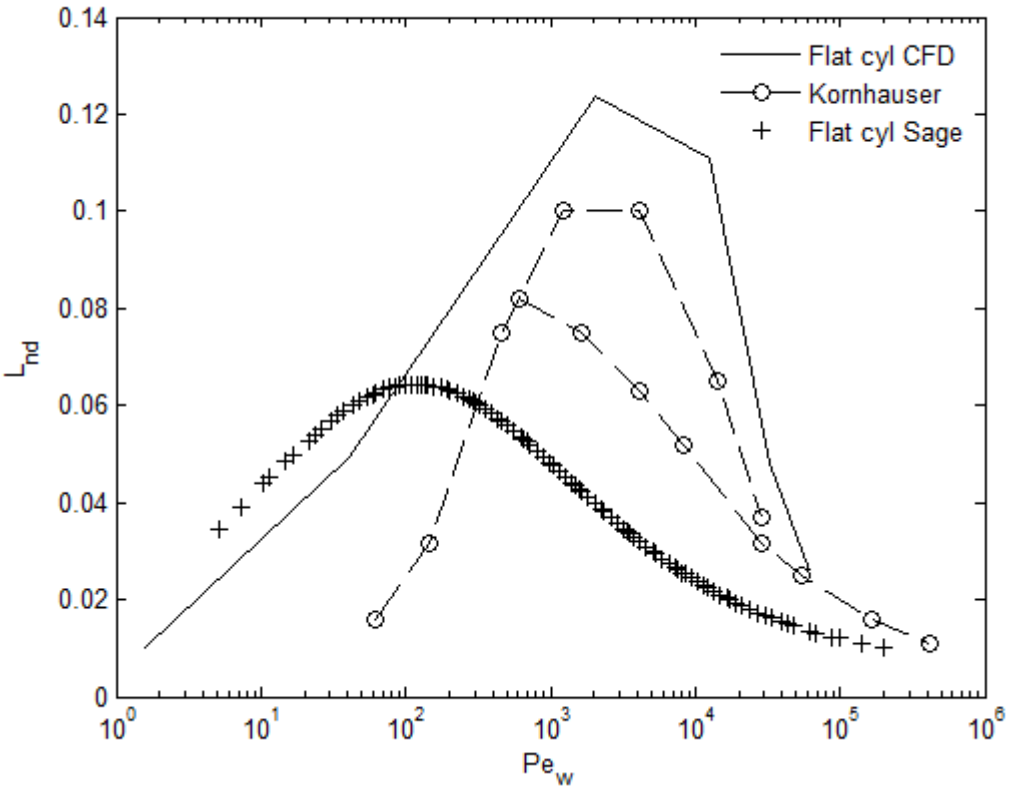

Figure 4-20: Non-dimensional loss versus the Peclet number for the CFX prediction of the flat cylinder model compared with Sage's prediction and Kornhauser's experimental results for a cylinder.

Figure 4-20 compares the CFX prediction of the flat cylinder with a Sage model of the same conditions and with Kornhauser's cylinder experiment. The CFX prediction of the peak hysteresis loss occurred at the same Peclet number for both the flat cylinder model and Kornhauser's cylinder experiments, indicating that CFX was modelling the polytropic compression well. The flat cylinder's hysteresis losses are larger than the losses in Kornhauser's cylinder.

Sage's prediction had the peak hysteresis loss at a lower Pe_w than the CFX model and Kornhauser's cylinder. The shift towards lower Pe_w values indicates that Sage predicts less heat transfer as adiabatic conditions are achieved at lower Peclet numbers. Additionally, the peak hysteresis loss was of lesser magnitude than the CFX result. The lower peak indicates reduced entropy generation, which is a function of the amount of heat exchanged with the walls, hence indicating again that Sage underestimated heat transfer for the flat model.

4.4.3 DISCUSSION OF THE FLAT CYLINDER RESULTS

CFX modelled the flat cylinder and produced results that were intuitively consistent. The magnitude of the hysteresis loss calculated for the flat cylinder was larger than Kornhauser's piston-in-cylinder. A possibly cause for the difference in the magnitude of the non-dimensional loss (L_{nd}, Equation 2-3) is that the flat cylinder has a larger area available for heat transfer (than its equivalent volume cylinder), which would increase the heat transferred for a given Peclet number and volume ratio. The hysteresis loss is generated through irreversible heat transfer over a finite temperature gradient in the gas; therefore an increase in heat transferred, under the same gas conditions, will result in an increase in the hysteresis loss. The adiabatic work done per cycle (Equation 2-3) is a function of pressure and volume so will remain the same for the flat cylinder model or Kornhauser's cylinder with the same Peclet numbers. The non-dimensional loss is the ratio of the hysteresis loss and the adiabatic work in the cycle, hence it's magnitude will be different for different volume-area ratios. The important observation is that the peak hysteresis loss is at the same Peclet number for the different geometries.

The Peclet number effectively non-dimensionalised the oscillating compression conditions, showing that a change in geometry and hydraulic diameter produces a maximum hysteresis point at the same Peclet number for the flat cylinder and Kornhauser's experiment.

The Sage model of the flat cylinder appeared to under-predict the heat transfer with the walls which was evidenced by the lower hysteresis peak at lower Peclet numbers. These results erode confidence in Sage's predictions for heat transfer in diaphragm systems and further justify the present CFD analysis.

The flat model with no radial flow can be used for comparison with the next step in validation, the T-cylinder model, which has a similar geometry but with a radial flow.

4.5 T-cylinder model

The third stage in developing a validated model for the Stirling cryocooler was to add a radial flow component to the flat cylinder model, as shown in Figure 4-21 below. Known as the 'T-cylinder model' this stage tested the capability of CFX to model geometry typical of the diaphragm Stirling cryocooler, and will allow study of a radial flow section and its interaction with the cylinder. Methods of analysing heat flux were developed on this simpler model before being implemented on more complicated geometries.

4.5.1 MODEL

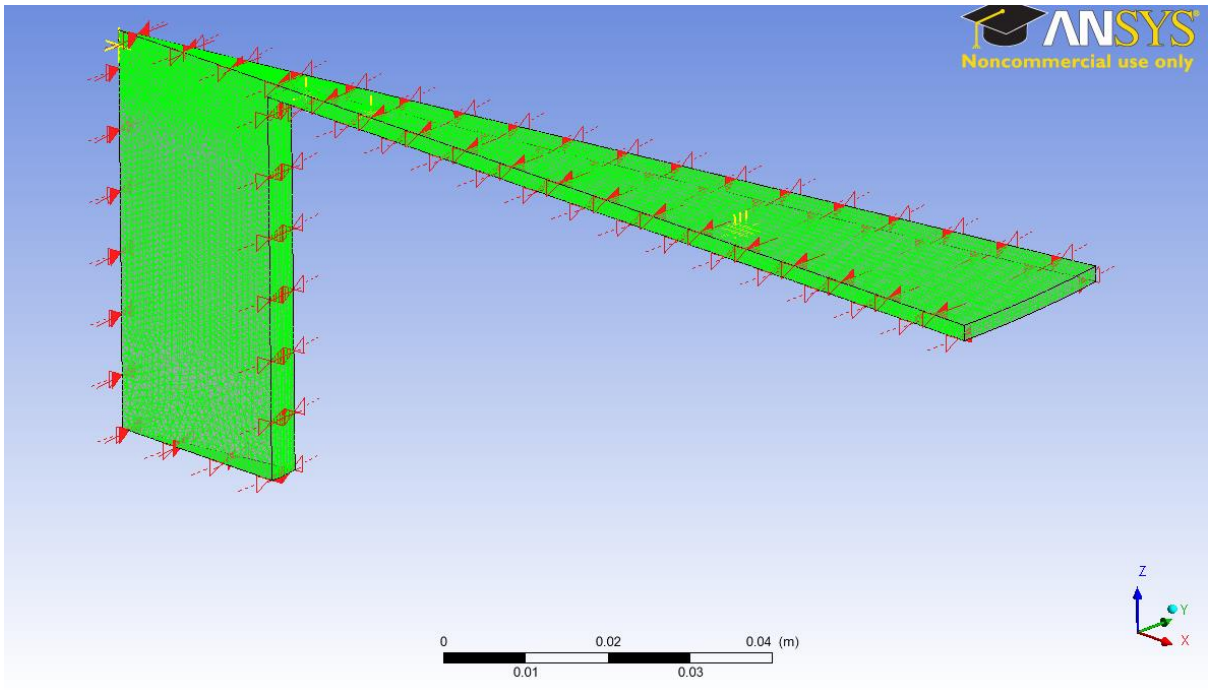

Figure 4-21: CFD model and mesh of a segment of the T-cylinder.

The T-cylinder model used the same volume and pressure ratio as Kornhauser and Smith's piston and cylinder, with bore 50.8 mm and stroke 76.2 mm. The average cylinder height was reduced from 114 mm to 50 mm and the remaining volume converted into a flat radial space 2 mm thick with an outer diameter of 288 mm, to maintain the same overall volume and therefore volume ratio as Kornhauser and Smith's experiment. Additionally, the only difference between the T-cylinder model and the flat cylinder model is the presence of the compression cylinder. A 10° segment was used for analysis to reduce computation time. Symmetry conditions

were used for the sides of the segment. Like previous models, the walls were isothermal with heat transfer.

A valid question for this situation is the appropriate characteristic dimension for use in the Peclet number definition for the various models. The model has two distinct geometries with distinct characteristic dimensions. The cylinder has a diameter and significant piston stroke (piston motion inducing velocity to aid heat transfer to walls) and the radial section acts like flow between parallel plates. The resultant behaviour will be a combination of the two section behaviours. If one section dominates the heat transfer for the model then its hydraulic diameter will be the most appropriate for calculation of the Peclet number for the whole. It is therefore hypothesised that the hydraulic diameter of the section that makes the position of the maximum hysteresis loss match Kornhauser's maximum, will indicate the over-riding characteristic dimension for the model.

4.5.2 RESULTS FROM THE T-CYLINDER MODEL

Figure 4-22 summarises the results of this CFD model. With the Peclet number based on the 50.8 mm diameter cylinder, the peak loss occurs around a Peclet number of 85,000. Basing the Peclet number on the radial section, the peak loss occurs at a value of approximately 7,000. The radial section based Peclet number positions the plot close to Kornhauser's data, indicating that the radial section's heat transfer is dominating. A slight shift of the peak to the right could be due to the cylindrical section's influence.

The CFD analysis was repeated with the wall conditions set to adiabatic, that is no heat transfer allowed. The 'T cyl adiabatic' curve on Figure 4-22 is flat with L_{nd} near 0.01 over the whole range, confirming the assumption that the power required to overcome flow losses was small compared to the heat transfer effects. Moreover it confirms that the heat transfer with the walls is the main source of the high hysteresis loss.

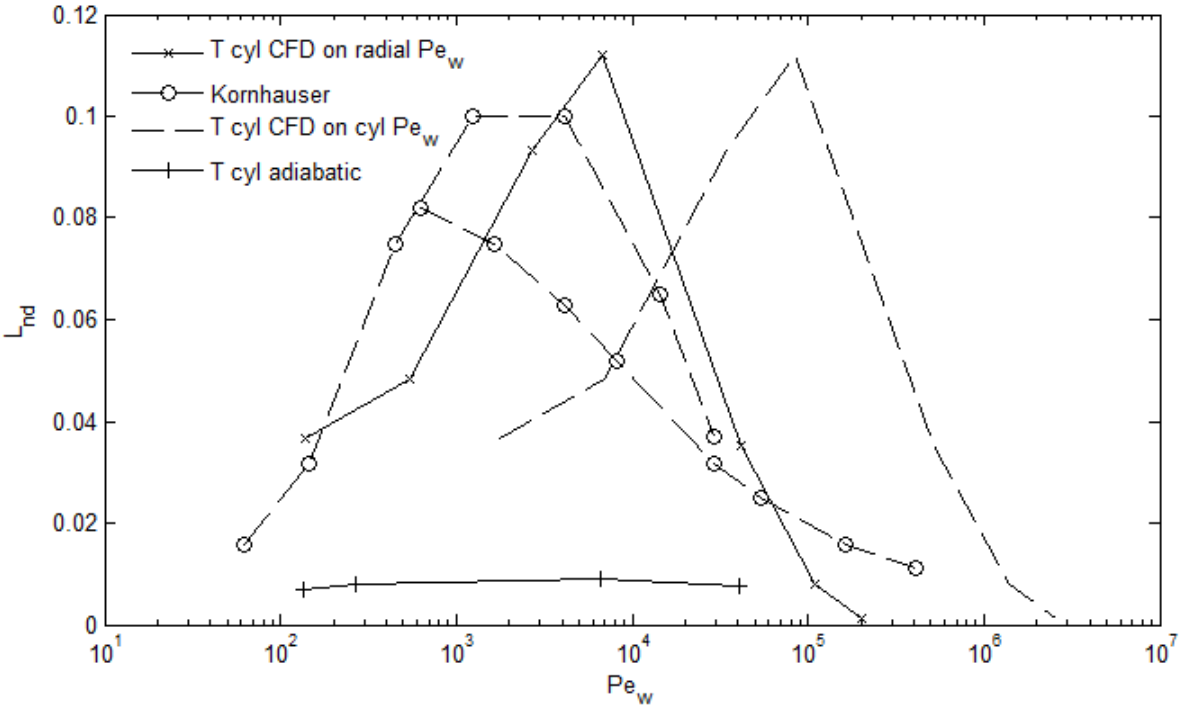

Figure 4-22: Non-dimensional hysteresis loss, $L_{nd,}$ as a function of Pe_w for the T-cylinder model.

Figure 4-23 shows streamlines calculated by CFX for the T-cylinder. A significant eddy vortex was created by flow near the cylinder wall feeding the radial section on the compression stroke. On the expansion stroke, flow out of the radial section jetted out towards the centre of the cylinder, further feeding the vortex. The sharp edge appeared to contribute greatly to this effect.

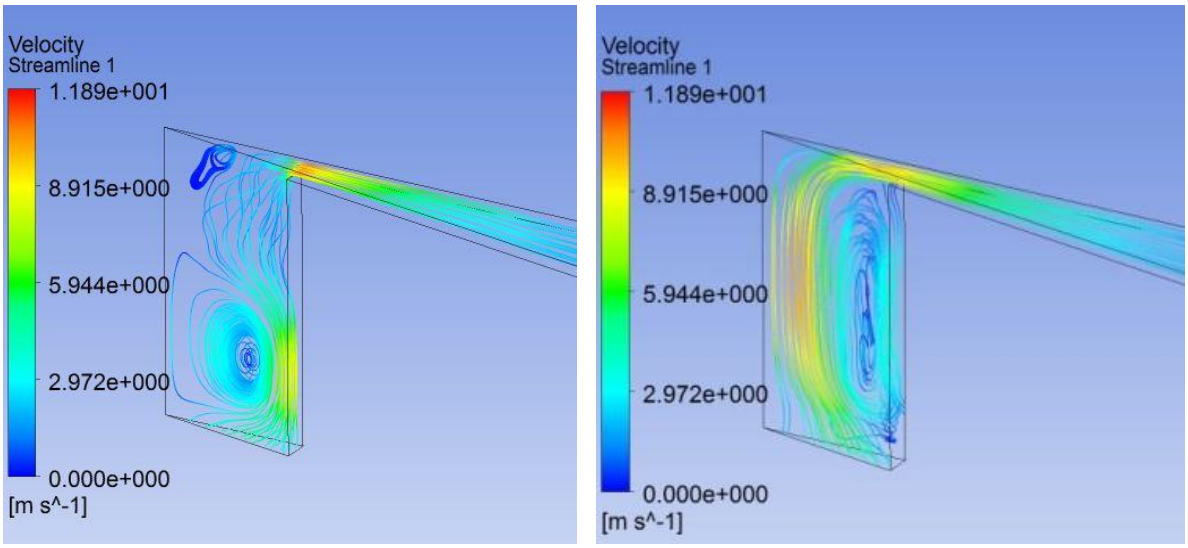

Figure 4-23: Streamlines from mid-stroke compression (left) and expansion (right) for the high loss run with a Pe_w of 6700.

As stated earlier, the polytropic index is an indicator of the transition between isothermal and adiabatic compression. Figure 4-24 shows the polytropic index for the T-Cylinder model. The polytropic index transitions from just above 1 to 1.65 (γ = 1.67) as expected. The transition from isothermal to adiabatic occurs from below a Pe_w of 100, to essentially adiabatic behaviour above a Pe_w of 40,000. The adiabatic wall condition plot indicates that pressure gradients required to drive flow are minimal compared to the compression ratio in this study.

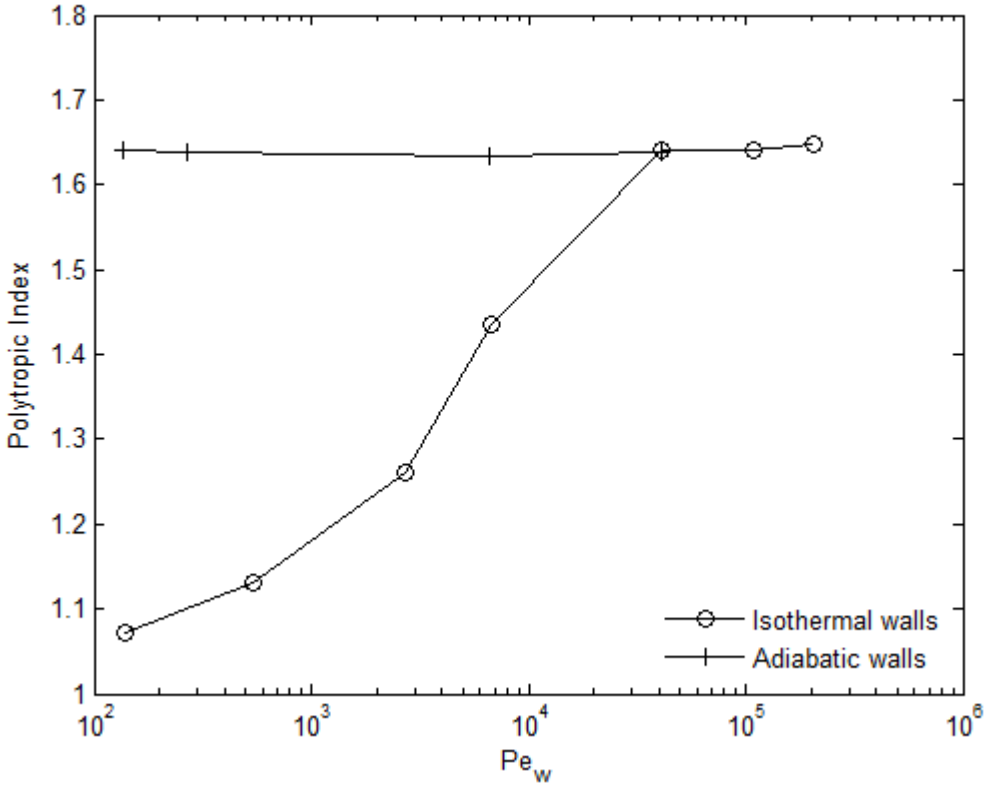

Figure 4-24: The polytropic index as a function of Peclet number comparing isothermal and adiabatic cylinder walls for the T-cylinder model.

4.5.3 TEMPERATURE FLUCTUATIONS DURING THE CYCLE FOR THE T-CYLINDER MODEL

CFX can offer detailed insights to flow conditions at any point during the cycle. In this section we will consider three cases: near-isothermal, high hysteresis loss, and near adiabatic. Figure 4-25 to Figure 4-27 show the gas temperatures during the cycle. The temperature is monitored in the model at the top centre of the cylinder and at three points in the radial section: near the cylinder, mid-radius, and near the outer rim. The crank angle for the plots starts with zero degrees being mid-stroke while compressing. Table 4-4 summarises the three cases. The near-isothermal case has a Peclet number of 135, a low hysteresis loss of 0.037 and a polytropic index of 1.07; all being consistent with near-isothermal conditions. The high loss case, at a Pe_w of 6700 has a high hysteresis loss of 0.11 and mid-range polytropic index of 1.43. The near adiabatic case, with a Pe_w of 40701, has a low hysteresis loss of 0.035 and polytropic index of 1.64 ; both consistent with near adiabatic conditions.

Table 4-4: Comparison of running parameters for near-isothermal, high loss and near-adiabatic conditions.

Parameter	Near Isothermal	High Loss	Near Adiabatic
Operating frequency, Hz	1	10	20
Mean Pressure, kPa	100	500	1500
Pe_w	135	6700	40701
L_{nd}	0.037	0.11	0.035
Pressure Ratio	2.101	2.70	3.12
Polytropic Index	1.07	1.43	1.64

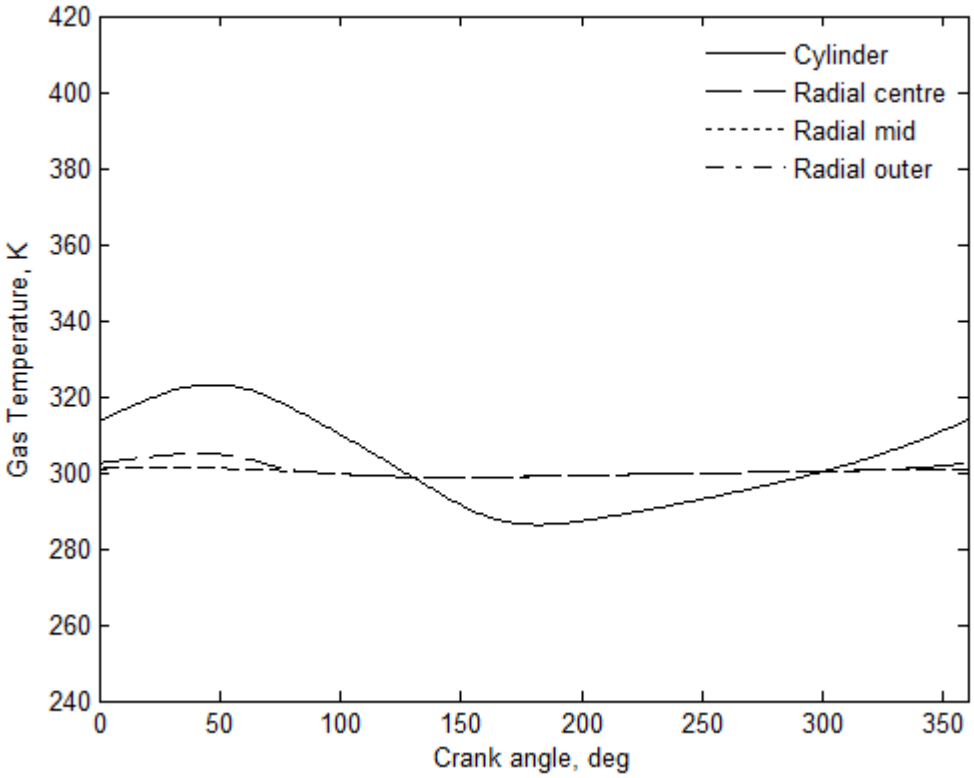

Figure 4-25: Gas temperatures in the T-cylinder model for the near-isothermal case. Note the scale is the same as the following two figures for comparison of the oscillation amplitudes.

The near isothermal case, Figure 4-25, shows a small temperature fluctuation in the cylinder, with very little fluctuation in the radial section. The monitor point near the centre of the radial section shows a small temperature increase on the compression part of the stroke, most likely from warm gas moving in from the cylinder; on the expansion stroke the gas that moves past the centre monitor point is from the radial section and therefore at the same temperature as the other radial monitors. The radial section's ability to suppress the temperature fluctuations throughout the cycle is evident.

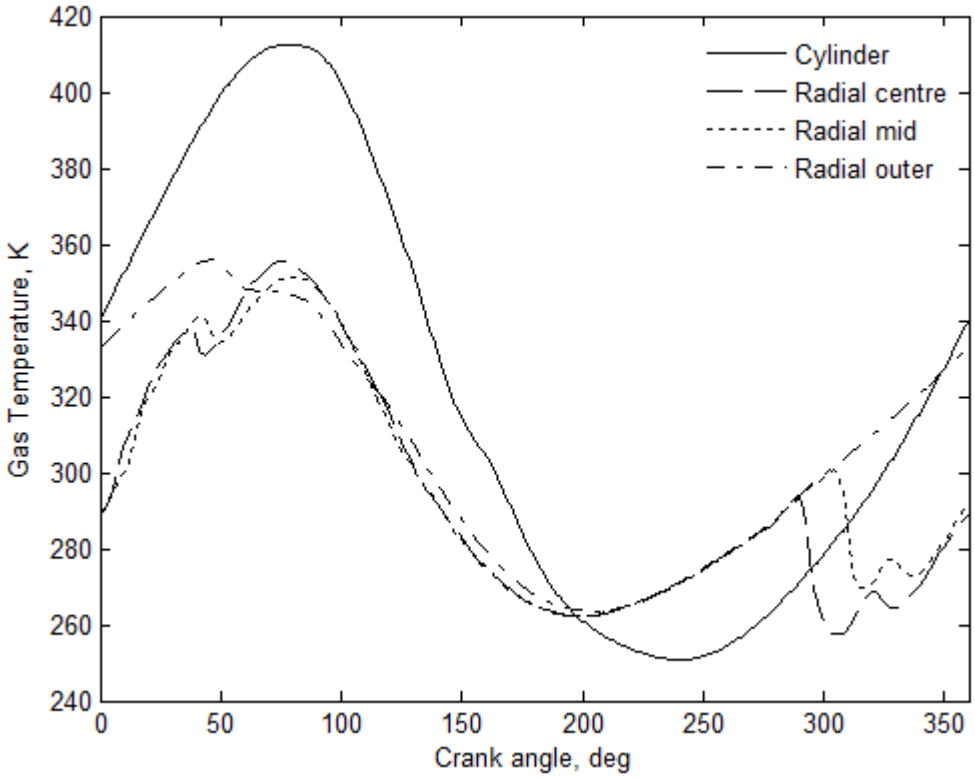

Figure 4-26: Gas temperatures in the T-cylinder model for the mid-range case.

The mid-range case, Figure 4-26, shows increased temperature swings, as expected. The cylinder exhibits a temperature swing consistent with near-adiabatic compression. The temperature oscillations in the radial section are dampened by heat transfer with the 300 K walls. The effect of the radial-cylinder interaction becomes more prevalent with the temperature monitors in the radial section having perturbations due to gas moving between sections of different temperature. As with the near-isothermal case, the expansion stroke shows all three expelling similar gas temperatures to the cylinder. The compression stroke shows a point, at approximately 300 degrees crank angle, where cooler gas from the cylinder moves past the temperature monitor on its way into the radial section. The centre radial monitor registers the cool gas before the mid radial monitor, indicating the flow direction of the gas.

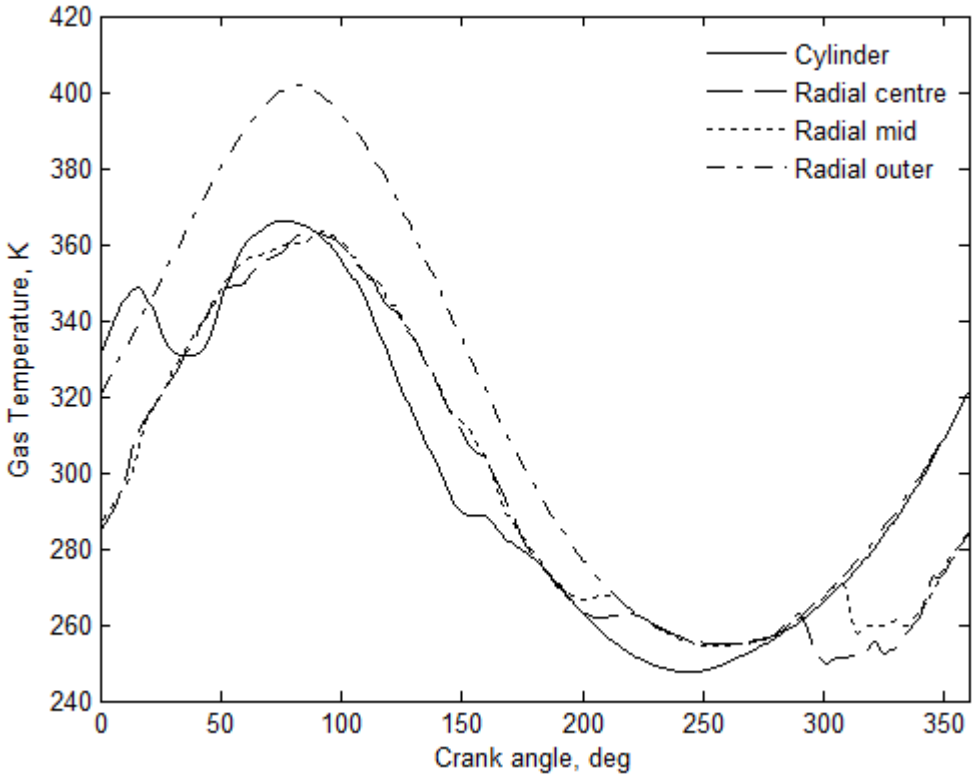

Figure 4-27: Gas temperatures in the T-cylinder model for the near-adiabatic case.

In the near-adiabatic case, Figure 4-27, an unexpected result occurs. With a Peclet number of 40,000 one would expect near-adiabatic compression throughout the gas. The outer radial position shows near-adiabatic compression because it has little disturbance from other parts of the machine. However, the cylinder temperature has a severely attenuated rise from approximately 30° to 180° of crank angle, after which the flow temperature swings look adiabatic. This could be explained by a parcel of gas that transitions between the cylinder and radial sections, and experiences higher heat transfer (therefore cooling the gas more) due to increased velocities. The large vortex in the centre of the cylinder in Figure 4-28 below confirms the hypothesis. The vortex is dragging cold gas from contact with the walls towards the centre-top of the cylinder which is the location of the monitor point. It can be seen that the thermal boundary layer is thicker near the centre of the radial section, confirming that convective heat transfer from the radial flow is cooling the gas, thus attenuating the centre and mid temperature positions as observed.

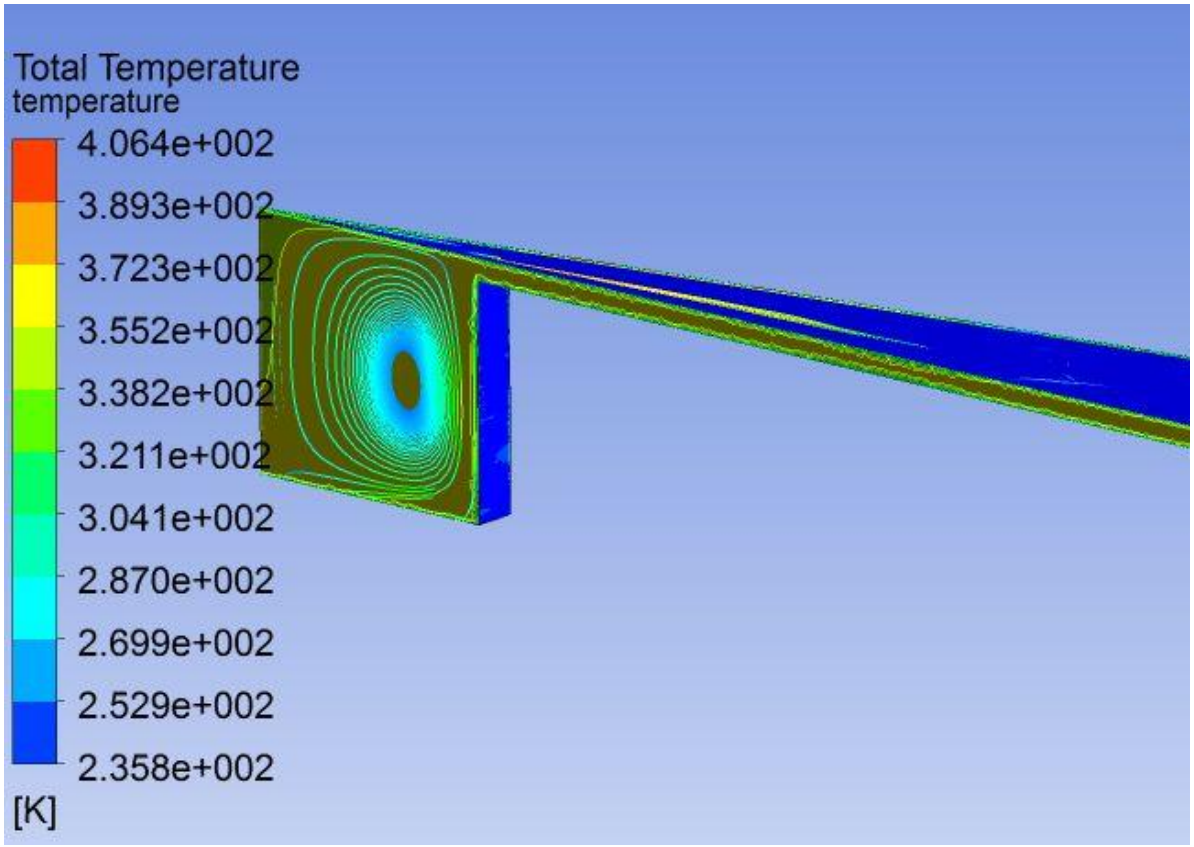

Figure 4-28: Near-adiabatic case close to the top of the compression stroke showing a vortex and temperature profiles.

4.5.4 SAGE PREDICTION OF T-CYLINDER MODEL

A Sage model of the T-cylinder model was run for a range of conditions between near-adiabatic, 1 bar, 0.038 Hz up to typical cryocooler running conditions of 25 bar and 60 Hz. The Sage model of the T-cylinder tests Sage's empirical and theoretical models of heat transfer for the radial section. As was seen in Section 4.3, Sage predicted the point of maximum entropy loss of Kornhauser's experiment well. Any error in the model of the T-cylinder should therefore be due to the radial section.

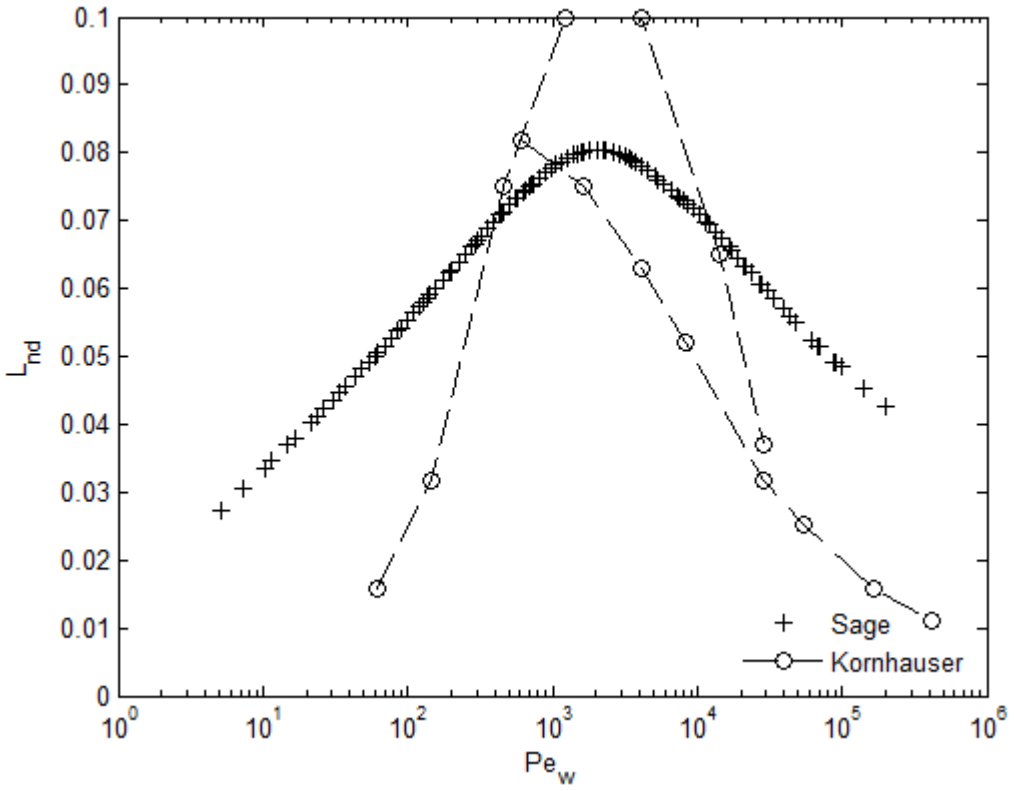

Figure 4-29: Sage's calculation of L_{nd} for the T-cylinder model, Pe_w calculated using the radial section thickness for hydraulic diameter (0.004 m).

Figure 4-29 shows Sage's prediction of the T-cylinder model using a Peclet number calculated from the radial section hydraulic diameter. Sage accurately models the position of high hysteresis and agrees with CFX that the radial space dominates heat transfer. Interestingly the shape of the Sage curve has higher hysteresis loss than CFX or Kornhauser and Smith's predictions when approaching the isothermal and adiabatic extremes. Sage predicted the adiabatic end well for Kornhauser's cylinder, indicating that Sage might be over-calculating heat transfer for high Peclet number conditions.

4.5.5 *DISCUSSION OF RESULTS FROM THE T-CYLINDER MODEL*

The CFX model of the T-cylinder situation produced results indicating that the radial section of the model dominated the hysteresis losses and therefore the heat exchange between the gas and walls. The CFX model's hysteresis curve matched Kornhauser's cylinder hysteresis curve when calculating the Peclet number based on the radial section's hydraulic diameter. This supports the second major hypothesis of this thesis, namely that the radial flows produced by diaphragm geometry have the potential to add heat exchange to a cryocooler.

The Sage model agreed with the CFX model on the position of maximum hysteresis and therefore the radial sections dominance of heat exchange. However, the Sage model predicted higher hysteresis losses at higher and lower Peclet numbers. Since typical cryocooler operating conditions are at high Peclet numbers, this suggests that Sage would over-estimate the heat exchange in a diaphragm cryocooler, evidence of which was seen when comparing Sage's predictions with experimental results of the proof-of-concept prototype in Chapter 3.

The CFX model's behaviour has shown its ability to model diaphragm gas spaces and provides the confidence to move to the next step which is a validation experiment using parts of the actual cryocooler to be modelled.

4.6 Validation experiment and modelling

In the previous sections of this chapter it was demonstrated that CFX was able to model polytropic compression of gas in an enclosed space. Heat transfer to and from isothermal walls in a cylinder was verified against the experimental work by Kornhauser and Smith. The validated model was modified to represent the flat compression geometry in a diaphragm cryocooler. The flat geometry was then merged with Kornhauser's cylinder geometry to produce a radial flow situation which was successfully modelled. Results of the modified models were consistent with expectation and the Peclet number was a useful gauge for the type of compression and expansion that would be expected under given conditions. The next step in the validation process was an experiment that extended the model to be one step closer to the final Stirling cryocooler geometry.

4.6.1 EXPERIMENT

The complete diaphragm Stirling cryocooler is a complicated machine to validate. Hence, a simplified test rig, shown in Figure 4-30, was designed for verification purposes. It uses the same geometry, volume and pressure wave generator (Figure 4-31), as the second prototype Stirling cryocooler. The key difference was that the verification experiment had no regenerator or moving displacer. The regenerator was removed for the validation as any error in modelling the complex heat transfer in its matrix could overshadow an otherwise good model of the rest of the system. Additionally, the presence of a regenerator would produce a refrigeration cycle that would also dominate results. The regenerator was replaced in the experiment with a tube of the same length and gas volume (taking porosity into account) as the cryocooler's regenerator. In this way the volumetric compression ratio of the cryocooler was maintained. The experiment used as much hardware as possible from the second prototype. The final result was a CFD model that, with minor geometry modifications, and with the addition of a regenerator, and displacer movement, could become a model of the second prototype cryocooler.

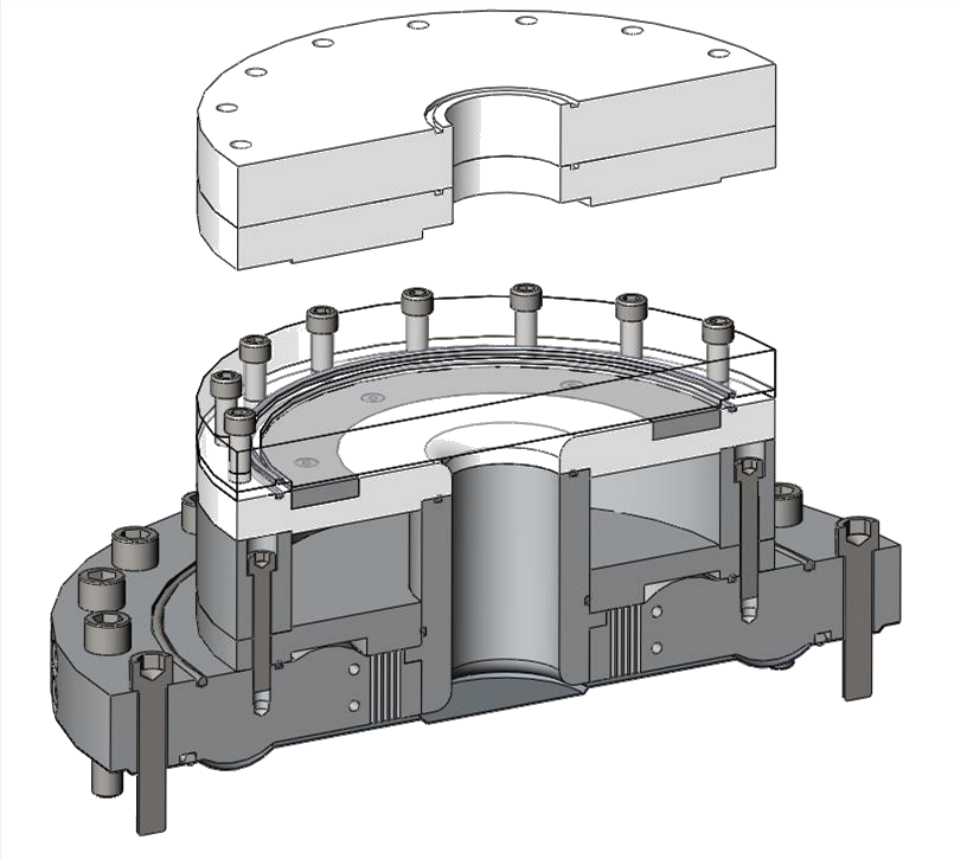

Figure 4-30: The validation test rig shown in its standard mode, and with spacer plates above.

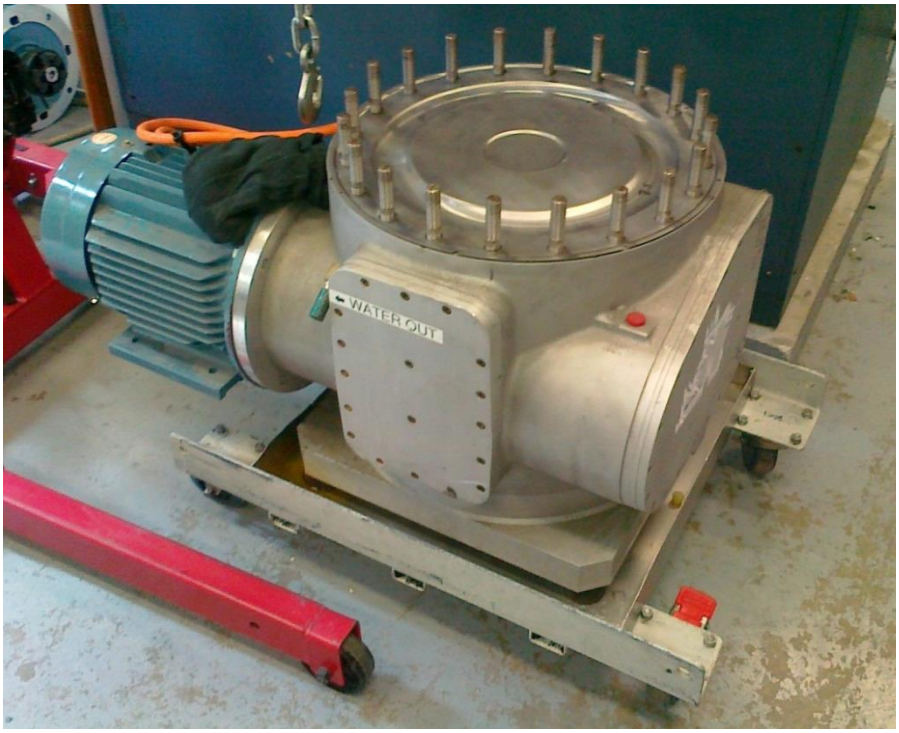

Figure 4-31: The CHC200 pressure wave generator used for the experiments.

When the validation experiment was originally planned, Particle Image Velocimetry (PIV) was proposed as a method of measuring and validating gas velocities in the radial section of the experimental device. However, further investigation of the viscosity and compressibility of the gas in the radial section identified significant challenges in finding a suitable particle for tracking the flow of the helium working gas. PIV requires particles of a similar density to the working gas to remain in suspension, which presents a challenge when the working gas is helium. Ideally for PIV the Stokes number, which compares the particle inertia with the drag forces, should be much less than one to ensure that the particles follow the flow:

$$Stk = \frac{\tau U_o}{d_c} , \qquad 4\text{-}10$$

where,

$$\tau = \frac{\rho_d d_d^2}{18\mu_g} \qquad 4\text{-}11$$

For example, a 10 micron-sized particle of density similar to plastic, oil or water, in helium gas, with a typical velocity of 10 m s^{-1}, has a Stokes number of 3 which would indicate that the particles will not follow the flow well. Water and other liquids that are commonly used for PIV (the high fluid density and viscosity of liquids reduces the Stokes number) could not be used for this experiment as they were incompressible. Consequently PIV was considered to be unsuitable for this situation.

Hysteresis loss and polytropic index measurements, as used in the preceding validation exercises were considered to be appropriate instead. If the pressure (and temperature) oscillations in the radial section match between experiment and the CFX model, then the mass flows and hence velocities have to match to satisfy the conservation equations. If the velocity-induced pressure drops are small, then the magnitudes of the pressure fluctuations are dependent on the heat transfer between gas and wall, which makes the polytropic index a good comparator between experiment and model. Checking the possible magnitude of the velocity-induced pressure drops is possible in CFX as the model can force the ideals of adiabatic or isothermal behaviour (which are physically impossible to achieve). Any deviation from the ideal pressure ratio would then be due to velocity induced pressure gradients.

The test rig was primarily constructed in aluminium because of its ease of manufacture. The top sealing plate was made from acrylic due to the early consideration of using PIV to measure gas velocities. The choice of materials was not considered a limiting factor for heat transfer as Kornhauser's experiments showed that even resin walls, which are generally considered an

insulator, behaved isothermally during oscillating conditions. The walls' conductivity, heat capacity and thermal diffusivity over the short time of the experiment were much greater than those of the adjacent gas.

Four cases with different geometries were trialled to strengthen the validation by changing the volume ratios and amount of radial flow present. The four cases were:

- Case 1, shown in Figure 4-32, was with the standard geometry and volume as per the prototype.
- Case 2, shown in Figure 4-33, was as per Case 1 with an added volume at the end of the radial section, to increase the radial flow.
- Case 3, shown in Figure 4-34, was as per Case 1 but truncated to remove the radial section, to remove the radial flow and reduce the volume.
- Case 4, shown in Figure 4-35, was as per Case 3 with added length to the cylindrical section, to regain the volume of Case 1 but without the radial flow.

.

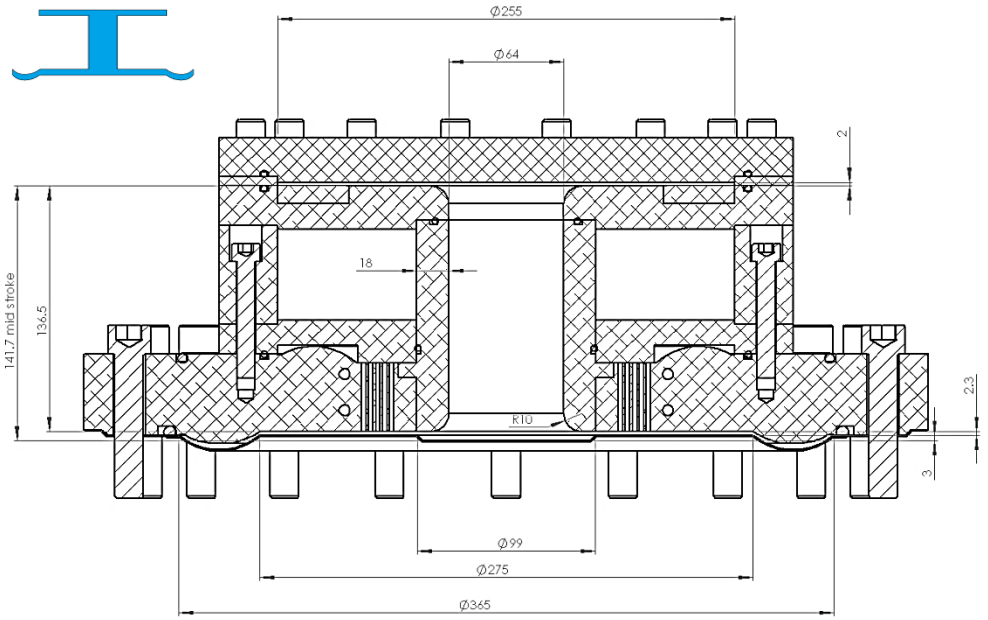

Figure 4-32: Case 1. Radial flow section close to the standard cryocooler design.

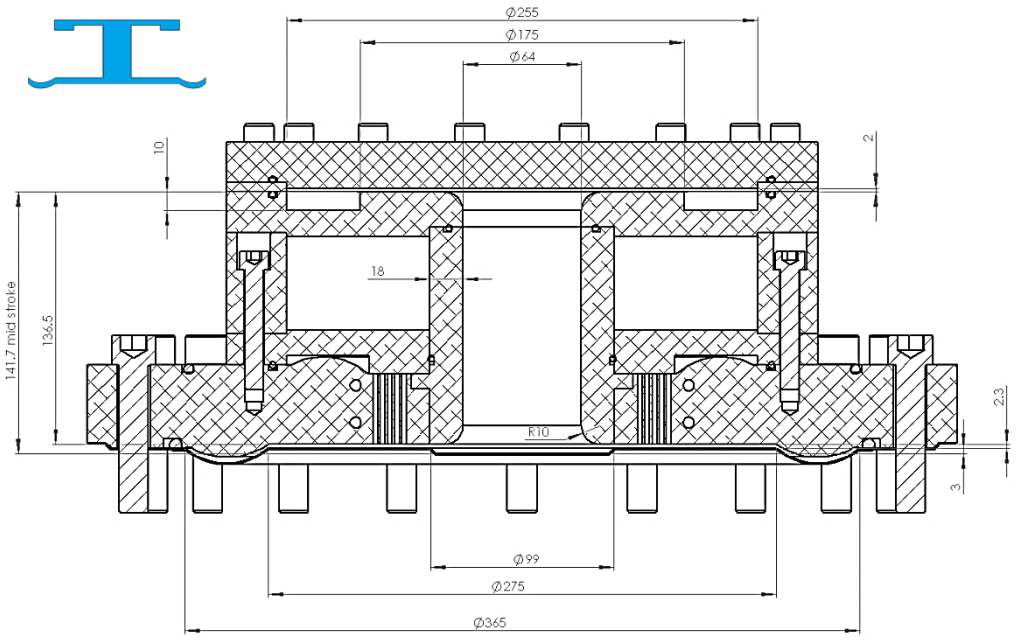

Figure 4-33: Case 2. Radial flow with extra volume at the end of the radial section.

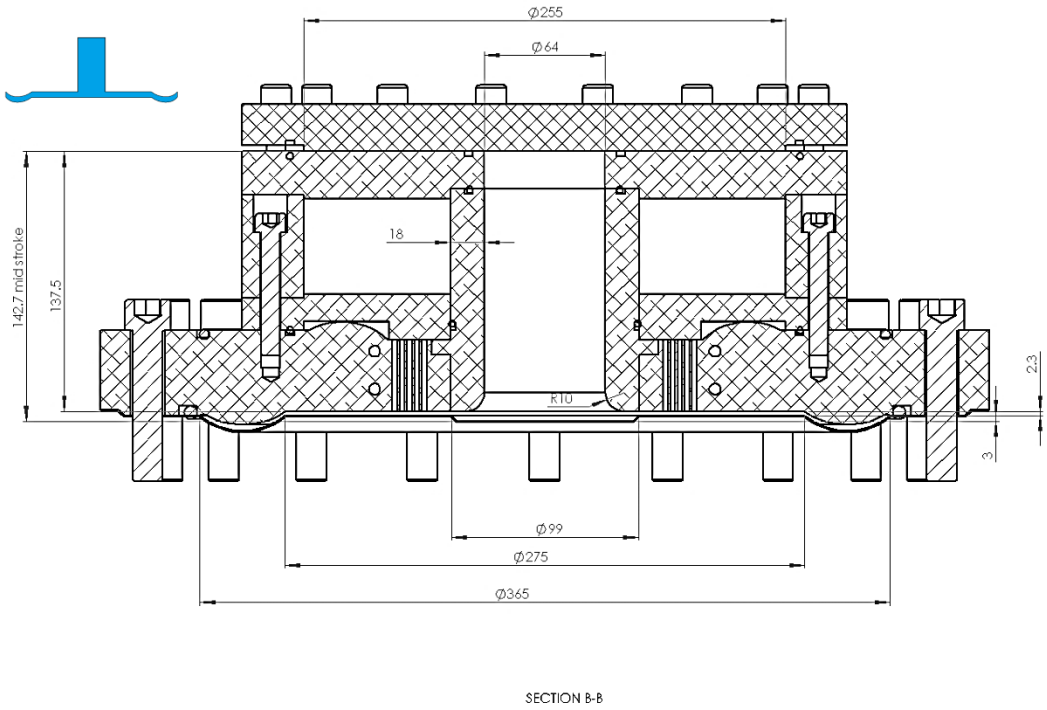

Figure 4-34: Case 3. Shortened bare cylinder, Case 1 truncated to remove the radial section.

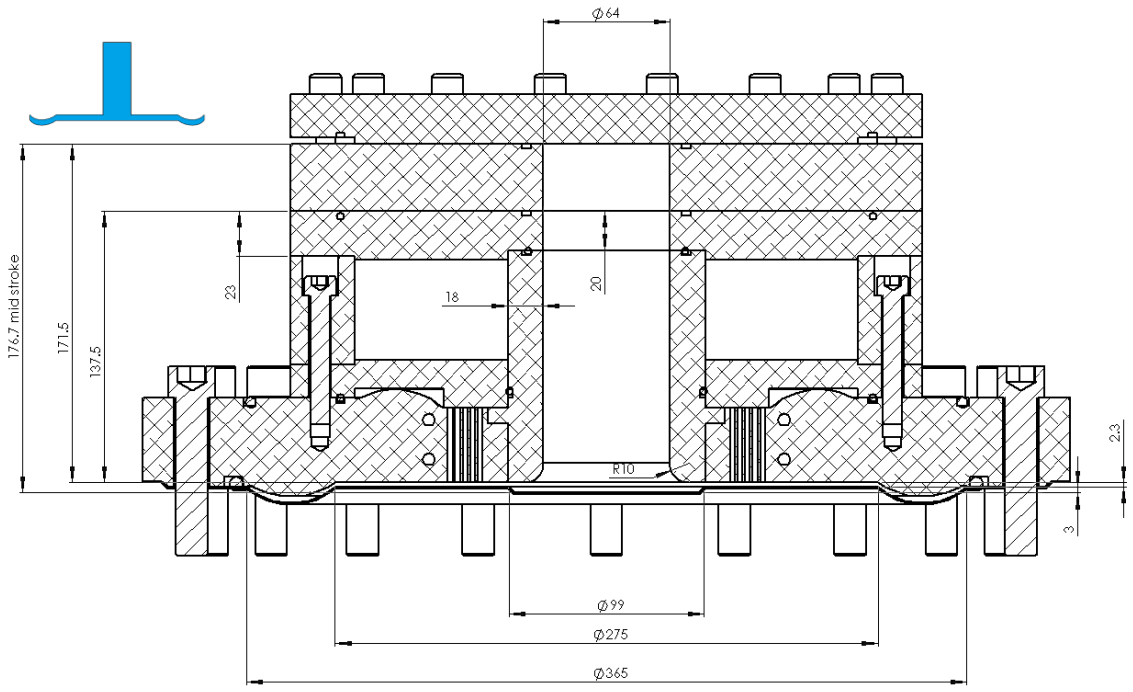

Figure 4-35: Case 4. Spacer added to Case 3 to achieve the same volume as Case 1.

4.6.1.1 Instrumentation

Data capture was performed with a National Instruments compact Rio data acquisition system connected to a LabVIEW interface on a computer. Pressure, temperature and position measurements were stored for later post-processing in Matlab. The pressure wave generator piston position was measured with a Waycon TX1 eddy current sensor. Calibration of the eddy current sensor was carried out statically using a dial gauge on the back of the DPWG piston. Pressure was measured in the pressure wave generator using a Gems 0-10 bar transducer that was calibrated using the University of Canterbury's dead-weight pressure tester. Pressure in the radial section was measured using a 0-100 bar transducer, again calibrated on the dead-weight tester. The 0-10 bar gauge was used for analysis as it provided better resolution data. The average temperature of the test rig was measured using a PT100 probe in a well that was drilled into the pressure wave generator top plate. Data capture was performed at 10 kHz. Filtering of the data in LabVIEW was kept to an absolute minimum to reduce phase lag errors, and averaging was performed later during post-processing.

4.6.1.2 Measurement of pressure wave generator swept volume

The swept volume of the pressure wave generator was originally assumed to be 200 ml, based on an assumed effective piston diameter of 320 mm and stroke of 2.5 mm. The effective piston diameter is the diameter of an equivalent piston in a cylinder that sweeps the same volume as the flexing diaphragm. The original values were from measurements by the author many years prior on an early pressure wave generator of the same specifications. An initial comparison of the experimental pressure ratios with expected theoretical values highlighted the need for investigation into the effective piston diameter of the pressure wave generator used in the experiment.

The first method used to measure the swept volume involved turning the machine over slowly by hand, stopping every 30° and waiting until the pressure had stabilised, to produce the equivalent of isothermal compression. By comparing the isothermal compression ratios with two different compression volumes, such as Case 1 and Case 2, the average volume for each case and the volume ratio for the two cases can be calculated. Unfortunately this method is very sensitive to the pressure ratio values and resulted in a large error, predicting effective diameters between 266 and 305 mm with average volumes that were up to 15% different from the actual values.

A second, more direct, method of measuring the swept volume involved partially filling the experimental rig with coloured liquid and observing the rise and fall, with piston position, of the liquid against a scale placed inside the regenerator tube. The transparent top of the experimental rig, Figure 4-36, allowed the experiment to be performed at a range of pressures. Figure 4-37 shows volume versus piston position for a range of pressures typical of the validation experiment. The fitted line indicates an effective piston diameter of 310 mm +/- 5 mm giving a swept volume of 189 +/- 7 ml. The value of 310 mm is used for the diameter in further calculations and modelling.

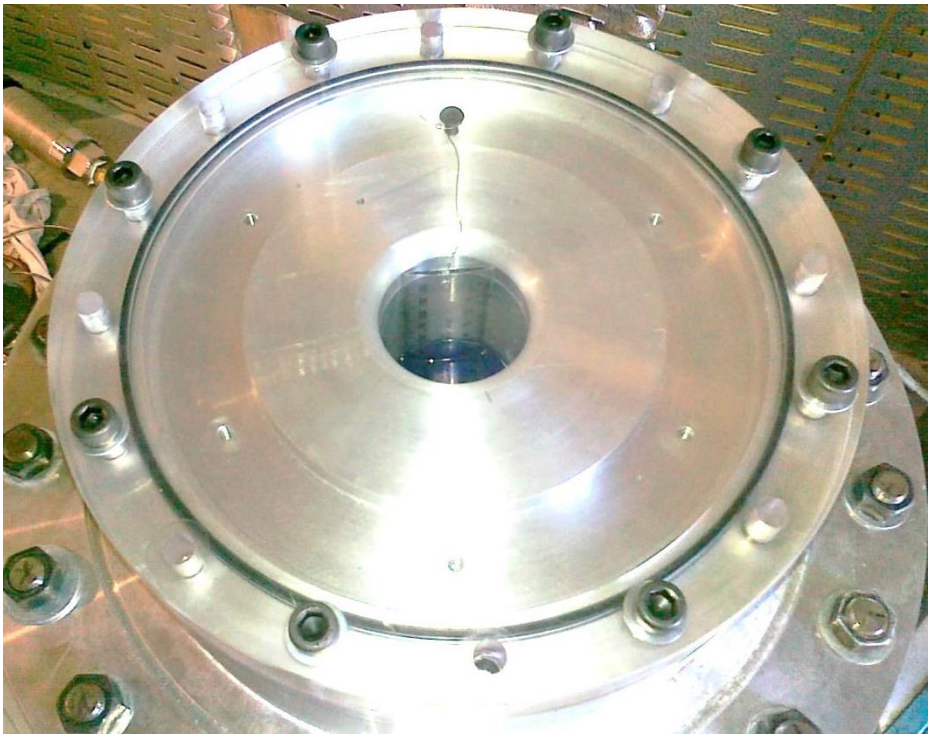

Figure 4-36: Coloured fluid measurement of swept volume of pressure wave generator

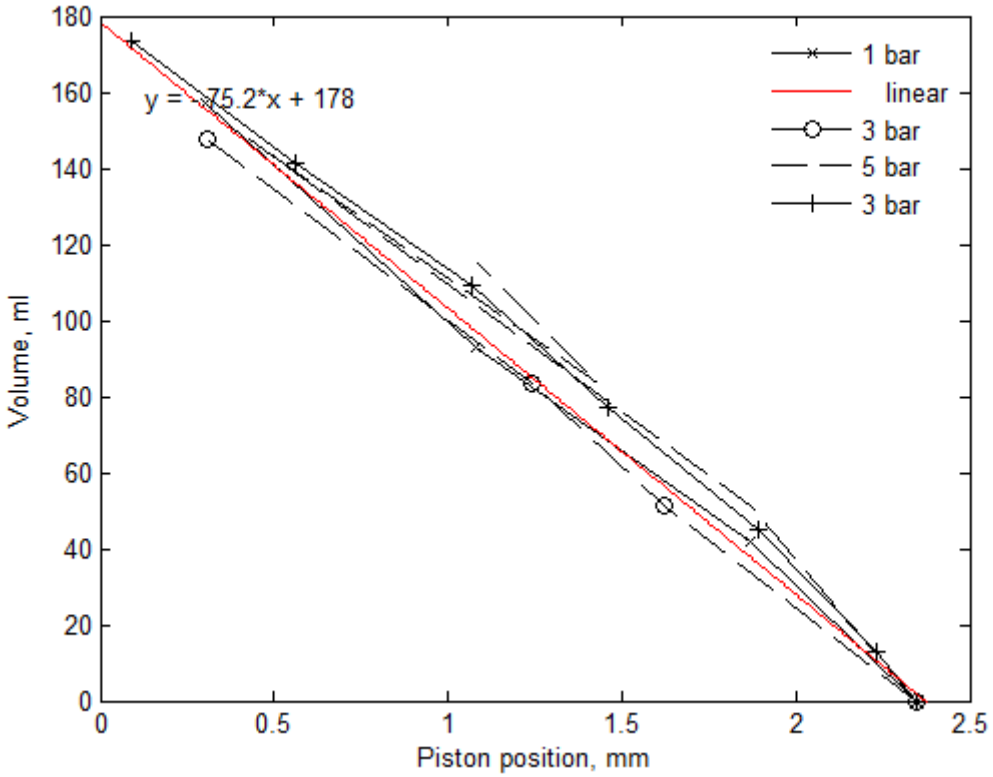

Figure 4-37: Volume versus piston position at different pressures for CHC200 PWG.

4.6.2 *EXPERIMENTAL PROCEDURE*

As with Kornhauser's experiments, each data point consisted of a brief run a few seconds long. The heat capacity of the walls was sufficient to simulate isothermal boundary conditions. For each geometry case the charge pressure was varied from 1 to 5 bar (gauge) in steps of 1 bar, and the oscillation frequency was varied from 5 to 50 Hz in steps of 5 Hz. For each data point:

- the oscillation speed control was set;
- the data acquisition was started; then the PWG motor was started;
- the data acquisition recording lasted 10 seconds;
- after which the motor was stopped.

The resulting raw data in the form of pressure, piston position and temperature was saved to a series of *.csv (comma separated values) files which were analysed with a Matlab program.

Table 4-5 lists the measurement error levels, showing that the effective piston diameter was the largest potential error source.

Table 4-5: Error levels for the validation experiment

Property	**Conditions**	**Error level raw**	**Error %**
Pressure Measurement P2 error.	0-10 bar, standard calibrated	0.025 bar 0.005	0.25% 0.05%
Displacement error	Eddy current transducer – calibrated, 0-2.5 mm	0.01 mm	0.4%
PWG piston diameter error	From fluid calculations	5 mm	1.8%
Resulting error in Polytropic Index	Low pressures High pressures	0.10 0.05	7% 3.5%

4.6.3 *Experimental Results*

When the pressure ratio is plotted against the Peclet number (Figure 4-38), the curves for each pressure are shifted relative to each other; however, plotting the polytropic index puts all the curves on top of each other (Figure 4-39). The superimposition of the lines for different pressures is a good indication of the correlation between the polytropic index and the Peclet number. The polytropic index vs Peclet number plots for the remaining three cases are shown in Figure 4-40 to Figure 4-42. The range of polytropic index values, from 1.25 to 1.55, indicates that the experiments spanned the region of high hysteresis losses.

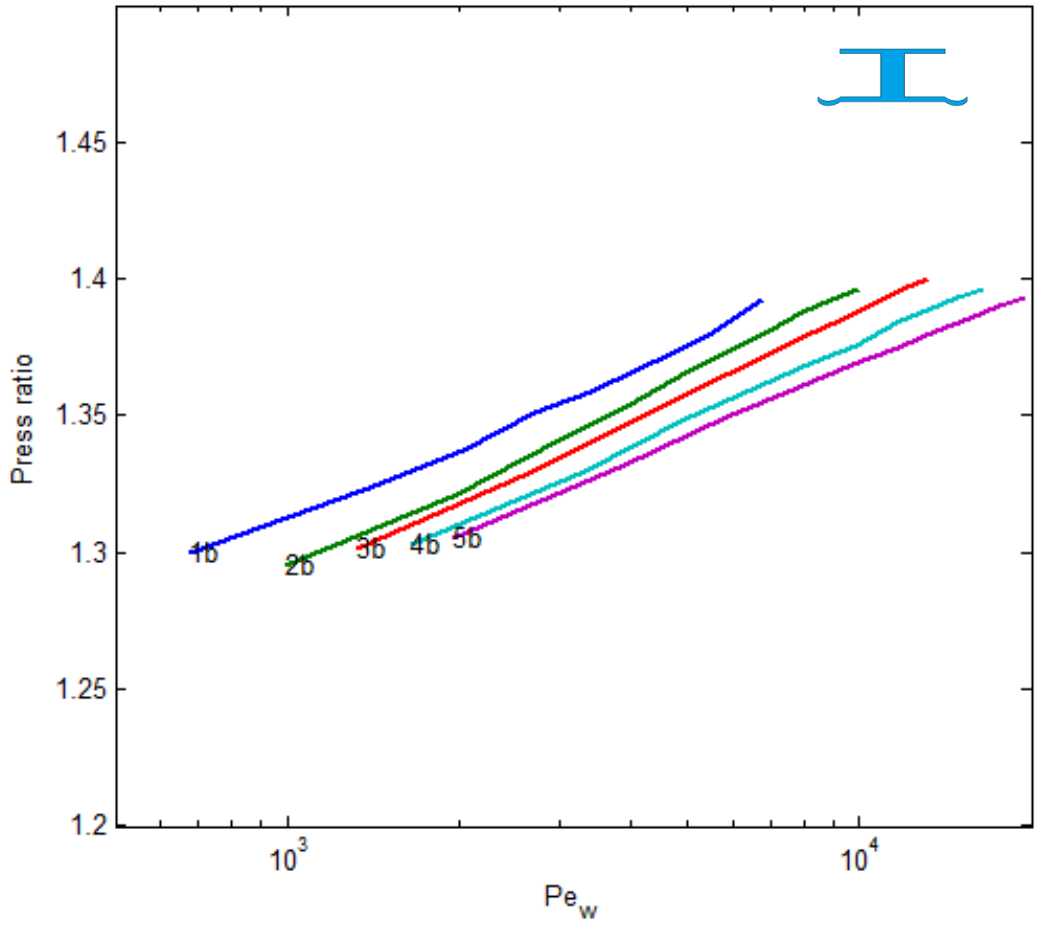

Figure 4-38: Case 1: Pressure ratio versus Peclet number. Each line represents a frequency sweep at a fixed average pressure. The line numbers indicate the pressures; for example Line 1b is a sweep at an average pressure of 1 bar gauge.

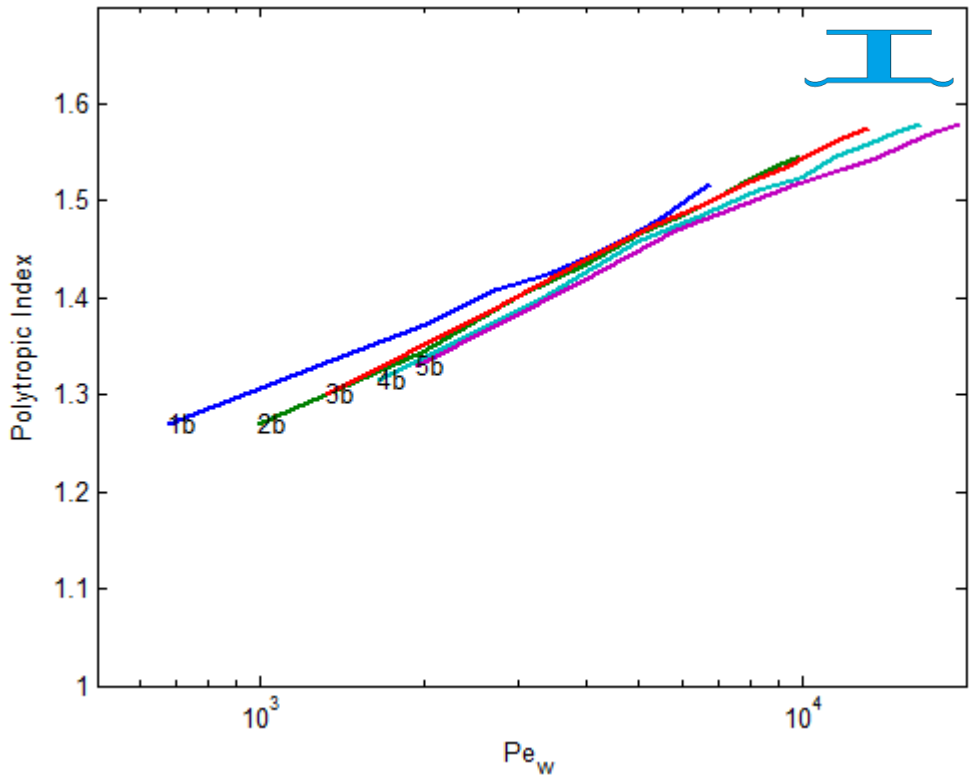

Figure 4-39: Case 1: Polytropic index versus Peclet number.

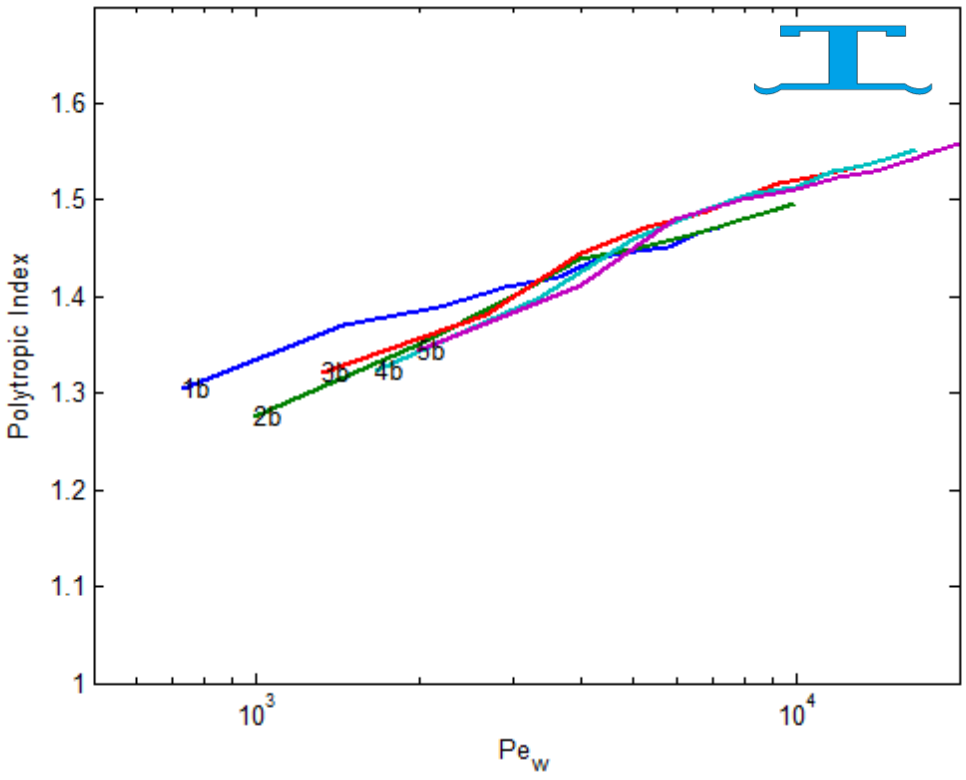

Figure 4-40: Case 2: Polytropic index vs Peclet number.

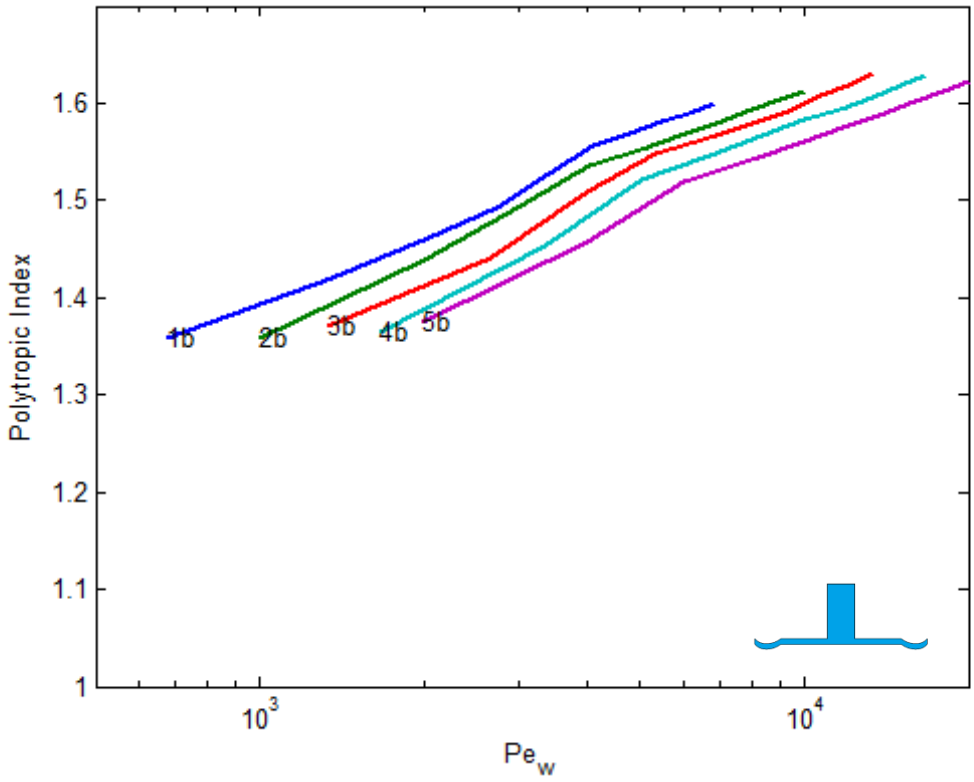

Figure 4-41: Case 3: Polytropic index vs Peclet number.

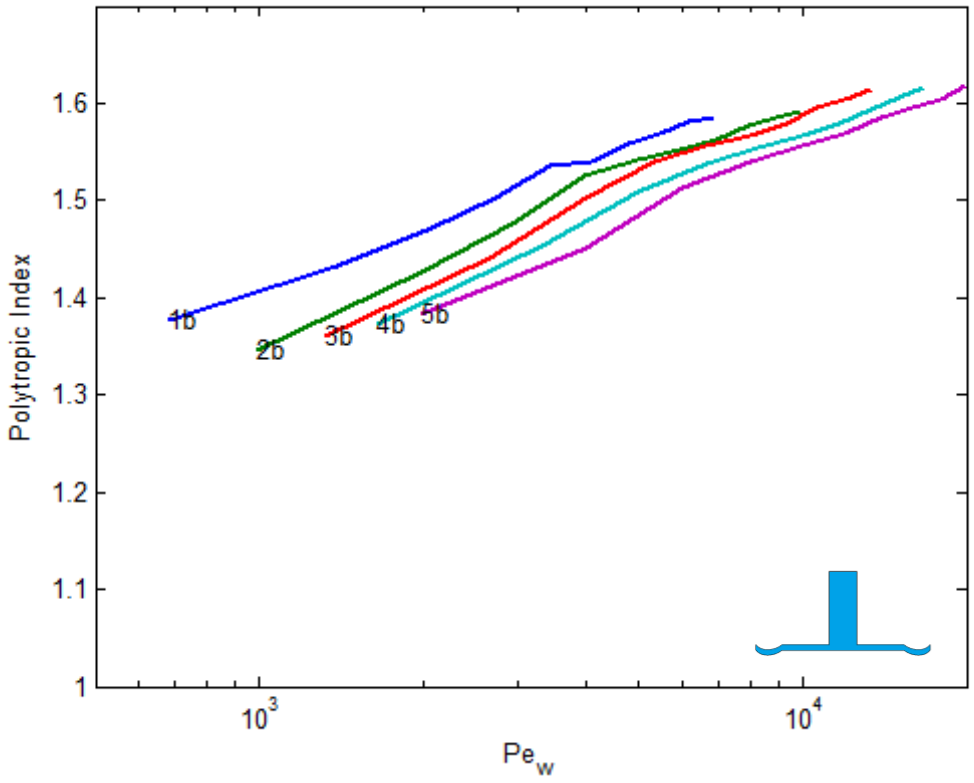

Figure 4-42: Case 4: Polytropic index vs Peclet number.

Cases 1 and 2 show similar polytropic index plots; all the lines are superimposed and the polytropic index varies from approximately 1.27 to 1.6. Cases 3 and 4, without the radial space, have more spread in the polytropic index lines and have an elevated range of values, from 1.35 to 1.62. Figure 4-43 shows on the same plot the 3 bar lines for all cases and has a clear separation between Cases 1 and 2, and Cases 3 and 4. To give an indication of data spread and more confidence to the data, the curve for Case 1 at 5 bar is also plotted, and is close to the 3 bar curves for Cases 1 and 2. Cases 1 and 2 having lower polytropic indices than Cases 3 and 4 is consistent with Cases 1 and 2 having a section of smaller hydraulic diameter than Cases 3 and 4. The small hydraulic diameter and radial flow in Cases 1 and 2 increases heat transfer which reduces compression heating, and that in turn lowers the polytropic index.

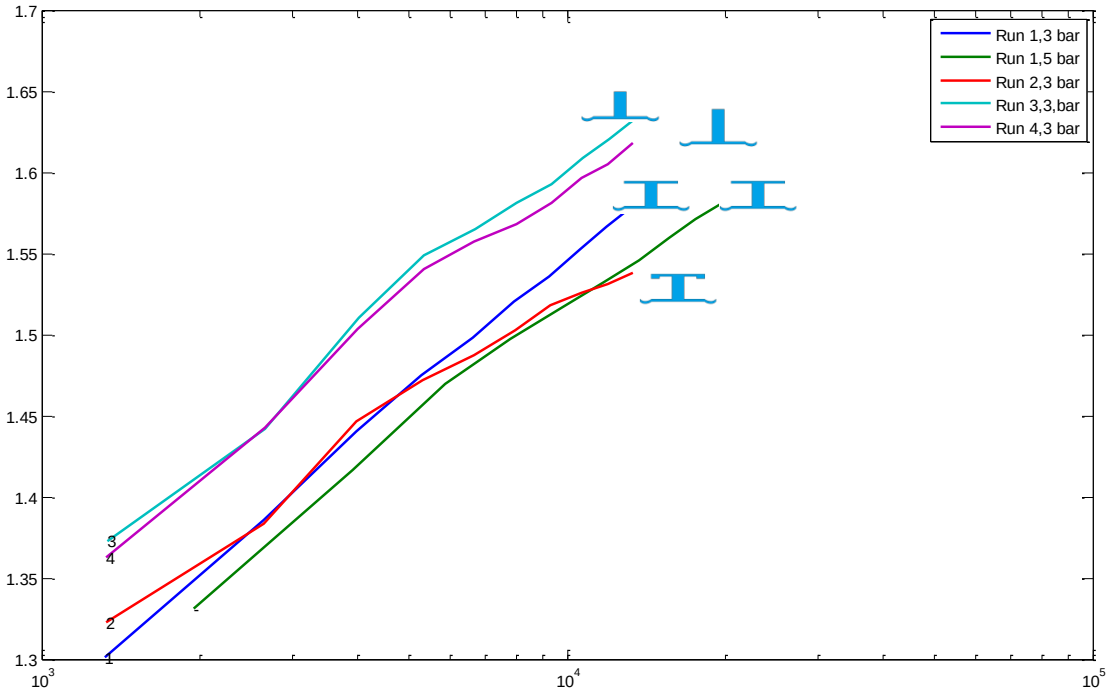

Figure 4-43: Polytropic index vs Peclet number for the four cases at 3 bar charge pressure.

4.6.4 *MODELLING THE VERIFICATION EXPERIMENT WITH CFX*

The CFX model of the verification experiment was constructed by adding the pressure wave generator gas space to the bottom of the T-cylinder model. Dimensions of the cylinder and radial section were changed to match those of the experimental rig. As with previous models, a wedge, this time with an included angle of 5°, was used to reduce calculation time.

Boundary conditions were the same as previous models and were:

- No-slip, isothermal walls held at 300 K.
- The sides of the wedge had symmetry conditions, i.e. no flow passes through but there is no friction or heat transfer with the wall.
- The working fluid was helium, modelled as an ideal gas.
- The diaphragm's piston movement was modelled as a moving wall.

The swept volume was modelled with the experimentally-measured 310 mm effective piston diameter and with the piston stroke as measured experimentally for each corresponding experimental run. The experiments showed that the amplitude of the piston movement was a function of the running speed. This is thought to be due to clearance in the pressure wave generator's pivot bearings, which rely on squeeze film lubrication. The bearings' oil supply pressure increases with running speed; hence the piston stroke has a small dependence on the running speed. Table 4-6 below lists the values of the piston amplitude as used in the model for varying frequencies.

Table 4-6: Piston movement amplitudes used for modelling. The values are measurements from the experimental rig at 3 bar charge pressure.

Frequency, Hz	**Amplitude, mm**
5	1.180
10	1.200
15	1.205
20	1.205
25	1.210
30	1.230
35	1.235
40	1.240
45	1.245
50	1.245

While measuring the assembled device it was found that the DPWG diaphragm sat 0.9 mm lower than designed at top dead centre. The CFX model was adjusted to match the experiments by lowering the PWG piston section by 0.9 mm to produce an average height of 3.2 mm, returning to the ideal height of 2.3 mm at the circumference of the membrane. The effect was to increase the average system volume which resulted in a lower pressure ratio.

The mesh density of the model was set to achieve nine elements across the thickness of the radial sections to ensure temperature gradients were spread over a number of elements. A laminar flow model was used. The number of steps per cycle was 200, a number that previous modelling indicated was sufficient for the conditions.

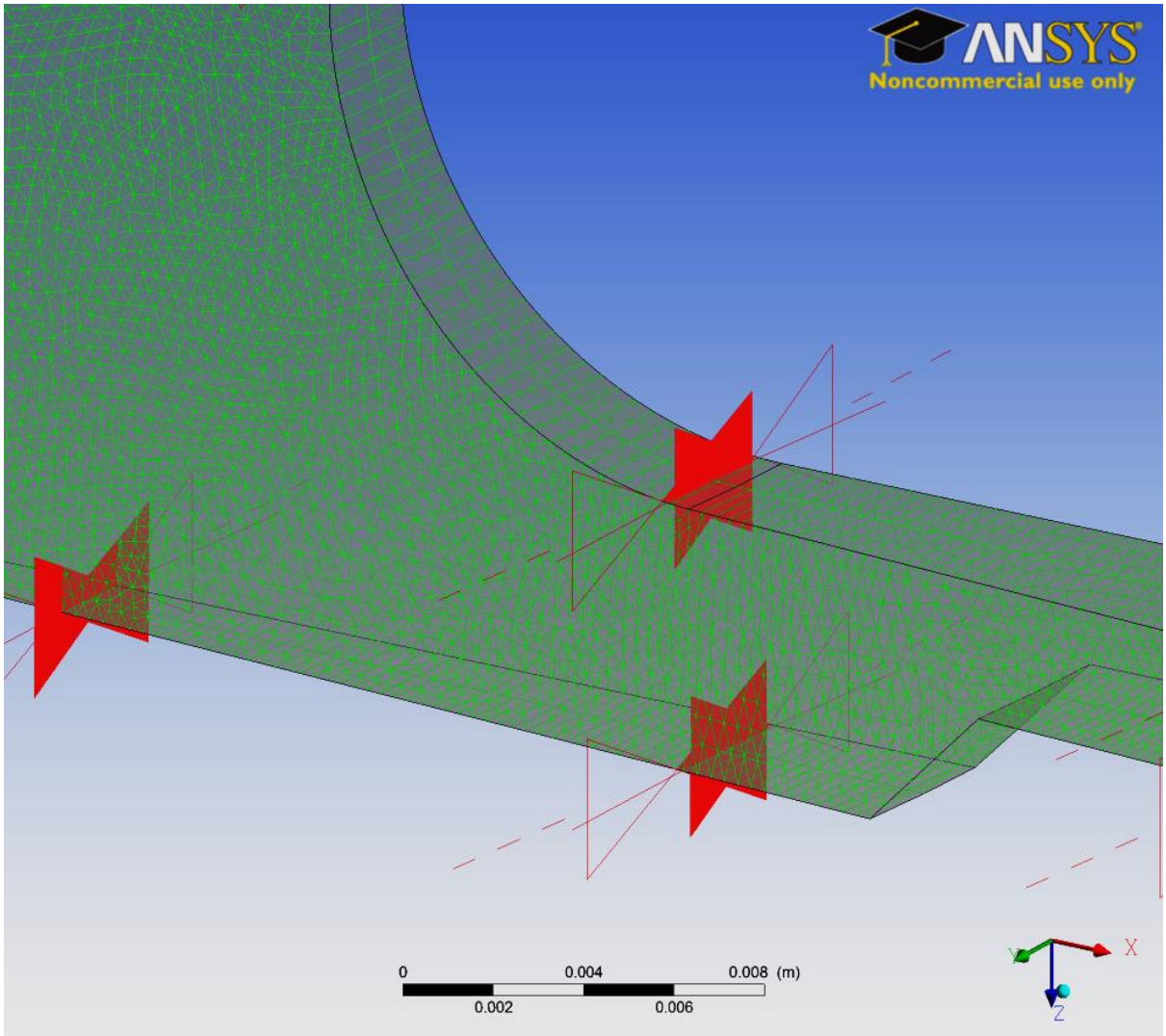

Figure 4-44: Close-up of the mesh used for the Case 1 model. The radial section has 9 elements across its thickness. The cylindrical section had the same mesh density as the rest of the model.

The flexing pressure wave generator diaphragm membrane was a new feature in the modelling. The previous validation exercises modelled the piston movement by moving an end wall and using a 'moving mesh' condition in CFX for the cylinder wall. Movement was in line with the cylinder wall which compressed the mesh evenly and produced a very smooth change in the mesh and geometry during the cycle. In the diaphragm system the 'piston' movement is perpendicular to the wall that is defined as having a moving mesh. The mesh movement happened in the element next to the moving face, and not evenly over the membrane as happens in reality. The way around this potential difficulty was to model the diaphragm membrane as a rigid inner ring up to its effective diameter of 310 mm. The ring from 310 mm outwards was defined as a moving wall, with the deformation occurring in the element next to the movement, as shown in Figure 4-45 below.

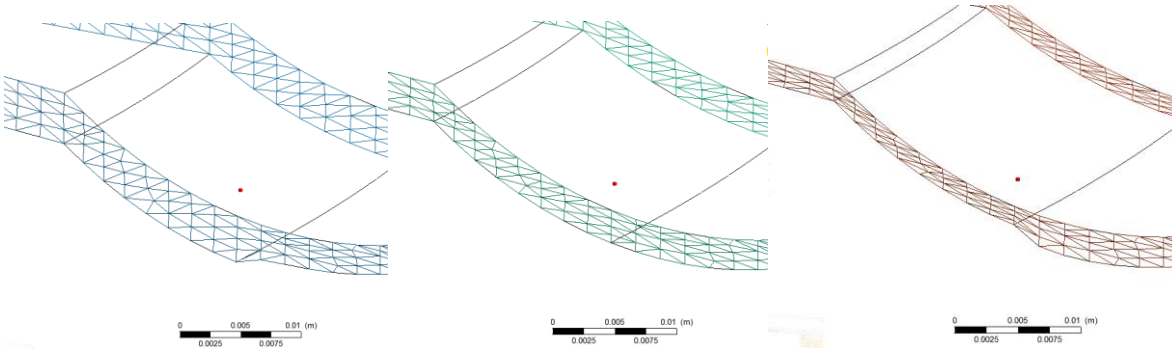

Figure 4-45: The shape of moving mesh for the diaphragm membrane. A coarse mesh with four elements across the thickness is shown for clarity of the illustration. Left is bottom-dead-centre; Centre is mid-stroke; Right is top-dead-centre.

A set of monitor points was incorporated in the model as shown in Figure 4-46. Temperature monitors were placed mid-section in the diaphragm, cylinder and radial sections. Heat flux was reported from the CFX calculation of the area-average value for: the top radial section; the tube; and the pressure wave generator. Pressure was monitored at a point in the tube away from walls. For Cases 3 and 4, the monitoring points that were originally in the radial section were moved to the top of the cylinder. Dimensions of each model are detailed in Figure 4-47 to Figure 4-50. The numerical outputs from the monitor points were saved for later analysis.

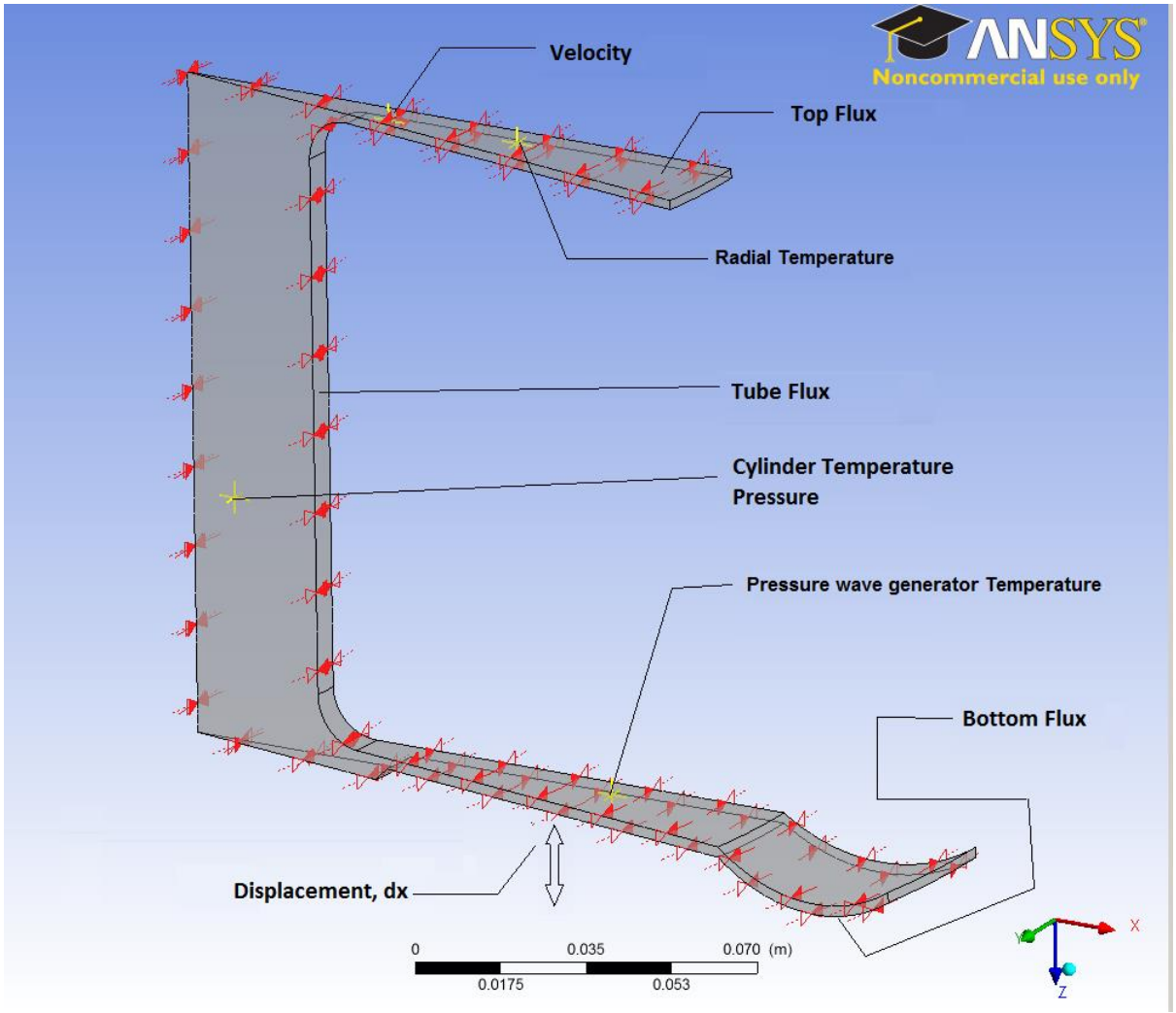

Figure 4-46: Positions of the monitoring points for the CFD analysis. Case 1 model shown. The red arrows indicate symmetry conditions.

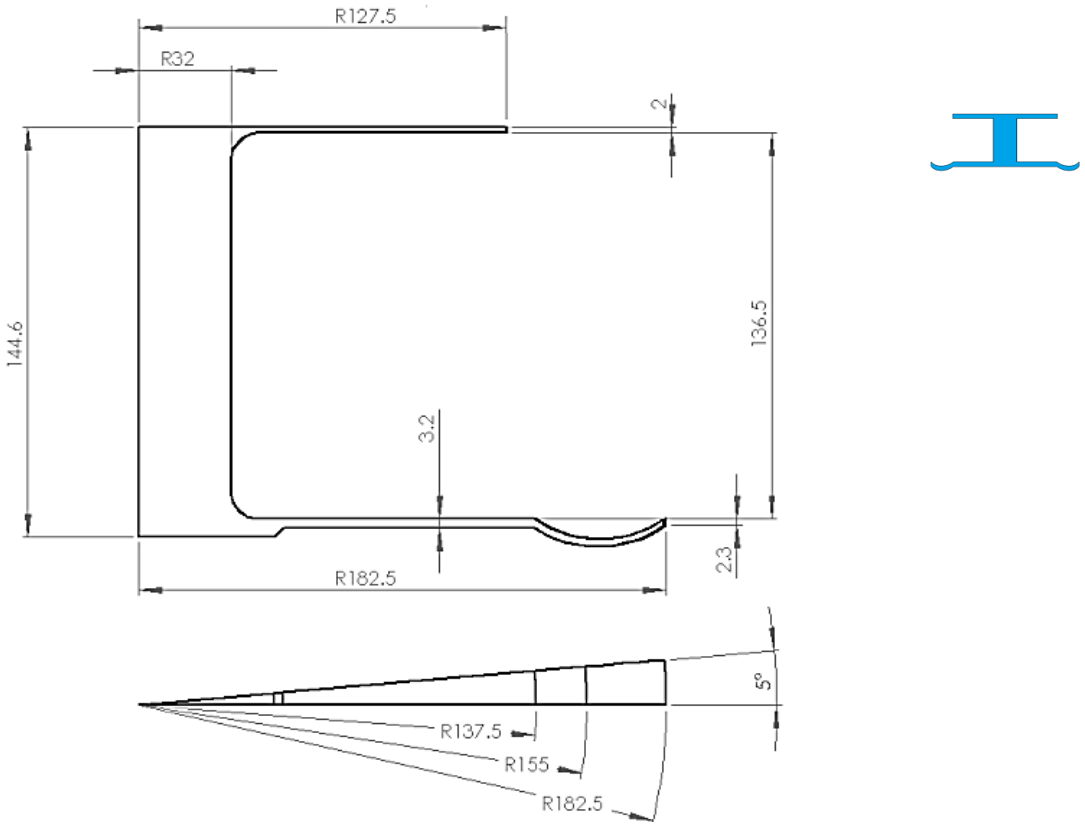

Figure 4-47: Case 1 model dimensions giving a mean volume of 8.83 x 10^{-4} m^3

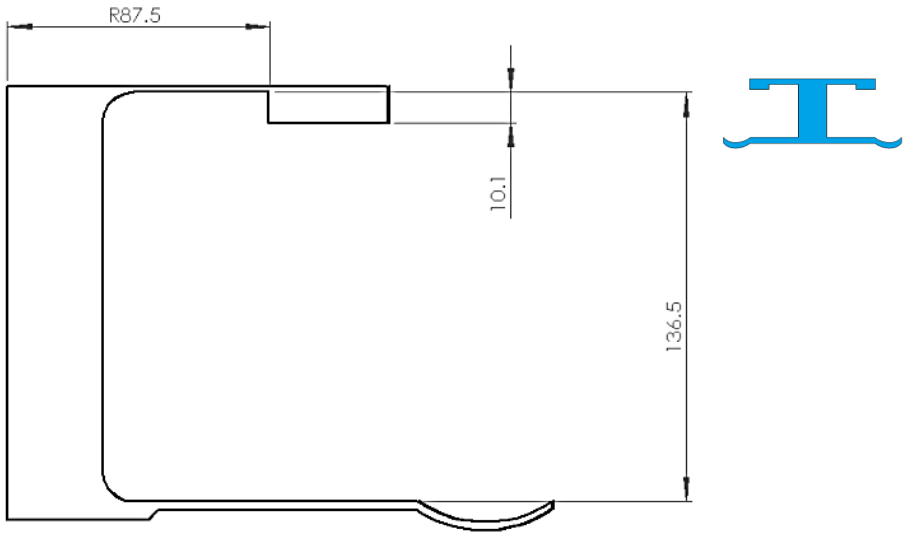

Figure 4-48: Case 2 model dimensions giving a mean volume of 1.156 x 10^{-3} m^3

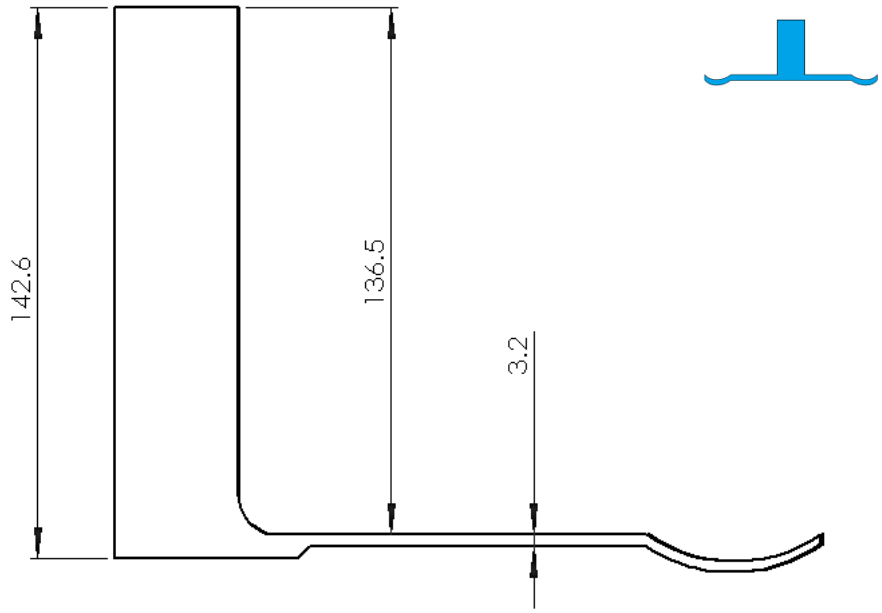

Figure 4-49: Case 3 model dimensions giving a mean volume of 7.761 x 10^{-4} m^3

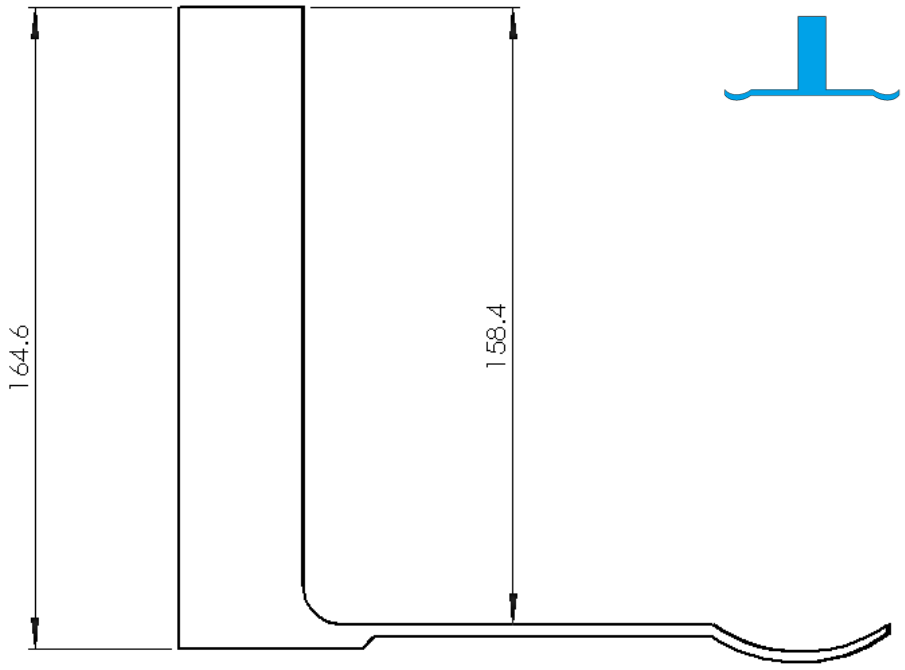

Figure 4-50: Case 4 model dimensions giving a mean volume of 8.85 x 10^{-4} m^3

4.6.5 CFD RESULTS

Figure 4-51 shows CFX's polytropic index predictions for the 3 bar gauge run of Case 1, superimposed on top of the experimental results. The CFX results are indicated as circles marked with their run number, the experimental results are the coloured lines, each line represents a frequency sweep from 5 to 50 Hz at a set average pressure. The CFX results are for the 3 bar pressure experiment. Data point C18 is a CFX run with isothermal gas conditions imposed and shows a polytropic index of 1.02, which is close to the ideal value of 1.00 for isothermal compression. Exactly 1.00 for the polytropic index would be unattainable as flow losses, however small, would slightly increase the pressure ratio. Data point C20 is a CFX run with adiabatic walls and has a polytropic index of 1.68, which is close to the ideal value of gamma for helium (1.67). There is a clear correlation between the calculations and the measurements with CFX calculations following the trend of the experimental curve. The offset implies that the CFX calculations are predicting compression that is slightly more adiabatic than the experiment, or that there is still discrepancy between the experimental and CFX swept or average volumes. The latter is likely as changing the experimental data's effective diameter within the bounds of its error can move the lines much closer to the CFX results as shown in Figure 4-52.

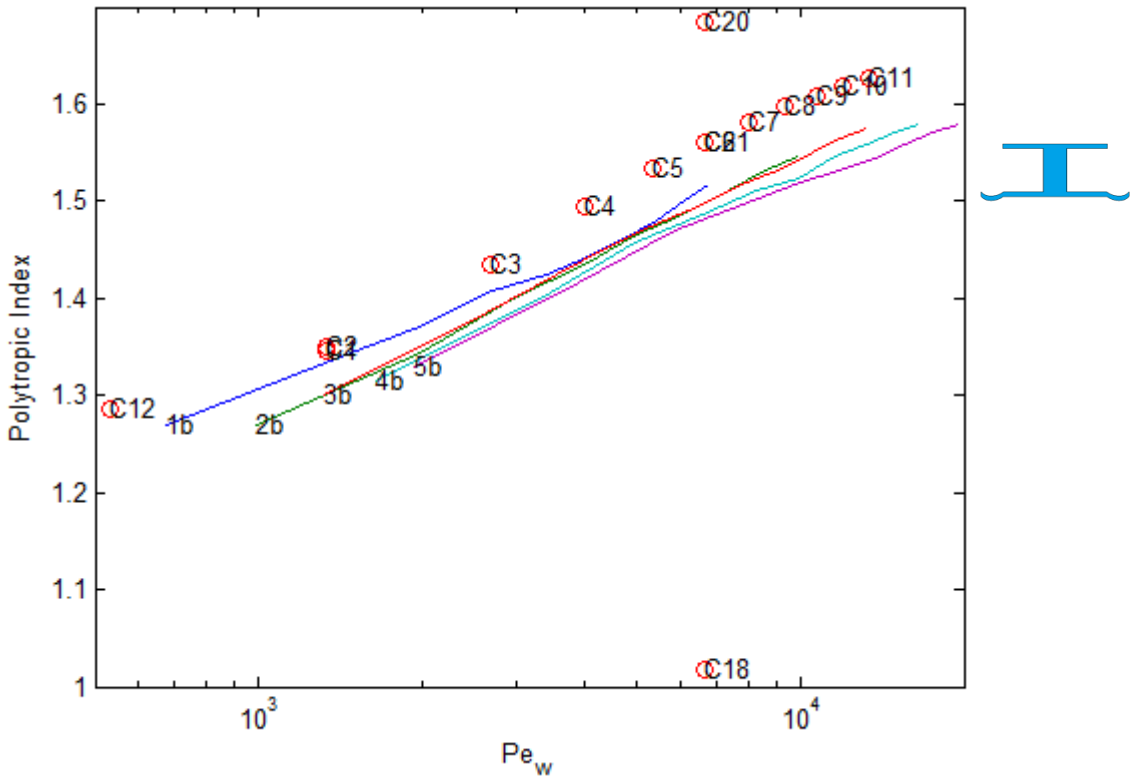

Figure 4-51: Comparison of the polytropic index for the CFD Case 1 at 3 bar. The coloured lines 1b to 5b are experimental results for 1 to 5 bar runs respectively. The numbered circles are individual CFD runs.

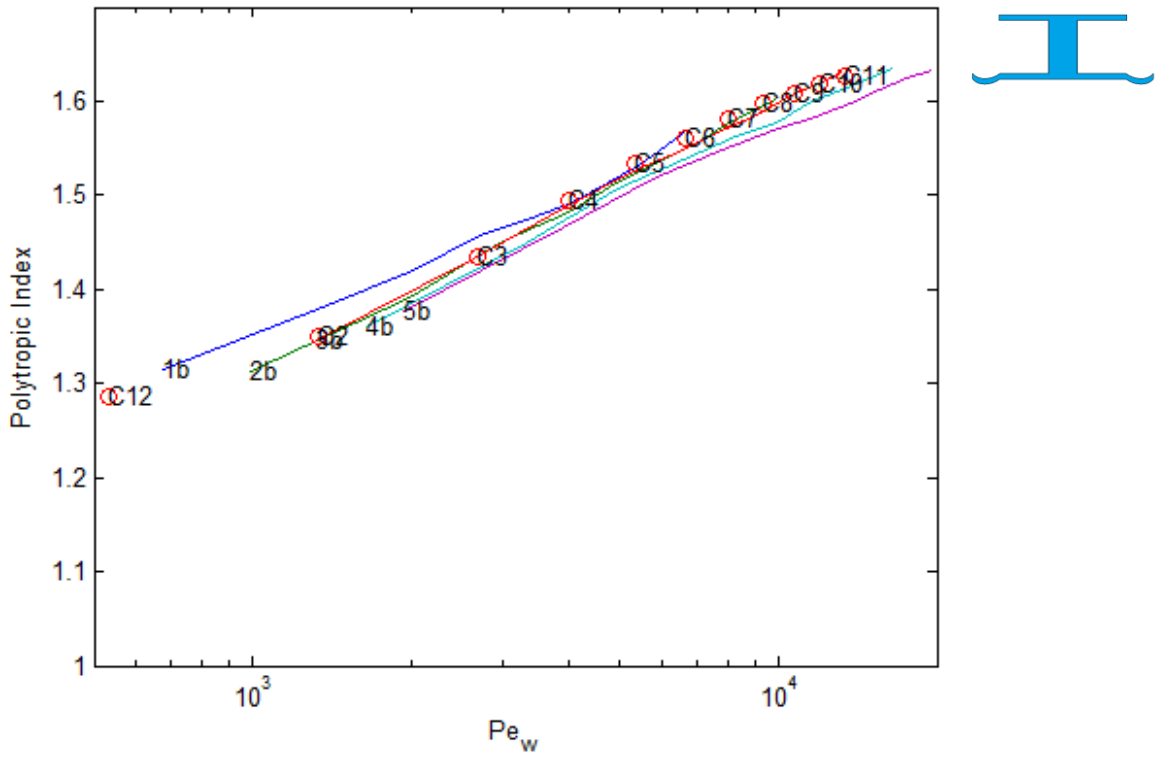

Figure 4-52: The polytropic index versus Peclet number for Case 1 when using the minimum value allowed by the error, 0.305 mm, for the effective diaphragm diameter.

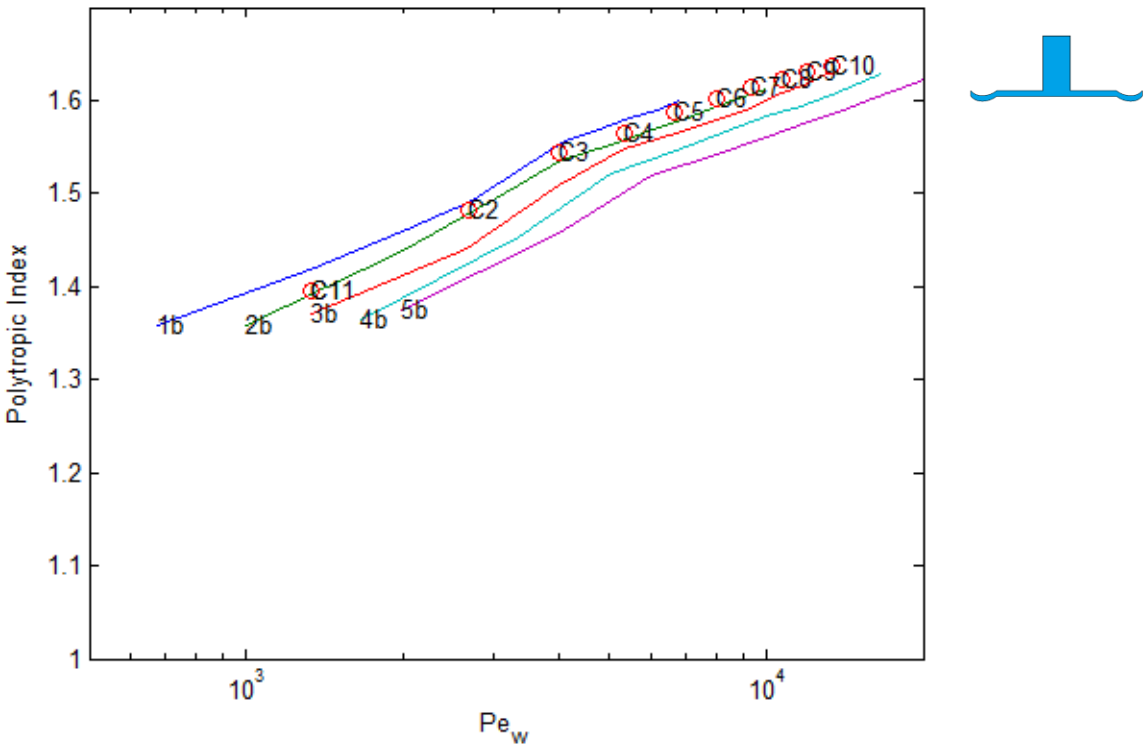

Figure 4-53: Comparison of polytropic index for CFD Case 3 at 3 bar.

Figure 4-53 shows the CFX prediction compared with experimental results for Case 3, without the radial section. The CFX curve follows the experimental curve closely, with only a small offset. Of particular note is that there is a knee is the experimental data, around point C4, which is replicated by the CFX results, indicating that the model is following an unidentified effect in the experiment very well.

Figure 4-54 and Figure 4-55 show the polytropic index correlations with the experimental measurements for Cases 2 and 4 respectively. The CFX calculations trended well with the experimental results and were close in absolute value to the experimental to give confidence in the modelling. The slopes of the experimental curves matched well with CFX. In particular for Cases 3 and 4, the knee in the curves, around a Peclet number of 4000, was replicated by CFX. Again, the offset between CFX and the experimental values can be explained by the uncertainty of the measurement of the experiment volume.

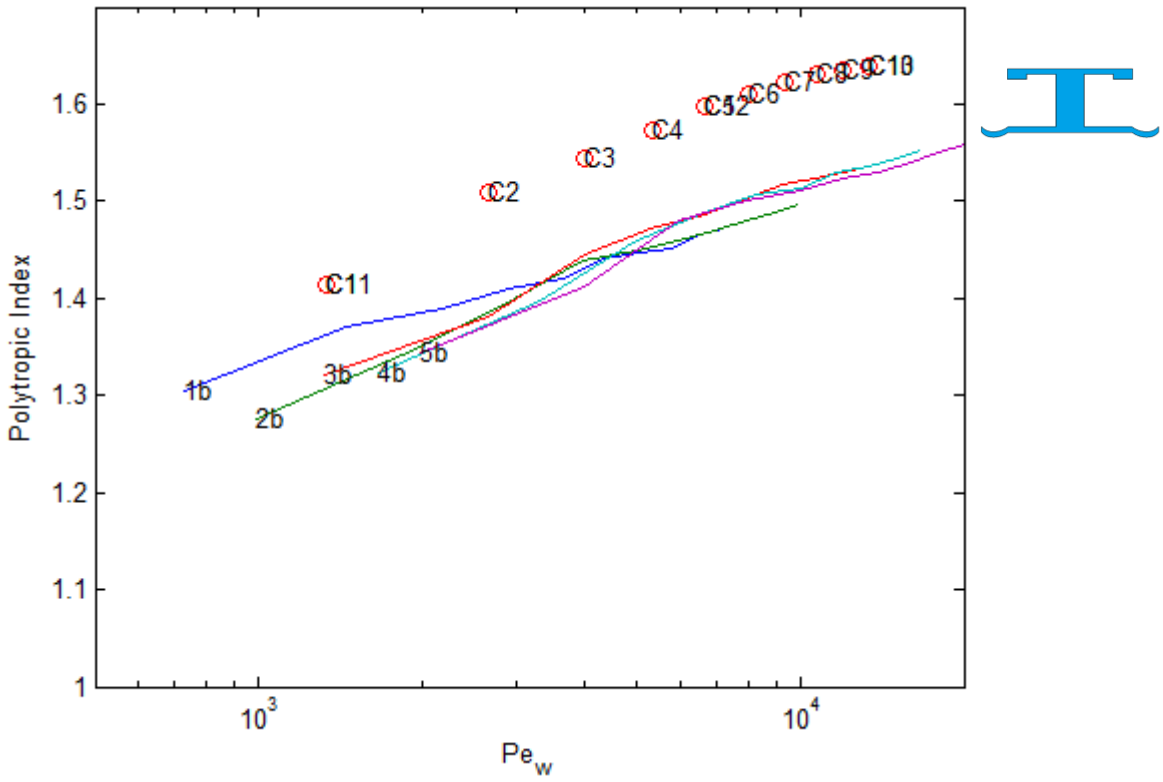

Figure 4-54: Comparison of the polytropic index for CFD Case 2 at 3 bar.

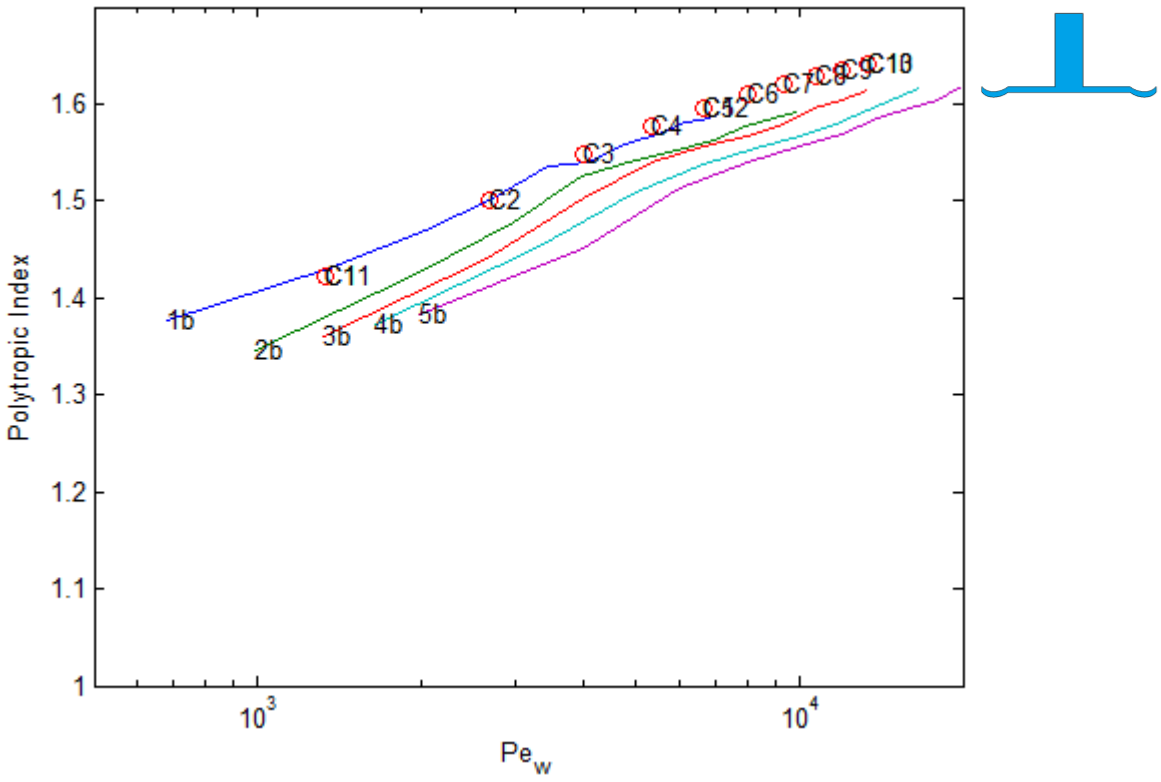

Figure 4-55: Comparison of the polytropic index for CFD Case 4 at 3 bar.

Figure 4-56 to Figure 4-59 show the non-dimensional hysteresis loss as calculated by CFX compared to the experimental results. The shape and position of the experimental result curves was predicted well by CFX for all the experiments. The peak loss occurring at a Peclet number of 2000-3000 demonstrates that the experiments were across the high-loss transition zone between isothermal and adiabatic behaviour. The agreement in the position of the point of peak loss implies that CFX is predicting the position between isothermal and adiabatic well. However, the magnitude of the experimental values is consistently lower than the CFX predictions. Moreover, the experimental hysteresis loss figures are much lower than even the lowest low-loss figures measured by Kornhauser which suggests an experimental error.

A simple reality check that brings into question the experimental values is the observation that the high-speed end of some of the runs had near-zero or negative hysteresis loss. Zero hysteresis loss is, of course, a perfect spring which is a practical impossibility, and a negative hysteresis loss is power output which implies perpetual motion, which is also impossible. The hysteresis loss is not very sensitive to diaphragm diameter, as an error in swept volume is cancelled out by the adiabatic work done, a calculation which is also dependent on the volume

ratio. To achieve a negative hysteresis loss in the experiment requires a timing lag in the displacement measurements to make the phase angle between pressure and volume negative. The first error source considered was the sampling rate of the data. At 50 Hz, with the sampling frequency at 10 kHz, there are 200 points in a cycle. Hence one data point is worth 1.8° of phase angle. With small phase angles between pressure and displacement as found in gas springs, this is significant. However at 5 Hz there are 2000 points in the cycle and hence the same sample time error is 0.18°. Hence if sampling frequency is the cause then the error should be dependent on running speed. The discrepancy is consistent across the frequency range, which indicates that the sample number is not the cause. The CFD results were without the phase error as data for each step is reported without a physical measurement. The consistency of the offset with different cases points towards a systematic measurement error. Shifting the phase angle between the p and dV by 3° (in each cycle) pulls the experimental and CFD together for all cases. The source of this error is still unknown as the opportunity for repeating the experiments passed before the timing error was discovered. The possibility of timing errors occurring early in the data acquisition process further points to the usefulness of the polytropic index as a robust method of validation.

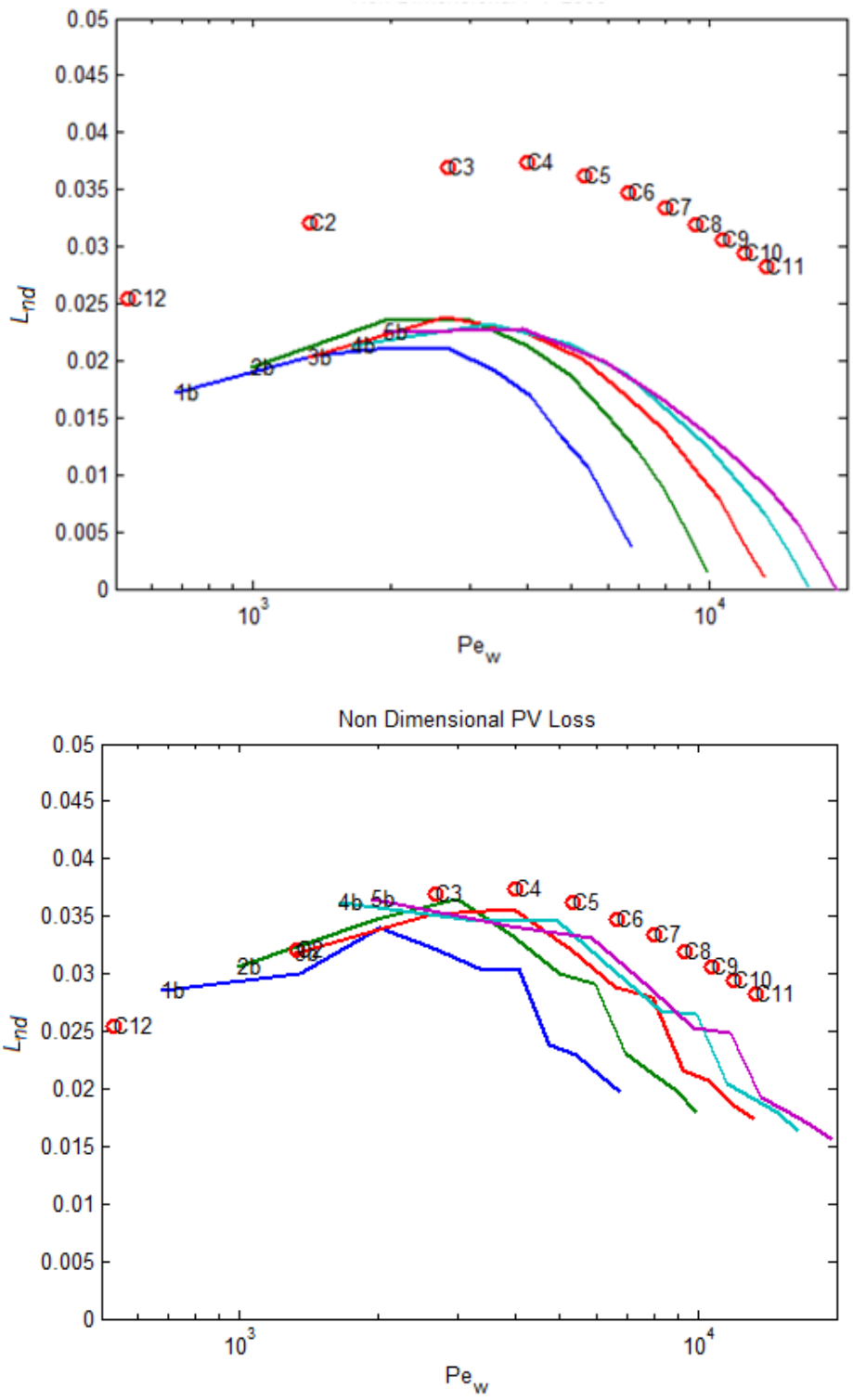

Figure 4-56: Comparison of the hysteresis loss for CFD Case 1 at 3 bar and experimental. Top, raw data. Bottom, with a 3° phase shift advancing the displacement measurement.

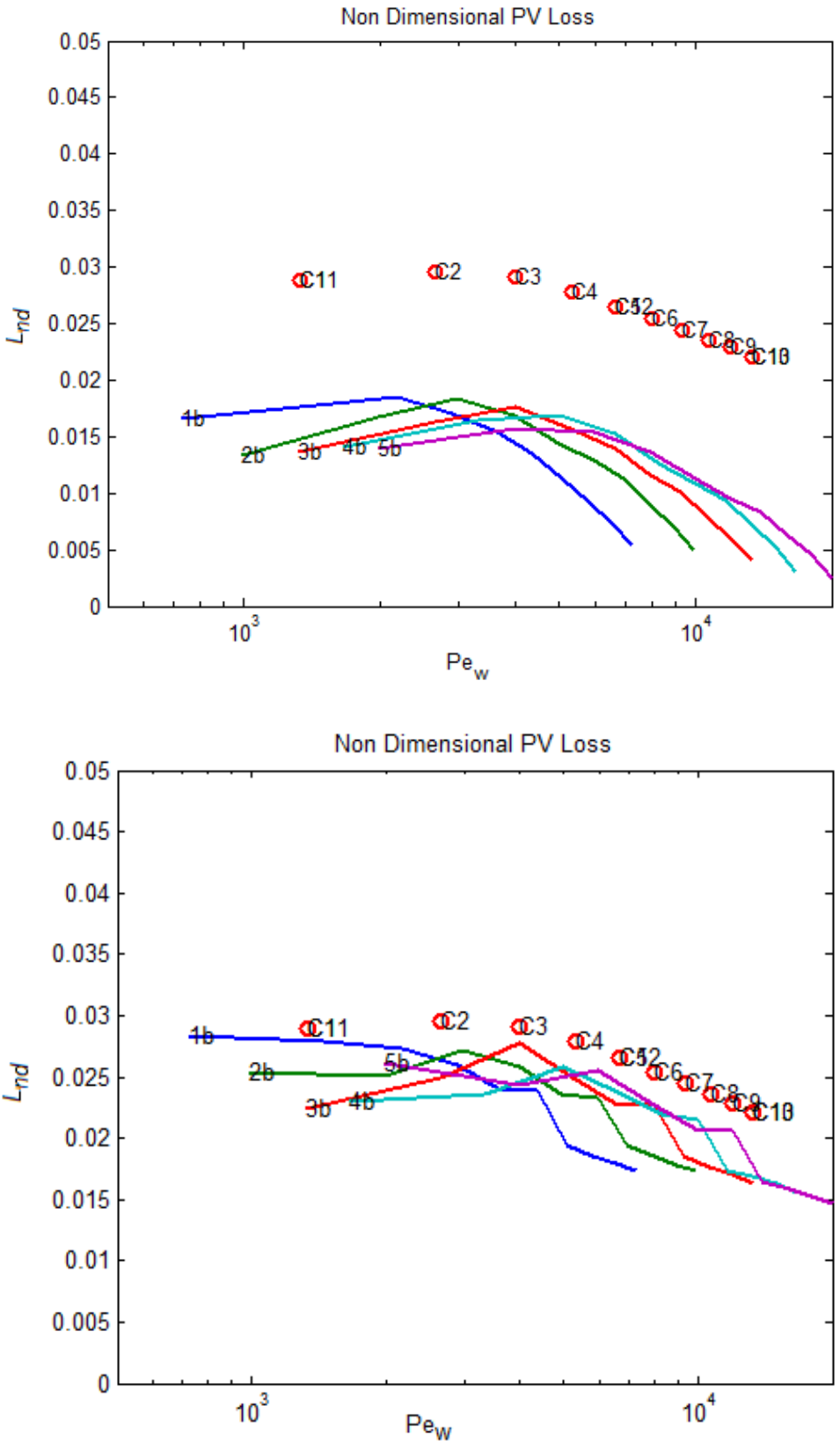

Figure 4-57: Comparison of the hysteresis loss for CFD Case 2 at 3 bar and experimental. Top, raw data. Bottom, with a 3° phase shift advancing the displacement measurement, *dx*.

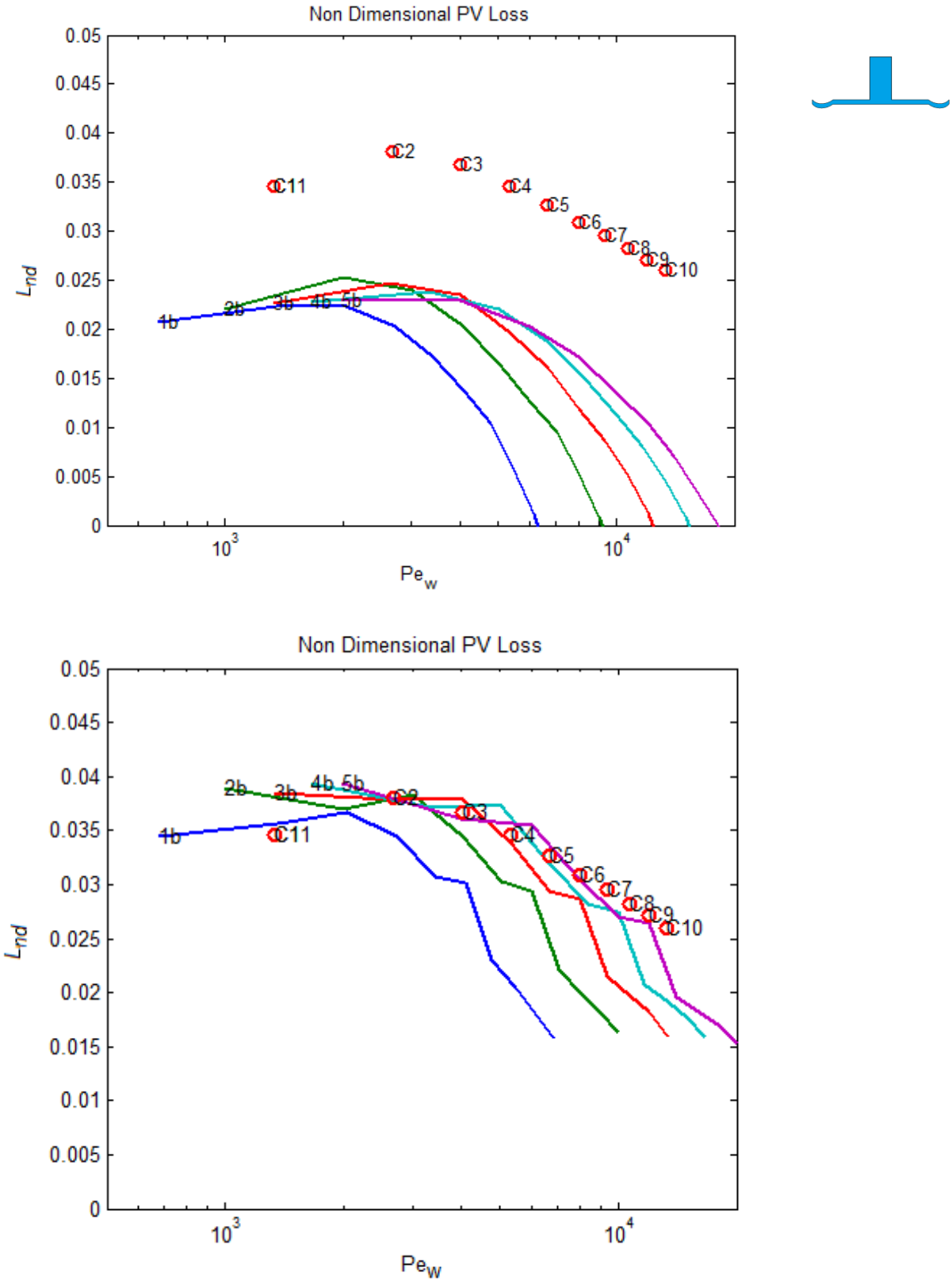

Figure 4-58: Comparison of the hysteresis loss for CFD Case 3 at 3 bar and experimental. Left is raw data, right is with a 3° phase shift advancing *dx*.

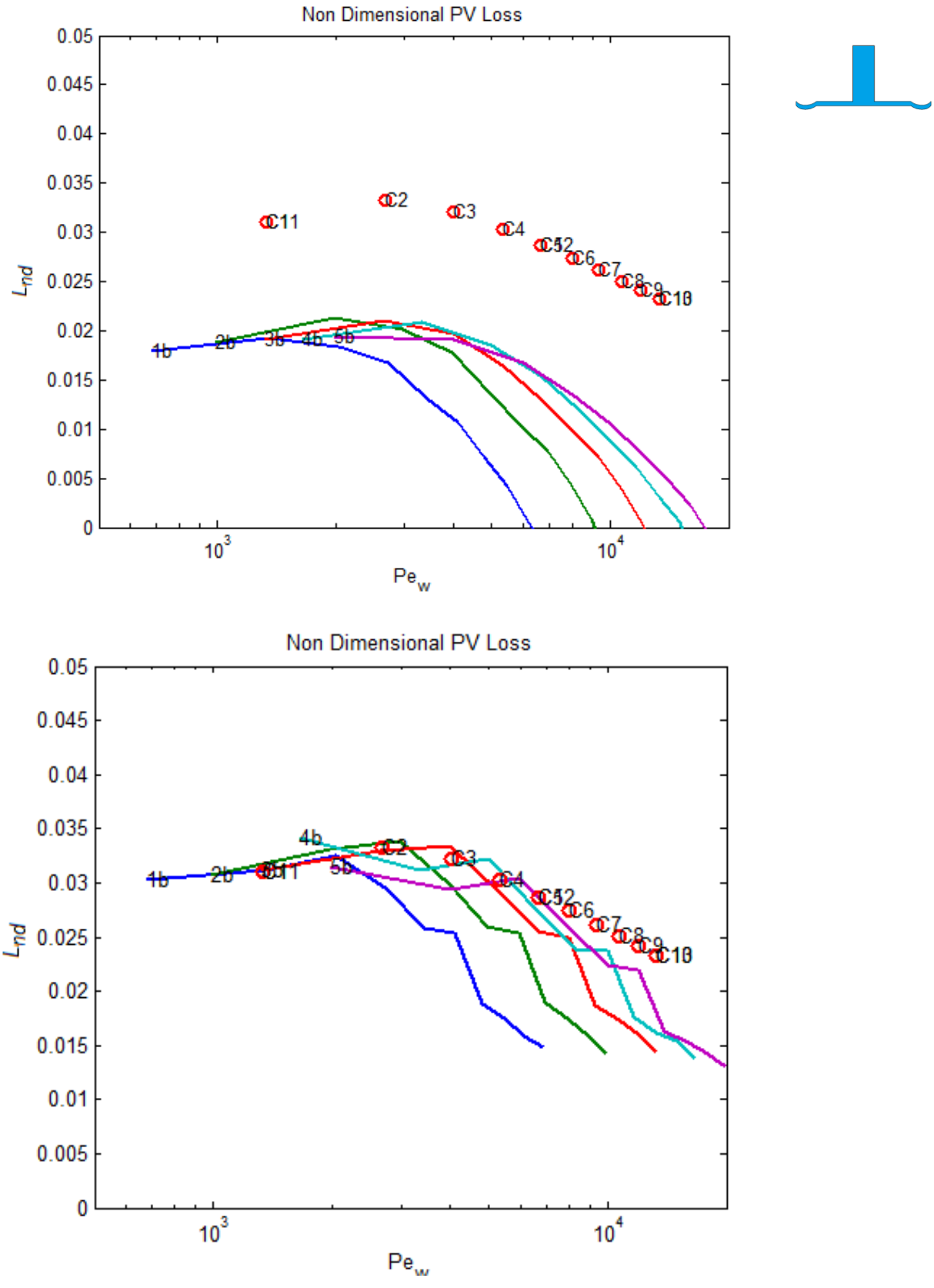

Figure 4-59: Comparison of the hysteresis loss for CFD Case 4 at 3 bar and experimental. Left is raw data, right is with a 3^0 phase shift advancing *dx*.

4.6.6 *MODELLING THE ISOTHERMAL AND ADIABATIC EXTREMES*

The CFX model allows exploration of the extreme ends of the adiabatic to isothermal spectrum, which was beyond the practical limitations of the experimental apparatus. Figure 4-60 shows Case 1 with additional CFX predictions of the polytropic index down to a Peclet number of 133 and up to 213,000. The shape of the curve, points C12, C14 and C16, starts to flatten out towards the isothermal end. The polytropic index for isothermal compression is still some way off, most likely because the cylindrical section, with a higher Peclet number than the radial sections, is still not close to being isothermal. For the high Peclet number points, C13, C15 and C17, the slope might be expected to asymptote towards γ for helium (1.67) but the polytropic index continues to rise with Pe_w number. Point C13 is close to 1.67, but point C15 exceeds 1.7 and C17 is 1.85. Further investigation of C15 and C17 shows that there were significant pressure gradients in the gas, required to move the gas back and forwards at high speed. Figure 4-61 shows the pressure gradients during the latter parts of compression and expansion in C17, where a pressure gradient of up to 0.6 bar is observed. This gradient is enough to produce the high polytropic index in the high speed runs. If the pressure monitor was positioned at the end of the flow path then a polytropic of 1.67 would be expected to be reported.

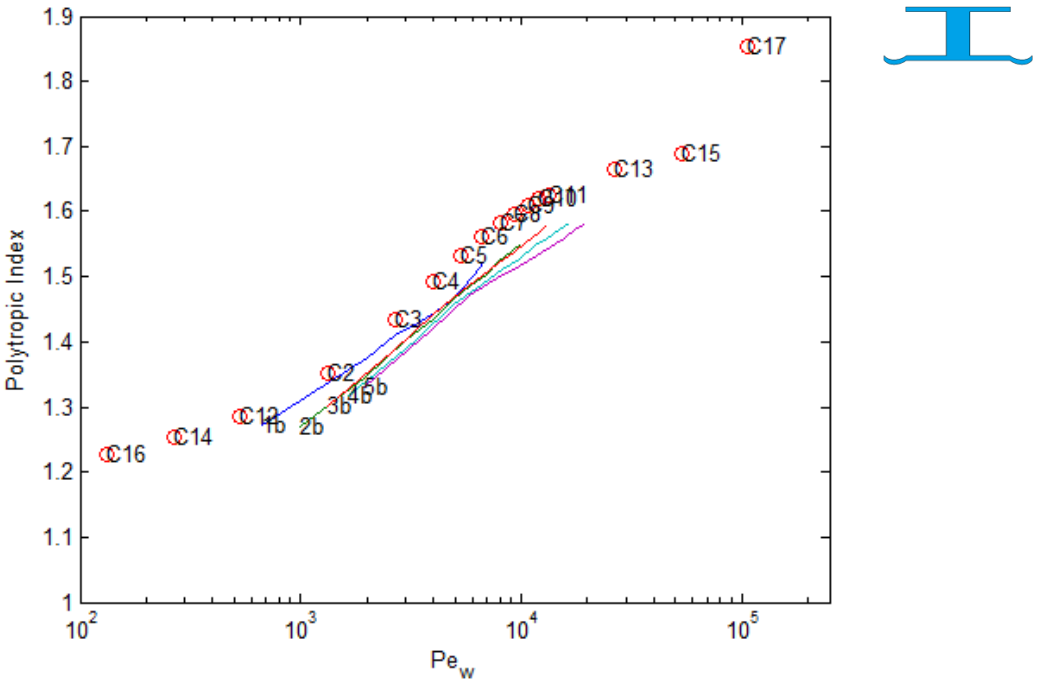

Figure 4-60: Polytropic index of Case 1 showing effects of extending the Pe_w range.

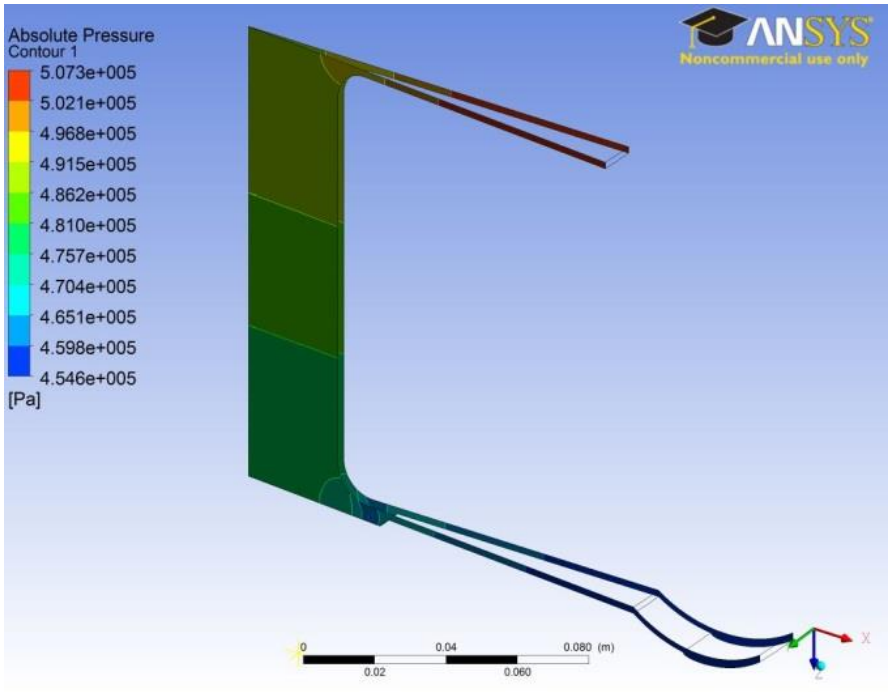

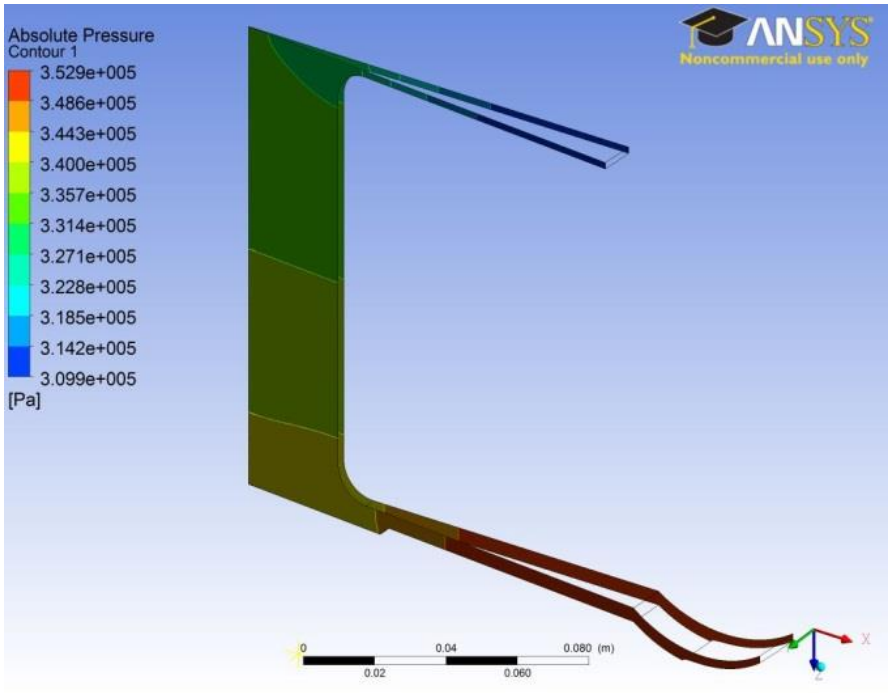

Figure 4-61: Case 1 pressure distribution for CFD run C17 showing significant gradients at very high Peclet numbers. The top image is for compressing near the top of the stroke, while the bottom image is for expansion near the bottom of the stroke.

4.6.7 *TEMPERATURE GRADIENTS IN THE GAS*

The CFX analysis can show temperature variations in the gas during the cycle which is very difficult to achieve experimentally due to the heat capacity of temperature sensors. Figure 4-62 shows the gas temperature during a cycle for the different parts of the gas space in Case 1 at low speed, and Figure 4-63 at high speed. The 'Cylinder', 'Pressure wave generator' and 'Radial' values are from the monitor points shown in Figure 4-46. The cylindrical section has a D_h of 64 mm which is an order of magnitude higher than the top radial section with a D_h of 4 mm, and the compression space varies from 2 mm to 9 mm. The low speed run (Figure 4-62) has a large temperature oscillation for the cylinder section; with a Pe_w of 2128 it is in the high entropy loss region. The radial sections have a Pe_w of 133, resulting in small temperature oscillations with a consequent trend towards isothermal. For the high speed run (Figure 4-63) the Pe_w in the radial section becomes 3328, indicating high-loss to near-adiabatic behaviour. The cylinder has a much higher Pe_w of 2.1 x 10^5, and is close to adiabatic. The oscillations in temperature during the high speed cycle can be attributed to flow effects, such as pressure and temperature dropping as the flow accelerates near the centre of the radial sections.

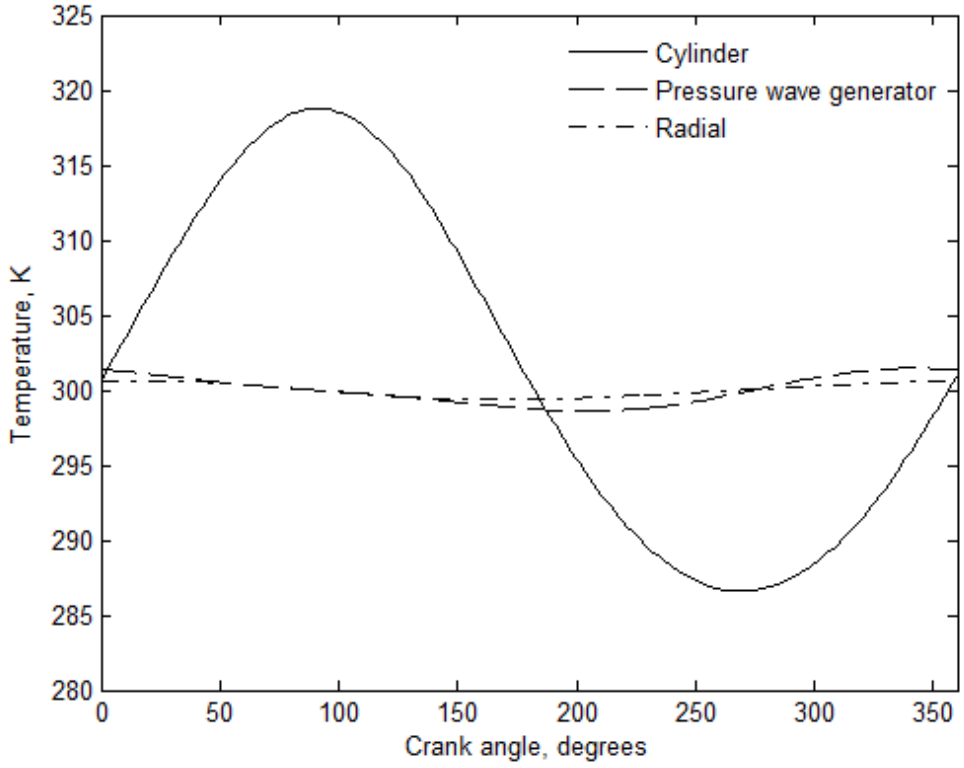

Figure 4-62: Temperature variation in a cycle for Case 1, 400 kPa, at 5 Hz.

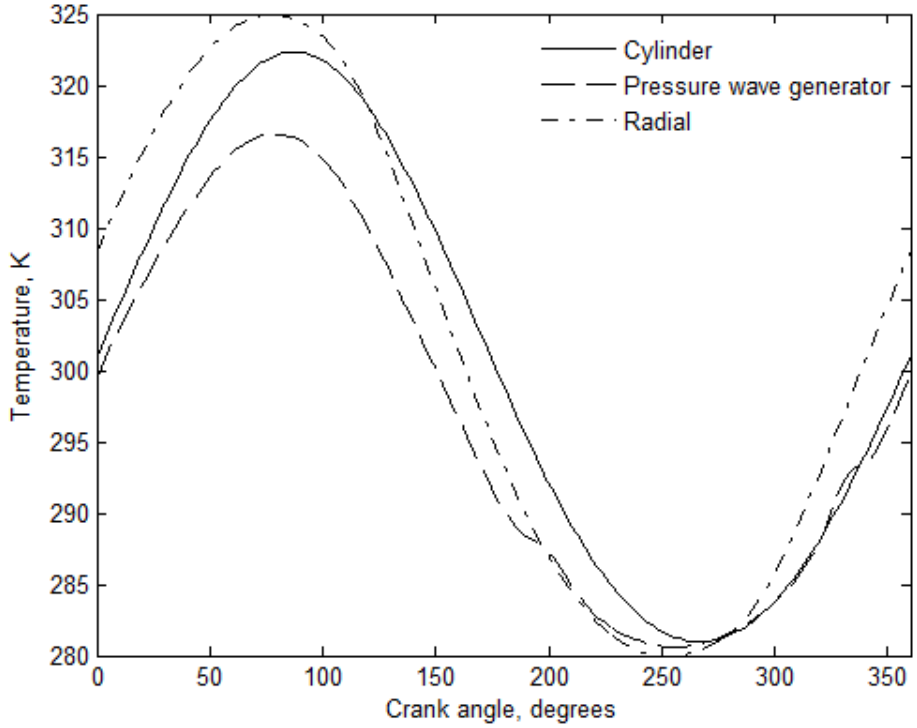

Figure 4-63: Temperature variation in a cycle for Case 1, 400 kPa, at 50 Hz.

4.6.8 *Discussion of CFD modelling of validation experiment*

The verification experiment has shown that ANSYS® CFX is able to model the gas spring dynamics in a diaphragm pressure wave generator with volume and geometry typical of the diaphragm Stirling cryocooler prototype. CFX was able to correctly predict the transition between isothermal and adiabatic compression via the value of the polytropic index. The Peclet number has again proved to be a reliable dimensionless number for normalising the conditions during oscillating compression of a gas.

CFX produced predictions of the hysteresis loss that were consistent, across a range of Peclet numbers, with the validations discussed earlier in this work. However, the experimental measurements produced hysteresis losses that were much smaller than previous validation exercises indicated were reasonable, even to the point where the loss was negative for high Peclet numbers. In particular, the negative hysteresis losses calculated from the experimental work were not physically possible as they would represent power output. The reason for the experimental results is most likely due to built-in filtering in the instrumentation producing a small timing error. A small timing error is significant as the phase angles between pressure and system volume, as required for accurate measurement of the hysteresis loss, were small in the

experiments. Even though the magnitudes of the CFX prediction and experiment were different, the shape of the curves and peak positions were similar, indicating a correlation between the two. Measurement of the polytropic index was a far more robust metric as it did not require such precise timing; it confirmed CFX's results.

CFX was used to explore situations that are difficult to measure with an experiment. Fixing the gas to isothermal behaviour produced a polytropic index of one, as expected. Similarly fixing the boundary walls to be adiabatic produced a polytropic index of the value of gamma for helium, 1.67, also as expected. Slowing the cycle speed to produce a low Peclet number reduced the polytropic index, moving towards one. The value of the slowest run was still above one as the cylindrical section, with a hydraulic diameter an order of magnitude greater than the radial section, had the consequence of increasing the polytropic index. Increasing the cycle speed raised the polytropic index past the value of γ, 1.67, because of pressure gradients required to drive the flow became significant.

The CFX case with adiabatic walls had a polytropic index of 1.67, showing that in the speed range of interest, pressure gradients within the compression volume were negligible and the assumption of uniform pressure throughout the volume is appropriate. For speeds significantly greater than 50 Hz, however, the pressure gradients required to drive the flow become significant and the assumption of uniform pressure is no longer valid.

The exact swept volume of the pressure wave generator is critical for experimental accuracy and it was not a trivial task to estimate or measure this critical parameter. Measurement of the swept volume of the system gave an effective diameter for the diaphragm for modelling, as if it were a piston-in-cylinder, of 310 +/- 5 mm.

The temperature plots from the CFD analysis showed that the cylinder and radial regions had distinctly different Peclet numbers and behaved quite differently at low speeds. The overall polytropic index for a geometry and set of running conditions is a combination of the individual sections. For Cases 1 and 2 the radial sections dominated; for Cases 3 and 4 the cylinders had more influence.

4.7 Conclusions

ANSYS® CFX has been able to model the compression in a cylinder experimentally measured by Kornhauser and Smith. The model was then modified, firstly into a flat geometry, then into a cylinder compressing into a radial section. Finally, CFX was validated with an experiment and model incorporating a DPWG compressing from a radial compression space, through a tube into a second radial section. CFX was able to predict the transition from isothermal to adiabatic compression for the experiment. The prediction demonstrates that CFX can model compression (and expansion) of a gas, heating during compression (and cooling during expansion), flow friction and heat transfer both within the gas and between the gas and the walls. The assumption of isothermal walls in the CFX model is valid for the conditions of interest.

The Peclet number proved to be a useful characteristic number to describe oscillating compression of the type found in gas springs and Stirling machines. Peclet numbers below 100 tend towards isothermal conditions, with low entropy losses and efficient compression. Peclet numbers above 20,000 tend towards adiabatic compression and efficient compression. In the intermediate range, between 100 and 20,000 hysteresis losses climb as significant heat transfer occurs with significant temperature gradients. The Peclet number versus polytropic index is a good measure of the isothermal-adiabatic range and is experimentally much easier to measure.

The CFX model has been sufficiently validated for continuing to the next stage of modelling the full cryocooler prototype.

5 CFD MODEL OF THE SECOND PROTOTYPE

5.1 Introduction

The CFD model developed and validated in Chapter 4 is geometrically close to the second prototype cryocooler developed and characterised in Chapter 3. This chapter details the development of a full CFD model of the second prototype using ANSYS® CFX. The CFD model is validated by comparing the CFD model predictions with the Sage model predictions and the prototype's characterisation experiments; which were performed with the cold end at 200 K due to instrumentation not fitting in the cryostat.

Once validated at 200 K, the CFD model is then used to model refrigeration at 77 K, as would be the case if the cryocooler was used to liquefy nitrogen. Again the CFD model is validated against experimental measurements and Sage models. The CFD model is then used to study the oscillating radial flow and heat transfer in the cryocooler, in particular in the cold region, with the aim of improving performance and utilising the radial flows present for enhanced heat exchange.

The full cryocooler adds complexity to the model developed in Chapter 4. In particular, the cryocooler has a regenerator, a porous matrix that consists of a stack of approximately 1000 stainless steel mesh discs. The purpose of the regenerator is to cool gas as it moves from the warm side of the cryocooler to the cold side, and to warm the gas on the return journey. The regenerator's function involves a considerable amount of heat transfer which comes at the cost of entropy generation, which reduces performance. A second complexity is the significant temperature difference between the ends of the cryocooler. Helium acts close to an ideal gas between 300 and 77 K (refer to Section 4.1.1), but is 3.9 times as dense at 77 K as at 300 K. The CFD model needs to account for the density change to accurately model cryocooler performance. Additionally, the material properties (in particular heat capacity and conductivity) of the regenerator matrix change significantly between 300 and 77 K.

The process for constructing the model described was an iterative one. Firstly, the geometry of the prototype was created in Solidworks® and imported into ANSYS® CFX. ANSYS® meshing was used to create a coarse mesh of elements. The model was then set up with the movement of the diaphragm and displacer specified and basic porous media properties applied. A number of runs were necessary to get the model running smoothly and to set up the monitor points which are locations in the model that act like transducers in an experiment. The mesh was then progressively refined to its final state and temperature-variable material properties applied for the regenerator.

In total 70 runs of the model were performed before the final 200 K and 77 K analyses were completed. Calculation times varied from a few minutes (when it crashed quickly) to three weeks per run, and were performed over a period of 2.5 years on a computer with an Intel i7 processor typically running 7 cores at 3 GHz clock speed, resulting in an estimated 140,000 CPU hours for calculation of the results contained herein.

5.2 Model Construction

5.2.1 GEOMETRY AND MONITORING

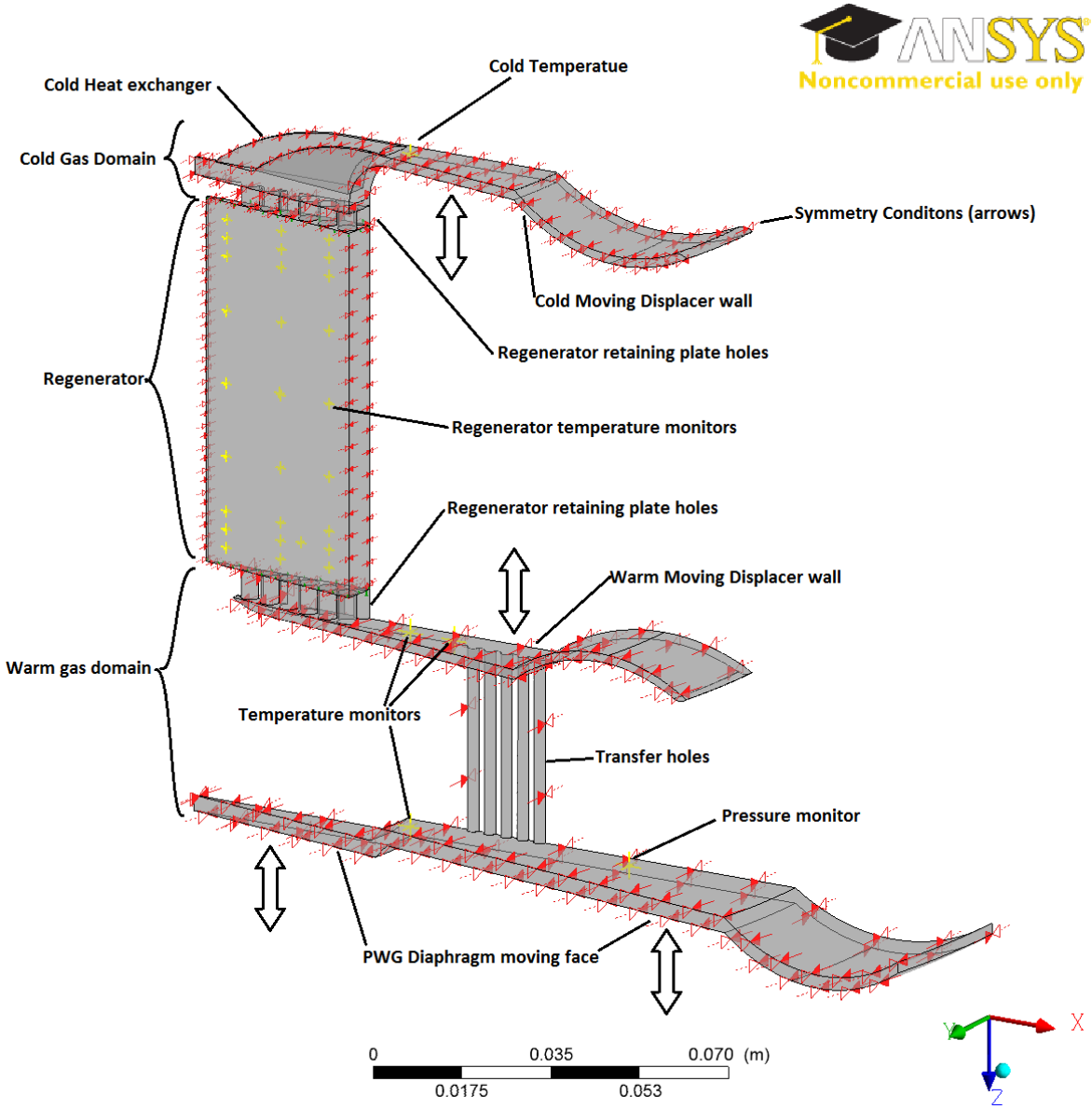

Figure 5-1: CFD model geometry and monitor points for second prototype.

The prototype gas space was defined as a repeating segment as shown in Figure 5-1. The periodicity of the cold heat exchanger slots and hole-pattern connecting the pressure wave generator gas space to the warm side of the displacer was 20°. The 20° segment included one pattern of the slots in the copper block in the cold plate. The segment was symmetrical, so was able to be cut down the centre line, resulting in a 10° segment for the model. The short transfer holes in the regenerator retaining plates were in a square pattern and so were arbitrarily cut to match the segment. The dashpot was not modelled as its purpose was to facilitate displacer movement and not take part in the gas cycle.

5.2.2 BOUNDARY AND INITIAL CONDITIONS

The gas space was modelled as a closed volume, so there were no inlet or outlet boundaries to model. Figure 5-2 shows the boundary conditions on the model.

The walls of the cold domain, with the exception of the displacer diaphragm's cold moving wall, were set to either 200 K to match the characterisation experiment detailed in Section 3.4.4, or 77 K to match the cool-down experiment in Section 3.4.6. The cold side of the displacer was included as a cold heat exchange wall as, in the experimental cool-down, its heat capacity represented a heat load for the cold gas.

The walls of the warm domain were set to 300 K with the exception of the displacer moving walls and the entire surface of the DPWG's diaphragm which were set to adiabatic. The reason for making the DPWG diaphragm surfaces adiabatic is because the piston side of the DPWG is not actively cooled, so will tend to float with the average temperature of the gas. Likewise the moving walls of the displacer diaphragms and the warm side of the displacer will float with the average gas temperature. The ideal boundary condition for these surfaces would be a floating isothermal surface, one that floats with the average gas temperature, which was not an available boundary condition. The adiabatic wall assumption, although not an exact representation of the experimental situation, is closer to the experiment than the isothermal surface condition and represents a conservative model as it reduces the model's heat exchange area.

Initial conditions were manually set at the start of each run of 50 cycles. The warm domain gas was set to 300 K and the cold gas set to either 200 K or 77K, depending on the situation to analyse. A linear temperature gradient between 300 K and 200 K (or 77 K) was imposed on the regenerator as an initial condition for the gas and matrix. After each run of 50 cycles, the average temperatures for the gas domains and the end conditions of the matrix were used for the initial conditions of the next run.

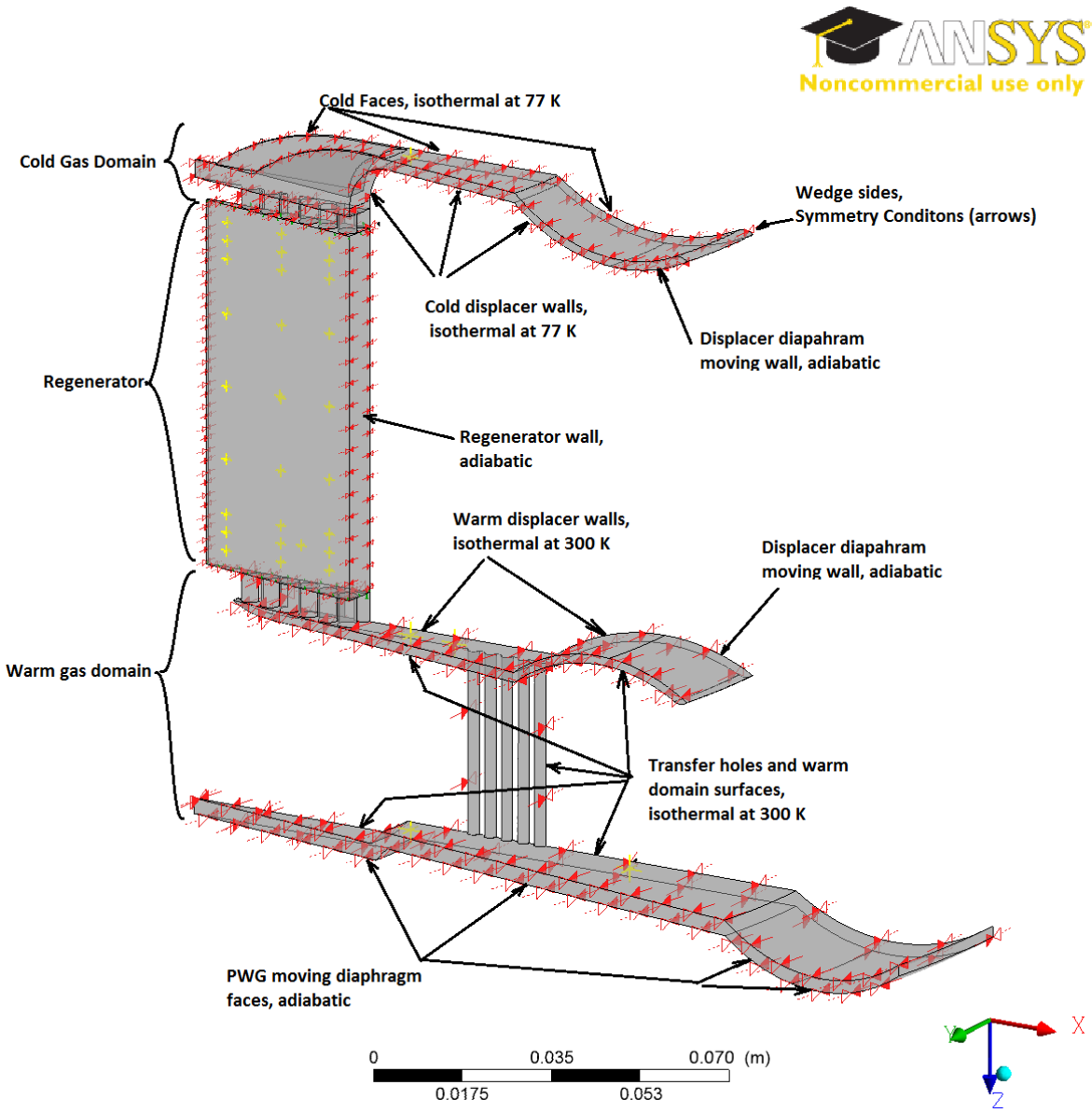

Figure 5-2: Boundary conditions for CFD model.

5.2.3 *Determination of porous media parameters for the regenerator*

The regenerator in the prototype consisted of a stack of stainless steel (SS) '400 mesh' discs with 30 micron wires and a volume porosity of 0.69. The porosity parameter is defined as the void volume divided by the total volume. ANSYS® CFX modelled the regenerator with the five parameters: porosity, interfacial area density, resistance loss coefficient, permeability, and heat transfer coefficient. The interfacial area density was directly calculable from the physical geometry of the SS mesh discs and was defined as the wire area divided by the total volume. The resistance loss coefficient, permeability and heat transfer coefficients did not have directly calculable values. Sage has a well verified internal model for mesh regenerators based on a combination of theory and empirical experience. Cha [70] measured flow and heat transfer

properties for various cryocooler regenerator materials. Cha's measurements determined porous media parameters for use in Fluent, a CFD code also owned by ANSYS®. Fluent's regenerator model has equivalent properties to CFX but with a different nomenclature.

A factorial experiment (a mathematical technique to determine the effects of variables on a system's response) was carried out to determine values of the resistance loss coefficient, permeability and heat transfer coefficient that would model a regenerator with the same behaviour as a 400 mesh regenerator in Sage.

A simple model was constructed in Sage. The model, Figure 5-3, consisted of a piston compressing in a cylinder, through a regenerator stack, and into a volume. The same situation was modelled in CFX (Figure 5-4). The 'Compr cylinder' walls were set to 300 K and the 'Volume' walls to 200 K to simulate the temperature gradient in a cryocooler. It was hypothesised that if CFX could predict the same compression and temperature ratios on either side of the regenerator as Sage, then its parameter values could be used for the cryocooler model. The resistance loss parameter is analogous to Darcy's flow loss coefficient and affects the pressure drop across the regenerator. The permeability and heat transfer coefficients determine the amount of heat transfer within the matrix, and would affect the overall pressure ratio and temperature oscillation magnitude. Starting values for the factorial experiment were derived from Cha's experimentally measured values. Figure 5-5 shows the best match achieved between Sage and CFX. The factorial experiment identified that the dominant parameter was the resistance loss coefficient, whereas the heat transfer coefficient could be varied between 100 and 1000 W m^{-2} K^{-1} (typical values for gas-to-wall heat transfer) with little effect. The final values chosen to achieve a good correlation were close to Cha's measurements. The values that produced the best correlation were: a porosity of 0.7; interfacial area density of $4x10^{8}$ m^{-1}; heat transfer coefficient of 100 W m^{-2} K^{-1}; permeability of $4x10^{-11}$ m^{2}; and a resistance loss coefficient of $7x10^{3}$ m^{-1}.

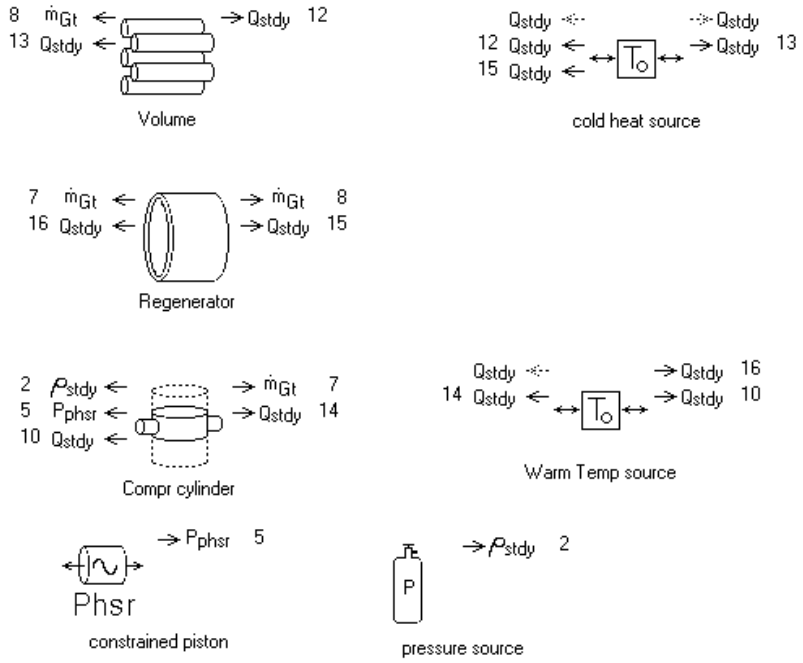

Figure 5-3: Sage model components for porous regenerator factorial experiment.

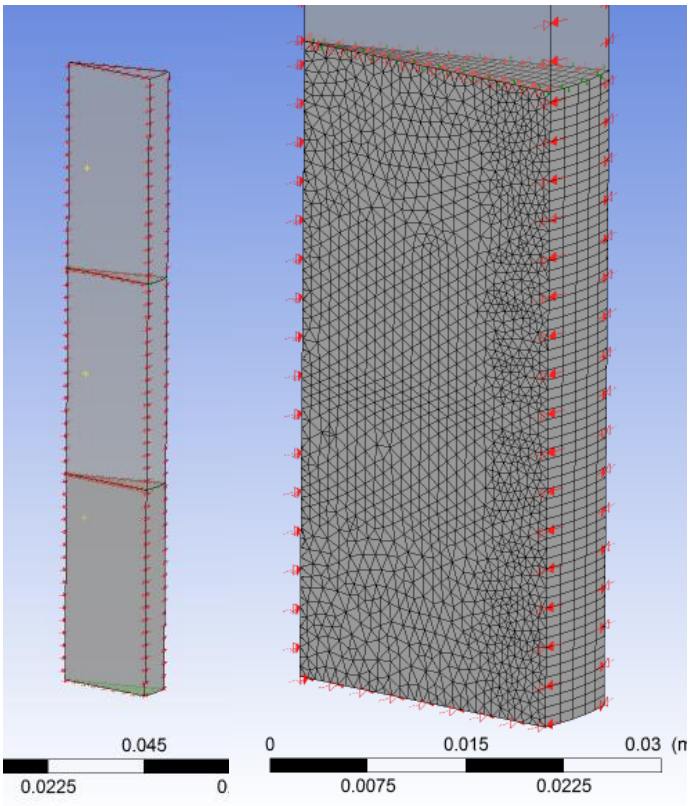

Figure 5-4: CFD model of porous regenerator experiment. The complete CFD model is shown on the left. The bottom section is the compression cylinder with its lower face moving; the centre section is the porous media section simulating the regenerator; and the top section is the volume. The CFD mesh of cylinder section is on the right; all three sections have identical meshes.

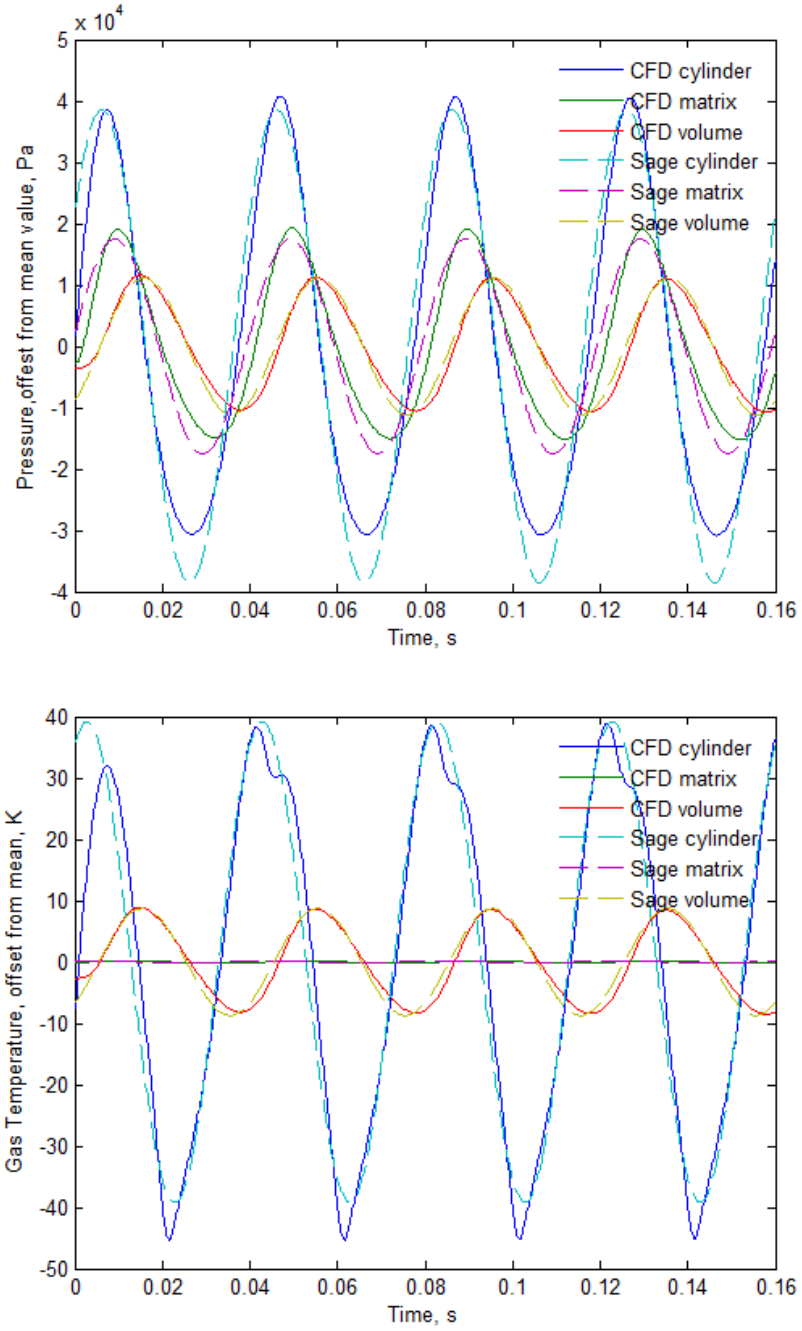

Figure 5-5: Match between CFD model and Sage showing the pressure wave (top) and gas temperatures (bottom) for the piston/cylinder space, matrix and the blind volume. The mean values have been subtracted showing the variation only.

The regenerator performance is affected by the stainless steel's material properties which change significantly over the temperature range from 300 K down to 77 K. The matrix material properties were set to match the heat capacity and thermal conductivity of the 316 stainless steel mesh. NIST's published values [76] for 316 stainless steel were in the form of a logarithmic series that was not compatible with ANSYS®' material property input format. Simplified polynomials, Figure 5-6, were fitted to NIST's curve to produce ANSYS® compatible coefficients that were sufficiently accurate between 60 K and 300 K, the temperature region of interest.

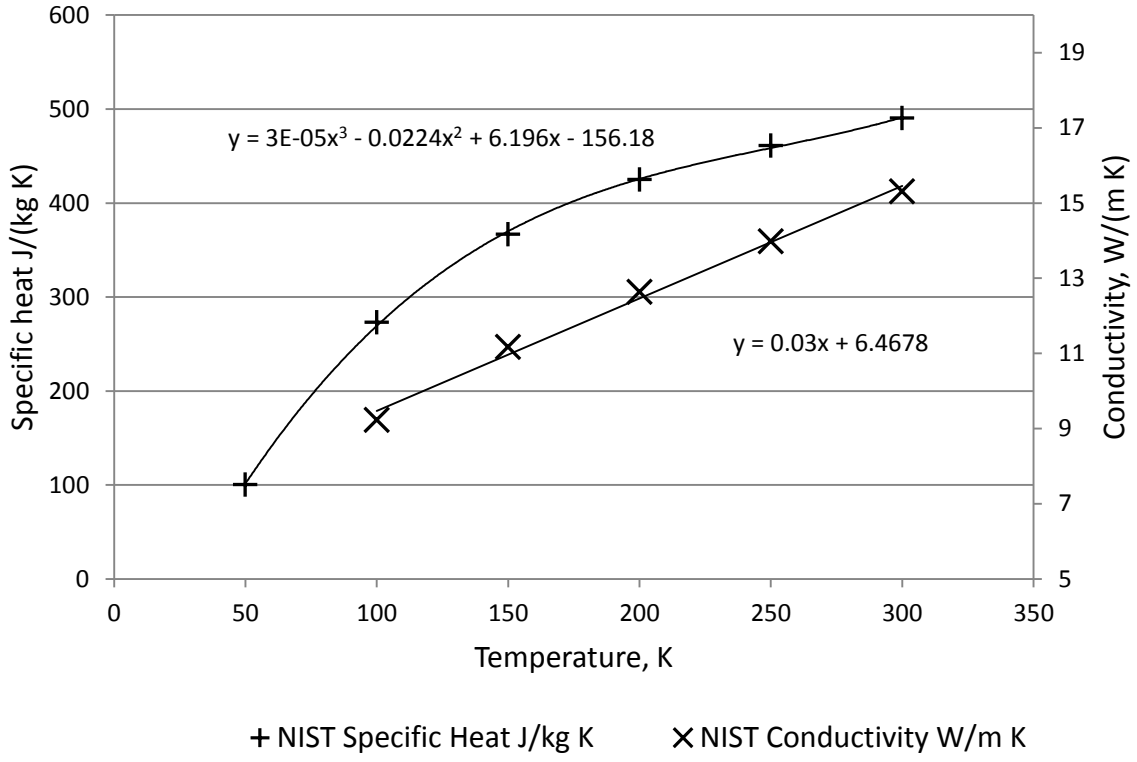

Figure 5-6: Polynomials used to approximate the NIST data for conductivity and specific heat of the 316 stainless steel regenerator mesh.

5.2.4 MESH

The model was broken up into three sections, called domains in ANSYS® terminology. The warm gas domain, shown in Figure 5-7 below, contained: the pressure wave generator, transfer holes, the warm side of the displacer and the holes through the regenerator retaining plate. It was meshed with tetrahedral elements which could achieve a good transition between the transfer holes and the diaphragm geometry.

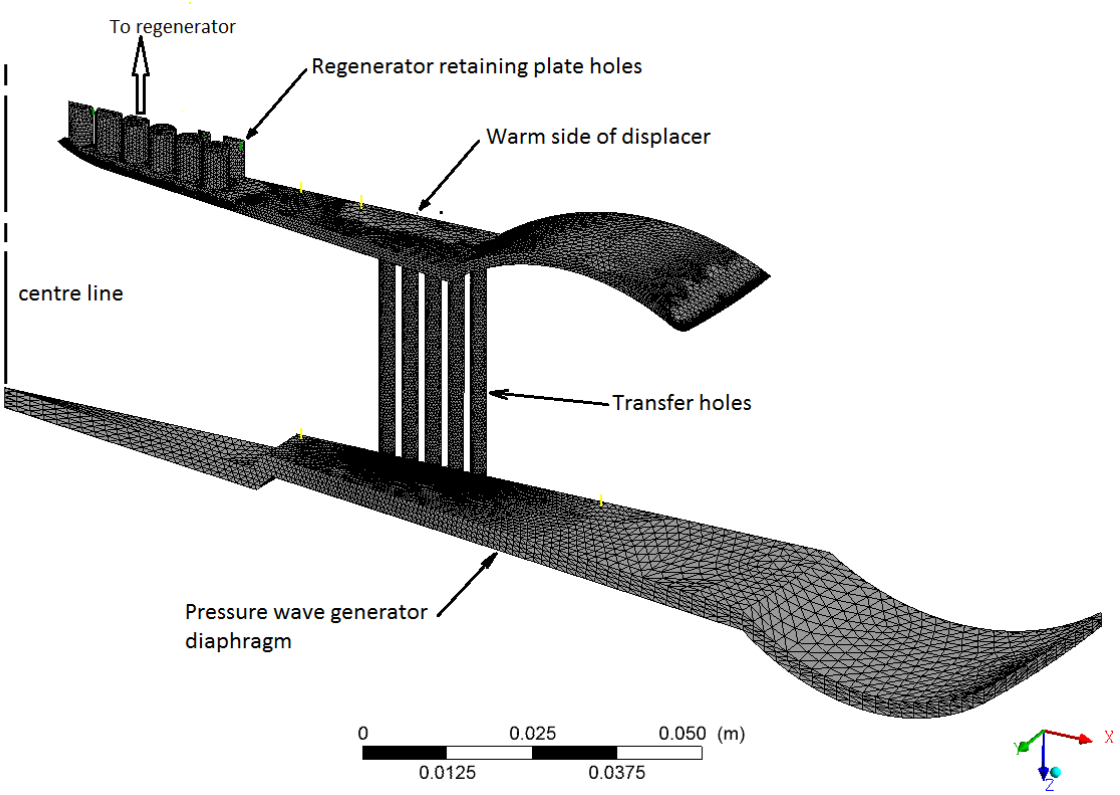

Figure 5-7: The warm gas domain's mesh with 725,426 elements.

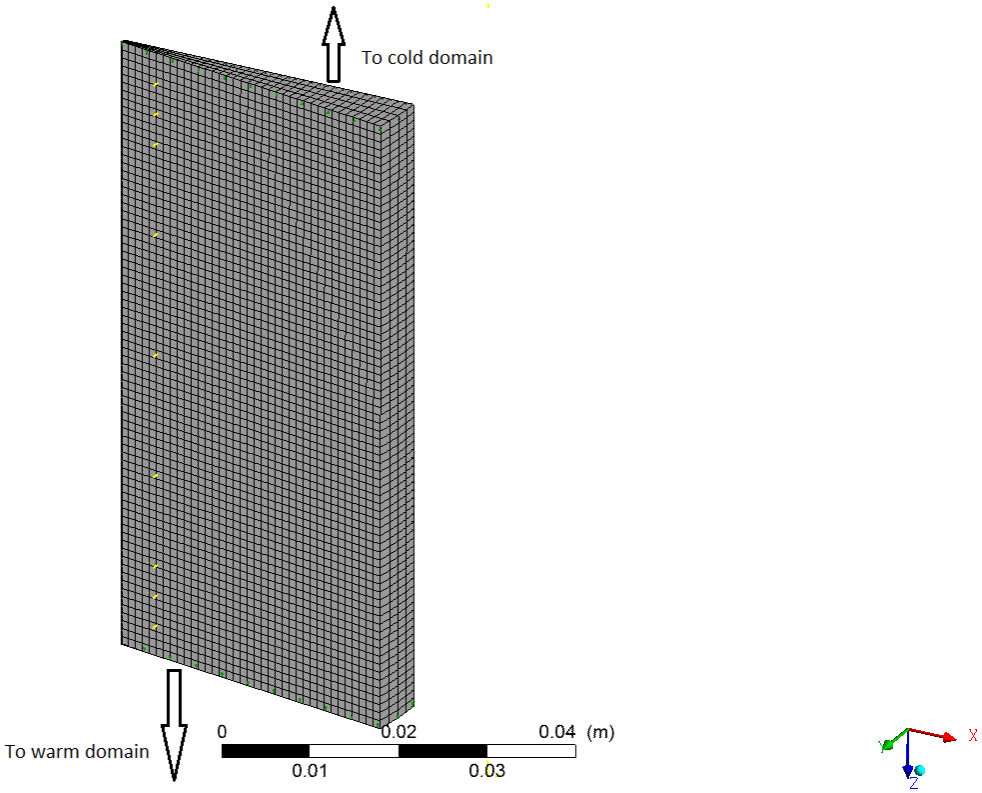

Figure 5-8: The regenerator domain's mesh with 11,100 elements.

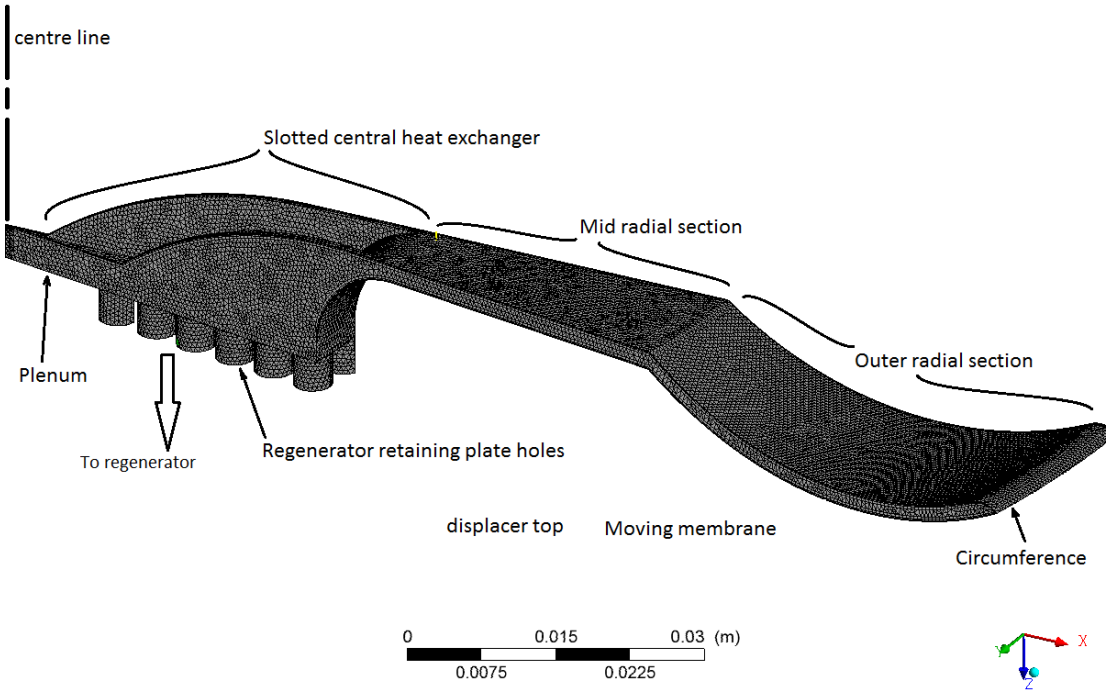

Figure 5-9: The cold gas domain's mesh with 226,817 elements.

The regenerator domain (Figure 5-8) contained only the porous regenerator and was meshed with hexahedral elements.

The cold gas domain (Figure 5-9) contained the regenerator retaining plate holes, a small plenum, the slotted central heat exchanger and the cold side of the displacer and diaphragm. The cold gas domain was again a complex geometry and modelled with tetrahedral elements. Prismatic inflation elements were used next to the heat exchanger walls to achieve thin elements normal to the walls and retain a lower density mesh tangent to the walls.

ANSYS® uses 'domain interface' definitions to connect the flow between domains. The domain interface function maps different meshes together to allow fluids to flow between the domains as if they were connected.

5.2.5 THERMAL DIFFUSION LENGTH AND MESHING

In the cryocooler the bulk gas temperature oscillates as a function of the pressure. The isothermal walls conduct heat away from, or, to the gas. There is a layer of gas next to the wall where the gas temperature is affected by the walls and the bulk gas temperature oscillations are damped. Right next to the wall the gas is always very close to the wall temperature. The distance away from the wall where the influence of the wall temperature becomes insignificant is called the thermal diffusion length in Sage terminology (Section 21.6.2 of Sage manual). Accurate CFD modelling of the heat transfer between the walls and the oscillating temperature of the gas requires more than one CFD element across the thermal diffusion length. If the element size is significantly larger than the thermal diffusion length, then the model will assume a temperature gradient and calculate conduction across the element according to the CFD element's internal equations. The heat transfer to the wall will be underestimated because the conduction from the bulk gas temperature to wall will be over too large a distance.

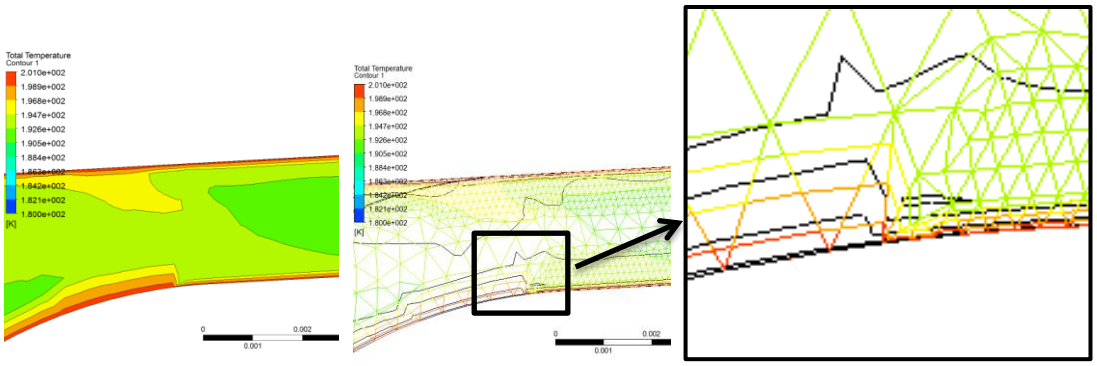

Figure 5-10: Effect of mesh density on thermal gradient next to the walls. Left is the gas temperature profile in the cold domain at the start of the radial section. Middle is the same plot with the element mesh visible and temperature contour lines. Right is an enlargement of the transition between large and small elements.

Figure 5-10 is an example mesh showing the effect of element size on the temperature gradient. On the left, the mesh (triangles) size is large up to the walls. The temperature gradient (coloured contour lines) is visible through the elements next to the wall. To the right the mesh is much finer, with the gradient still confined to the elements next to the walls. The finer mesh has a shorter distance between the bulk gas temperature and the wall, hence heat transfer via conduction will be higher.

5.2.5.1 Using the validation model to estimate the maximum element size

One way of estimating the thermal diffusion lenght is to consider the validation model in Section 4.6.4. The validation model required 9 elements across the 2.3 mm thickness of the flat regions to produce good results, which resulted in an element size of 0.25 mm. This suggests that the element size was similar to, or smaller than, the thermal diffusion length and hence at ambient conditions the element size should be 0.25 mm or smaller.

5.2.5.2 Using the viscous penetration depth to estimate the maximum element size

Another method of estimating the thermal diffusion length is to consider the viscous flow gradient next to the wall. Sage uses a parameter called the viscous penetration depth to determine the height of the viscous boundary layer in a flow. The viscous penetration depth is the distance from the wall beyond which the wall no longer slows the flow. The predominant heat transfer mechanism inside the viscous penetration depth is conduction. Outside the viscous penetration depth the flow will provide advection which will tend towards maintaining the fluid at the bulk temperature. The Prandtl number is the ratio between momentum transport and thermal transport in convective heat transfer. In the range of interest, for the working gas (helium) the Prandtl number is 0.7 which means that the velocity boundary layer is less than the thermal boundary layer thickness, so calculation of the viscous penetration depth will give an element size smaller than the thermal diffusion length, and hence be conservative with respect to the mesh. The Sage manual, Section 21.6.2, defines the viscous penetration depth δ as

$$\delta = \sqrt{\frac{2\mu}{\rho\omega}} \qquad 5\text{-}1$$

where μ is viscosity, ρ density and ω rotational velocity. For helium at 21 bar pressure and 200 K, the viscous penetration depth is 0.1 mm and at 77 K it reduces to 0.08 mm.

5.2.5.3 Using the Peclet number to estimate the maximum element size

A final method of estimating the thermal diffusion length is to consider the Peclet number. Kornhauser's experiment shows that for Peclet numbers around 2000, maximum entropy occurs, and the CFD model of this condition showed significant temperature gradients all the

way across the gas. The hydraulic diameter required to achieve a Pe_w of 2000 for the running conditions of interest, would then be a distance that is close to the thermal diffusion length.

Re-arranging the Peclet number definition gives

$$D_h = Pe_\omega \frac{\alpha_o}{\omega} \quad . \qquad 5\text{-}2$$

The conditions of the validation experiments, being 5 bar, 50 Hz and 300 K, give a D_h of 0.2 mm which is close to the element size needed in the validation model to produce good results. At 20 bar and 300 K; D_h is 0.57 mm, at 20 bar pressure and 200 K, D_h reduces to 0.29 mm; and at 77 K D_h further reduces to just 0.06 mm. Anecdotally, the 77 K value agrees with the author's experience with slotted heat exchangers in pulse tube cryocoolers [18]–[20], which needed slots of 0.15 mm width or thinner in the cold end heat exchanger for best effectiveness while the warm end slots could be wider at 0.3-0.5 mm. This analysis suggests that the warm end of the model would need elements smaller than 0.57 mm (4 elements across 2 mm thickness), and in the cold domain the elements would need to be smaller than 0.06 mm (33 elements across 2 mm thickness)

5.2.5.4 Inflation meshing

One key driver for meshing is to reduce the number of elements in the model to reduce the computational load. A mesh with 33 elements across the 2 mm thick cold domain section represents a prohibitively large model. ANSYS® meshing has a capability called inflation, where a number of thin layers can be added next to a boundary; leaving the rest of the domain with a coarser mesh. Use of inflation layers in the cold domain enabled the model to have several thin elements across the thermal boundary layer next to the wall, whilst retaining a relatively coarse mesh for the bulk gas in the centre of the domain to reduce computational time. Figure 5-11 shows the inflation layers in the cold domain. The thinnest element next to the wall was 0.033 mm thick which gives two elements over the estimated 0.06 to 0.08 mm thick thermal boundary layer.

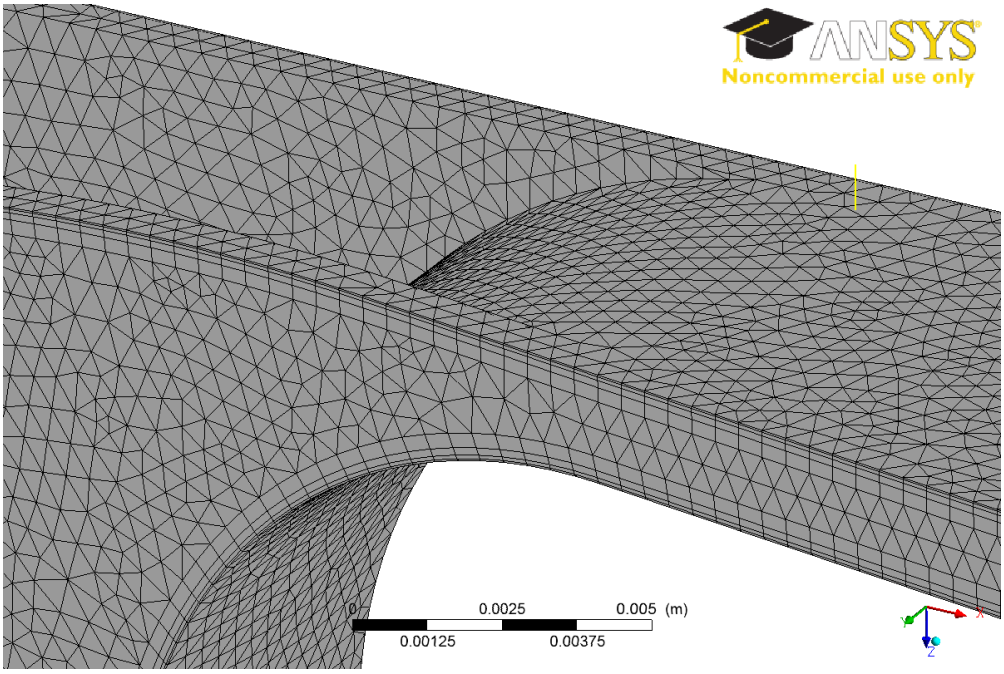

Figure 5-11: Close up of the cold gas domain mesh showing the inflation layers next to the walls.

5.2.5.5 Element sizes

Element sizes were checked on an early model, as detailed in Table 5-1. The element size was varied in the cold flat region from 1 mm thick elements to 0.14 mm thick elements, which still did not achieve mesh independence. The element size did not have a significant effect on the *pV* input power, pressure-volume phase angle, or diaphragm heat flow. However, an increase in the cold heat flow was observed with decreasing element size, consistent with the thermal boundary layer size. However, as the element size decreased, the computation time increased. Mesh independence was achieved with acceptable computational times by using inflation layers with a thickness of 0.03 mm next to the walls.

Table 5-1: Effect of the cold domain element size on the model outputs.

No. of elements between walls	2	6	8	14
Element size, mm	1.00	0.30	0.25	0.14
pV input, W	956	954	956	960
pV phase, ^{0}	13.06	13.37	13.37	13.50
Diaphragm heat flow, W	342	326	359	334
Cold heat flow at 200 K, W	204	248	256	283

5.2.6 *MOVEMENT*

The movement of the pressure wave generator diaphragm was achieved in the same manner as the validation experiment, which is a sinusoidal displacement imposed on the DPWG diaphragm faces according to Equation 5-3 with the mesh deforming accordingly.

The movement of the displacer was more complicated because it involved relative movements between three gas domains in CFX (the warm gas domain, the porous regenerator domain and the cold gas domain). As with the pressure wave generator diaphragm, the displacer movement was achieved by moving faces of the gas domains with the mesh deforming accordingly. The more complicated geometry meant that the mesh deformation could produce badly distorted elements that had the potential for negative volumes. A number of movement regimes were tried and the one that produced the most stable model was one that kept the regenerator domain stationary and moved the surfaces in the warm and cold domains that corresponded to the displacer. The moving surface meshes that changed shape were the diaphragms of the DPWG and displacer, and the regenerator retaining plate holes which changed in length. The displacer movement was small, less than 0.4 mm in amplitude, which represented a 10% length change in the 4 mm long retaining plate holes.

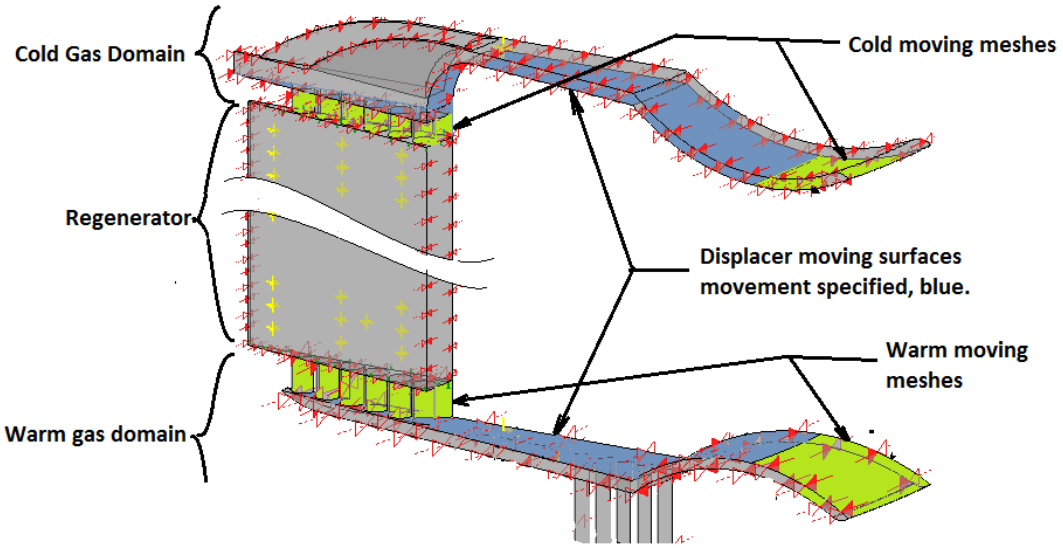

Figure 5-12: Moving surfaces for the displacer movement. The surfaces with specified movement are blue, the surfaces with unspecified movement are green and stationary surfaces are grey.

The displacer movement was defined as a sinusoid with a phase angle relative to the pressure wave generator position. The phase angle and displacement were defined as parameters that could be changed in the model. The model always started a run with the pressure wave generator and displacer at mid-position. A mid-position start point allows the displacer amplitude and phase to be entered as parameters into the pre-processor. The alternative of starting each run with the displacer in the correct position relative to the pressure wave generator, would require re-meshing and re-defining the boundary conditions for all surfaces of the model for every change in displacer amplitude or phase, a time consuming process. The problem of starting with the displacer in mid-position is that the second step in the transient run would then have a large movement of the displacer from mid-position to its phase-shifted position. Such a large movement within one step created shock waves and transients through the fluid as CFX modelled the rapidly changing geometry. Sometimes the transient was too severe for CFX to model and convergence failed; other times it modelled it but took a large number of cycles to dampen out the shock waves. The solution was to include a 'soft-start' function for the displacer amplitude with a time constant set so the displacer took approximately one cycle to reach full amplitude movement.

The pressure wave generator movement, x, was defined as

$$x = a\ sin(\omega t)\ , \tag{5-3}$$

and the displacer movement, x_2, as

$$x_2 = a_2 \left(1 - \frac{T_c}{t+T_c}\right) sin(\omega t + \emptyset_2) \tag{5-4}$$

where a is the amplitude of the DPWG movement, a_2 the amplitude of the displacer movement, ω the operating speed (radians per second), t the time, and $\emptyset_2$ the phase difference between the displacer movement and the DPWG movement.

The term $\left(1 - \frac{T_c}{t+T_c}\right)$ is the soft-start function, it equals zero at t=0, asymptoting to 1 over the first cycle when $T_c = 1/50\ f$. At 50 Hz T_c equals 1/2500.

5.2.7 TRANSIENT RUN MODE

The model was run in transient mode which time-steps through the analysis, each step depending on the conditions calculated in the previous step. The final analysis was performed with 180 steps per cycle, each step representing 2^0 of crank angle in the cycle. The number of steps per cycle was varied up to 400 steps per cycle with little change in results. A full set of post-processor results was saved for each fifth step. Monitor point results were saved for each step.

One effect of the transient analysis was that, although the model itself was not large (being in the order of 1 million elements) and used less than half the 16 GB memory available on the computer, the analysis took a long time as the process is sequential. At 3 minutes per step, a 9000 step run would take 19 days.

5.2.8 SIGNIFICANT POINTS IN THE CYCLE

The points in the gas cycle of most interest are when the velocity, pressure, temperature and heat transfer are near extreme values. For reference, position in the cycle will be referred to in degrees of rotation of the crankshaft driving the pressure wave generator's diaphragm with zero degrees being mid-stroke during compression. The four obvious points for investigation are: top dead centre (TDC); bottom dead centre (BDC); mid-stroke compressing (MSC); and mid-stroke expanding (MSE).

TDC is close to the point of maximum pressure and temperature, likewise BDC will be close to minimum pressure and temperature. MSC and MSE will have high velocities and be close to average temperatures and pressures.

There are four other points in the cycle to consider; these are on either side of TDC and BDC where temperatures and pressures are close to extremes and gas velocities are significant (at TDC and BDC velocities are low). The side points are high stroke compressing (HSC) and high stroke expanding (HSE) and their counterparts: low stroke expanding (LSE) and low stroke compressing (LSC).

Appendix A details results for the 77 K model at each significant point: MSC, HSC, TDC, HSE, MSE, LSE, BDC and LSC.

5.3 Results of the model at 200 K cold temperature and comparison with experiment

The model was run with the surfaces of the cold domain set to 200 K and the warm domain to 300 K, to simulate the characterisation experiment on the second prototype as described in Section 3.4.4. A linear temperature gradient was imposed on the regenerator and its gas from 300 K to 200 K. The model was run for sets of 50 cycles, the equivalent of one second of actual run time on the prototype machine. The temperatures of the ends of the matrix moved much more rapidly than the centre of the matrix. Instead of running the model for a very long time - possibly months - each run of 50 cycles was started again with the end temperatures of the regenerator from the previous run and a linear temperature gradient re-imposed on the regenerator. Hence after several runs of 50 cycles, the regenerator stabilised and the change of temperature at the regenerator ends reduced.

Convergence for each step was set to 10^{-4} for momentum, mass and energy. The models achieved steady cyclic behaviour (second timescale discussed in Section 4.1) in the first few cycles, steady-state in the long timescale firstly involved setting up temperature gradients in the gas (which took approximately 10 cycles) and then very slowly moved the regenerator matrix temperature. It was assumed that the model was close enough to steady-state when the temperatures of the regenerator ends moved less than 5 degrees during 50 cycles. It is likely that the regenerator gradient in the prototype is not linear. The linear assumption was made for expedience as the aim of this study is the heat exchange in the radial flow fields and not regenerator performance. Regenerators are worthy of, and have been, a study topic of their own [81]–[84]. The linear temperature gradient is justified if the model gets the inlet and outlet temperatures close to steady-state and if the model is shifting slowly towards the final internal regenerator gradient. In this case the net cyclic heat transfer to or from the regenerator should be less than or in the order of the cooling effect, and much less than the work input to the cycle. Additionally, the change in internal energy of the gas from one cycle to the next should be very small compared with the energy flows in or out of the gas domains.

5.3.1 EXAMINATION OF THE NUMERICAL OUTPUTS

Figure 5-13 shows the monitor point results of the final 200 K run which comprised 50 cycles. Figure 5-14 shows the same plots for the final four cycles of the run for more clarity. The descriptions which now follow address the sub-figures in the order left-to-right, top-to-bottom within each of Figures 5-13 and 5-14.

The pressure trace shows that steady state for the pressure wave was reached in approximately 5 cycles. The diaphragm and warm side of the displacer pressures were very close, and the cold

side of the displacer's pressure wave was attenuated, as expected, from the flow loss in the regenerator. A phase shift of the pressure wave is evident between the warm and cold domains. The phase shift is a result of the flow taking time to get through the regenerator; temperature gradients making the cold domain behave as if it were a larger volume, and the displacer movement shifting gas between warm and cold out of phase with the main pressure wave.

The gas temperature plot shows the highest temperatures are *T warm1* and *T warm2*, which are on the warm side of the displacer, *T warm1* being closer to the regenerator. The temperature oscillation on the warm side of the displacer deviates considerably from sinusoidal as it involves warmed gas exiting the regenerator on the expansion stroke, when expansion would otherwise attempt to reduce the gas temperature. The diaphragm gas temperature, *T dia*, is lower on average than *T warm1* and oscillates in a sinusoidal manner with a large magnitude, consistent with adiabatic compression and expansion. The mid-regenerator temperature, *T regen*, reports very low temperature oscillations, demonstrating the damping effect of the regenerator mesh's heat capacity. The cold side of the displacer temperature, *T cold*, oscillations are smoothly sinusoidal in shape as conditions are close to compressing a gas spring.

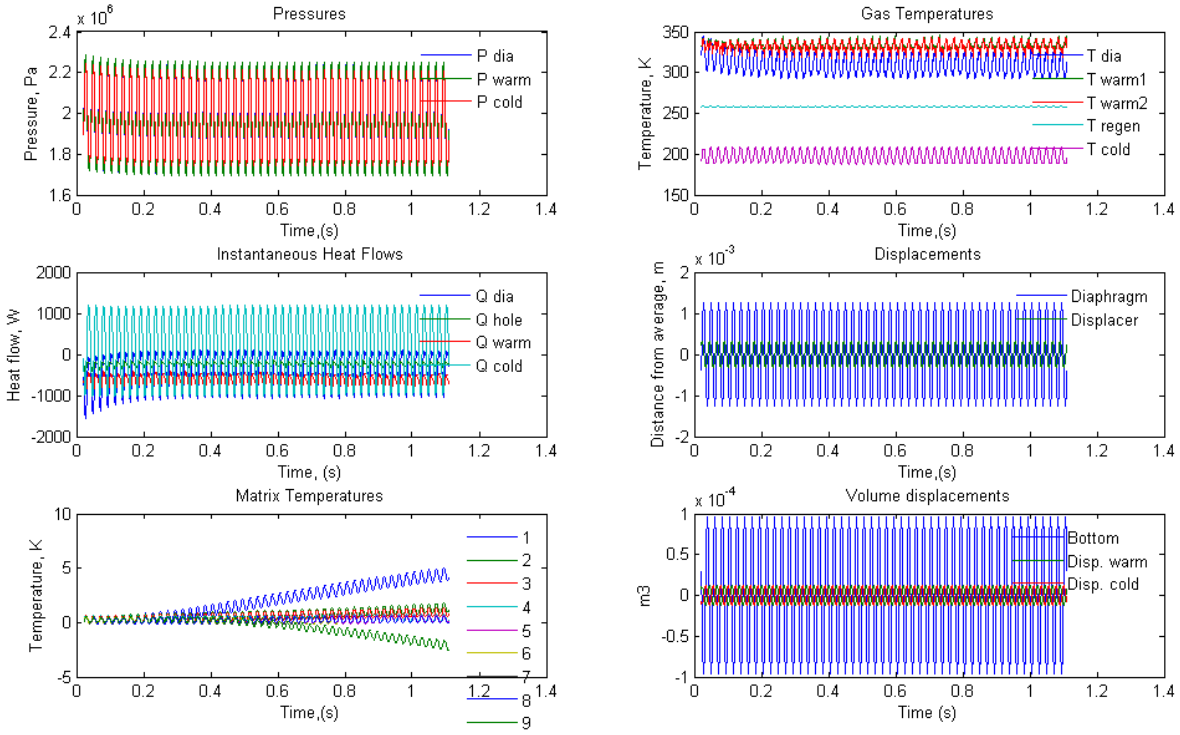

Figure 5-13: Summary of the CFD run with the cold end at 200 K.

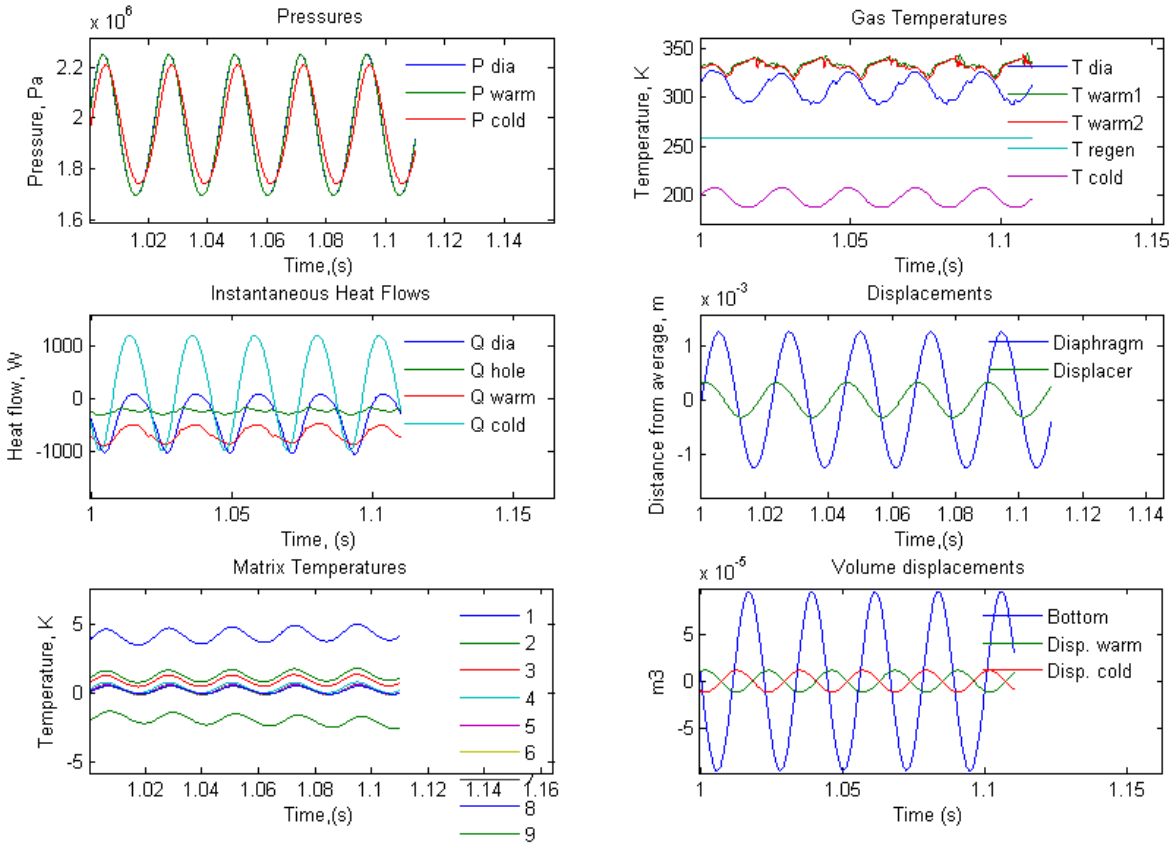

Figure 5-14: The last four cycles of the CFD run with the cold end at 200 K

The heat flow plots, shown mid-left in Figure 5-14, show heat flows oscillating in phase with the temperature oscillations. *Q dia* is the heat flow from the walls of the pressure wave generator to the gas; it is mostly negative, indicating that the gas temperature is usually above the wall temperature and that the energy flow is from the gas to the walls. *Q hole* is the heat flow from the transfer tube walls to the gas and is constantly negative which indicates heat always flows from the gas to walls. *Q warm* is the heat flow from the walls to the gas on the warm side of the displacer and is also constantly negative. The cold domain heat flow, *Q cold*, has a large amplitude oscillation, going positive and negative. From the heat flow plot it is difficult to determine whether the net heat flow is negative or positive, because the fluctuations are much larger than the cycle-average values. Integration of *Q cold* shows that the net heat flow is into the cold domain and is the useful cooling power of the cryocooler.

The displacement plot depicts the movement of the diaphragm and displacer and shows the displacer up (low volume in expansion space) during compression and down (large volume in expansion space) during expansion as is normal for a Stirling cycle refrigerator.

The matrix temperature plot in Figure 5-13 shows that the matrix is still changing in temperature and has not reached steady state. The warm end has warmed by close to 5 K over 50 cycles and the cold end has cooled by 2 K. However, the difference in temperature between the last two cycles is small, so a pseudo steady state condition is assumed.

The volume plot shows the volume displacements for the pressure wave generator diaphragm, the warm side of the displacer, and the cold side of the displacer. It shows the displacer phase and that the pressure rises when the pressure wave generator volume decreases. The amplitude of the DPWG volume change is 10^{-4} m^3 which indicates a swept volume of 200 ml, matching the specification for the DPWG and indicating that CFX is correctly modelling the movement of the DPWG diaphragm. The displacer volume amplitude is 1.16 x 10^{-5} m^3, indicating a swept volume of 23.2 ml, also as expected; Sage predicted 31 ml with 0.427 mm amplitude, scaling to 0.32 (experimental amplitude) gives 23.2 ml indicating that the displacer boundary condition has been correctly imposed.

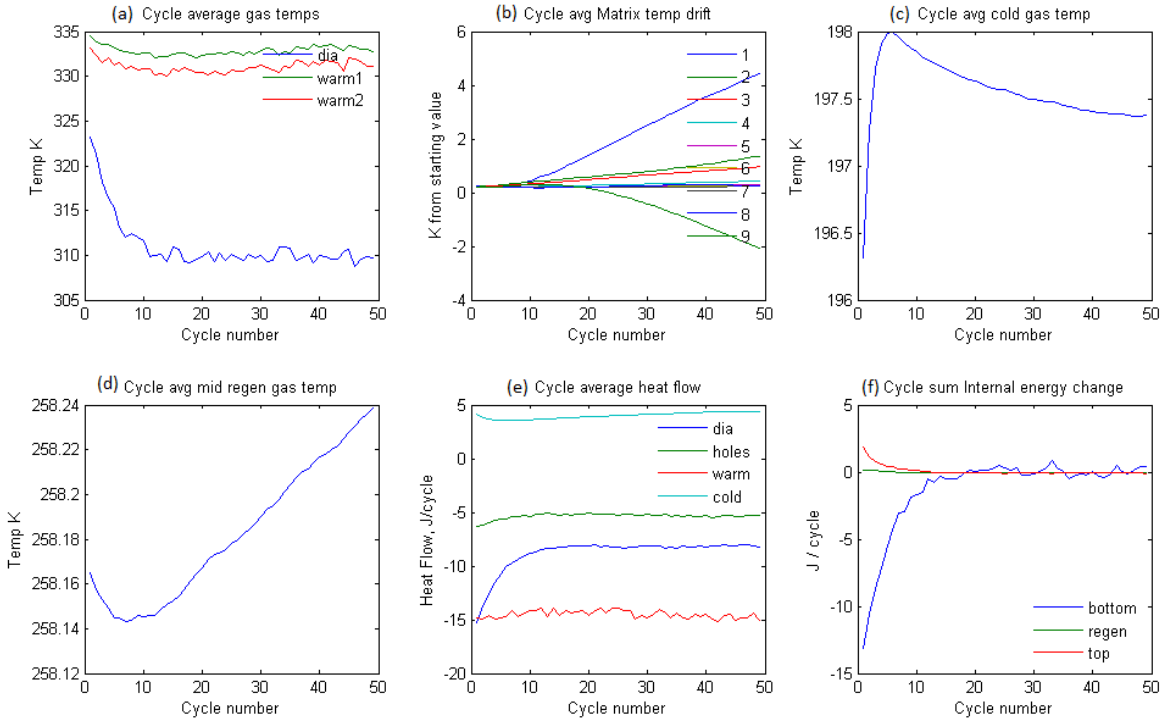

Figure 5-15: Cycle averages for the CFX model with the cold domain walls at 200 K. From top left: (a) warm domain gas temperatures; (b) regenerator matrix temperatures; (c) cold gas temperature; (d) gas temperature in the middle of the regenerator; (e) wall-to-gas heat flows (per cycle); (f) change in gas internal energy over each cycle.

Figure 5-15 shows cycle averaged values over the 200 K run.

Figure 5-15 (a) describes the cycle average warm domain gas temperatures. The warm domain started with a uniform temperature of 330 K. It took 10 cycles to establish an average of 305 K in the DPWG's space, *dia*, and 325 K on the warm side of the displacer, where monitors *warm1* and *warm2* are placed. *Warm1* is at a slightly higher temperature than *warm2* as it is positioned closer to the regenerator. The temperatures *warm1* and *warm2* gradually climb, following the slow rise of the temperature of the warm end of the regenerator.

Figure 5-15 (b) shows the temperature drift in the regenerator. Lines 1 to 9 correspond to monitors placed in the regenerator from warm end (1) to cold end (9). Each line is normalised from the starting temperature for the analysis run. Of interest is Line 9 which rises initially then after about 10 cycles decreases steadily in temperature. Line 1 rises 4.4 K over the 50 cycles, line 9 drops by 2.1 K. Both temperature changes are below 5 K over 50 cycles, the threshold chosen for steady state.

Figure 5-15 (c) describes the cycle-average temperature of the cold domain gas as measured at the start of the radial section. The run takes approximately 10 cycles to stabilise as shown by the transient in the temperature graphs. The temperature transients are reflected in the heat flow and internal energy change graphs. The start-up transient is due to the warm and cold domains having uniform temperatures imposed as initial conditions. It takes a number of cycles to establish the temperature gradients within the domains.

Figure 5-15 (d) describes the gas temperature at the middle of the regenerator. The temperature of the middle of the regenerator moves only 0.1 K over the 50 cycles. The temperature dips in the first 10 cycles of the run, reflecting the other plots that show that it takes approximately 10 cycles for the run to settle down after the start-up transient.

Figure 5-15 (e) describes wall-to-gas heat flows. The majority of the heat rejection (negative value means heat out of the gas) occurs on the warm side of the displacer, much more than the DPWG diaphragm, or the transfer holes. The cold domain has a positive heat flow which implies heat flowing into the gas. Again, it took 10 cycles for the run to settle to steady values of heat flow. It is noteworthy that the cycle-average cold domain gas heat flow is small in relation to the warm cycle-average heat flows whereas Figure 5-14 shows the oscillating instantaneous wall-to-gas heat transfer power of the cold space gas was much higher than the warm sections.

Figure 5-15 (f) shows the gas internal energy changes per cycle. The start-up transient for the analysis takes about 10 cycles. The pressure wave generator's diaphragm space takes the longest time to settle down. This is consistent with the gas temperature plot showing that the

initial temperature condition of the diaphragm space was significantly different from its quasi-steady-state temperature.

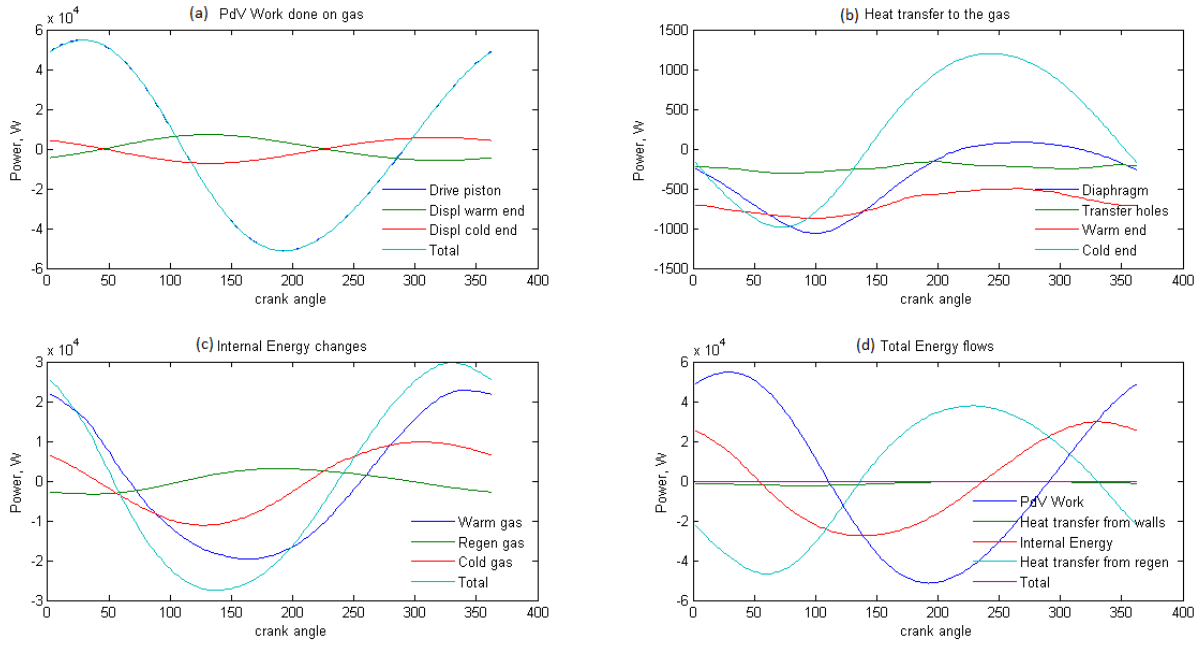

Figure 5-16: Energy flows during the last cycle: (a) work done on gas; (b) wall to gas heat transfer; (c) gas internal energy change; (d) combined energy flows.

Figure 5-16 shows energy flows in the last cycle of the run.

Figure 5-16 (a) shows the work done on the gas by the DPWG diaphragm and the two ends of the displacer. The work done by the two ends of the displacer very closely cancel each other, leaving the total work done on the gas effectively equalling the work done by the pressure wave generator diaphragm.

Figure 5-16 (b) describes the heat transfers from the walls to the gas. The cold region has a predominantly positive value that represents heat into the gas, or cooling of the walls. The warm end of the machine has a negative value which represents heat leaving the gas. The internal energy plot shows the variation in the gas internal energy as compression does work on the gas, increasing its energy.

Figure 5-16 (c) shows the change in the internal energy of the working gas in the three domains. The changes of internal energy can be achieved via convection (with the walls), advection (via mass flow between domains) or work done on the gas. The regenerator gas' internal energy is out of phase with the rest of the machine as it is dominated by the regenerator temperature and the high mass flows in and out. Hence the regenerator gains and loses energy with gas movement, as opposed to the compression driven oscillations in the rest of the machine. The

regenerator gas gains energy during the expansion stroke when flow is from cold to warm, and loses it on its return. The other domains gain internal energy primarily due to compression (work done on the gas).

Figure 5-16 (e) is a summation of the energy flows. The energy balance is shown by a zero total energy flow at any one time. It should be noted that the magnitudes of the energy changes associated with the work, matrix heat transfer and the internal energy are 50 to 100 times larger than the heat transfers with the walls. This demonstrates one of the challenges for a cryocooler, being that the useful function of the machine (the net cold end wall heat transfer), is much smaller than the instantaneous power that flows around in the machine. Cooling is achieved by a small difference between large numbers.

Table 5-2: Numerical summary of the energy flows in the last cycle of the 200 K run.

Parameter	**DPWG Diaphragm**	**Holes**	**Warm side of displacer**	**Regenerator**	**Cold side of displacer**	**Totals**
pV Power input, W	981		401		-389	993
Wall heat flow, W	-371	-235	-678	106	199	-979
Cyclic rate of change in the gas internal energy, W	-22			3	5.0	-14*

*The low but non-zero value for the total cyclic gas internal energy change indicates that steady-state has not been reached but the change between cycles is small. At steady-state this value would be zero.

Table 5-2 is a numerical summary of the energy flows in the CFX simulation. It predicts 199 W of cooling power at 200 K and 50 Hz running speed. The warm-up experiment (Figure 3-34) measured 37 W of conduction losses that are not accounted for in the CFX model which brings the prediction down to 167 W, which is only 11% more than the 150 W of cooling measured by the cool-down experiments at 200 K. The numerical summary indicates that the gas internal energy change per cycle is 22 W in the diaphragm space which is only 2.2% of the work the diaphragm does on the cryocooler gas. The change in internal energy of the cold gas per cycle is similarly 2.5% of the cooling heat transfer to the gas. These low internal energy changes indicate that the model is close to steady-state conditions. Another indication of steady-state is the heat transfer from the regenerator of 106 W, which is comparatively low compared to the 55 kW peak flows to and from the regenerator during the cycle (Figure 5-16). The wall heat transfer values show that the warm side of the displacer removes an average of 678 W of heat from the gas, as opposed to 235 W in the transfer holes and 371 W in the diaphragm space. This indicates that heat exchange on the warm side of the displacer is critical and also that the holes are not removing as much heat as intended. Ideally the warm side of the displacer and transfer

holes would have enough heat transfer to perform the majority of the heat removal and the diaphragm should not have to be removing as much as 371 W.

Table 5-3: Comparison between CFD, Sage and Experiment

Parameter	CFX	Sage	Experiment
Pressure wave amplitude, bar	2.94	2.95	2.8
p-V phase angle, °	13.6	25.5	15.5
pV power input, W	981	1720	924
Cooling power, W	199-37* = 162	249-37*=222	150

* 37 W of conduction losses at 200 K from the experiment, Figure 3-34.

Table 5-3 compares the CFX predictions with Sage and the experiments. CFX's prediction of 2.94 bar compares well with the experimental pressure wave amplitude of 2.8 bar and Sage's 2.95 bar. CFX's prediction of 981 W input power (*pV* power) is much closer to the experimental 924 W than the Sage prediction of 1720 W. Sage's discrepancy in *pV* power is reflected by the pressure-volume phase angle it predicted; 25°, as compared to the CFD's prediction of 13° and the experimentally measured 12.8°. Sage's high *pV* power is most likely due to its prediction of a greater displacer movement amplitude than the experiment or CFX, and is likely a reason for Sage's higher prediction of cooling power.

5.3.2 TO USE A LAMINAR OR TURBULENT GAS FLOW MODEL?

In Chapter 4, validating the CFX modelling was performed with a laminar flow gas model which provided a good validation with the various gas spring models. In the model of the second prototype, the flow velocities can get high as shown in Figure 5-17. The highest gas velocities are found on the warm side of the displacer and through the transfer holes which suggest a turbulent model would be valid. In the cold domain, velocities are lower and, as Figure 5-18 shows, are not uniform throughout the domain. The regenerator velocities were very low, and combined with a small hydraulic diameter would have laminar flow. The question then arises: Should a turbulent gas model should be used?

The ANSYS® CFX code has the capability to use turbulence models, such as the k-ε model, to efficiently model turbulent flow by including the turbulence mixing in the constitutive equations for the fluid. However, ANSYS® applies the same flow model to the entire analysis and cannot transition to turbulence locally when it occurs. Therefore a choice of fluid model has to be made.

The significance of the laminar-turbulent gas model was tested by running the 200 K model in both linear and k-ε turbulent modes. The effect of the k-ε model was that heat transfer was

improved in the warm domain, resulting in lower gas temperatures, but was less in the cold domain. Cooling power overall was not greatly affected, 140 W for the turbulent model compared with 158 W for the laminar model. The decision was made to continue with the laminar model as it was well validated for this situation and that the turbulent model's effect on the results was minor.

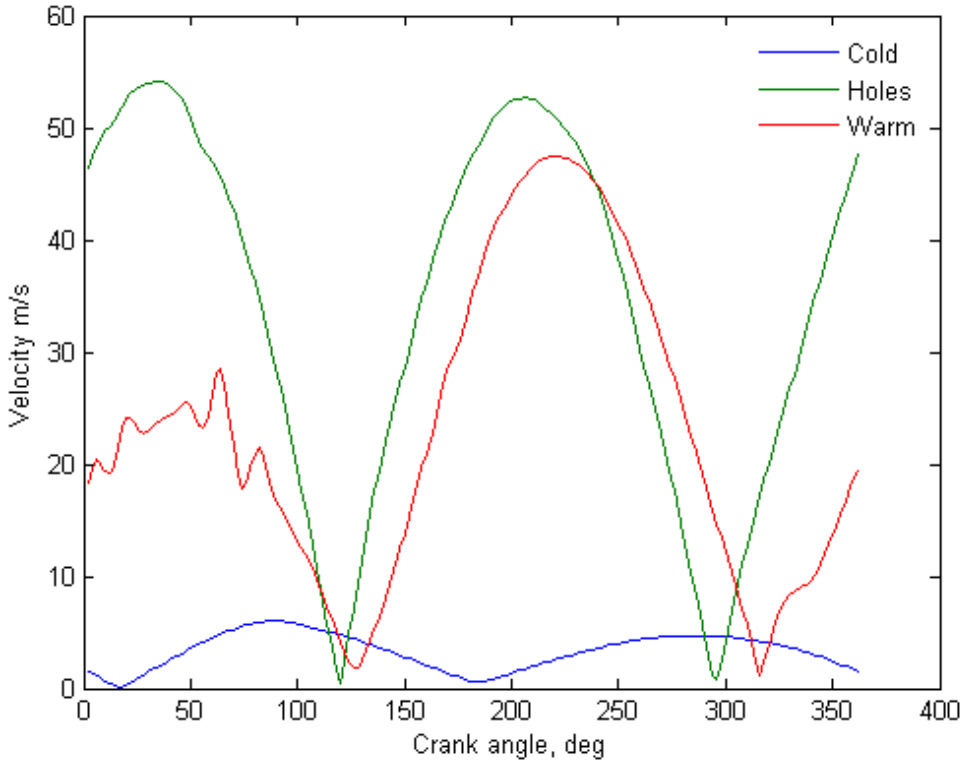

Figure 5-17: Gas velocities during a cycle. Velocity monitors were positioned at the start of the radial section in the cold space (blue); in the middle of one of the transfer holes (green); and mid-radial position on the warm side of the displacer (red).

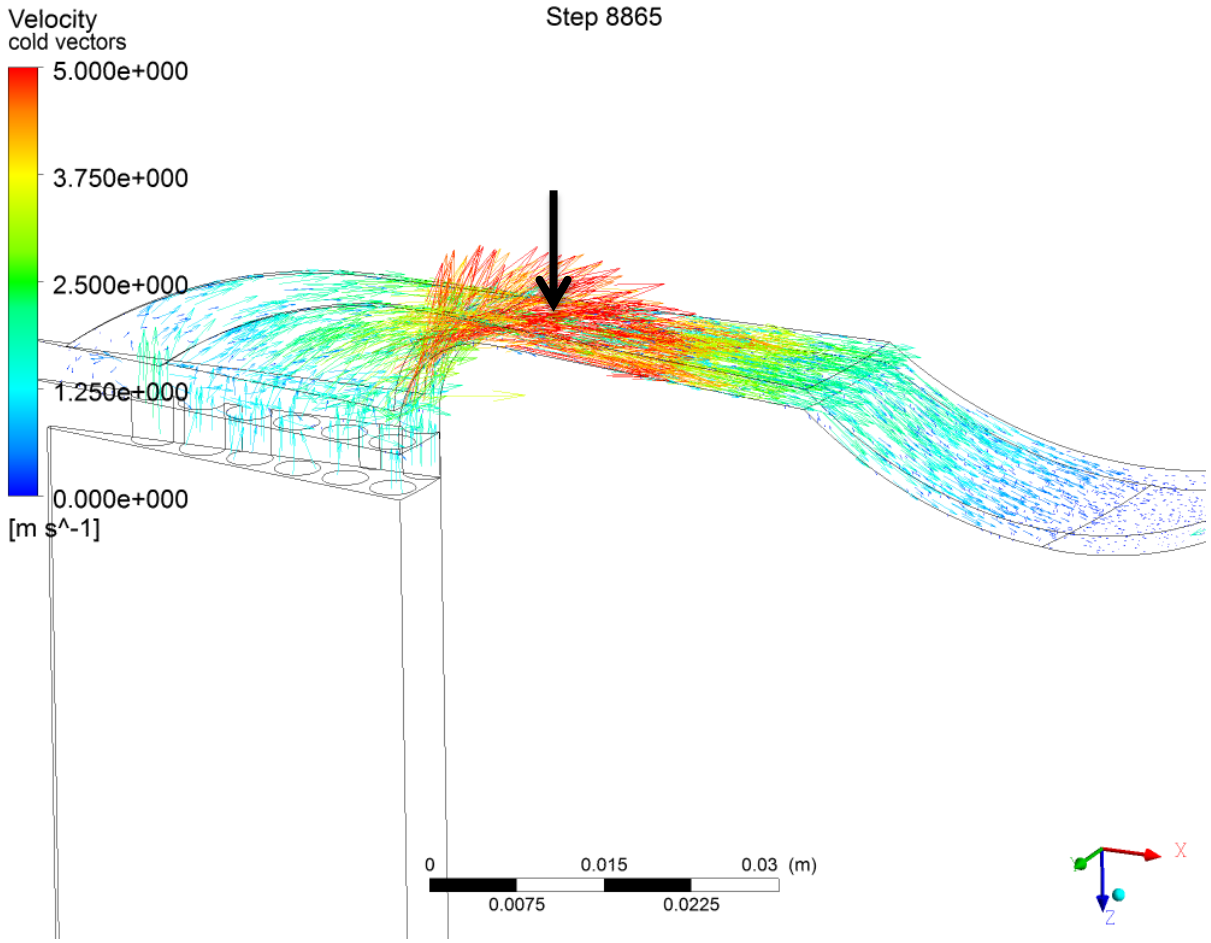

Figure 5-18: Velocity vectors for cold space at 90 degrees in the cycle, when gas velocity is at its highest. The black arrow shows the position of the velocity monitor.

5.3.3 PHASE DIFFERENCE BETWEEN HEAT TRANSFER AND VELOCITY

Of interest is the question as to whether the peak gas velocity corresponds to the time that peak heat transfer occurs. To answer this question, gas velocity (at the position shown in Figure 5-18) is plotted against heat transfer in Figure 5-19. If the gas velocity was in phase with heat transfer then the cyclic plot would be close to a straight line with the maximum velocity corresponding to the maximum heat transfer. Clearly the plots do not show that. The points of minimum velocity have significant heat transfer, and the maximum heat transfer points are at points where the velocity is high, but not at maximum. The heat transfer rate for the transfer holes is almost independent of the gas velocity. This brings into question of the usefulness of the radial flow to augment heat transfer.

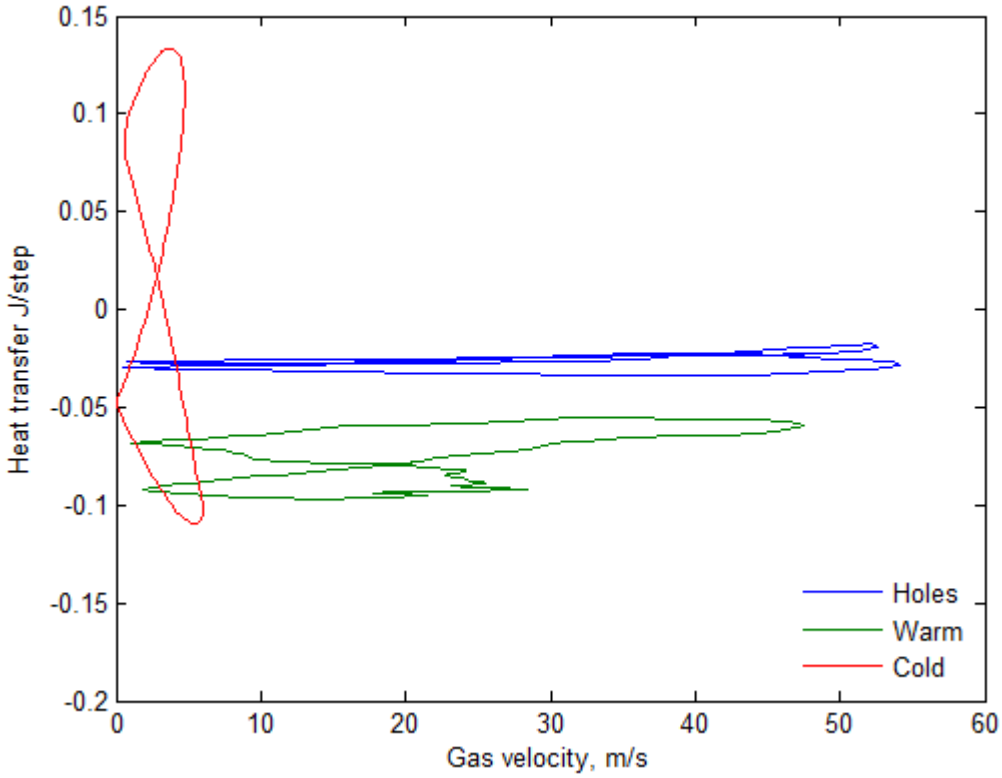

Figure 5-19: Gas velocity vs heat transfer for the transfer holes, warm side of the displacer and the cold domain. Velocities are from the same monitor points as Figure 5-17.

5.3.4 HEAT TRANSFER COEFFICIENT.

The heat transfer coefficient is a parameter commonly used for the calculation of convective heat transfer and according to Newton's Law of Cooling:

$$\dot{Q} = hA(T_w - T_g) \qquad 5\text{-}5$$

where $\dot{Q}$ is the heat transfer rate into the gas, h the heat transfer coefficient, A the heat transfer area, T_g the gas temperature and T_w the wall temperature. For this study, it is useful to know what the heat transfer coefficient is and how it relates to the gas flows in the different sections. For the purposes of this analysis, T_g is taken from the temperature monitor points in the cold and warm domains. As there was no monitor point for the transfer holes, T_g for the holes was assumed to be the average between the warm and cold domain temperatures. The heat transfer rate $\dot{Q}$ was calculated from the area integral of the wall heat flux (shown in Figure 5-16 (b)) for each section's heat transfer surfaces. Figure 5-20 plots the heat transfer coefficient for the centre, mid, outer and displacer wall sections of the cold gas domain versus crank angle. There are points in the cycle, at approximately 30° and 170°, where temperature of the gas monitor point equalled the wall temperature, (T_g-T_w) = 0, whilst heat exchange was non-zero, thus

producing an infinite value for *h* (and apparently violating second law of thermodynamics). This is a result of a non-uniform gas temperature where the oscillating flow produced an oscillating bulk gas temperature (where the monitor point was) that was out of phase with the temperature of the gas next to the walls (which drove the heat transfer). Additional error in the calculation of *h* comes from the temperature of the gas being non-uniform throughout the domain. The single point reading for T_g is therefore only generally representative of the gas interacting with the domains walls. Between angles of 50° to 150° and 200° to 360° in the cycle, *h* is reasonably stable. The value of *h* for the cold domain walls is in the order of 1000 to 2000 W m^{-2} K^{-1}.

Are these values of *h* useful or representative of the heat transfer? The cycle mean value of the cold gas is 197 K, the walls are at 200 K and have an area of 0.0675 m^2 from which 200 W was transferred from the walls. Re-arranging Equation 5-5 gives a heat transfer coefficient of 990 W m^{-2} K^{-1}, which is similar to the plot. Likewise, for the warm side of the displacer, the mean temperature was 331 K, area 0.0511 m^2, and 678 W heat transfer resulting in a cycle average *h*= 428 W m^{-2} K^{-1}, again similar to the numbers from the plot.

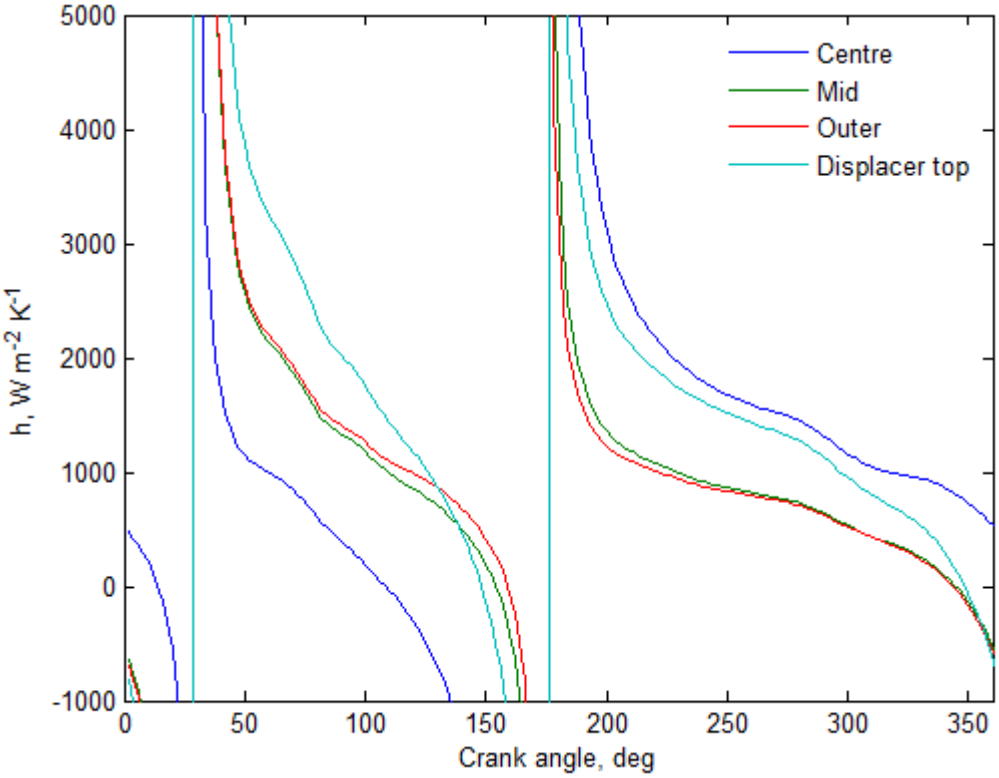

Figure 5-20: Variation of the heat transfer coefficient of the centre, mid, outer and displacer walls in the cold domain.

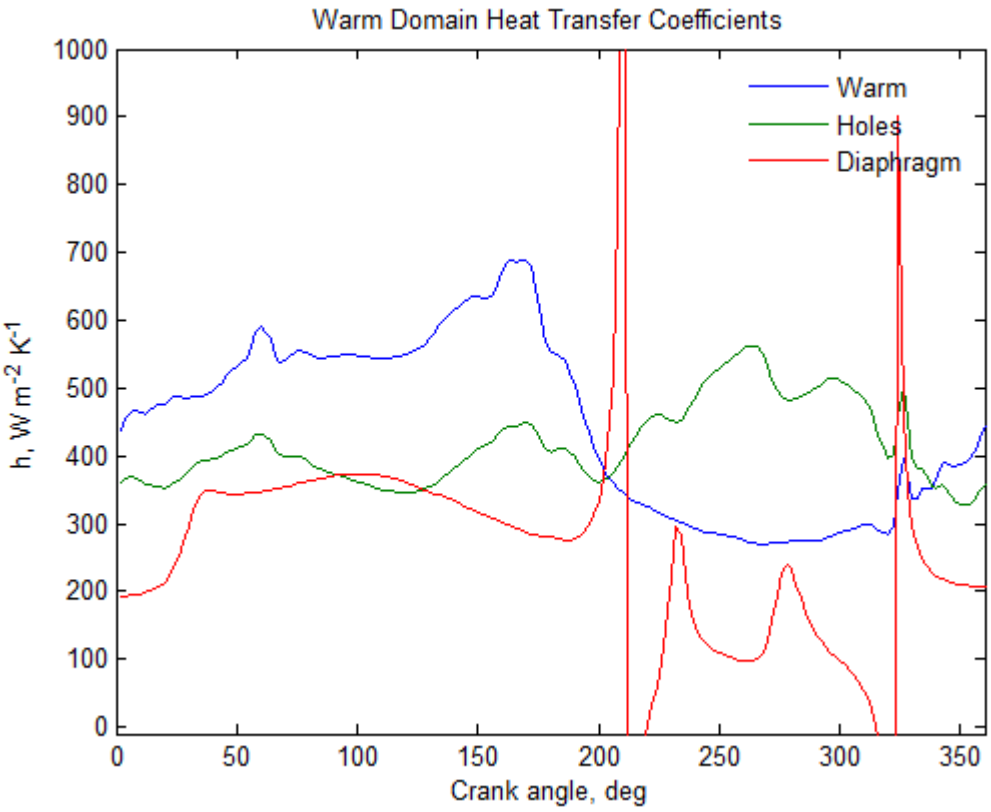

Figure 5-21: Heat transfer coefficients for the warm domain walls: warm side of displacer, transfer holes and PWG diaphragm.

Figure 5-21 shows the heat transfer coefficients for the warm domain walls. The warm domain has three distinct sections: the DPWG diaphragm space; the transfer holes; and the warm side of the displacer. Like the cold domain, the DPWG diaphragm space has points (210° and 320°) where the temperature oscillations produce a zero (T_g-T_h) and therefore an infinite h. The DPWG diaphragm h is around 300 W m^{-2} K^{-1} for the high side of the cycle (crank angle 0°-180° where the gas pressure is higher than average) and around 200 W m^{-2} K^{-1} for the low side of the cycle. There is a phase lag of approximately 20° which roughly corresponds to the pressure-volume phase lag.

The gas in the warm side of the displacer and the transfer holes remains above the wall temperature throughout the cycle and thus does not have the inflections. It shows a similar trend to the DPWG diaphragm space with h being around 500 W m^{-2} K^{-1} for the high side of the cycle and 300 W m^{-2} K^{-1} on the low side of the cycle.

The value of h is relatively constant for the transfer holes throughout the cycle, at around 400 W m^{-2} K^{-1}.

The following examples compare the h from these calculations with a designer's exercise for calculating heat transfer areas.

Example 1 : Heat exchange in the cold domain.

> Ideally the second prototype would absorb 200 W from the cold surfaces with less than 5 K temperature difference between gas and walls and an h of 1000 W m^{-2} K^{-1}. How much surface area would be required for the heat exchange?
>
> Rearranging Equation 5-5:

$$A = \frac{\dot{Q}}{h(T_w - T_g)} \qquad 5\text{-}6$$

gives an area of 0.04 m^2, which is slightly less than the current prototype's cold domain surface area of 0.068 m^2.

Example 2: Heat exchange area in the warm domain.

> In the warm domain, 1000 W is required to be removed from the gas over a 20 K temperature difference, with an h of 400 W m^{-2} K^{-1}. Substituting these numbers into Equation (5-6) yields 0.125 m^2 of area required, which is less than the prototype's 0.29 m^2 suggesting that not all of the warm domain's heat exchange wall area was actively involved in removal of the 1000 W.

The CFD analysis has shown that h is larger for the cold domain than the warm, being ~ 1000 W m^{-2} K^{-1} and ~ 400 W m^{-2} K^{-1} respectively. The warm domain's lower number will be because, even though velocities are higher, the gas is less dense.

The value of the heat transfer coefficient is a useful, if rough, guide for the design of the machine, especially for calculating heat exchange areas. One encouraging result is that the current area of the cold domain is sufficient to remove 200 W of heat with a small average temperature difference. The other result is that the warm domain in the prototype has sufficient total surface area but it appears that not all of it is involved in useful heat exchange. These support one of the main aims of this work which is the reduction or removal of the cold heat exchanger in the Stirling machine.

5.3.5 *COMPARISON BETWEEN CFX AND SAGE MODELS*

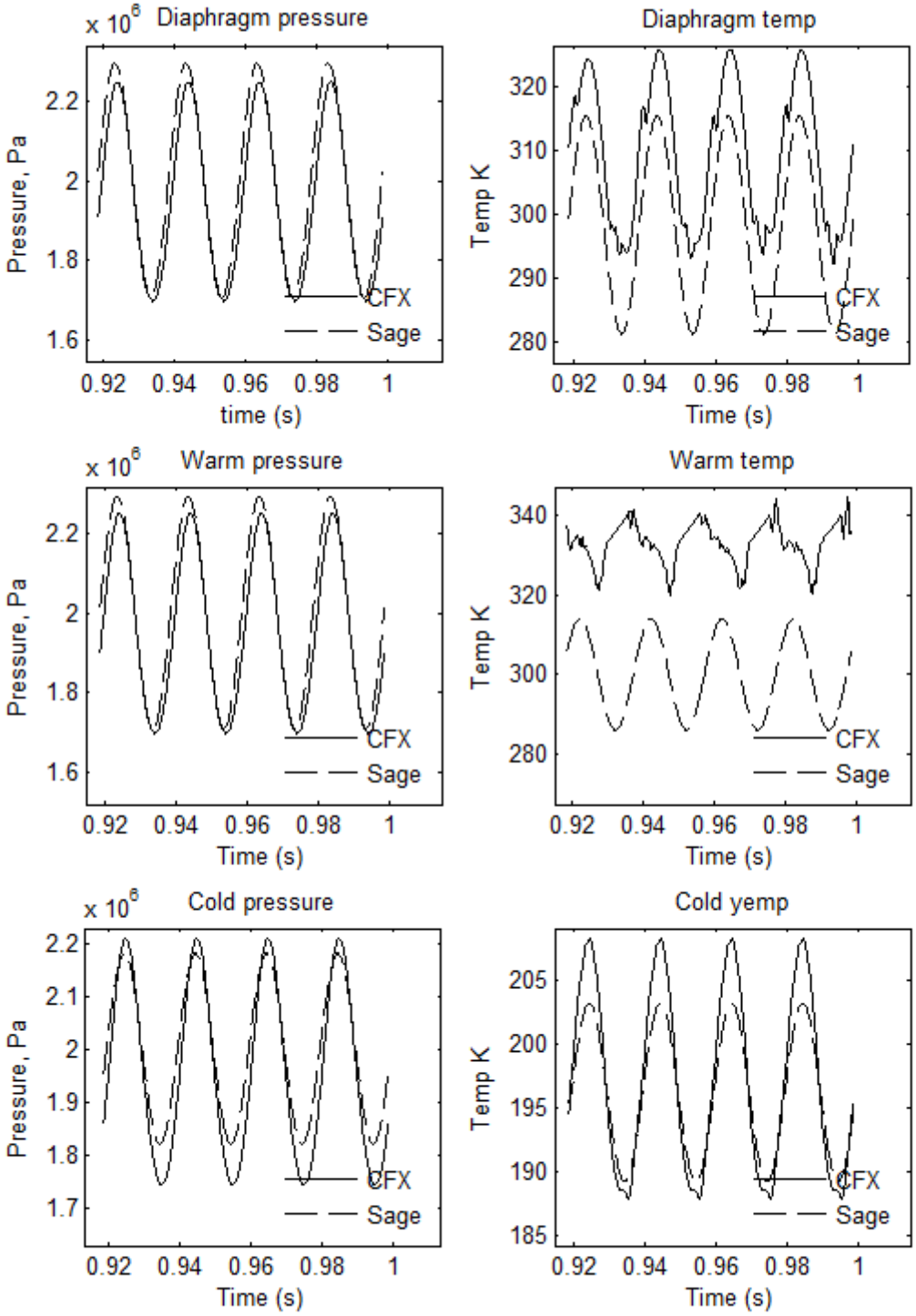

Figure 5-22: Comparison of Sage and CFX results for the 200 K run at 50 Hz.

Figure 5-22 compares the pressure and temperature oscillations predicted by the CFX model and the Sage model. The pressure waves predicted by both models are sinusoidal in shape. The warm domain pressures show a small phase difference between the models, with Sage lagging CFX, reflecting the *p*-*V* phase difference between the two models. The Sage model has a slightly higher pressure wave amplitude. Sage's prediction of the cold domain pressure wave is of smaller magnitude than CFX, indicating the possibility that CFX's regenerator has less flow losses than Sage's regenerator.

The temperature predictions differ more. The DPWG diaphragm temperature plot shows similar amplitude oscillations between the two models but with an offset, indicating that CFX is calculating a lower heat transfer coefficient thus a higher average temperature is required to reject heat in the diaphragm space. The CFX model consistently has perturbations at BDC and at one place during compression. The BDC perturbation is likely due to vortices and mixing of gasses from different temperature regions when the flow is changing direction. The perturbation during compression is from colder gas passing the temperature monitor point; gas that oscillates back and forth and does not reach the regenerator will be cooler than gas that has been heated by the regenerator. Figure 5-23 shows streamlines and temperature profiles of the warm domain at BDC. The streamlines show that vortices are present as the gas slows its flow into the DPWG diaphragm space; the temperature profiles are uneven, showing the effect of the gas coming from the warmer side of the transfer holes and swirling into the cooler PWG diaphragm space.

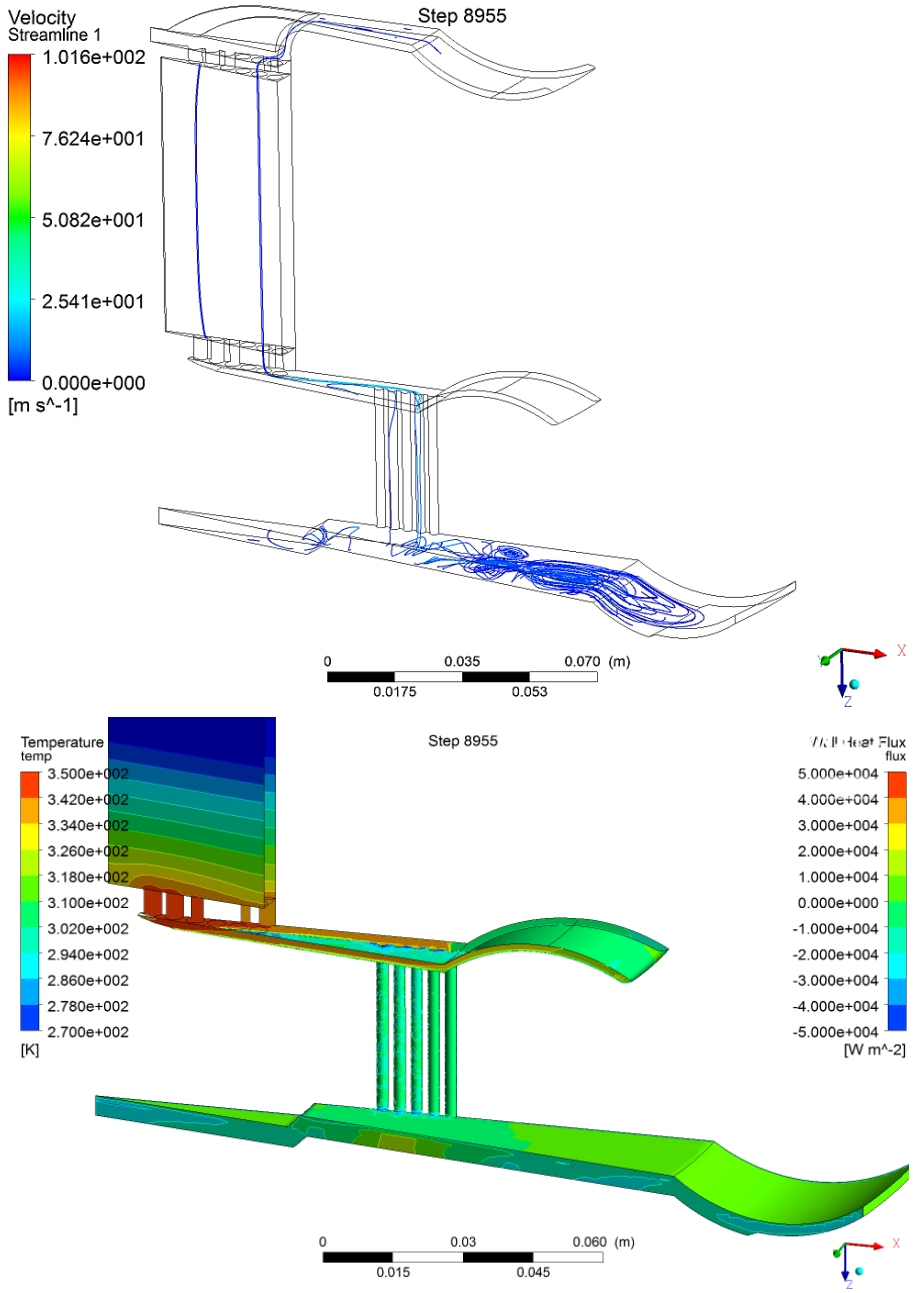

Figure 5-23: The 200 K CFX analysis at BDC showing the effect of the eddies and vortices on the gas temperatures. Above is a streamline plot showing gas direction and velocity. Below are temperature contours on the wedge faces and heat flux contours on the gas surfaces.

The Sage and CFX predictions for the warm side of the displacer are quite different. Sage has a sinusoidal prediction, typical of a solver that works in the frequency domain. CFX however shows a much less orderly shape, with perturbations and variation between cycles indicating that it is modelling eddies and vortices as well as a warmed flow out of the regenerator. The significant offset between CFX and Sage shows that, like the diaphragm space, CFX effectively

has a lower heat transfer coefficient and thus requires a higher temperature difference between wall and gas to reject heat. CFX predicts the cold domain to have larger amplitude temperature oscillations, consistent with the larger pressure oscillations. Sage, however, has a lower average temperature, suggesting that Sage is under-predicting the heat transfer in the cold domain.

Table 5-4: Comparison between analysis & experimental results for 200 K cold end and 50 Hz. Numbers in bold are input values, the remainder are results.

Parameter	**Validation, experiment**	**CFD**	**Sage**
Frequency, Hz	**50**	**50**	**50**
Pressure, x 10^5 Pa (absolute)	**21**	**20**	**20**
Displacer amplitude, mm	0.32	**0.32**	0.45
Displacer phase, degrees w.r.t PWG.	65	**65**	69
Warm end wall temperature, K	290	**300**	**300**
Cold end wall temperature, K	230	**200**	**200**
Pressure wave amplitude, K	2.80	2.93	2.95
Pressure wave phase, pressure lagging PWG diaphragm position, ^{0}	15	14	25
Diaphragm *pV* work, W	920	980	1720
Heat rejected in diaphragm, W	Not measured	370	23
Heat rejected in holes, W	Not measured	240	120
Heat rejected warm side of displacer, W	Not measured	680	1800
Displacer work (warm/cold sides), W	Not measured	400/390	320/320
Heat absorbed in cold domain, W	150 measured + 32 losses = 182	199	249

Table 5-4 compares the experimental measurements, CFX and Sage. CFX's displacer movement was set to match the experiment, whereas the Sage model derived its displacer movement from its force (pressure/area), mass and spring calculations. Sage's different displacer movement will in part explain the higher *pV* work and cooling power of the Sage model as compared with the CFX model and experiment. Of importance is the difference between CFX and Sage in the relative amounts of heat rejected in the different parts of the warm domain. Sage predicts that the vast majority of the heat coming out of the regenerator is transferred to the walls on the warm side of the displacer. CFX, however, has a much more even distribution of heat rejection between the warm side of the displacer, the transfer holes and the DPWG diaphragm. Unfortunately gas temperatures in the different warm gas spaces were not measured in the experiment so the most accurate model cannot be confirmed. Further experimentation with

temperature probes could clarify the discrepancy as the average gas temperature in the DPWG diaphragm domain is an indicator of the amount of heat that has been removed in the transfer holes and warm side of the displacer, and could be compared with the predictions.

5.4 Results of the model at 77 K cold temperature

The major task of the diaphragm Stirling cryocooler will be to liquefy nitrogen for storage or use as a cryogenic coolant. The condensation temperature of nitrogen at atmospheric pressure is 77.13 K, which has become a common industry-standard temperature used to characterise cryocoolers.

The previous CFX model was run with the cold surfaces set to 77 K and the regenerator temperature gradient adjusted accordingly. The displacer movement was set to 0.34 mm amplitude and phase angle to 44.3° as per the Sage prediction in Table 3-3. The running speed was set to 60 Hz. In this way the CFD model matched the cool-down experiment from Section 3.4.5.

As previously, the model was run for a series of 50 cycle long runs; the initial conditions for each run were taken from the gas and matrix temperatures of the previous run. As with the 200 K model, the internal regenerator gradient for each run was linearized from the end points of the previous run. The final 'quasi-steady state' run was determined when the regenerator temperatures moved less than +/-5 K over a 50 cycle run.

5.4.1 NUMERICAL OUTPUT FROM CFD

Figure 5-24 shows the cycle average results for temperatures, heat flows and internal energy. As with previous models, the matrix temperature drift was present but low; the model had not reached its final conditions but the changes per cycle were sufficiently small to allow the study of the gas and heat transfer in the cold and warm gas spaces. The internal energy change plot (bottom right of Figure 5-24) shows that transients from the start-up of the model had settled down. The cold gas temperature plot shows that although the initial cold gas temperature was too low; it stabilised within 20 cycles and subsequently changed slowly with the change in the cold end of the regenerator. The cold temperature at the end of the run was less than 0.2 K different from the previous run. The end of the 50 cycle run was at a 'pseudo steady-state' condition.

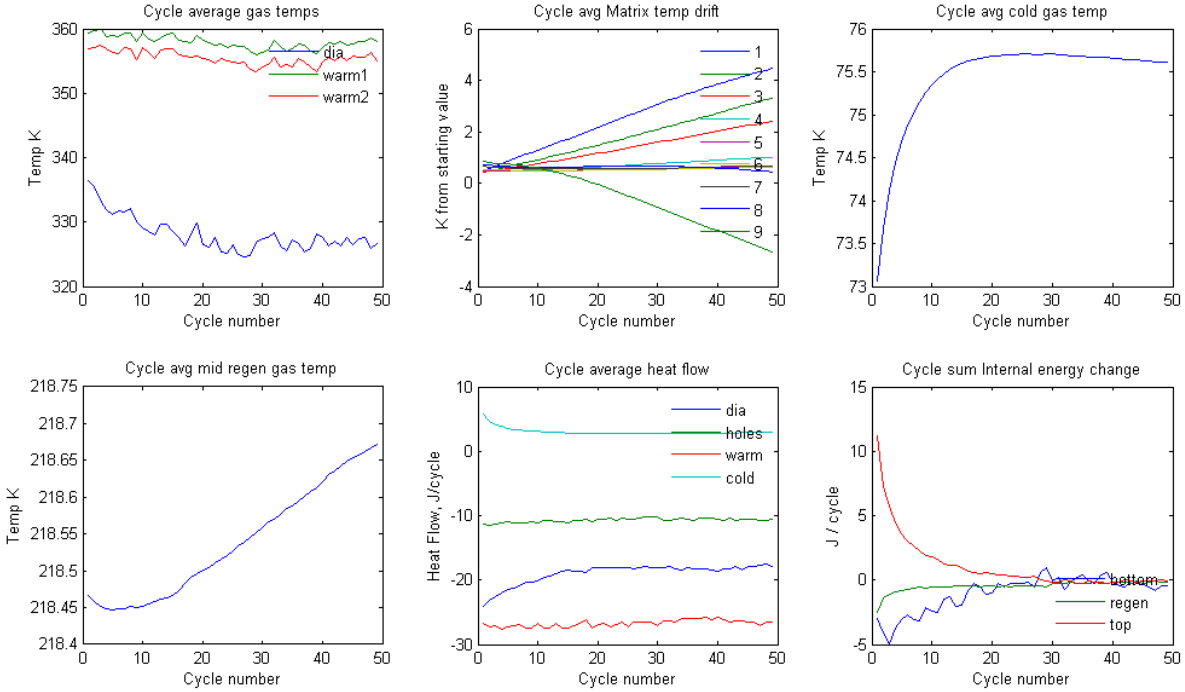

Figure 5-24: Cycle-averaged results for CFD run with the cold walls held at 77 K.

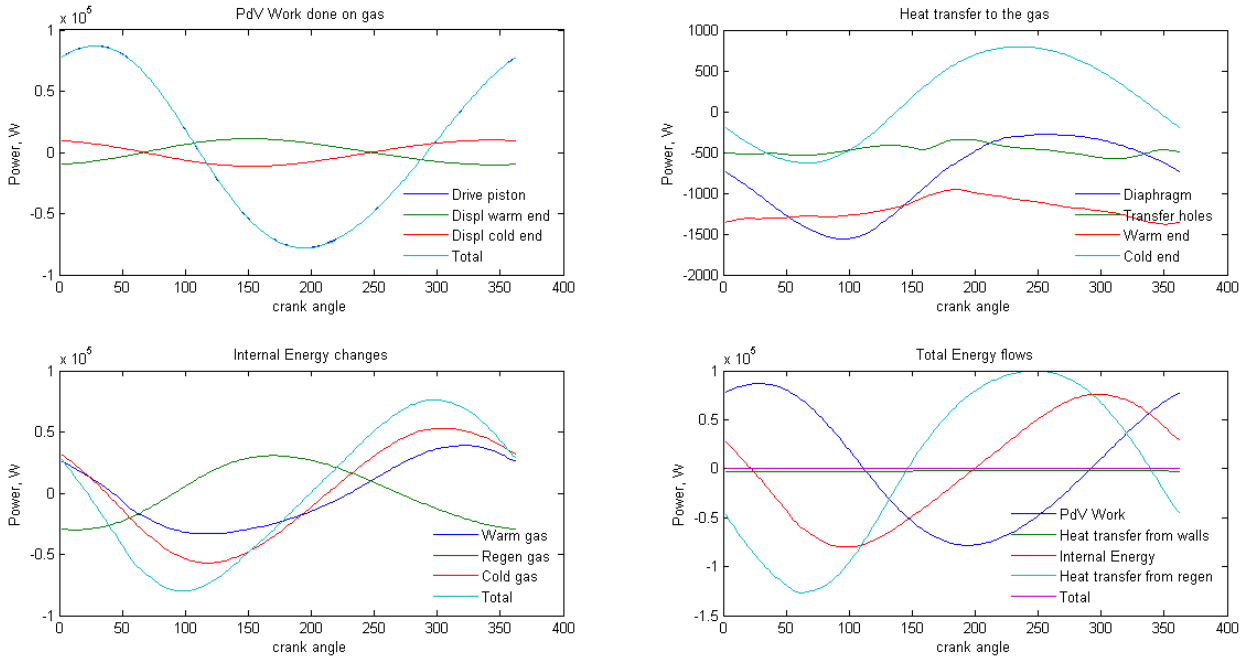

Figure 5-25: Energy flows in last cycle of the 77 K run.

Figure 5-25 shows the energy flows for the last cycle. Zero degrees crank angle represents mid stroke compressing (MSC). The plot is very similar in shape to the 200 K runs (presented in

Figure 5-16), the key differences being that, in the 77 K case, the cold section heat flow is lower and the warm fluxes are more negative, indicating more heat rejection. The lower value of cold heat flow is expected as the cooler had less refrigeration effect at 77 K than at 200 K. The greater magnitude of the warm heat flow is a reflection of the greater work input, which needs to be rejected as heat in the warm side of the refrigerator. The heat transfer to and from the regenerator relative to the *pV* work input is greater for the 77 K case than the 200 K case, due to the greater temperature difference between the regenerator ends, and results in more entropy generation.

Table 5-5: Numerical summary of the energy flows in the last cycle of the 77 K CFD run.

Parameter	**PWG Diaphragm**	**Holes**	**Warm side of displacer**	**Regenerator**	**Cold side of displacer**	**Totals**
pV power input, W	2260		266		-305	2221
Wall heat flow rate, W	-806	-477	-1196	89	130	-2260
Rate of internal energy change in gas, W	-24			-8	-5	-37

Table 5-5 summarises the energy flows in the model at 77 K. The energy balance is preserved, with the sum of the *pV* power and wall heat flow rate being very close (within rounding errors) to the rate of change in the internal energy of the gas. As with the 200 K model, heat rejection is shared between the DPWG diaphragm, the transfer holes and the warm side of the displacer. In this model the regenerator matrix is losing heat from its internal energy into the gas at a rate of 89 W and energy is absorbed at a rate of 130 W by the gas from the cold surfaces (the cryocooler's useful function).

Table 5-6: Comparison between CFD, Sage and Experiment for the 77 K CFD run.

Parameter	**CFD**	**Sage**	**Experiment**
Pressure Wave Amplitude, bar	3.14	3.48	3.36
p-V phase angle, degrees	23.4	30.6	19.6
pV power input, W	2260	3090	2280
Cooling power, W	130	104	29+60 losses = 89

Table 5-6 compares CFX with Sage and the cool-down experiment described in Section 3.4.6. The CFX and Sage predictions of the *p-V* phase angle bracket the experimental value. The *p-V*

phase angle of 23.6° as predicted by CFX is closer to the 19.6° measured than Sage's 30.6°. The work input reflects the phase angles with the CFX work input being very close to the experiment, much closer than Sage. The heat absorbed by the cold surfaces is the cooling power available. When comparing cooling powers, the 60 W of conduction loss experimentally measured in the prototype needs to be added to the cooling power experimentally measured by the cooling of the cold mass. Hence the 29 W of cooling experienced by the cold mass becomes 89 W of heat absorbed by the gas. Considering the assumptions in both the Sage and CFX models, and the magnitude of the energy inputs and heat flows in the cryocooler, Sage's 104 W and the CFX's 130 W compare well with the 89 W measured.

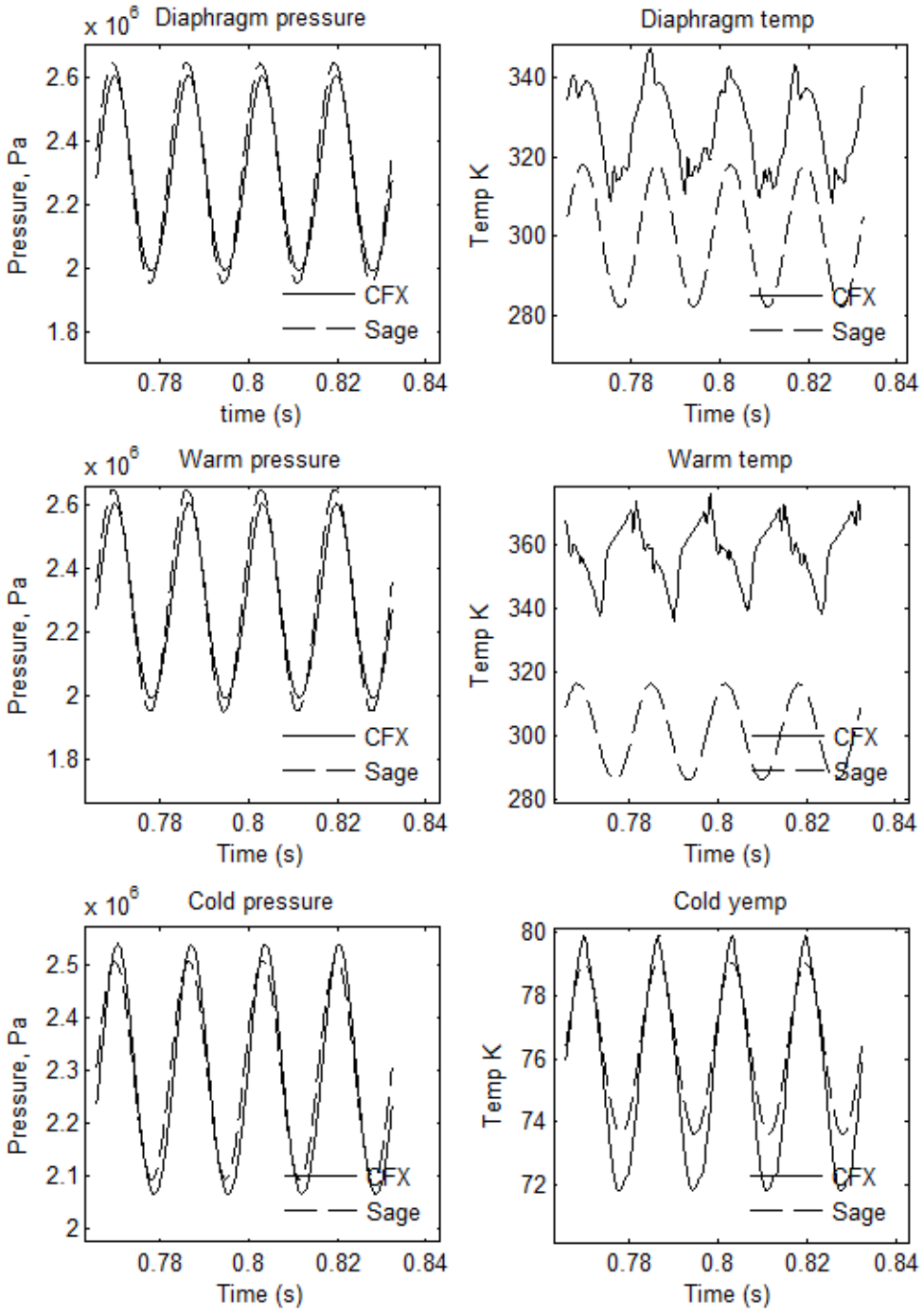

Figure 5-26: Comparison between Sage and CFX predictions for the 77 K run.

Figure 5-26 compares the CFX predictions with Sage's predictions. The DPWG diaphragm pressure waves are similar, with Sage predicting a larger amplitude pressure wave than CFX. Sage's pressure wave lags CFX's prediction as reflected in Table 5-6, where Sage predicts 30° and CFX 23°; therefore Sage predicts more *pV* work input to the machine. CFX predicts a larger amplitude pressure wave than Sage in the cold domain, although the difference is not as pronounced as in the 200 K run.

The diaphragm temperatures (top right in Figure 5-26), show that Sage predicts significantly more heat transfer in the warm side of the machine than CFX does. CFX requires average temperatures of 330 K in the diaphragm space and 360 K on the warm side of the displacer in order to reject the heat from the machine, while Sage predicts average temperatures close to the 300 K walls. CFX's temperature oscillations in the cold gas space are significantly larger than the Sage prediction, which, in this case, is not consistent with the pressure wave amplitude difference as previously postulated for the 200 K case. The CFX cold domain average temperature is slightly lower than Sage's prediction, indicating that Sage predicts more heat transfer than CFX, and is consistent with the larger amplitude temperature oscillations.

5.4.2 THERMAL DIFFUSION LENGTH AND MESH DENSITY.

As discussed in Section 5.2.5 the thermal diffusion length is the distance into the gas from the walls where the effect of the walls' steady temperature no longer dampens the flow or pressure driven temperature oscillations.

The CFX post-processor's graphical output can be used to check that the mesh used is fine enough near the walls to model the thermal diffusion length. If the temperature gradient between the bulk gas and the walls occurs across several, or many, mesh elements then the actual temperature gradient will be approximated reasonably well. If, however, the gradient is across only one element, then the conduction model in the element will dominate, producing a result that is different and, as implied by the exercise conducted in Section 5.2.5.5, will produce a lower heat transfer than a finer mesh would.

Figure 5-27 shows the mesh and temperature profiles for the cold section at BDC, which is close to the coldest part of the cycle. The thermal diffusion length can easily be seen as the temperature gradient at the edges of the gas space. The close-up of the corner where the slotted section transitions to the radial section shows that the temperature gradient goes from green to yellow across the inflation layers adjacent to the boundaries. The gradient is spread across several elements showing that the elements are sufficiently small to correctly model the gradient and therefore the heat transfer from the bulk gas to the wall.

The thermal diffusion length is an indication that the walls of the expansion space are not able to completely dampen out the temperature oscillations from compressing the gas; hence the temperature oscillations in the bulk gas are approaching adiabatic even in the slots. The coldest gas is adjacent to the regenerator; this is the region where desirable heat transfer (from walls into the gas) is highest.

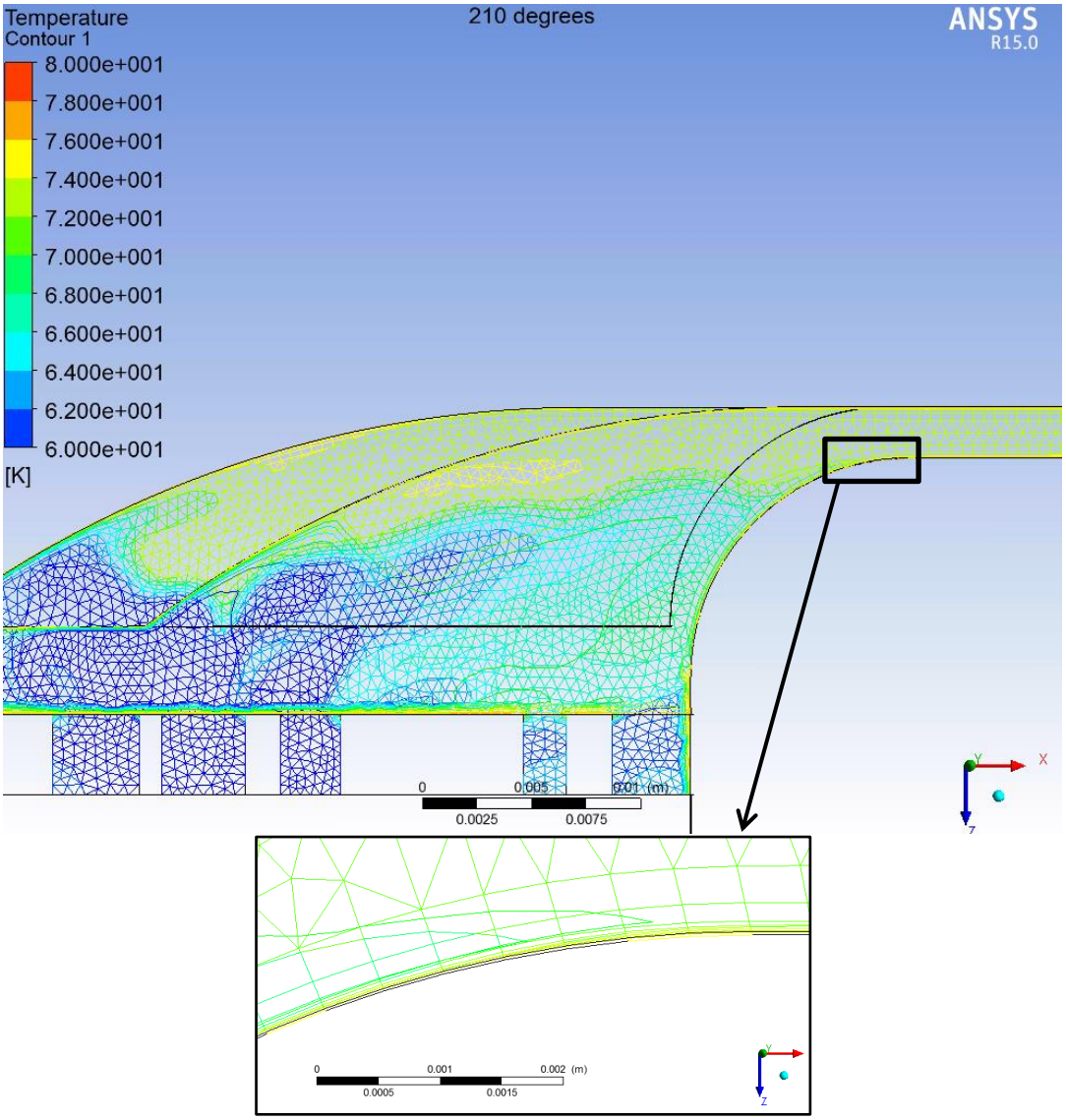

Figure 5-27: Cold gas temperature profiles and mesh at BDC. Above is the region near the centre; below is a close-up of the profiles.

5.4.3 *Peclet number and polytropic compression in the cold gas space at 77 K*

The prototype's cold domain gas spaces have a thickness in the order of 2 mm, whilst the thermal boundary layer has been estimated to be in the order of 0.06 mm, which is confirmed by the CFX graphical outputs. The very thin thermal boundary layer implies that the compression conditions in the cold domain will be close to adiabatic. Adiabatic compression can be confirmed by comparing the oscillating temperature in the model with the theoretical adiabatic temperature amplitude for the same pressure oscillation. A high Peclet number is another predictor of adiabatic compression.

The temperature rise during adiabatic compression is

$$\frac{T_2}{T_1} = \frac{p_2}{p_1}^{(1-\frac{1}{\gamma})} \quad , \qquad 5\text{-}7$$

where T_2/T_1 is the temperature ratio, p_2/p_1 is the pressure ratio, and γ is 1.667 for monoatomic gases. In the case of the 77 K CFX run, the pressure ratio p_2/p_1 = 1.226, which leads to adiabatic compression having a temperature ratio T_2/T_1 = 1.085. From the numerical outputs of the CFD monitor point in the cold domain, T_2/T_1 = 1.087, which is very close to the adiabatic temperature ratio.

Reflecting that the Peclet number is defined as

$$Pe = \frac{\omega D_{\mathrm{h}}}{\alpha}, \qquad 5\text{-}8$$

and α is the thermal diffusivity defined as

$$\alpha = \frac{\kappa}{\rho C_p}. \qquad 5\text{-}9$$

It is clear that the thermal diffusivity, α, is affected primarily by the density, ρ, and conductivity, κ, both of which increase at low temperatures. Helium at 77 K is 3.8 times as dense as it is at 300 K and 2.6 times as dense at it is at 200 K where the initial characterisation was performed. A high density lowers the thermal diffusivity. Conductivity has a smaller increase between 300 and 77 K. The net effect is a significantly lower thermal diffusivity at 77 K, which increases the Peclet number, therefore pushing the heat transfer conditions towards adiabatic. For 50 Hz running and hydraulic diameters of 4 mm (flat channels 2 mm thick), the thermal diffusivity becomes 9.75 x 10^{-7} m^2 s^{-1} and the Peclet number therefore becomes 1.3 x 10^6, which from Kornhauser's work (Figure 2-2), indicates conditions that are very close to adiabatic compression.

5.4.4 FLOW AND HEAT TRANSFER HIGHLIGHTS FOR THE COLD DOMAIN

The points of highest heat flux in the cold domain are HSC and LSE (refer to Section 5.2.8), rejecting heat and absorbing heat respectively, as shown in Figure 5-28. Gas velocities at these points are not at their maximum value of 2.5 m s^{-1} but are mostly below 1 m s^{-1}.

The cold domain velocities peak at TDC and LSC as shown in Figure 5-17 . Figure 5-29 shows gas velocity vectors in the cold domain at TDC and LSC. The effect of the radial flow can be seen, with velocities much higher towards the centre and lower towards the circumference. TDC has the highest velocity, which is counter-intuitive as the DPWG diaphragm is at the top of its stroke and therefore stationary. The gas movement into the cold domain at TDC is due to displacer movement rather than due to compression. LSC sees the peak velocity of gas moving out of the cold domain, again driven by displacer movement rather than compression as the flow is leaving the cold domain while the DPWG is starting its compression stroke which would otherwise move gas into the cold domain.

The different timing between peak heat transfer and peak velocity suggests that gas velocity is not the only contributor to heat transfer. In fact, it is the gas temperature oscillation which dominates heat transfer rate. Additionally, the flow required for compression, driven by the DPWG diaphragm, is not as large in the cold domain as the flows driven by the displacer movement. So radial flows, while helpful, do not dominate heat transfer.

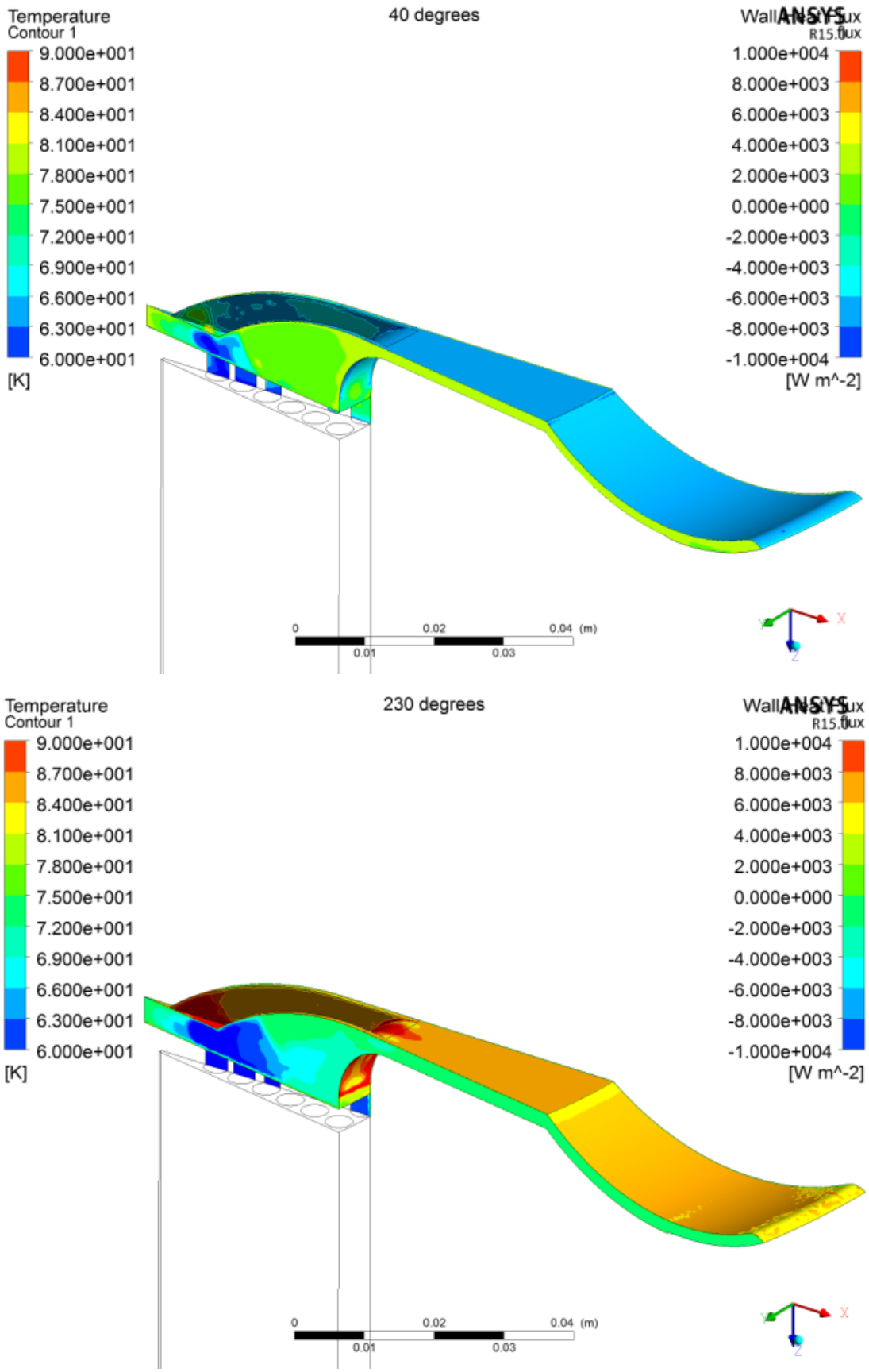

Figure 5-28: Peak wall heat fluxes in the cold domain: left at HSC; right at LSE.

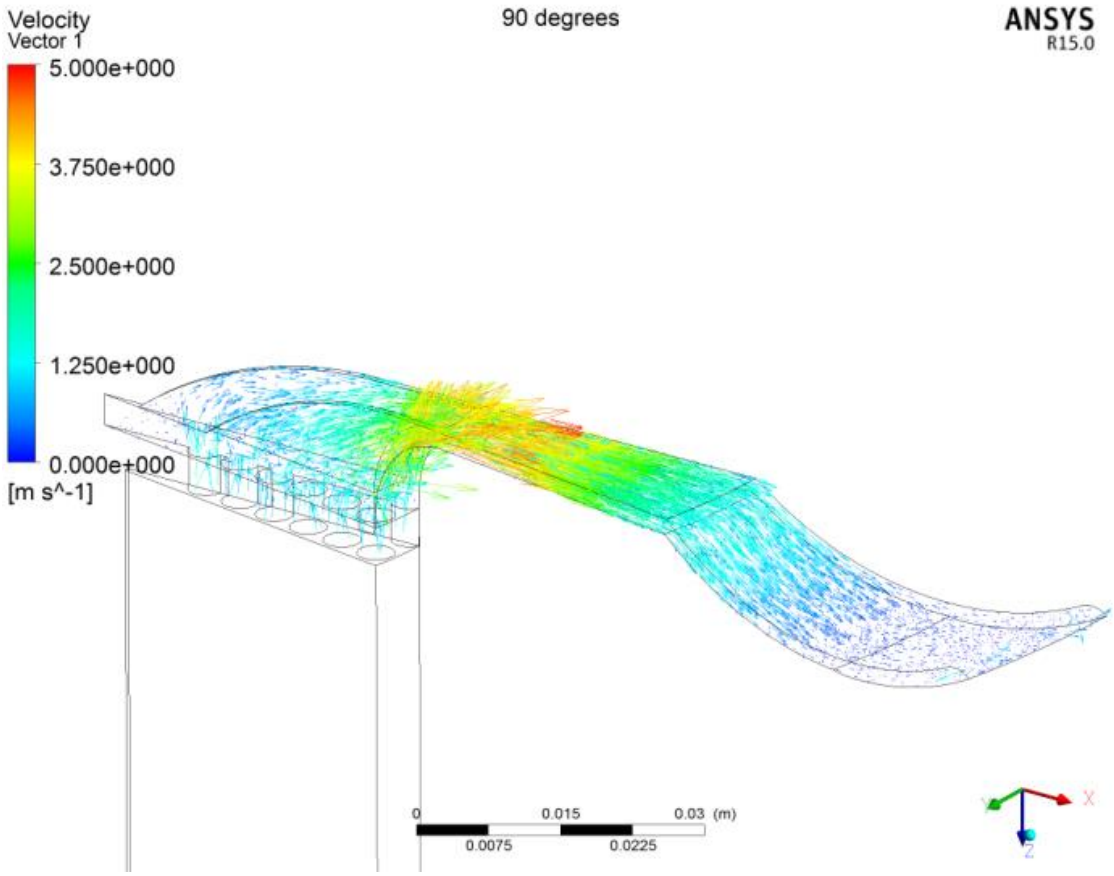

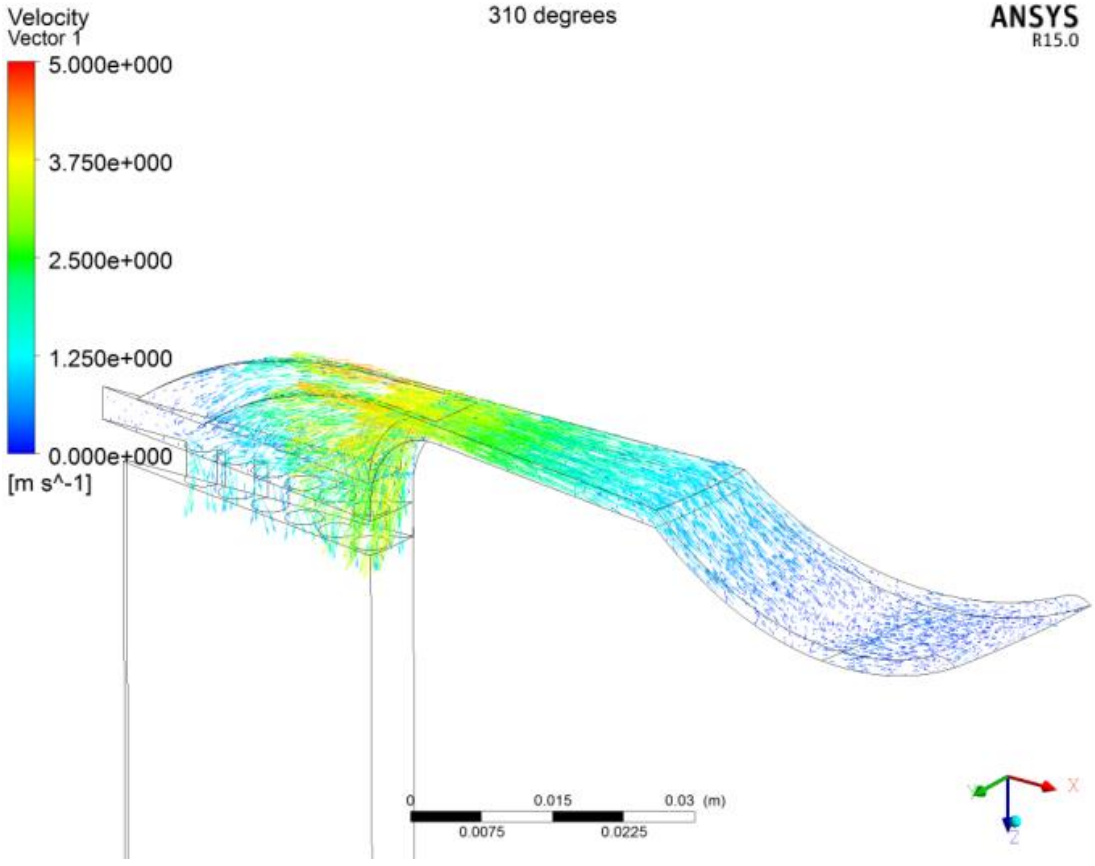

Figure 5-29: Peak velocities in the cold domain, left at TDC and right at LSC

5.4.5 FLOW AND HEAT TRANSFER HIGHLIGHTS FOR THE WARM DOMAIN

Peak heat transfer in the warm domain occurs at different points for the DPWG diaphragm surfaces and the warm side of the displacer surfaces. Figure 5-30 shows on the left the wall heat flux plot for the DPWG diaphragm's highest wall flux, at HSC, and on the right the wall heat flux plot for the highest wall heat flux on the warm side of the displacer surfaces, at LSC.

Similar to the cold domain, the timing of the warm domain peak heat transfer does not match the peaks in velocity. Peak heat transfer occurs near the ends of the stroke, TDC and BDC, whereas the velocities peak at mid-stroke, MSC and MSE. This result strengthens the observation that heat transfer in the oscillating pressure field is driven more by the temperature oscillations than the flow velocities.

Peak Velocities for the warm domain are shown in Figure 5-31. On the left velocity vectors are shown for the compression stroke at MSC with gas moving from the DPWG through to the rest of the cryocooler; on the right are the velocities for gases returning to the DPWG, peaking at MSE.

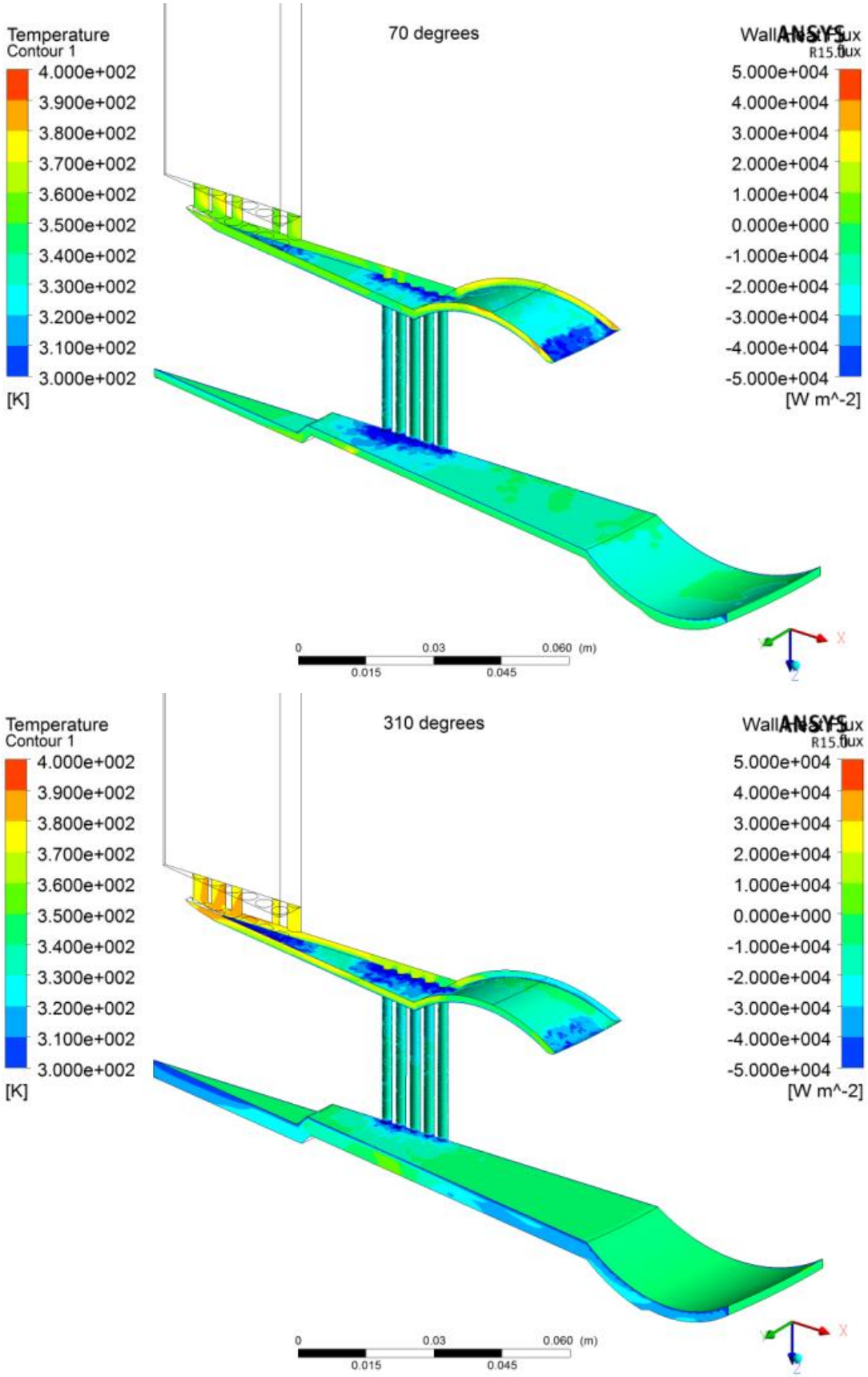

Figure 5-30: Peak heat rejection in the warm domain. Left is HSC which has the peak heat transfer for DPWG space. Right is LSC which has the peak heat transfer for warm side of displacer.

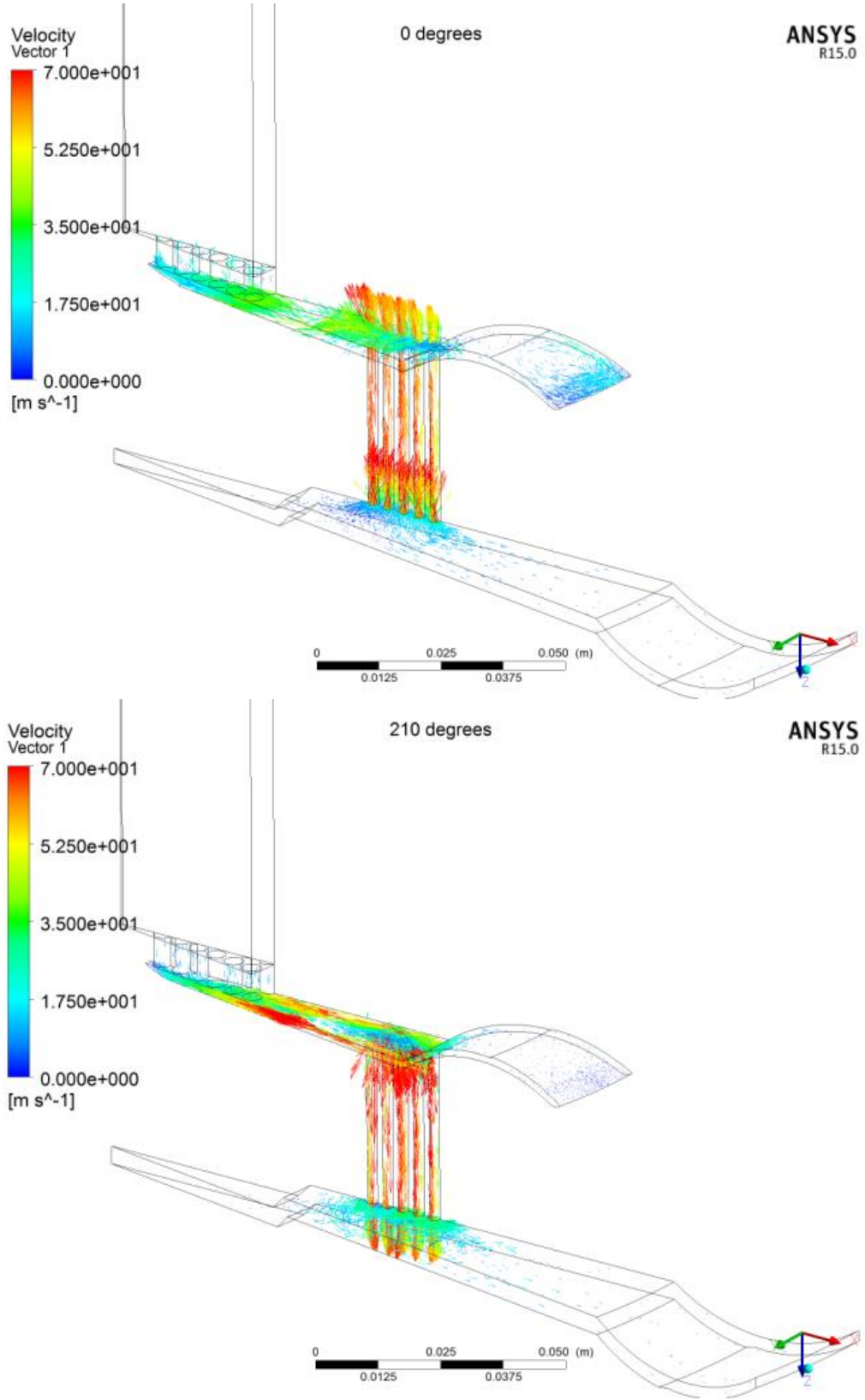

Figure 5-31: Peak gas velocities in warm domain. Left, MSC, peak velocity for compression. Right, MSE, peak velocity for expansion.

5.5 Conclusion

ANSYS® CFX has modelled the second prototype diaphragm Stirling cryocooler's oscillating cycle well enough to gain insights into the inner workings of the machine, to roughly predict cooling performance and predict input power well. The CFX model's results were reasonably close to the experimental results, predicting 130 W of cooling power at 77 K as opposed to the experimental 89 W. This is acceptably close considering that the input power was measured at 2280 W, with the CFX model predicting 2260 W. Thus the 40 W difference in cooling power is only 1.8% of the input power into the machine. Moreover, the cooling power is a small difference between much larger numbers. The 130 W cooling power is the integration of an oscillating heat transfer between the gas and walls in the cold domain which has a peak heat flow of 800 W into the gas and 600 W out of the gas. The work input to the gas, via the DPWG diaphragm, is an oscillation with an amplitude of 80 kW and the heat transfer between the gas and regenerator matrix oscillates with an amplitude of 100 kW. Predicting a mere 130 W of net energy movement in the correct direction (from wall to gas) in one part of a system with such large energy flows is an achievement. It should be noted that when comparing models with performance of near-ambient heat pumps with COPs close to 5 (instead of 0.04 for the cryocooler modelled here); the COP is a good heat parameter for comparison as the refrigeration effect is significantly larger than the work input.

The CFX model could be improved, firstly by experimenting with the porous media parameters to get a closer match with the flow loss; secondly by more experimentation with the mesh; and thirdly a gas model that predicts the laminar/turbulent transition in the oscillating flow could help model the widely varying velocities in the cryocooler. The CFX model does, however, offer some valuable insights and useful guidance to the designer for improvement to be incorporated into the next prototype.

One of the main hypotheses of this thesis was that the large areas and radial flows produced by the flat diaphragm geometry could be used for enhanced heat transfer, especially in the cold domain. The CFX model shows quite clearly that the points in the cycle with high radial flow do not match up well with those of maximum beneficial heat transfer. Indeed maximum heat transfer from the walls to the gas in the cold domain occurs at 210°- 230° (LSE), when the general flow velocity is fairly low, with peak velocity occurring later at around 270° (BDC) - 300° degrees. Likewise in the warm domain there is a mismatch between high velocities and the peak heat transfers. However, the model has shown that the diaphragm geometry produces sufficient area in the cold domain's flat-round shape to achieve the desirable heat transfer without the need for a separate (and expensive) cold heat exchanger. The area of the cold

domain is sufficient for transferring 200 W at 77 K with minimal gas-to-wall temperature difference; however, the warm domain needs more area, close to the regenerator, to be able to reject the heat more efficiently. The phase difference between the times of maximum temperature and velocity means that heat transfer is primarily driven by the temperature oscillations and, while flow velocity is useful, it does not dominate the heat transfer. The times of the cycle that have the highest velocities, and therefore high heat transfer coefficients, also have low gas to walls temperature differences, which counters the benefits of the high heat transfer coefficients.

The warm side of the displacer is an area where radial velocities are high. The high temperature of the gas exiting the regenerator makes high heat transfer necessary. CFX predicts high overall temperatures on the warm side of the displacer, higher than desirable, which will affect overall performance. Additionally the current position of the transfer holes is too close to the centre line of the machine, leaving a large dead volume at the circumference that does not contribute usefully to the thermodynamic cycle of the cooler. Positioning the transfer holes close to the circumference would give more heat exchange area and reduce the average gas temperature, and would improve performance.

The Sage model over-predicted the cooling power of the second prototype by a similar amount to CFX. The Sage model's prediction, however, had a different displacer movement, of its own calculation, which resulted in a very different input power. Another significant difference between CFX and Sage was the predicted gas temperatures in the warm domain. CFX's prediction can be viewed with greater confidence as its overall energy flows were closer to the experiment, and there was evidence of high gas temperatures on the warm side of the displacer in early experiments. Sage overestimates the heat transfer ability of the warm domain walls. Sage's purely numeric outputs would not have allowed the insights above and therefore the CFD modelling process has been invaluable for understanding and developing the cryocooler.

These conclusions inform the design process for improving on the second prototype, which is discussed in the next chapter.

6 IMPROVED DESIGNS

6.1 Learnings from experiment and model

The CFX model of the second iteration prototype indicated a number of deficiencies of the design that could be improved upon. The deficiencies were:

- There was not enough heat transfer area in the warm domain and consequently a high temperature differential was needed between the gas and wall to remove the heat from the machine: 50 K on the warm side of the displacer and 30 K in the DPWG diaphragm space. Additionally, the position of the transfer holes between the DPWG and the warm side of the displacer produced a dead volume; which did not add its area effectively to the heat rejection process; and performed as a gas spring.
- The dead volume of the cold domain's central slotted heat exchanger detracted more from performance than the additional heat exchange surface area aided performance.
- The displacer movement could have been greater. The Sage model predicts that more displacer movement produces more cooling.
- The CFD modelling showed that the thermal boundary layer was small compared with the hydraulic diameter of the gas flow passages; this means that a significant amount of the gas in the cold and warm domains did not interact with the heat exchange surfaces.
- The pressure wave amplitude was much lower than the 5 bar amplitude that the DPWG is capable of. This suggests that the DPWG did not have enough swept volume to fully utilise the cold head. Additionally, the low pressure wave amplitude resulted in a smaller displacer movement.

6.2 Improvements

The three most achievable improvements for the next iteration of the development are to:

- Increase the warm domain heat exchange area by adding more transfer holes closer to the circumference.
- Remove the slotted cold heat exchanger.
- Increase the DPWG swept volume.

The improvements were added to both the CFX and Sage models, one at a time, to determine the effect of each improvement. The proposed design for the next prototype would incorporate all three improvements.

6.2.1 INCREASED WARM DOMAIN HEAT TRANSFER VIA MORE TRANSFER HOLES

The first improvement addresses the high temperatures on the warm side of the displacer, which experiences hot gas flowing from the regenerator and is the section with the highest heat rejection. The Sage model predicts that the majority of heat rejection happens on the warm side of the displacer, before the transfer holes. The CFX model predicts that the transfer holes and DPWG perform a more significant portion of the heat rejection in the warm domain. Early experimental work on the proof-of-concept prototype, Section 3.3.4, supports the CFX model as it showed evidence of high gas temperatures on the warm side of the displacer.

Moving the transfer holes radially outwards as far as possible would address the dead volume at radii beyond the transfer holes and allow more flow area for heat transfer.

Added to the position of the transfer holes is the need for more surface area. The heat transfer coefficient for the warm domain was estimated by CFX to be 400 W m^{-2} K^{-1}. The 200 ml swept volume DPWG is capable of producing 4 kW of pV power and, in an ideal machine, this would be rejected in the warm domain as heat. To remove 4 kW of heat with a 30 K temperature difference and heat transfer coefficient of 400 W m^{-2} K^{-1}, a surface area of 0.33 m^2 would be required. The warm side of the displacer, with only one side available for heat exchange, has an area of 0.05 m^2; each 2 mm diameter hole has 2.6 x 10^{-4} m^2 area and the DPWG compression space has 0.105 m^2 available for heat exchange. The DPWG and warm side of the displacer areas are fixed, so to achieve the desired 0.33 m^2, 673 holes are required. Rounding to 37 holes in each segment would be sufficient. Alternatively for the current ~2 kW of pV power to be rejected, 0.165 m^2 of heat exchange area would be needed. Assuming that the combination of holes and the warm side of the displacer perform all the heat transfer, 442 holes would be

required, which is 24 - 25 holes per segment. A layout of 28 holes, arranged in 7 rows of 4, was able to be neatly fitted as shown in Figure 6-1 below.

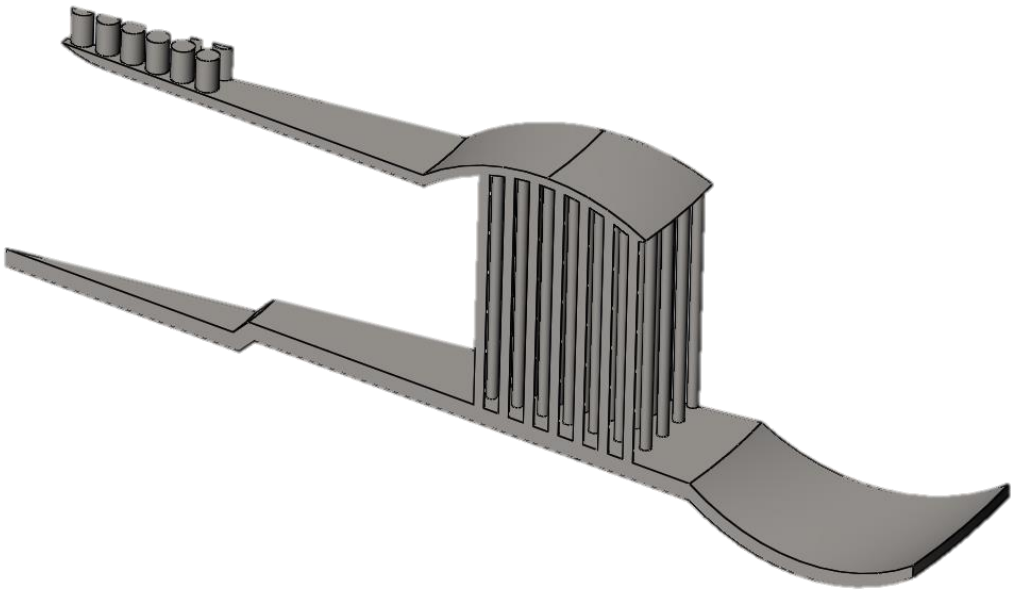

Figure 6-1: Warm domain gas space with 28 transfer holes.

Sage's prediction of the effect of adding extra cooling holes is shown in Table 6-1 below. Sage predicts a slight loss in cooling power due to the lower pressure wave amplitude and therefore input power. However, an improvement in efficiency is predicted.

Table 6-1: Sage prediction for the second prototype model with transfer holes

Parameter	**Second prototype**	**With additional transfer holes**
Connecting duct No. of tubes Diameter, mm Length, mm	 80 2.5 40.75	 28 x 18 = 504 2.0 40.75
pV work, W	3090	2691
Cooling, W	104.0	96.4
Displacer amplitude, mm	0.448	0.433
Displacer phase, ^{0}	44.5	43.8
Carnot eff, %	9.78	10.40
Pressure amplitude, bar	3.40	3.24

The CFX model was changed to incorporate the new warm domain model and the model re-run. The model had stabilised sufficiently to draw conclusions on the effect of the changes after 8 runs of 25 cycles. The reason for only 25 cycles per run was instability in the mesh movement

causing a negative element condition after running for 25 cycles. The model stabilised from start-up in less than 10 cycles, leaving the remaining cycles to move the model towards quasi-steady-state conditions.

The result was that the warm side of the displacer gas temperatures were 335 K, which is 20 K cooler than the 355 K of the second prototype and similar to the 30 K gas-to-wall temperature difference predicted by the heat transfer coefficient calculations. The diaphragm gas space was 309 K, which is 16 K lower than the 325 K of the second prototype model. This resulted in a smaller temperature gradient across the regenerator and ultimately better efficiency. As with the Sage model, the extra volume of the added transfer holes reduced the pressure wave amplitude, which in turn resulted in reduced input pV power but only slightly less overall cooling power. CFX predicted the cooling power to be 126 W which was slightly down from the second prototype's 130 W, but the 1800 W input power was significantly lower than the second prototype's 2260 W, resulting in an increase in efficiency from 17% to 20.3% of the Carnot COP.

The conclusion is that the addition of more transfer holes aids the cooling and is consistent with the heat transfer coefficient calculation. The temperatures in the warm domain are reduced which results in an efficiency increase of 3.3 percentage points. The extra volume, from the added transfer holes, reduces the pressure wave amplitude resulting in a smaller amplitude pressure wave, which counters any gain in cooling power from the higher efficiency.

6.2.2 REDUCED COLD DOMAIN VOLUME BY REMOVAL OF THE SLOTTED HEAT EXCHANGER

The second design improvement addresses the dead volume and heat exchange area on the cold side of the displacer. The cold domain has relatively slow gas flows, being at the end of the oscillating flow path. Reduction of dead volume in the cold gas is imperative as the high gas density due to low temperature makes the cold domain like a volume 3.9 times larger at 77 K than at 300 K.

The cold side of the displacer has a very thin thermal boundary layer. Therefore, the bulk of the gas undergoes oscillating temperatures at near-adiabatic conditions. To make most use of the gas' heat capacity, the hydraulic diameter of this section should be as small as possible. Practicality limits the hydraulic diameter as the cold domain has to have a swept volume produced by the moving displacer. The distance between the cold domain walls is therefore determined by the amplitude of the displacer movement and the minimum distance allowable at the end of the stroke. It should be noted that the diaphragm geometry allows for a much smaller hydraulic diameter than in an equivalent volume piston-in-cylinder arrangement.

Both the CFX model and experiments demonstrate that significantly more cooling happens at the centre of the cold section than at the circumference, in spite of the circumference's larger area. Maximum flow velocities are present at the centre and CFX shows the coldest gas is found nearest the regenerator. Hence the ideal design maximises the surface areas and minimises hydraulic diameters in the centre. So logic would call for more and larger cooling slots/fins next to the regenerator, which is why the slots were added to the second prototype. However, adding more cooling slots adds volume, which is amplified by the cold temperature and has a negative effect on cooling.

"What is the effect of removing the slots"? "Is the area produced by the diaphragm geometry sufficient for heat exchange"?

The heat transfer coefficients estimated by CFX suggest that the cold side of the displacer, without extra slots or fins, has enough surface area to transfer 200 W from the walls to the gas with a minimal gas-to-wall temperature difference. This means that the slotted heat exchanger in the second prototype was not necessary and its dead volume was more detrimental to the cycle than the extra heat transfer it achieved. Sage agreed with the above argument; removing the heat exchange item from the Sage model increased its cooling power prediction from 96 W to 169 W, dropped the input power to 2460 W, increased the pressure wave amplitude to 3.3 bar, and increased the Carnot efficiency to 19.9%. To make best use of the heat transfer, the wall of the cold section directly adjacent to the gas could be made of copper in the next prototype (the cold gas space walls were stainless steel in the second prototype).

CFX was used to verify Sage's predictions. The CFX model with the improved warm domain was modified to incorporate a cold domain without the central slotted heat exchanger as shown in Figure 6-2.

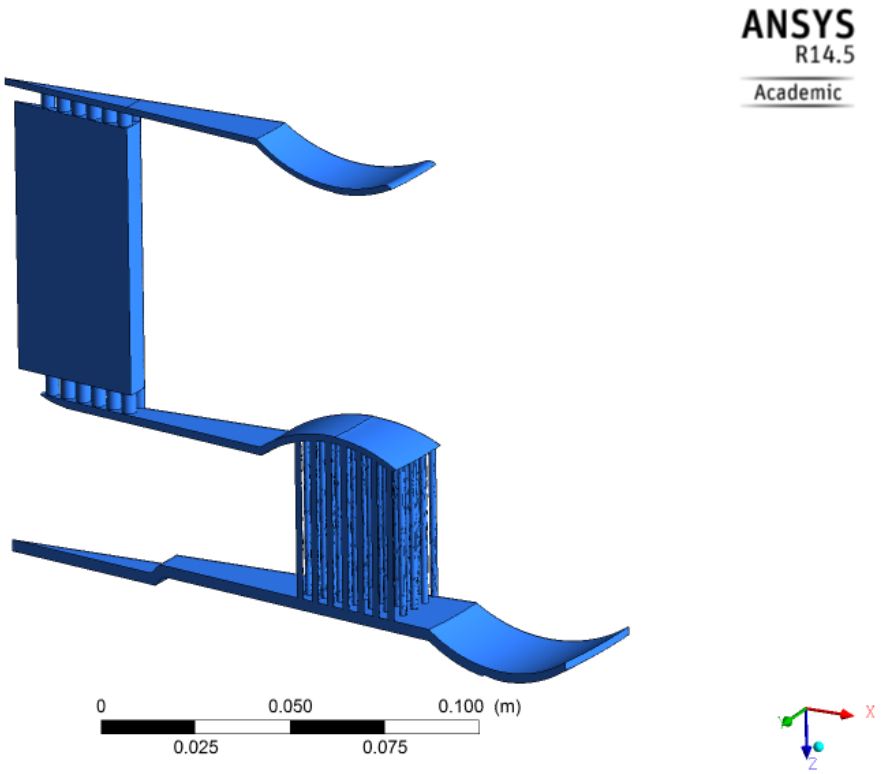

Figure 6-2: The CFD model of the improved design without the central cold heat exchanger.

CFX predicted an increase in cooling power from 126 W to 175 W when the slotted heat exchanger was removed. The *pV* input power was very similar to the previous model at 1750 W (c.f. 1800 W). Efficiency increased significantly, from 20.3% to 29% of Carnot. The pressure wave amplitude of 2.90 bar was little changed from its previous value of 2.87 bar. The cold gas temperature, which was measured from a monitor point near the start of the radial section, was significantly lower, indicating that removal of the volume of the heat exchange slots allowed the cold gas from the regenerator to move further into the radial section, aiding beneficial heat exchange and reducing the dead volume at the circumference.

Figure 6-3 shows the cold domain at the LSE position, where the gas in the cold domain is at its coldest, for the second prototype and the improved design without the central heat exchanger. It shows that the cold gas in the improved version "light blue colour represents 66 to 69 K" penetrates further into the cold domain interacting with a larger percentage of the surface area. When the heat exchanger is removed, the peak heat flux on the top surface "red colour representing over 10^4 W m^{-2}" is spread over a significantly larger area of the cold surface, which results in more cooling power for the refrigerator.

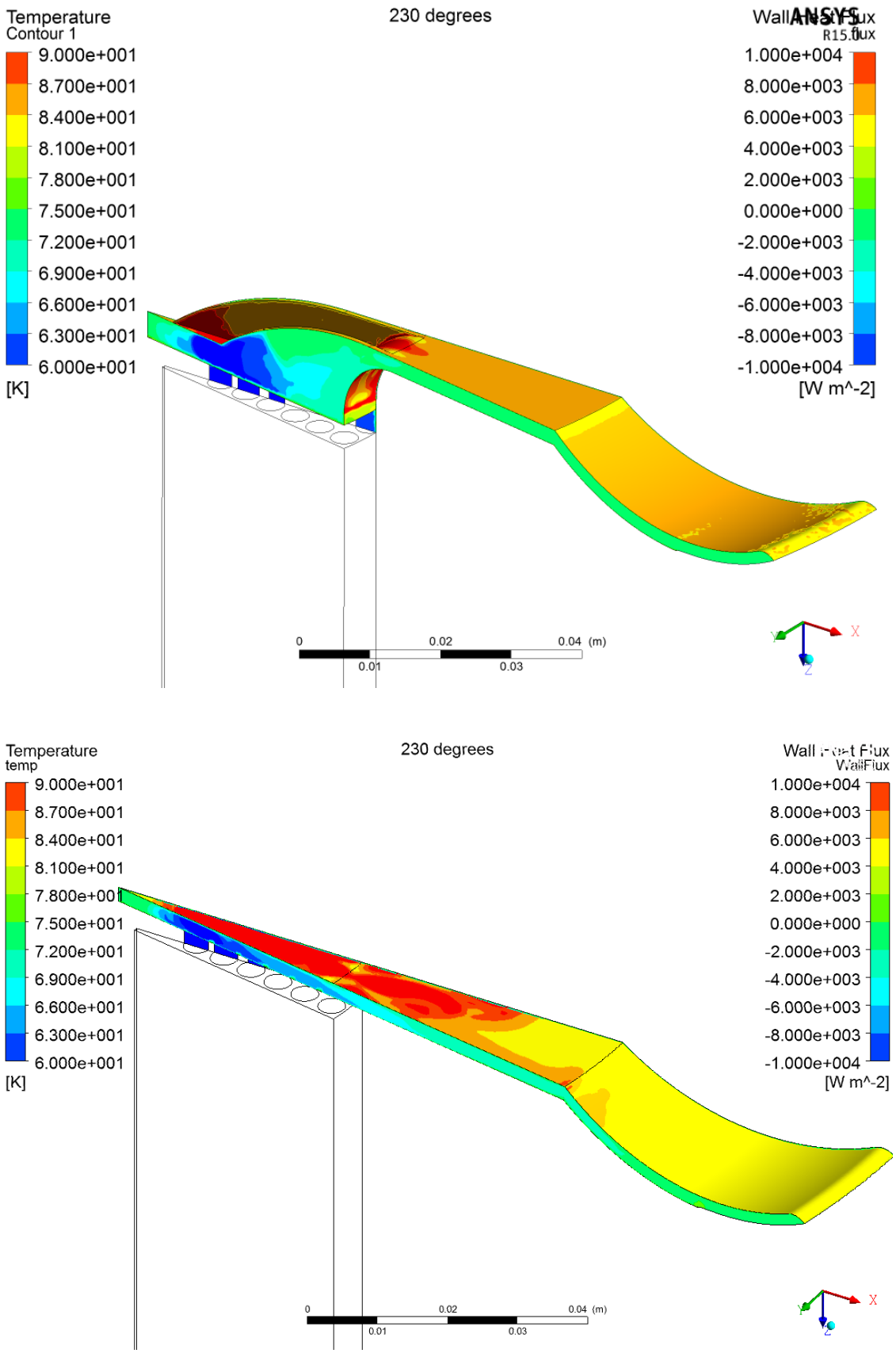

Figure 6-3: The cold domain at LSE showing the wall heat flux and gas temperature. Above, the second prototype and below the model without the central cold heat exchanger slots.

6.2.3 *THE EFFECT OF A LARGER PRESSURE WAVE*

The third improvement is to increase the swept volume of the DPWG. The pressure wave amplitude is 2.90 bar whereas the DPWG is capable of up to 5 bar of pressure wave amplitude. More swept volume from the DPWG will produce a larger amplitude pressure wave, more work input and therefore more cooling potential. Additionally, a larger pressure wave will produce more displacer movement which will further enhance the cycle. The CHC200 DPWG had at one stage been over-stroked with a full stroke of 3 mm [15], as opposed to the 2.5 mm standard, for a swept volume of 240 ml which increased its delivered pV power input by 70%, showing the benefits of increased swept volume.

Sage was first used to model the consequences of increasing the swept volume. The Sage model from Section 6.3 was run with an increased PWG stroke of 3.5 mm (amplitude 1.75 mm) to produce a swept volume of 280 ml. A 3.5 mm stroke was chosen as it was close to the largest stroke that could be achieved by the CFX mesh movement without bad distortion causing negative volume elements. The result of the modified Sage model was an increase in the pressure wave amplitude from 3.27 bar to 4.7 bar, the pV power increased from 2460 W to 4730 W and the cooling power from 169 W to 326 W. More importantly Sage predicted an increase in the displacer movement with the higher pressure wave amplitude; from the original 0.43 mm at 45.6° phase angle (with respect to the DPWG crank angle) to 0.61 mm at 41.4°.

The CFX model for Section 6.2.2 was run with 1.75 mm amplitude movement on the DPWG and 0.51 mm displacer at 41.4^0, remembering that to be closer to the experiment, the original CFX model had a displacer stroke of 0.1 mm less than the Sage prediction. The CFX result was similar to Sage, with the cooling power increasing to 326 W, and an efficiency of 27% of Carnot from a lower input power of 3520 W. CFX predicted the pressure wave amplitude to be 4.1 bar which, although less than Sage's predicted 4.7 bar, is still closer to the 5 bar maximum.

Noting that the DPWG pressure wave amplitude limit is 5 bar, an even larger DPWG would be necessary to take full advantage of the pressure wave. Of importance is that the trend is for better performance.

There are some notable scaling factors with the increase in swept volume. Increasing the swept volume by a factor of 1.4 scales the pressure wave amplitude by close to 1.4 (proportional), the input power by close to 2 (1.4^2) and the cooling power by 1.9 (almost 1.4^2).

6.3 Summary of Improvements

Table 6-2 summarises the predicted performance of the proposed design improvements. The effect of increasing the area of the warm domain for heat transfer is a reduction in the warm domain temperatures with no increase in cooling power but a significant increase in efficiency. Removing the slotted cold heat exchanger has a significant effect on the cooling power but little change in the conditions in the warm domain. The overall result is higher performance and an increase in efficiency. The low amplitude of the pressure wave means that a larger swept volume pressure wave generator is desirable for the cold head. Increasing the stroke of the DPWG on the model from 2.5 mm to 3.5 mm almost doubled the cooling power.

Table 6-2: Summary of CFD and Sage predictions for improved designs

Parameter	**Second prototype. CFD/Sage/experiment**	**Stage 1. Enhanced warm heat exchange. CFD/Sage**	**Stage 2. Removed cold heat exchanger. CFD/Sage**	**Stage 3. Increased stroke. CFD/Sage**
pV work in, W	2260 / 3090 / 2280	1800 / 2961	1750 / 2460	3520/ 4763
Pressure wave amplitude, bar	3.14 / 3.40 / 3.36	2.87 / 3.24	2.90 / 3.3	4.131/ 4.71
Cooling power at 77 K, W	**130 / 104 / 89**	**126 / 96.4**	**175 / 169**	**326/ 326**
Carnot Efficiency, %	16.7 / 9.8 / 11.3	20.2 / 10.4	29.0 / 19.9	27.0/ 19.8
Heat rejection – warm, W	1196 / 2941 / -	984 / 2190	945 / 2078	1567/ 3970
Heat rejection – holes, W	477 / 211 / -	809 / 560	825 / 518	1772/ 1060
Heat rejection – PWG, W	806 / 41 / -	380 / 39	350 / 34	660/ 65
Cycle average warm side of displacer gas temp, K	357 / 301 /-	335 / 306	335 / 305	345/ 310
Cycle average cold gas temperature, K	75.6 / 76.3 / -	75.6 / 76.4	69 / 72.4	67.5/ 69.7

Throughout the modelling, the Sage models predicted more heat transfer on the warm side of the displacer than the CFD models. This difference in heat transfer was then reflected by the temperatures of the gas in the transfer holes and DPWG gas space and hence the amount of heat

transfer occurring with the walls. The difference in heat transfer rates between the two models was further exaggerated by Sage's lower average gas temperatures. Intuitively, looking at the pV input power and considering the displacer movement, CFX would appear closer to the experiment than Sage. However, Sage's predictions of the pressure amplitude and cooling power were closer to the experiment than CFX. Practically, both models replicate the experiment well; the early experiment that showed heat on the displacer adds weight to CFX as it predicts higher average gas temperatures to achieve heat transfer. This was demonstrated by the very first proof-of-concept run-up, where the composite displacer showed signs of high temperatures on the warm side. However, in the cold domain, Sage and CFX were closer to each other in both the predicted heat transfer (cooling effect) and average gas temperature.

Near the conclusion of this work, the cryocooler team at Callaghan Innovation (a renamed IRL) had built a 330 ml swept volume DPWG which could be used in the future to provide the required pressure wave to achieve a full 5 bar pressure wave and hence even more performance. Using the scaling factors from Section 6.2.3, it is estimated that the 330 ml DPWG would produce ~440 W from 4700 W of pV with a pressure wave amplitude of ~ 4.8 bar. Taking into account the 100 W difference between the second prototype's modelling and experiment, a net 340 W of cooling could be expected from such a machine; the input power would still be 4700 W and Carnot efficiency then be 21%.

To put these numbers into context, the 330 cc DPWG currently powers a pulse tube that produces 480 W of cooling from 7 kW of pV power, with a Carnot efficiency of 12%. The metal diaphragm free-piston Stirling head would produce a similar power to the pulse tube with significantly better efficiency. It is recommended that the next prototype iteration is made with extra warm domain cooling, no cold heat exchanger and is fitted to the new 330 ml PWG.

A key result of the improved design is that both the Sage and CFX models confirm the second question in the hypothesis of this work for the cold domain; that the diaphragm geometry does provide sufficient heat exchange area in the cold domain to remove the requirement for a separate heat exchanger.

More importantly, the modelling confirms the first question in the hypothesis of this work; that it is possible to make a useful diaphragm free-piston Stirling cryocooler with similar or better performance than existing pulse tube cryocoolers of the same size.

7 CONCLUSIONS

This work explored the concept of using metal diaphragms in the construction of a free-piston Stirling cryocooler. Well-known free-piston Stirling cryocooler theory is combined with the novel metal diaphragm pressure wave generator technology to produce a cryocooler with the high efficiency and performance typical of Stirling cryocoolers and the potential for long life at a reasonable cost. This was achieved by suspending and sealing the displacer with metal diaphragms, which remove the necessity for rubbing seals, oil ingress or expensive clearance gap pistons. Cryocoolers, being refrigerators that remove heat from below 120 K for rejection at ambient temperatures, are challenging machines to design and manufacture as they involve significant amounts of heat exchange when moving the working gas from the warm parts of the machine to the cold parts and back again. Small shifts in individual component performances can be the difference between useful refrigeration at the target temperature and a useless machine that warms the intended cold application.

7.1 Hypotheses

Two hypotheses have been tested in this thesis. The first hypothesis was that a free-piston Stirling cryocooler could be made using metal diaphragms to suspend and seal the displacer, achieving a balance of gas forces in a similar manner to the diaphragm pressure wave generator (DPWG) previously invented by the author. The second hypothesis was that the flat geometry of metal diaphragms produces a large surface area-to-volume ratio that can be used efficiently for heat transfer, thus eliminating, or at least significantly reducing, the need for expensive heat exchangers.

7.1.1 HYPOTHESIS 1

The first hypothesis was tested by construction of a proof-of-concept prototype using a 200 ml swept volume DPWG and a displacer that was suspended and sealed with identical diaphragms as the 200 ml DPWG. The one-dimensional frequency domain modeller Sage was used to model the system and guide the prototype's design. The first model predicted a very promising performance. The completion of the prototype's design and the subsequent manufacture of the prototype introduced a number of compromises that significantly reduced the performance. The proof-of-concept prototype produced cooling, reaching a lowest temperature of 109 K. Whilst the experimental performance was less than originally anticipated, the Sage model, once updated to include all the changes that occurred during construction of the prototype, modelled the experimental performance well. In particular, the Sage model produced a good prediction of the displacer movement over a range of frequencies and two configuration changes. Moreover,

the Sage model predicted that the cooling performance would not be very good, and the measured 109 K low temperature was consistent with the Sage model.

The model and experiment indicated that improvements could be made to the design, such as a softer spring rate for the intermediate diaphragm, smaller diaphragms for the displacer and more heat exchange in the middle of the cold gas space. During that time, DPWG development had progressed at IRL and a DPWG had been developed with 60 ml swept volume making smaller diaphragms available. The diaphragms from the 60 ml DPWG were incorporated into the design of a second prototype along with a softer intermediate diaphragm (made of rubber) and a slotted heat exchanger in the centre of the cold space. The Sage model predicted better performance and, importantly, refrigeration at 77 K (the temperature of nitrogen liquefaction which will be the main purpose of this cryocooler).

A second prototype was constructed and tested. Its performance was much better than the first prototype and its macroscopic behaviours, such as displacer movement, correlated well with the Sage model. There were discrepancies between the Sage model and the experiment, such as Sage over-estimated the displacer movement amplitude by 0.1 mm. The prototype produced 29 W of cooling at 77 K and reached a lowest temperature of 55 K, which is a significant improvement in performance on the first prototype and, while not sufficient for a commercial cryocooler of its size, confirms this first hypothesis.

7.1.2 HYPOTHESIS 2

The second hypothesis questioned whether the diaphragm geometry produces a compression or expansion space with radial flows and sufficient area to make heat exchangers redundant. The main driver behind the desire to remove heat exchangers is cost, as the manufacture of many fine heat exchanger slots or holes is expensive. Heat exchangers are used in conventional Stirling machines because the pistons used for compression and expansion typically have stroke-to-diameter ratios of around one, producing small surface area-to-volume ratios and thus are poor for heat exchange. Since heat exchangers are essentially dead volumes and require large areas, the flow channels in them are very small, requiring expensive manufacturing processes such as wire cutting. In comparison to pistons, metal diaphragms have very short strokes due to the stiffness of the metal. Therefore metal diaphragms require large moving areas to achieve the required swept volume for a gas cycle. This large area can be used for heat exchange and produces radial flows that can enhance heat exchange.

The first proof-of-concept prototype relied entirely on the diaphragm areas for heat exchange. Performance was poor for a number of reasons other than the heat exchange area, so it neither supported nor refuted the hypothesis. The second prototype had a slotted heat exchanger in the

centre of the cold space. The prototype worked better than the first, but not as well as desired and again did not provide much insight into the second hypothesis. The Sage model predicted similar behaviour to the prototype with regard to the displacer movement and pressure wave, but not the heat transfers in the diaphragm spaces on the cold or warm sides of the displacer.

More understanding of the heat transfer in the diaphragm spaces was necessary to test the hypothesis, and improve performance. The CFD approach was used to understand more about the flows inside the diaphragm Stirling cryocooler and test Hypothesis 2.

7.2 Modelling the diaphragm geometry heat transfer with CFD

The Sage modelling tool developed over the past two to three decades has become an industry standard modelling tool for cryocoolers. Sage is a one-dimensional modeller that combines thermodynamic theory with empirical correlations, so is able to model standard cryocooler components, such as variable-volume cylinders, slotted heat exchangers, resonant pistons, and their interactions with good accuracy. The diaphragm geometry is modelled in Sage as a large area short-stroke piston with a variable-volume cylinder object. Its surface area-to-volume ratio is very different to the norm that Sage was developed for, and the radial flows created by the diaphragm geometry are not found in typical piston cylinders. Hence Sage's in-cylinder heat transfer calculations are not well verified for the diaphragm geometry. Moreover, Sage interprets the surface area and volume of the diaphragm system as a long thin cylinder; in other words a tube with a long stroke piston.

The CFD modelling tool, in this case ANSYS® CFX, is a good tool for modelling flow in complex geometries as it breaks a complex geometry into small simple elements, the theory for each element being well verified. The CFD solver then solves for the whole set of elements simultaneously. To get an accurate model from the CFD code, the model needs to be properly constructed with appropriate boundary conditions applied. So for each type of problem, a methodology for construction of the model needs to be validated. The normal approach is to model a situation, similar to the one for study, which has a well-known experimental or analytical solution. When the model is validated, it can then be adapted to the geometry for study with confidence.

This thesis has shown that Sage, despite being developed for a different geometry, can model free-piston Stirling cryocoolers having metal diaphragms with sufficient accuracy to be a very useful optimisation tool, and its fast run time allows mapping of the many parameters in the cryocooler design. CFD, being an excellent tool for refining the design through understanding of the flows within the cryocooler, complements Sage very well. The long run times associated with CFD - weeks for a single data point - limit its utility for optimisation which means that it is best used for confirming the Sage model, as well as understanding and refining the final design.

7.2.1 Validation of ANSYS® CFX for the diaphragm Stirling cryocooler

The validation of the CFX methodology started with modelling an oscillating volume gas space, validated against experimental work by Kornhauser [32]. In each validation case, a Sage model was constructed to compare with the CFX and experimental results. Kornhauser used entropy-driven hysteresis losses in a gas spring as the dependent variable in the experiments; dividing the work done in a single cycle by the adiabatic compression produced a non-dimensional

hysteresis loss and allowed comparison of experiments over a wide range of conditions. Kornhauser and Smith found that both adiabatic and isothermal compression had low hysteresis losses and there was an in-between condition with high hysteresis losses. Kornhauser used the magnitude and position of the high-loss condition to validate a range of analytical solutions to the problem.

Kornhauser introduced two concepts that proved very useful in the subsequent study of the diaphragm systems. The first was the Peclet number (Pe_w) based on the hydraulic diameter and rotational frequency of the oscillation to predict whether an oscillating compression is essentially adiabatic or isothermal, or in-between. The general form of the Peclet number, is the ratio of the advective transport rate to the diffusive transport rate. Kornhauser replaced the advective rate term with an equivalent for oscillating systems that have energy added via a piston, which then defined Pe_w as the ratio of the speed of heat generation to the ability to diffuse that heat to the walls. The maximum hysteresis loss for each case studied occurred within the same Pe_w range, namely 1×10^3 to 5×10^3. Near isothermal conditions occurred below $Pe_w = 10^2$ and near adiabatic over $Pe_w = 10^5$. The second concept was that, with the oscillating conditions in a typical Stirling machine, just about any solid material behaves as an isothermal wall with respect to the gas over a short period of time. Kornhauser successfully used micata which is normally thought of as an insulator. The aluminium, copper and stainless steel materials used in this thesis' prototypes and validation experiments were much better conductors than micata, so the assumption was valid. This simplifies modelling considerably as thermal oscillations in the walls did not need to be modelled.

The CFX model was able to predict Kornhauser's in-cylinder compression over a wide range of conditions from near-isothermal to near-adiabatic. Sage also predicted Kornhauser's results well, although Sage's prediction in the middle ground of high-hysteresis loss was not as good as the CFX prediction.

Once the CFX method had been validated using gas spring hysteresis of a standard piston-in-cylinder geometry, the geometry was progressively changed to become more like the diaphragm Stirling system to be studied. The first change was to produce a flattened geometry of the same volume and 2:1 volume-ratio as Kornhauser's experiment. The key change was the hydraulic diameter, which should be accounted for by the Peclet number, meaning that a similar plot to Kornhauser's would be expected. The CFX model of the flat cylinder predicted very similar results to Kornhauser's experiment, confirming its validity. The Sage model of the same situation, however, had an offset in the position with the high loss region occurring at a lower Pe_w, suggesting that adiabatic conditions were achieved at lower frequencies or smaller

hydraulic diameters, which is consistent with an under-prediction of the heat transfer in the flat cylinder.

The next validation step was to combine Kornhauser's compression piston/cylinder section with a flat radial geometry section, keeping Kornhauser's original volume and a volume ratio of 2:1. This model, called the T-cylinder model because of its shape, would then introduce a radial flow component to the flat section. It would also be closer to a Stirling machine that has sections with different hydraulic diameters. A key question was: Which dimension should be used to calculate the hydraulic diameter for the Pe_w; the piston diameter or the thickness between the walls of the radial section? The CFX model showed that the radial section dominated heat transfer with the high loss section matching Kornhauser's Pe_w when the radial section's dimension was used. Interestingly, in this case, the Sage prediction of the position of the high-loss section agreed with CFX; however, Sage predicted much higher losses at near-isothermal and near-adiabatic conditions. Graphical outputs of streamlines and temperature profiles provided by CFX showed the formation of vortices in the model, created by the sharp transition between the two sections and the relative damping of the temperature oscillations between the two sections. In the T-cylinder model, the polytropic index was considered as a dependent variable for validation, as it depends on the isothermal/adiabatic transition and is not dependent on accurate timing in an experiment.

The third validation of the CFX method was to add a diaphragm-based compression space to the T-cylinder model. The geometry of the 200 ml DPWG used in the proof-of-concept experiments was used. As the geometry and situations now deviated considerably from Kornhauser's experiments, a fresh set of validation experiments was performed. In both the validation experiment and the model, the pressure wave was produced by movement of the DPWG diaphragm and propagated through a tube into a flat volume that was the same diameter as the 60 ml DPWG diaphragm. Thus the experiment had the typical volumes and hydraulic diameters of the second prototype Stirling cryocooler. The tube in the centre was an empty tube, rather than being filled with a regenerator matrix, but was the same volume as the void volume of the regenerator in the second prototype. The choice to exclude the regenerator was made as regenerators are very complex heat transfer devices which would dominate the rest of the model's heat transfer. The polytropic index was chosen as the dependent variable for the experiments as it was time-independent, reducing one source of error. Small timing errors in the synchronisation of experimental recordings meant that the hysteresis results were not useful. The CFX model agreed well with the experiment over a range of conditions and Peclet numbers spanning the isothermal to adiabatic range. The CFX model gave insights into the flows

and interactions between sections of different hydraulic diameters and gave sufficient confidence in the CFX methodology to proceed with modelling the whole cryocooler.

7.2.2 CFX MODEL OF THE SECOND PROTOTYPE

A model of the second prototype was created with CFX. To reduce computational requirements, the full geometry was reduced to a wedge of the cryocooler gas space with symmetry conditions on the wedge sides, producing a semi-axisymmetric model. The model used moving meshes to model the diaphragms in the same manner as the validation experiment. The most significant change between the prototype model and the validation experiment model was the addition of the regenerator matrix. Being a porous matrix with a high surface area-to-volume ratio, the regenerator was modelled using the porous domain model provided in CFX. Modelling regenerators has been a study over the past decades and obtaining a very accurate regenerator model in CFX would have dominated this work and distracted from the task at hand. As the purpose of this study is the heat exchange in the radial flows of the compression and expansion spaces of the Stirling cryocooler, a simplified approach was used for the regenerator model. Instead, a simple factorial experiment was set up to determine the porous media properties, comparing the CFX model with a Sage model using standard piston-in-cylinder type geometry and conditions that are well within Sage's normal modelling range. The factorial experiment produced a set of properties that were similar to those determined by Cha [70], whose doctoral thesis was based on flow bench measurement of regenerator matrix properties for input into a Fluent CFD model of a pulse tube cryocooler.

Armed with a simplified porous regenerator model, the CFX model of the second prototype was run to simulate the cryocooler with its cold surfaces at 200 K, the temperature of a set of characterisation experiments performed on the second prototype, and at 77 K, the temperature of nitrogen condensation at atmospheric pressure. The 200 K and 77 K models broadly agreed with Sage and the experiments and, in all but a few aspects. Over all, CFX was closer to the experimental results than Sage.

The CFX modelling exercise showed the strengths and weaknesses of the approach.

The strengths were:

- CFX allowed much more interrogation of the conditions within the model than Sage.
- Numerical outputs showed how much, and where, heat was being absorbed and rejected by the gas

- It showed that the instantaneous heat transfer rates were orders of magnitude higher than the cyclic averages and that the gas temperatures within the warm and cold domains were not uniform.
- The graphical outputs showed hot gas exiting the warm side of the regenerator and cold gas exiting the cold side of the regenerator, and where in the cold space the gas was only performing as a gas spring.
- CFX predicted the overall energy flows in and out of the cryocooler better than the Sage model although both models agreed closely in their predictions of the cooling power.

The weaknesses of the CFX model were:

- It did not predict displacer movement, which had to be an input from either experiment or Sage (when no experimental data available).
- The computation time. Sage could solve a case in a few seconds, up to a minute at the most, whereas CFX took 2-3 weeks, or more in some cases, to reach a quasi-steady-state solution that was close to the final solution for a particular configuration.
- The CFX models frequently had mesh problems, when the moving mesh would stretch too far and produce a negative volume element. Fault finding and fixing a sub-standard mesh was a lengthy process with the long run times.

In spite of its limitations, CFX provided many insights into the inner workings of the Stirling cryocooler and would allow improvement and the eventual prediction of a useful cryocooler. These were:

- CFX was used to calculate cycle average heat transfer coefficients for the warm and cold domains. The heat transfer coefficients were then able to be used to calculate whether the heat exchange areas were sufficient. The cold domain was shown to have ample area whilst the warm domain needed more area.
- The model showed poor gas flow in the cold domain, with gas bypassing the sides of the slotted cold heat exchanger. It showed that the extra area provided by the slotted heat exchanger provided less benefit than the dead volume it created; the cold gas flowing from the regenerator did not penetrate the cold domain very well, leaving a significant part of the cold domain to operate as a gas spring. The intuitive improvement of adding the cold heat exchanger in the second prototype did not work.
- CFX showed very hot gas exiting the warm side of the regenerator, which was not cooled as well as the Sage model predicted, and raised the average rejection temperature. Dead volume at the circumference of the warm side of the displacer was shown to be not useful.

- CFX highlighted the need to understand the thermal diffusion length in oscillating heat transfer spaces. This is the distance from the wall in the gas space where the damping effect of the wall is significant on the oscillating temperature of the gas. The CFD elements adjacent to heat transfer walls need to be thin enough to have several elements through the thermal diffusion length. Several methods of calculating the thermal diffusion length were used, the most useful of which was to calculate the hydraulic diameter required to achieve a Pe_w of 2000 for the conditions modelled. Hence the oscillating compression conditions in the gas next to the wall were such that significant gas-to-wall heat transfer was taking place, but any distance further out the compression would be closer to adiabatic. The thermal diffusion length calculated from the Pe_w agreed with the other estimates well, including the CFD element size that produced the best results in the validation exercises, and with general slotted heat exchanger experienced by the author in design of pulse tube cryocoolers. It was found that the thermal diffusion length reduced with temperature and was significantly smaller at 77 K than at ambient.

7.2.3 *Confirmation of the second Hypothesis*

The second hypothesis postulated that the diaphragm geometry produced sufficient radial flow and surface area to make heat exchangers redundant. The analysis with CFX provided numerical results and insights into the heat transfer inside the cryocooler that were used to test this hypothesis. It was found that in both the cold and warm domains, a significant phase difference existed between timing of maximums of heat transfer and radial gas velocity. Heat transfer was dominated by the temperature oscillation in the gas (from compression and expansion) and, while the radial gas velocity aided convection, gas velocities were highest when the temperature difference was low and vice versa. Thus the radial flow part of the second hypothesis was not confirmed.

Calculation of the cycle-average heat transfer coefficient between the gas and walls showed that, in the cold domain, there was sufficient area to perform the heat transfer required for the cryocooler's function without an additional heat exchanger; which confirmed the hypothesis for the cold domain. The cycle-average heat transfer coefficient calculated for the warm domain (the DPWG and the warm side of the displacer) was sufficient to reject heat for the prototype; although if significantly more pV power was produced by the DPWG, then additional surface area would be required. However, the surface area provided by the diaphragms would still be able to provide a significant amount of heat transfer; thus reducing the size of the heat exchangers required in the warm domain. The second hypothesis was confirmed in regards to

the surface area and the analysis pointed to the potential for further improvements of the design.

7.3 Improved Design

The CFX model, backed up by Sage and experiments, indicated that the second prototype design could be improved further to achieve significantly better performance.

The first indicated improvement was to add more heat exchange area in the warm domain. The areas of the warm side of the displacer and DPWG were fixed by their diaphragm sizes so the only geometry available for increasing area was the area of the transfer holes. The number of transfer holes was increased in the model according to the heat transfer coefficient to drop the gas-to-wall temperature difference from 55 K to 30 K. The CFX model was altered accordingly and confirmed the effect of the extra area. CFX predicted that the change in warm gas temperature did not greatly affect the cooling power but increased the efficiency of the machine.

The second indicated improvement was to remove the small slotted heat exchanger in the cold domain. The heat exchanger was incorporated into the second prototype as a response to the observation that the centre of the cold domain cooled more than the circumference. However, CFX showed that the extra gas volume created by the heat exchanger lowered the amount of gas travelling further out in the cold domain, creating significantly more dead volume and, although increasing the area near the regenerator, had an overall negative effect on performance. CFX predicted a significant increase in cooling power with the heat exchanger removed, and since no increase in input power occurred, the efficiency was almost doubled. Interestingly, Sage agreed with CFX on this aspect.

The third and final indicated improvement was to increase the DPWG swept volume. The pressure wave amplitude of the second prototype was only 3.2 bar which is significantly lower than the 5 bar amplitude that the DPWG was designed to deliver. The way to increase the pressure wave amplitude was to increase the swept volume of the DPWG. The stroke of the DPWG was increased in the CFX model and the model re-run. The effect of extra swept volume was a proportional increase in pressure ratio, and an approximately squared increase in input and cooling power. The cycle efficiency was still close to the lower swept volume model. During this study the cryogenic refrigeration team at Callaghan Innovation had developed a 330 ml swept volume DPWG. Scaling the improved design to 330 ml swept volume produced a predicted 340 W of cooling with an input power of 4700 W and Carnot efficiency of 21%. This compares very well with the pulse tube tested for the 330 ml DPWG which achieved 480 W at 77 K with a Carnot efficiency of 12%. The metal diaphragm free-piston Stirling cryocooler indeed has the potential to be commercially competitive.

7.4 Future work

This thesis has shown that it is possible to use metal diaphragms to produce a free-piston diaphragm cryocooler that will provide useful refrigeration for the liquefaction of nitrogen to provide a cryogenic process liquid for industrial or superconducting applications. Further study and prototype development is required before a commercial cryocooler can be made.

The improved design from Chapter 6 has yet to be manufactured and tested. It is anticipated that the next prototype will produce competitive performance, both in terms of cooling power and efficiency. The prototype should be made for the new 330 ml swept volume DPWG. More instrumentation must be fitted to the next prototype, in particular for measurement of gas temperatures in the warm and cold domains. These measurements could be used to validate the CFX and Sage models. Additionally, for model validation a method is needed for measuring the displacer position while running the prototype with the cryostat fitted.

More work on determining the regenerator properties is required to improve the CFX model and get a better match between the CFX model and the prototype. Such a model will be instrumental in developing larger and better diaphragm Stirling cryocoolers. Similarly, work could be performed to improve the correlation between Sage, CFX and the prototype. Determination of empirical adjustment factors for Sage's heat transfer would aid the accuracy of Sage and make it a more accurate mapping tool for optimisation. In this role, the massively reduced computational time of Sage compared with running adequately realistic CFX models would be a particular advantage.

Once the cryocooler has demonstrated its ability to perform efficient refrigeration at the target 77 K, a condensation system needs to be incorporated into it so it can perform its duty as a nitrogen liquefier. Finally, once the prototype has demonstrated its function in a liquefaction mode, a detailed machine design that allows for economical manufacture must be developed.

REFERENCES

[1] W. E. Gifford, "The Gifford-McMahon Cycle," in *Proceedings of Cryogenic Engineering Conference*, 1965.

[2] W. E. Gifford and L. R.C., "Pulse Tube Refrigeration Progress," in *International Advances in Cryogenic Engineering - Volume 10*, 1964, pp. 69–79.

[3] E. I. Mikulin, A. A. Tarasov, and M. P. Shkrebyonock, "Low-Temperature Expansion Pulse Tubes," in *Advances in Cryogenic Engineering SE - 72*, R. W. Fast, Ed. Springer New York, 1984, pp. 629–637.

[4] J. F. Maguire, F. Schmidt, S. Bratt, and T. E. Welsh, "Development and Demonstration of a HTS Power Cable to Operate in the Long Island Power Authority Transmission Grid," *Supercond. IEEE Trans.*, vol. 17, no. 2, pp. 2034–2037, 2007.

[5] G. Snitchler, B. Gamble, and S. S. Kalsi, "The performance of a 5 MW high temperature superconductor ship propulsion motor," *Appl. Supercond. IEEE Trans.*, vol. 15, pp. 2206–2209, 2005.

[6] G. Snitchler, B. Gamble, C. King, and P. Winn, "10 MW Class Superconductor Wind Turbine Generators," *Appl. Supercond. IEEE Trans.*, vol. 21, pp. 1089–1092, 2011.

[7] R. Cable, N. D. Glasson, M. P. Staines, Z. Jiang, and N. S. Allpress, "Verification Testing for a 1 MVA 3-Phase Demonstration Transformer Using," *IEEE Trans. Appl. Supercond.*, vol. 23, no. 3, 2013.

[8] O. Naeckel and M. Noe, "Design and Test of an Air Coil Superconducting Fault Current Limiter Demonstrator," *Appl. Supercond. IEEE Trans.*, vol. 24, pp. 1–5, 2014.

[9] E. T. P. Sheahen and B. Mcconnell, "Cryogenic Roadmap, US Department of Energy Superconductivity Program for Electric Systems.," 2001.

[10] "Cyomech AL600 Cryocooler." [Online]. Available: http://www.cryomech.com/AL600.php.

[11] S. a. Potratz, T. D. Abbott, M. C. Johnson, K. B. Albaugh, J. G. Weisend, J. Barclay, S. Breon, J. Demko, M. DiPirro, J. P. Kelley, P. Kittel, A. Klebaner, A. Zeller, M. Zagarola, S. Van Sciver, A. Rowe, J. Pfotenhauer, T. Peterson, and J. Lock, "Stirling-Type Pulse Tube Cryocooler With 1Kw of Refrigeration At 77K," in *AIP Conference Proceedings*, 2008, vol. 985, pp. 42–48.

[12] "Stirling SPC-1 Cryocooler." [Online]. Available: http://www.stirlingcryogenics.com/products/cryogenic-cooling/cryogenic-cooling-plants-80K-1000W/all/spc-1/.

[13] A. J. Caughley, D. J. Haywood, and C. Wang, "A Low Cost Pressure Wave Generator Using Diaphragms," *Adv. Cryog. Eng.*, vol. 53B, no. 1, pp. 1122–1129, 2008.

[14] A. J. Caughley and C. Wang, "Development of a Diaphragm Pressure Wave Generator for Cryocoolers," *Cryocoolers 15*, pp. 309–315, 2008.

[15] A. J. Caughley, N. Emery, and N. D. Glasson, "Diaphragm Pressure Wave Generator Developments At Industrial Research Ltd," in *Advances in Cryogenic Engineering*, 2010, pp. 695–702.

[16] A. Caughley, P. Branje, and T. Klok, "30 kW Metal Diaphragm Pressure Wave Generator," in *Advances in Cryogenic Engineering*, 2013.

[17] C. Wang, A. J. Caughley, and D. J. Haywood, "Development of a Low Cost High Frequency Pulse Tube Cryocooler," *Adv. Cryog. Eng.*, vol. 53B, pp. 1555–1561, 2008.

[18] N. Emery, A. Caughley, N. Glasson, A. Tucker, and M. Gschwendtner, “Development of a High Frequency Pulse Tube,” in *Cryocoolers 16*, 2011, pp. 175–182.

[19] N. Emery, A. Caughley, N. Glasson, J. Meier, M. Nation, and J. Tanchon, “Co-axial pulse tube development,” *Cryocoolers 17*, vol. 1, pp. 135–141, 2012.

[20] N. Emery, A. Caughley, N. Glasson, and J. Meier, “Co-Axial pulse tube for oxygen liquifaction,” *Adv. Cryog. Eng.*, vol. 57A, pp. 183–189, 2012.

[21] J. Tanchon, Y. Contardo, T. Trollier, A. Ravex, A. J. Caughley, D. Pooke, R. Buckley, and T. Robinson, “Integration of Very High Capacity Pulse Tube Cryocoolers on cryo-trapping demonstrator,” in *CEC/ICMC 2009*, 2009.

[22] C. C. Lee and R. B. Pan, “Flexure Bearing Analysis Procedures and Design Charts,” in *Cryocoolers 9 SE - 48*, R. G. Ross Jr., Ed. Springer US, 1997, pp. 413–420.

[23] W. T. Beale, “Free Piston Stirling Engines - Some Model Tests and Simulations.” SAE, pp. 1–10, 1969.

[24] W. T. Beale, “Some Stirling Engine Designs for solar energy - concepts analysis and test results.” Presented to the Solar/energy Conference, Solar Energy Development Institute, Palm Stprings California - May 4 1977, p. 9–, 1977.

[25] W. T. Beale, “Development of Stirling Engines at Sunpower,” in *2nd international conference on stirling engines*, 1983, pp. 4–9.

[26] E. H. Cooke-Yarborough, E. Franklin, J. Geisow, R. Howlett, and D. West, “A new electrical power source for long term unattended operation,” in *Engineering in the Ocean Environment, Ocean ’74*, 1974, vol. 1, pp. 226–231.

[27] E. Cooke-Yarborough, “Small Stirling-Cycle Power Sources in Marine Applications,” *OCEANS’80*, pp. 457–462, 1980.

[28] D. Willem, J. Mullie, W. Groep, and B. T, “Increased capacity cryocoolers at Thales Cryogenics BV.”

[29] R. Radebaugh, “Cryocoolers: the state of the art and recent developments.,” *J. Phys. Condens. Matter*, vol. 21, no. 16, Apr. 2009.

[30] A. T. A. M. De Waele and W. Liang, “Basic dynamics of split Stirling refrigerators,” *Cryogenics (Guildf).*, vol. 48, no. 9–10, pp. 417–425, Sep. 2008.

[31] D. Gedeon, “Sage Modelling Software.” Gedeon Associates, Athens, OH 45701.

[32] A. Kornhauser and J. L. Smith, “A Comparison of Cylinder Heat Transfer Expressions Based on Prediction of Gas Spring Hysteresis Loss,” *Fluid Flow Heat Transf. Reciprocating Mach. ASME*, pp. 89–96, 1987.

[33] S. Carnot, *Reflexions sur la Puissance motrice du Feu Et sur les machines a developper cette puissance*. Paris: Gauthier-Villars, Imprjmer-Libraire, 1824.

[34] D. Haywood, “Investigation of Stirling-type Heat-pump and Refrigerator Systems as the Refrigerant,” University of Canterbuy, 2004.

[35] Brooks, “Polycold Cryotiger.” [Online]. Available: http://www.brooks.com/products/cryopumps-cryochillers/cryochillers/pcc-compact-coolers.

[36] J. H. Derking, D. W. Zalewski, M. Garcia, H. J. Holland, A. V. Mudaliar, H. Cao1, P. P. P. . Lerou, and H. J. M. ter Brake, “Progress in Joule-Thomson Microcooling at the University of Twente,” in *Cryocoolers 16*, 2011, pp. 463–471.

[37] B.-Z. Maytal and J. Pfotenhauer, “Special Topics,” in *Miniature Joule-Thomson Cryocooling SE - 9*, Springer New York, 2013, pp. 337–365.

[38] R. Radebaugh, “Development of the Pulse Tube Refrigerator as an Efficient and Reliable

Cryocooler," *Inst. Refrig.*, p. 1999, 2000.

[39] P. Kittel, a. Kashani, J. M. Lee, and P. R. Roach, "General pulse tube theory," *Cryogenics (Guildf).*, vol. 36, no. 10, pp. 849–857, Oct. 1996.

[40] P. C. T. Boer, "Pressure Heat Pumping in the Orifice Pulse-Tube Refrigerator," in *Advances in Cryogenic Engineering SE - 172*, vol. 41, P. Kittel, Ed. Springer US, 1996, pp. 1373–1382.

[41] P. Kittel, "Are P-V and T- S Diagrams Meaningful for Regenerative Cryocoolers ?," *Cryocoolers 16*, pp. 437–444, 2011.

[42] A. S. Tucker, M. A. Gschwendtner, and D. Haywood, "Some Insights into Stirling Machine Behavior," in *Cryocoolers 16*, 2011, pp. 317–326.

[43] Sunpower, "Cryotel Cryocoolers." [Online]. Available: http://sunpowerinc.com/cryocoolers/cryotel-family/.

[44] D. S. Glaister, M. Donabedian, D. G. T. Curran, and T. Davis, "An overview of the performance and maturity of long life crycoolers for space applicaitons.," in *Cryocoolers 10*, 1999, pp. 1–19.

[45] H. McCallion, "Forced vibration," in *Vibration of linear mechanical systems*, Longman Group Ltd, 1973, pp. 14–20.

[46] J. Tanchon, T. Trollier, A. Ravex, and E. Ercolani, "Prototyping a Large Capacity High Frequency Pulse Tube Cryocooler," in *Cryocoolers 14*, 2006, pp. 133–139.

[47] H. K. Versteeg and W. Malalasekera, *An introduction to computational fluid dynamics: the finite volume method*. Pearson Education Ltd, 2007.

[48] T. W. Simon and J. R. Seume, "A survey of oscillating flow in Stirling engine heat exchangers," 1988.

[49] I. Barreno, S. C. Costa, M. Cordon, M. Utar, I. Urrutibeascoa, X. Gomez, and G. Castillo, "Numerical correlation study of the pressure drop in Stirling engine heat exchangers," *Int. J. Therm. Sci.*

[50] A. J. Caughley and D. Haywood, "Pressure Wave Generator," WO2006/1127412006.

[51] E. H. Cooke-Yarborough and D. J. Ryden, "Mechanical Power Losses caused by imperfect heat transfer in a nearly-isothermal stirling engine," *SAE*, vol. 3, pp. 3.307–3.312, 1985.

[52] A. A. Kornhauser and J. L. Smith, "Application of a Complex Nusselt Number to heat transfer during compression and expansion.," *Trans. ASME*, vol. 116, pp. 536–542, 1994.

[53] D. Gedeon, "Mean-Parameter Modeling of Oscillating Flow," *ASME Jorunal Heat Transf.*, vol. 108, pp. 513–518, 1986.

[54] R. F. Barron, "Cryogenic Systems," in *Cryogenic Systems*, 2nd ed., NY: Oxford University Press, 1985, pp. 13–58.

[55] E. H. Cooke-Yarborough and F. Eng, "A stirling-cycle generator powered by radio-isotope," in *8th International Stirling Engine Conference and Exhibition*, 1997, pp. 361–370.

[56] E. H. Cooke-Yarborough, "Heat engines," US Patent 3,548,589.1970.

[57] R. Boukhanouf, S. B. Riffat, and R. Shuttleworth, "Diaphragm Stirling Engine Design," in *2nd International Heat powered Cycles Conference*, 2001, vol. 1, pp. 459–464.

[58] G. W. Swift and S. Backhaus, "Why High-Frequency Pulse Tubes Can Be Tipped," *Cryocoolers*, vol. 16, pp. 183–192, 2011.

[59] R. Radebaugh, a O. Gallagher, and J. Gary, "Secondary Pulse Tubes and Regenerators for Coupling to Room-Temperature Phase Shifters in Multistage Pulse Tube Cryocoolers," pp. 237–248.

[60] J. Tanchon, T. Trollier, S. Triqueneaux, and a. Ravex, "20–50K and 40–80K pulse tube coolers: Two candidates for a low temperature cooling chain," *Cryogenics (Guildf).*, vol. 50, no. 1, pp. 55–60, Jan. 2010.

[61] M. Arablu and a. Jafarian, "A modified two-stage pulse tube cryocooler utilizing double-inlet and multi-mesh regenerator," *Cryogenics (Guildf).*, vol. 58, no. September, pp. 26–32, Dec. 2013.

[62] P. Yan, G. Chen, J. Dong, and W. Gao, "15K two-stage Stirling-type pulse-tube cryocooler," *Cryogenics (Guildf).*, vol. 49, no. 2, pp. 103–106, Feb. 2009.

[63] A. A. Kornhauser and J. L. Smith, "Heat transfer with oscillating pressure and oscillating flow," in *Proceedings of the 24th Intersociety Energy Conversion Engineering Conference*, 1989, pp. 2347–2353.

[64] P. Lee K, "Lee, A simplistic model of cyclic heat transfer phenomena in closed spaces .pdf." .

[65] M. Mahajan, R. Jackson, and G. Flowers, "Experimental and Analytical Investigation of a Dynamic Gas Squeeze Film Bearing Including Asperity Contact Effects," *Tribol. Trans.*, vol. 51, no. 1, pp. 57–67, Jan. 2008.

[66] T. Huang, A. Caughley, R. Young, and V. Chamritski, "CFD Simulation and Experimental Validation of a Diaphragm Pressure Wave Generator," pp. 385–390.

[67] T. Huang and A. Caughley, "Comparison of sage and CFD models of a diaphragm pressure wave generator," vol. 1217, pp. 1217–1225, 2012.

[68] R. Gheisari, A. Jafarian, and M. R. Ansari, "Analytical investigation of compressible oscillating flow in a porous media: A Second-order successive approximation technique," *Int. J. Refrig.*, vol. 35, no. 6, pp. 1789–1799, Sep. 2012.

[69] D. Gedeon and J. G. Wood, "Oscillating-Flow Regenerator Test Rig: Hardware and Theory With Derived Correlations for Screens and Felts," 1996.

[70] J. J. Cha, "Hydrodynamic Parameters of Micro Porous Media for Steady and Oscillatory Flow: Application to Cryocooler Regenerators," Georgia Institute of Technology, 2007.

[71] J. S. Cha, S. M. Ghiaasiaan, and C. S. Kirkconnell, "Oscillatory flow in microporous media applied in pulse – tube and Stirling – cycle cryocooler regenerators," *Exp. Therm. Fluid Sci.*, vol. 32, no. 6, pp. 1264–1278, May 2008.

[72] R. Venkata, N. Bommisetty, D. S. Joshi, and V. R. Kollati, "Flow Loss in Screens: A Fresh Look at Old Correlation," vol. 3, pp. 29–34, 2013.

[73] D. W. Green and R. H. Perry, *Perry's Chemical Engineers Handbook*, 8th ed. McGraw-Hill, 2008.

[74] D. Gedeon, "Sage User ' s Guide." Athens, OH 45701, 2013.

[75] "Qdrive 2S241K cryocooler." [Online]. Available: http://www.qdrive.com/UI/Cryocoolers-.aspx?ptype=3&mcid=111&pcid=111&ccid=111&pid=6.

[76] "NIST Cryogenic Technologies group, material properties." [Online]. Available: http://cryogenics.nist.gov/MPropsMAY/materialproperties.htm.

[77] "Design guidelines for the selection and use of stainless steel." Nickel Development Institute courtesy of the Americaln Iron Institute.

[78] "CryoComp." Eckels Engineering, 2012.

[79] "ANSYS CFX-Solver Theory Guide," vol. 15317, no. November, pp. 724–746, 2009.

[80] E. Lenmmon, M. McLonden, and M. Huber, "Refprop." 2002.

[81] M. A. Lewis and R. Radebaugh, “Measurement of Heat Conduction through Bonded Regenerator Matrix Materials,” p. 80303, 2003.

[82] M. Stirling, “Improved flow patterns in etched foil regenerator,” *Cryocoolers 12*, pp. 499–505, 2003.

[83] Y. B. Tao, Y. W. Liu, F. Gao, X. Y. Chen, and Y. L. He, “Numerical analysis on pressure drop and heat transfer performance of mesh regenerators used in cryocoolers,” *Cryogenics (Guildf).*, vol. 49, no. 9, pp. 497–503, Sep. 2009.

[84] T. J. Conrad, E. C. Landrum, S. M. Ghiaasiaan, and C. S. Kirkconnell, “Anisotropic Hydrodynamic Parameters of Regenerator Materials Suitable for Miniature Cryocoolers,” in *Cryocoolers 15*, 2009, pp. 343–351.

APPENDIX A. GRAPHICAL OUTPUTS OF CFD MODEL OF 2ND PROTOTYPE AT 77 K

A.1 MID STROKE COMPRESSING

The first point of interest is mid-stroke while compressing, (MSC). For this analysis it is set at the 0° in the cycle. Figure A-1 shows streamlines and heat flows at MSC.

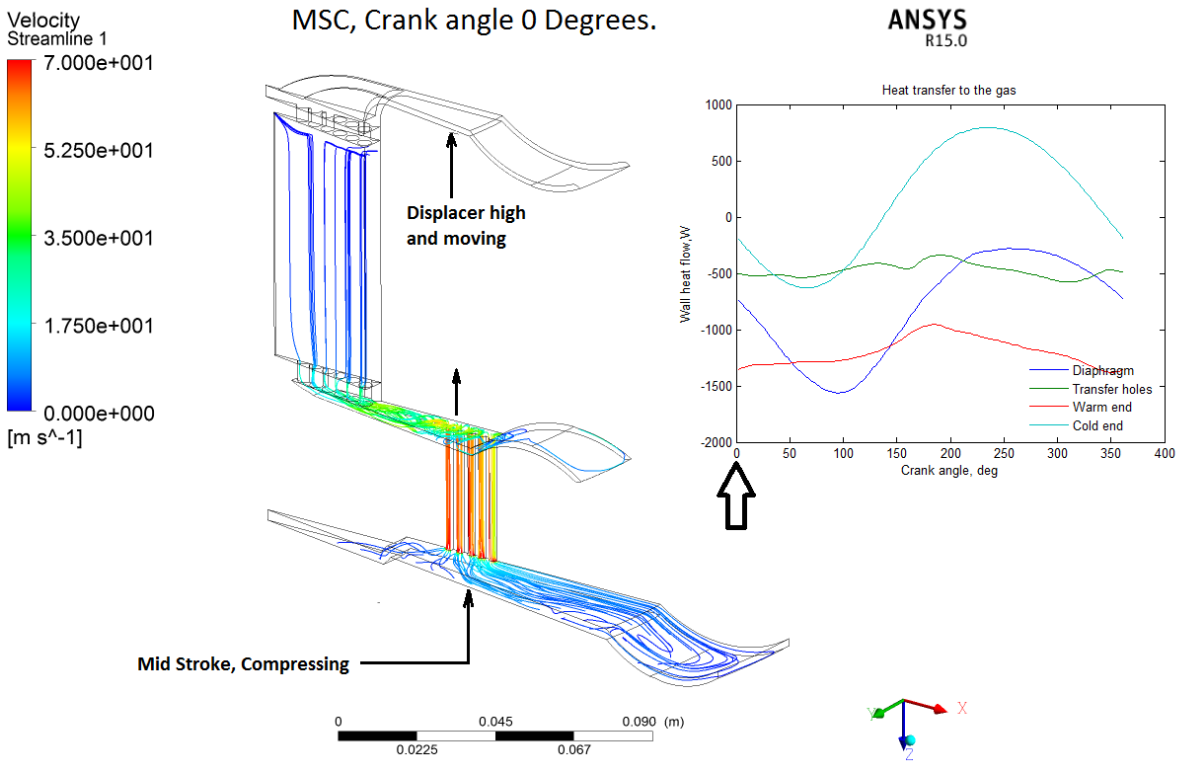

Figure A-1: Streamlines for 0° in the gas cycle, the compression diaphragm is Mid Stroke Compressing (MSC) .

At MSC the diaphragm piston is moving its fastest, and is associated with high gas flows in the direction from the diaphragm to the circumference of the cold space. Temperatures are near their cycle average values, as are the heat fluxes with the walls. At MSC the displacer, being ahead of the compression piston, is high and still moving up, reducing the volume of gas in the cold domain and forcing gas out of the cold volume. The horizontal streamlines at the top of the regenerator show where the flow (upwards) from the diaphragm meets the flow out of the cold domain. Heat transfer to the gas is negative in all regions, even in the cold domain, indicating that heat is rejected to the walls.

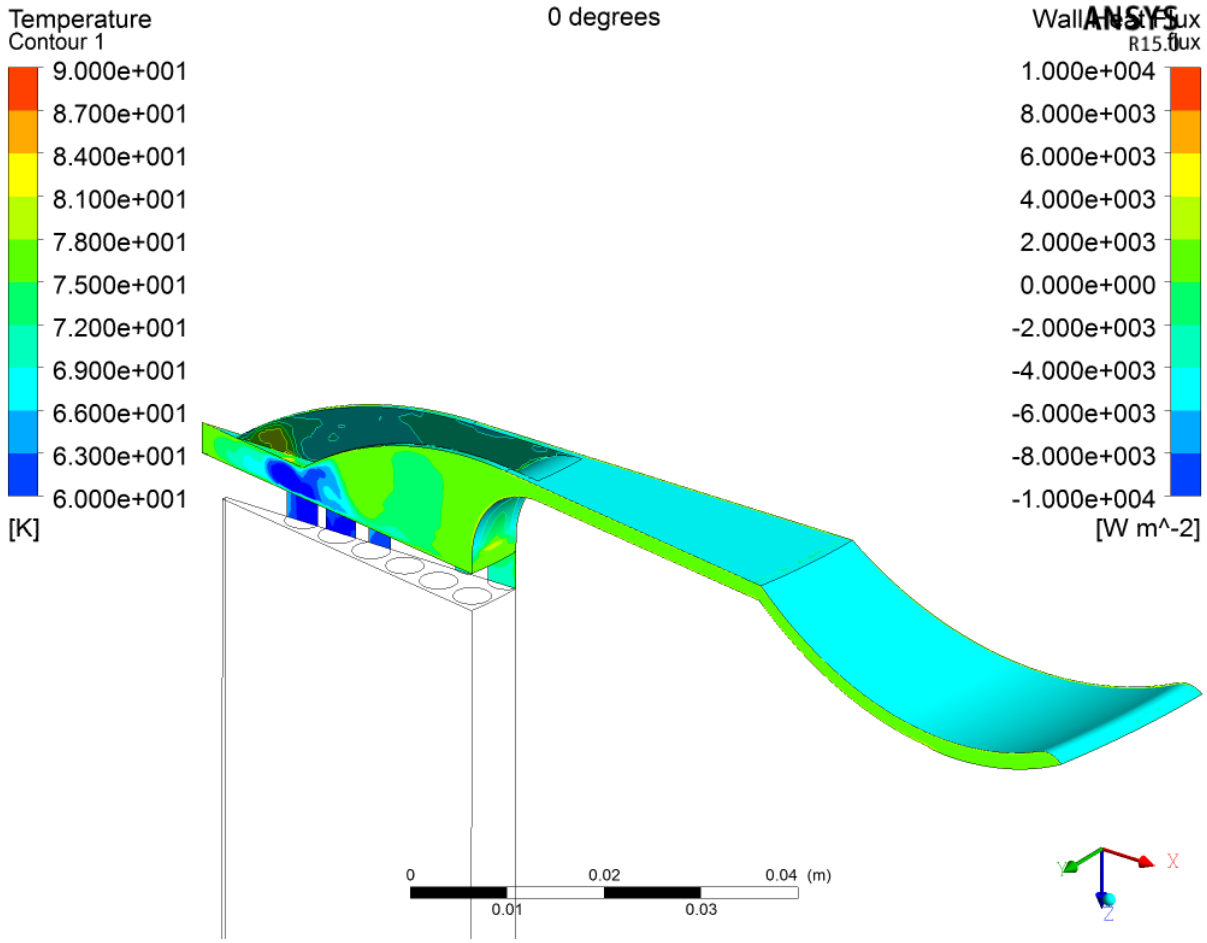

Figure A-2: Heat flux and gas temperature of the cold gas at MSC – crank angle 0°.

Figure A-2 shows the cold region's gas temperature and wall heat flux at MSC. The gas temperature in the majority of the cold region is close to the 77 K wall temperature, with a small amount colder, around 63 K next to the regenerator. The wall heat flux is low and negative, ~ 5 x 10^3 W m^{-2} for the majority of the wall area which indicates a net heat flow out of the gas.

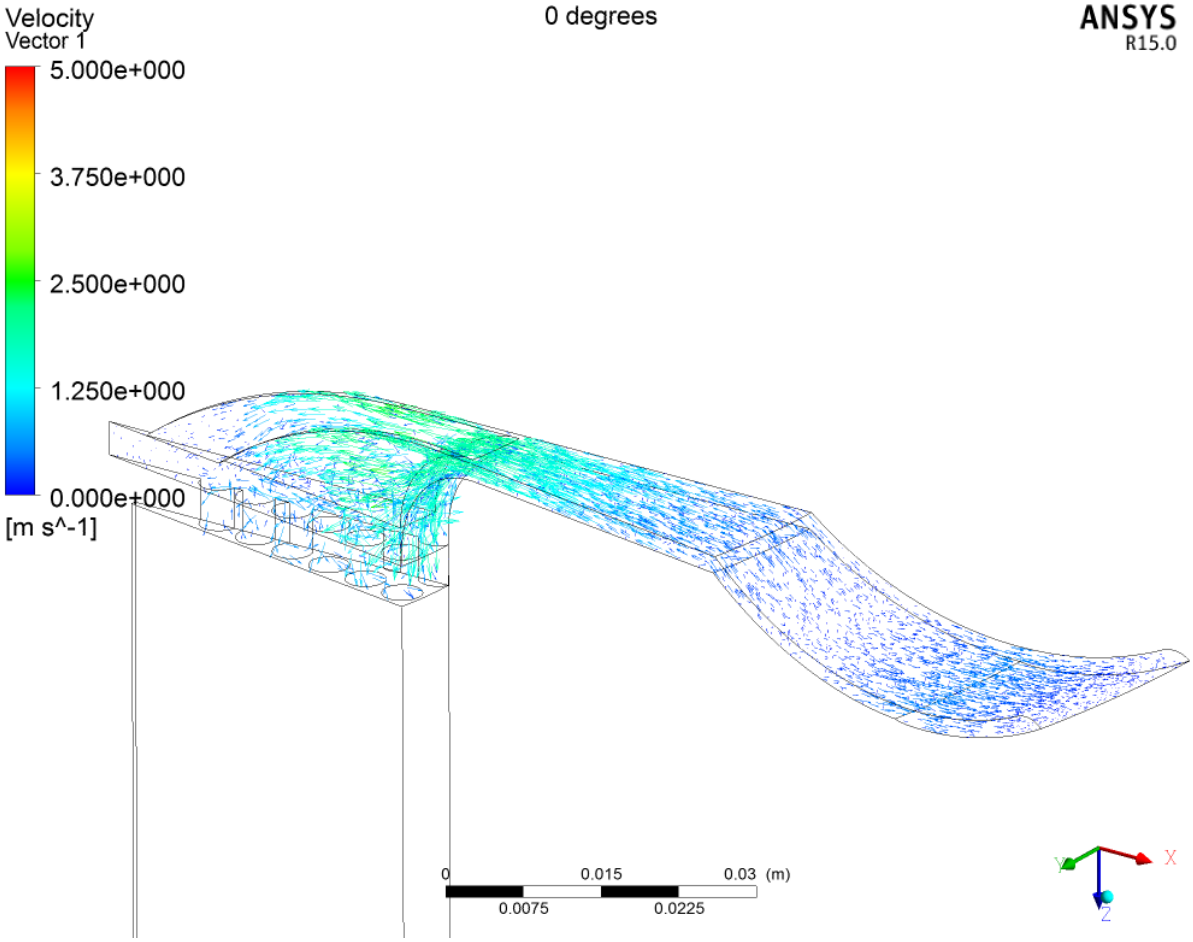

Figure A-3: Gas velocity vectors in cold gas space at MSC

Figure A-3 shows velocity vectors for the cold gas space. Where one might have expected gas to be entering the cold space from the maximum compression velocity of the DPWG, the vector plot shows that the gas is actually leaving the cold space. This is due to the upward movement of the displacer. The gas is only just leaving the cold space, as indicated by the streamlines in the regenerator in Figure A-1. Gas velocities are low, below 2.5 m s^{-1}, which is an indication of the appropriateness of the laminar gas model for this situation.

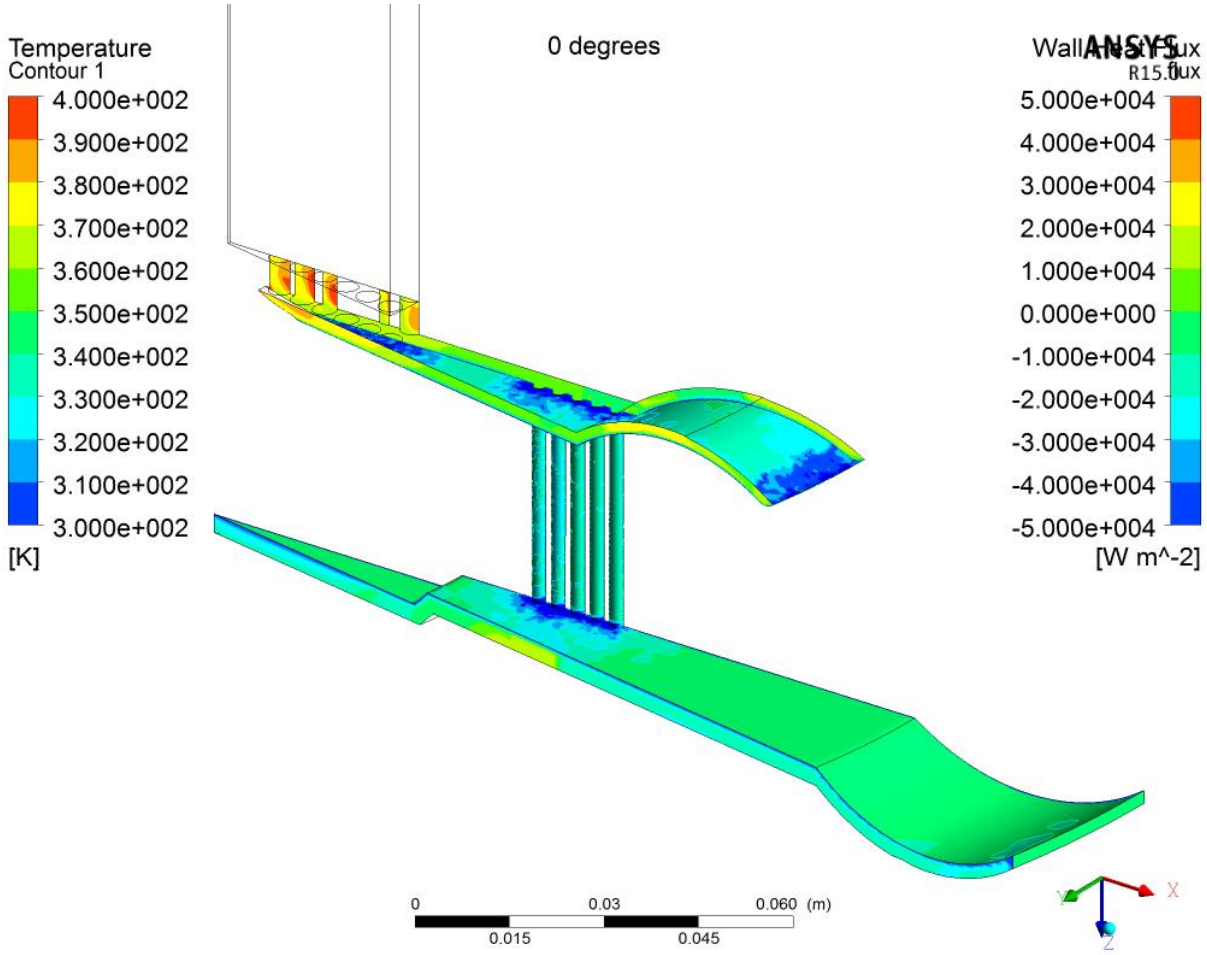

Figure A-4: Wall heat flux and temperatures for the warm gas space at MSC.

Figure A-4 shows the warm gas space wall heat flux and gas temperatures. Gas temperatures are close to cycle averages, which are above the 300 K walls, producing a negative heat flux. Heat flux is higher near the holes where velocities are higher. The thermal boundary layer is evident in the diaphragm gas temperatures with the gas temperature next to the wall close to 300 K. The last of the warm gas that came out of the regenerator in the previous cycle can be seen (yellow-red in the regenerator transfer plate holes) being pushed back into the regenerator.

A.2 High Stroke Compressing

HSC is 40° into the cycle and corresponds to a high compression piston which is moving up, producing significant velocities. Gas pressures and temperatures are high, approaching maximum values; the displacer is close to the top of its stroke (phase of 44.3°) with volume in the cold domain at its minimum. At this point it should be noted that in the ideal Stirling cycle, the displacer would lead the compression piston by 90°; thus the extreme displacer position would be at MSC. In the real machine analysed, the displacer phase leads by 44° with its maximum position at 46^0 into the cycle. HSC therefore has the displacer close to its maximum position. HSC has the potential for high gas-to-wall heat transfer as temperatures are close to their extremes.

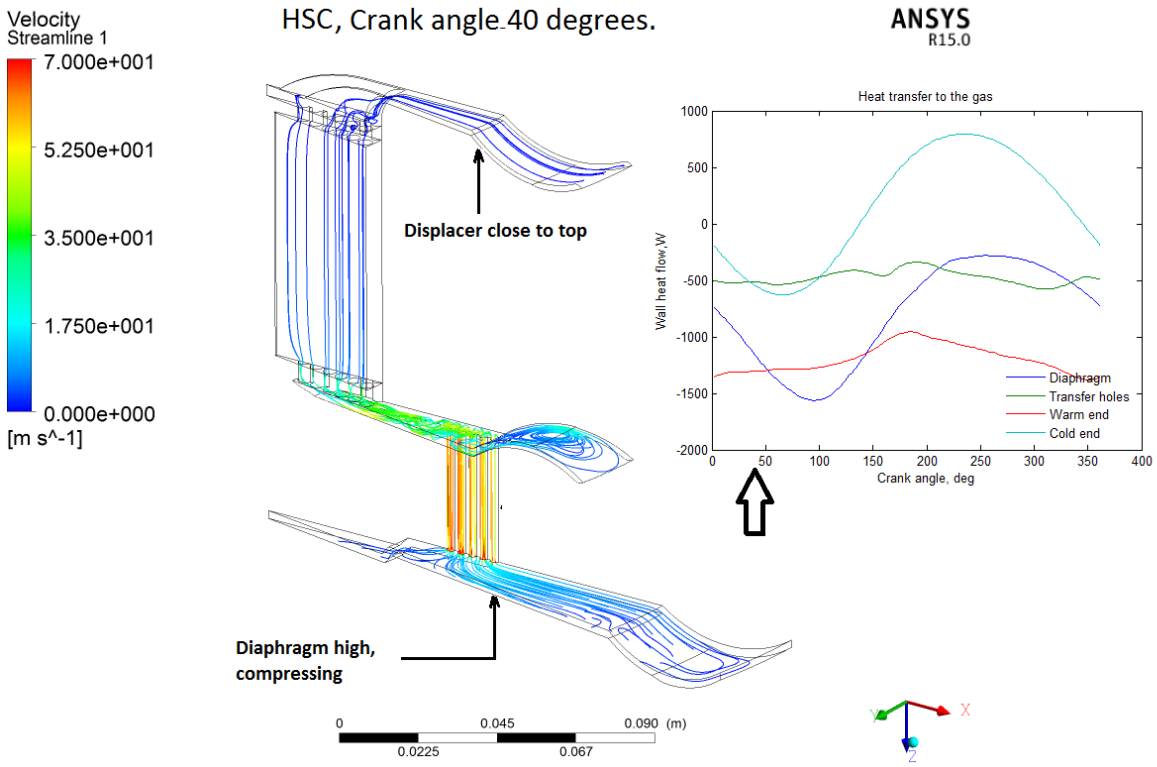

Figure A-5: HSC, 40° into the gas cycle where the displacer is close to the top of its travel.

Figure A-5 shows significant velocities flowing through the machine. The heat transfer plot shows that heat transfer in the diaphragm and cold spaces is high, but not at its maximum. There is a significant amount of eddy flow circulating at the outer diameter of the warm side of the displacer diaphragm.

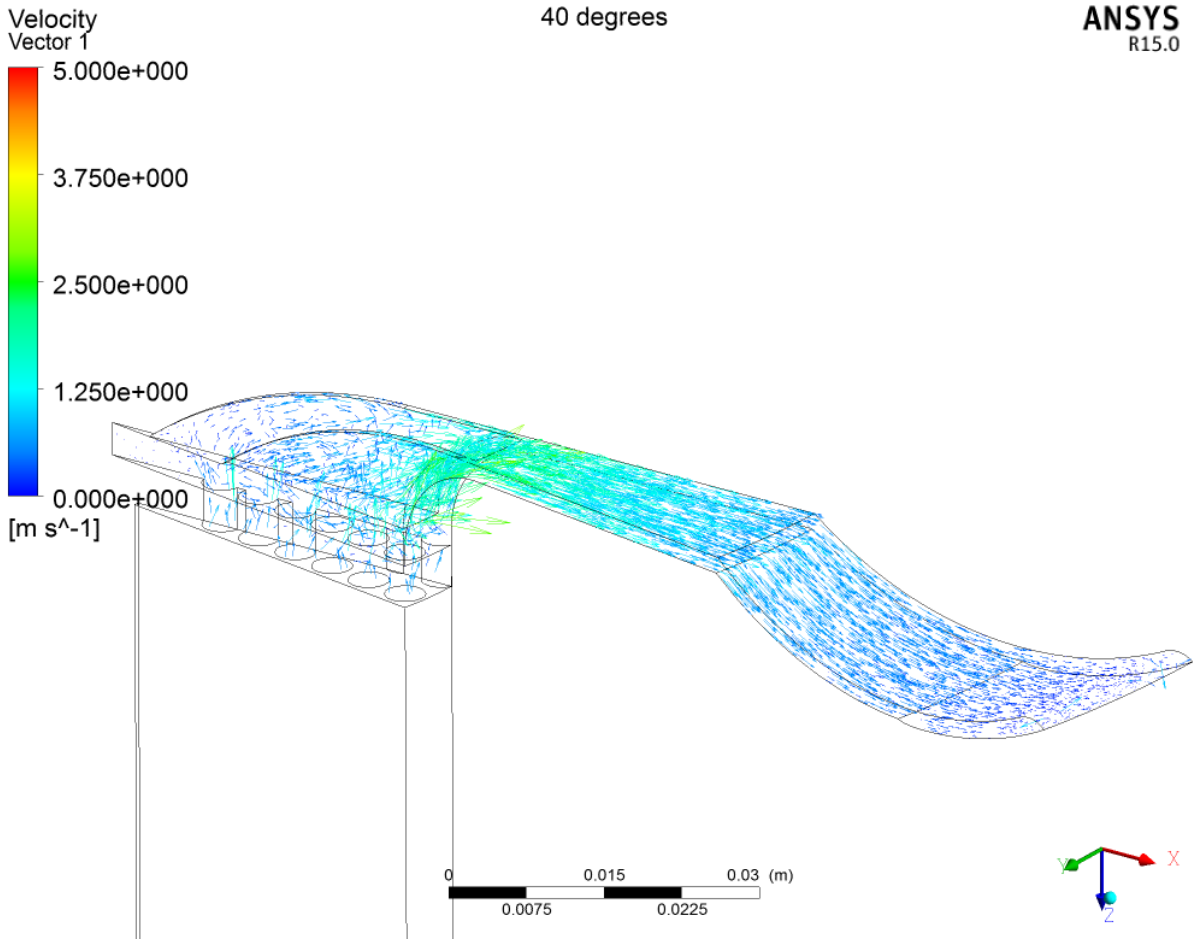

Figure A-6: Cold vectors for HSC; flow is leaving regenerator and going into cold space.

Figure A-6 shows the gas velocity vectors for the cold space at HSC. The gas is flowing into the cold space and velocities are low. The highest velocities are at the corner entering the radial section and decrease with increasing radius. It is also clear that the gas is not effectively flowing through the slots in the centre, rather it is bypassing by flowing around the corner.

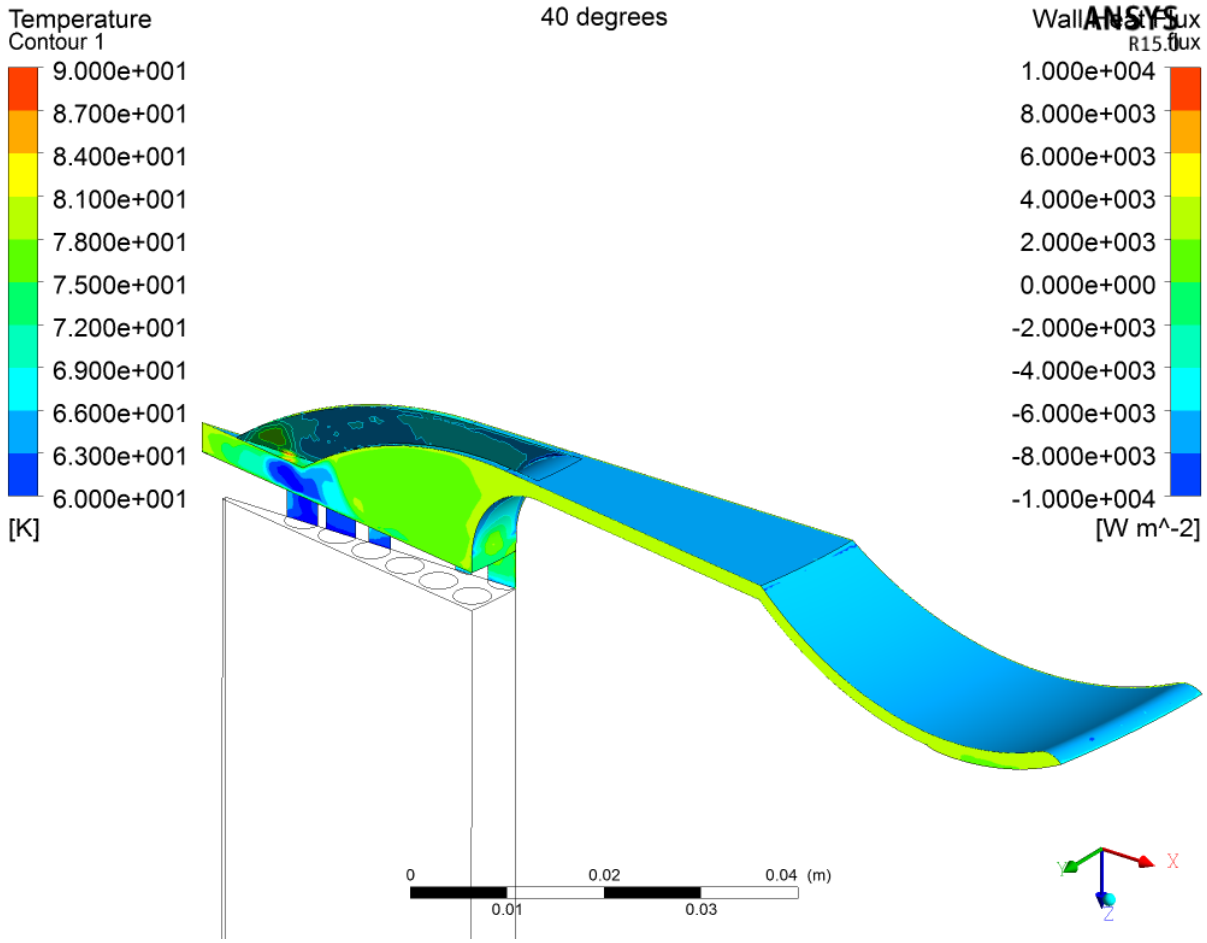

Figure A-7: Gas temperatures (wedge sides) and wall heat flux (surfaces) for the cold space at HSC.

Figure A-7 shows gas temperatures and wall heat flux for the cold space at HSC. The gas temperature for the majority of the radial sections is 78-81 K, above 77 K and the heat flux is in the order of -10^4 W m^{-2} ; indicating a high heat transfer from the gas to the walls. The heat flow plot in Figure A-5 shows that the total cold region heat transfer is at a rate of 500W at HSC.

The heat flux and gas temperatures in the warm space are very similar to the MSC condition.

A.3 Top Dead Centre

Top-Dead-Centre, TDC, is 90° into the cycle and shown in Figure A-8. The compression diaphragm is at the top of its travel, the overall system volume at its minimum, gas velocities are generally low and temperatures are near their highest. The displacer has started moving downwards. Heat exchange from gas to walls is high in the diaphragm and cold spaces.

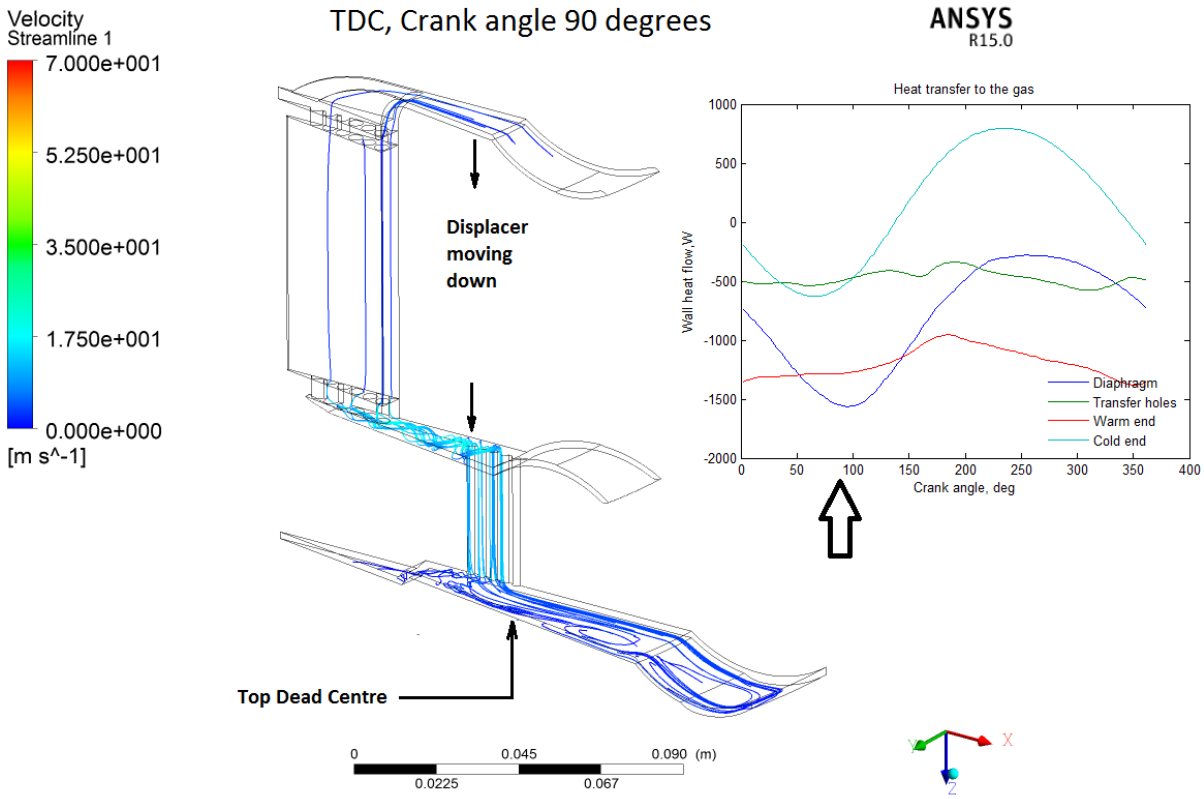

Figure A-8: Top Dead Centre, TDC, where the diaphragm is at its uppermost position and volume is minimised.

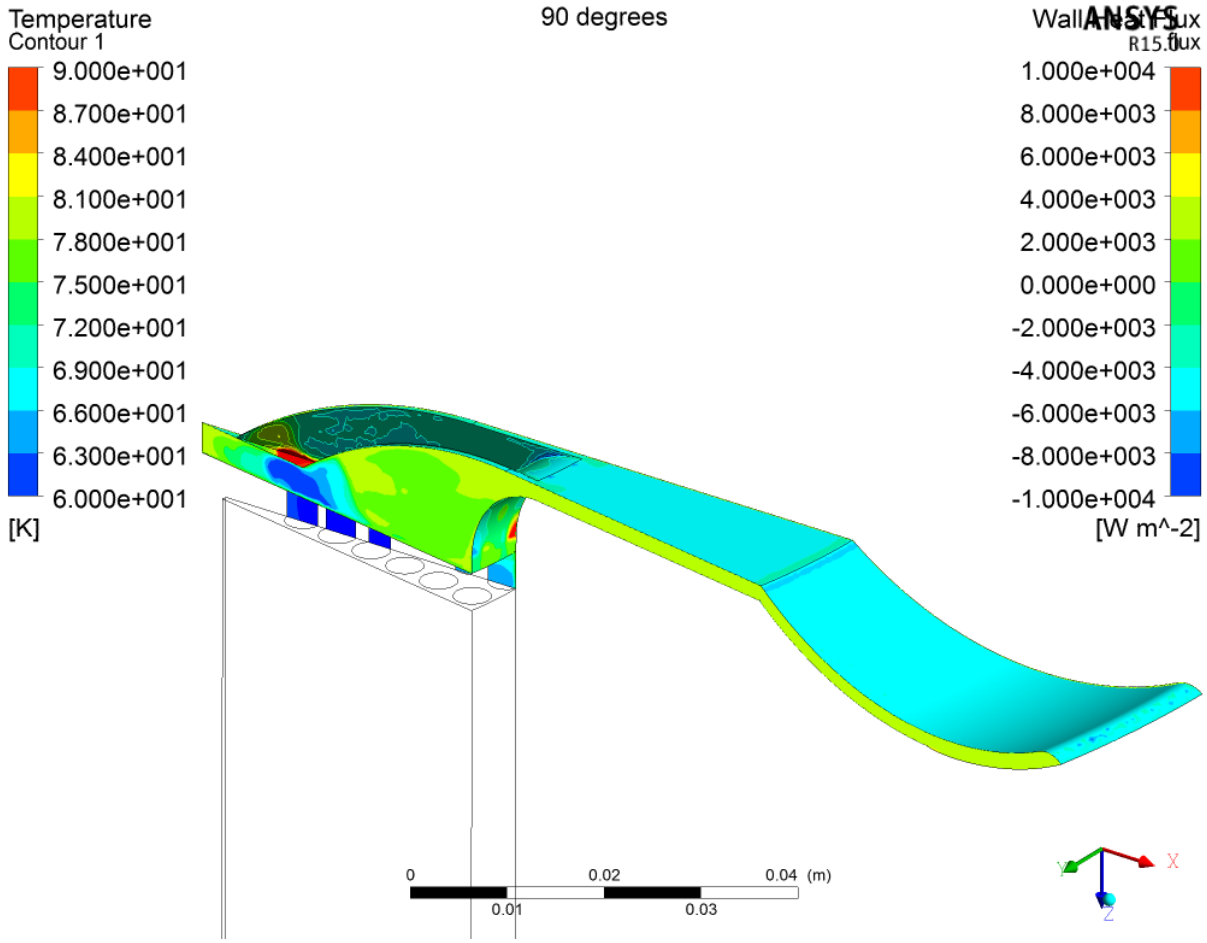

Figure A-9: Gas temperatures (sides) and heat flux (faces) for TDC.

Figure A-9 shows top dead centre with a negative heat flux, undesirable, is present due to the compression warming the gas above the 77 K walls. The gas volume is low due to the displacer being high. The displacer is moving downward bringing cold gas from the regenerator into the volume to complement the gas flow of the pressure wave, the cold gas flow from the regenerator moderates the compression heating effect, resulting in the gas near the regenerator being colder than the outer periphery which is acting more like a gas spring. Figure A-8 shows that the cold wall heat transfer, from gas to wall, is close to its maximum at TDC, with a transfer rate of - 600 W.

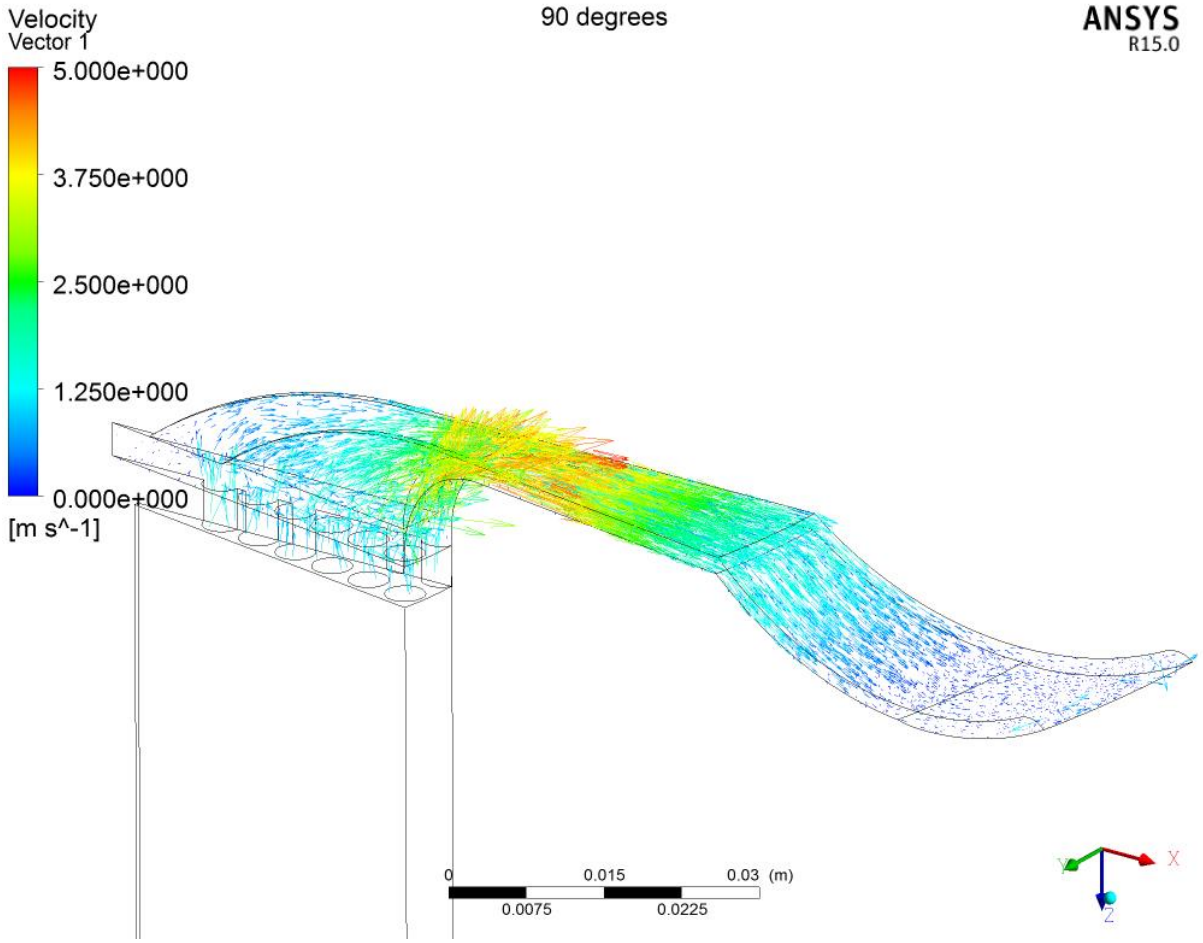

Figure A-10: Gas velocity vectors in the cold space for TDC

The gas velocities in the cold space, Figure A-10, show that the displacer movement is creating a high velocity gas flow into the radial space. The flow is near its maximum in the cycle, peaking at 5 m s^{-1}, and is short-circuiting the slots in the centre. The slowing of the flow with increasing radius is clear in the velocity plot. These relatively high velocities combined with the high temperatures are the reasons for the peak in heat flux at TDC.

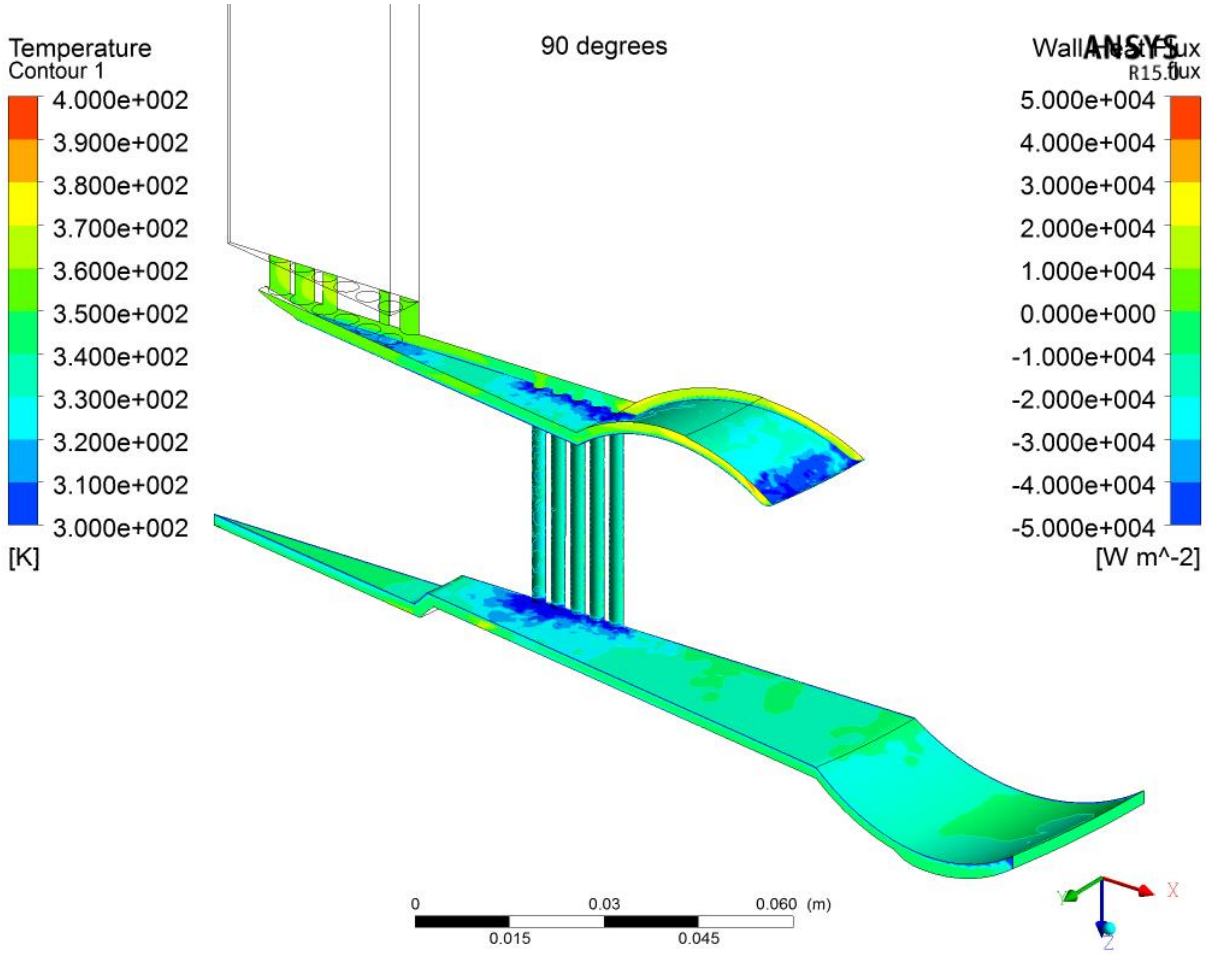

Figure A-11: Gas temperatures (sides) and heat flux (faces) for the warm domain at TDC

Figure A-11 shows the warm gas space temperatures and wall heat flux at TDC. Gas velocities are very low at TDC. Wall heat flux in the diaphragm space is high, around 2 to 3 x 10^4 W m^{-2} , totalling over the large area to its peak of 1550 W. The gas temperature on the warm side of the displacer is similar to the diaphragm at this point due to the origin of the gas being via the diaphragm. Hence the heat flux is similar to the diaphragm.

A.4 High Stroke Expanding

High stroke expanding, HSE, is 130° into the cycle,. The compression diaphragm has started moving downwards, expanding the gas. Additionally, the displacer is close to its maximum downwards velocity transferring gas into the cold domain; cold velocities into the cold domain are near maximum. These two opposing trends mean that the regenerator is being emptied from both ends which can be seen from the horizontal streamline in the regenerator in Figure A-12. At HSE the velocities in the cold region are near the maximum and Figure A-13 shows that the gas bypasses many of the slots in the cold heat exchanger.

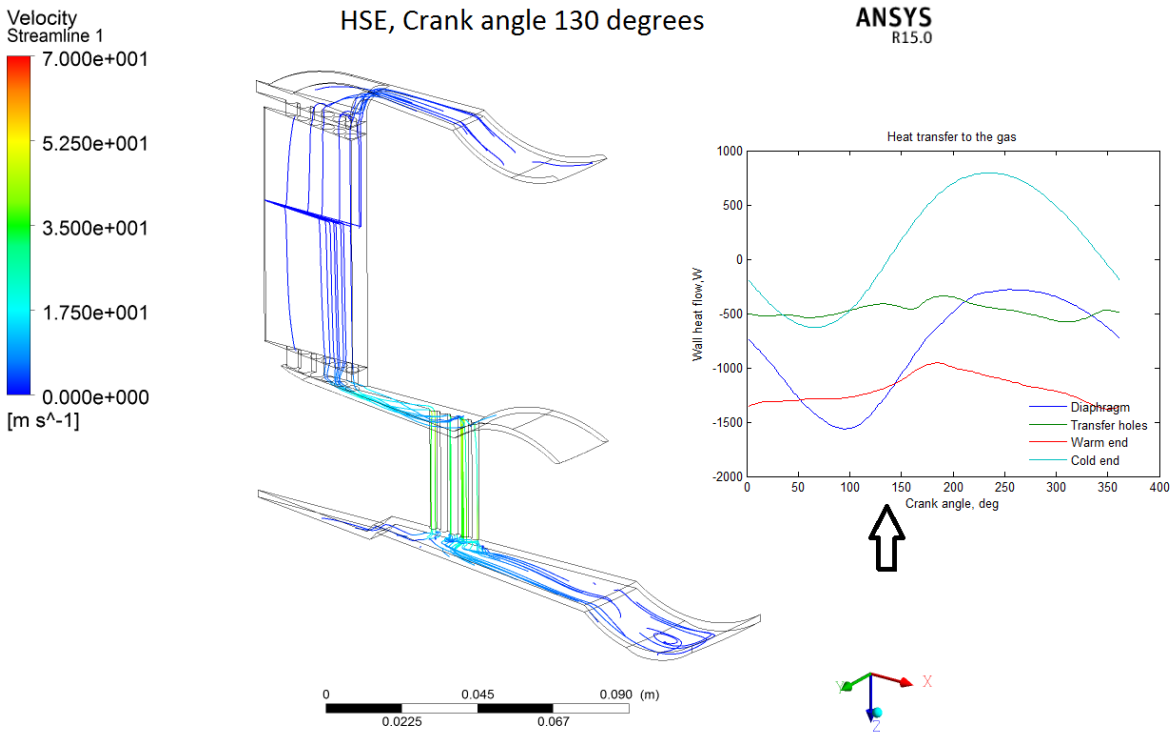

Figure A-12: Streamlines at High Stroke Expanding, HSE.

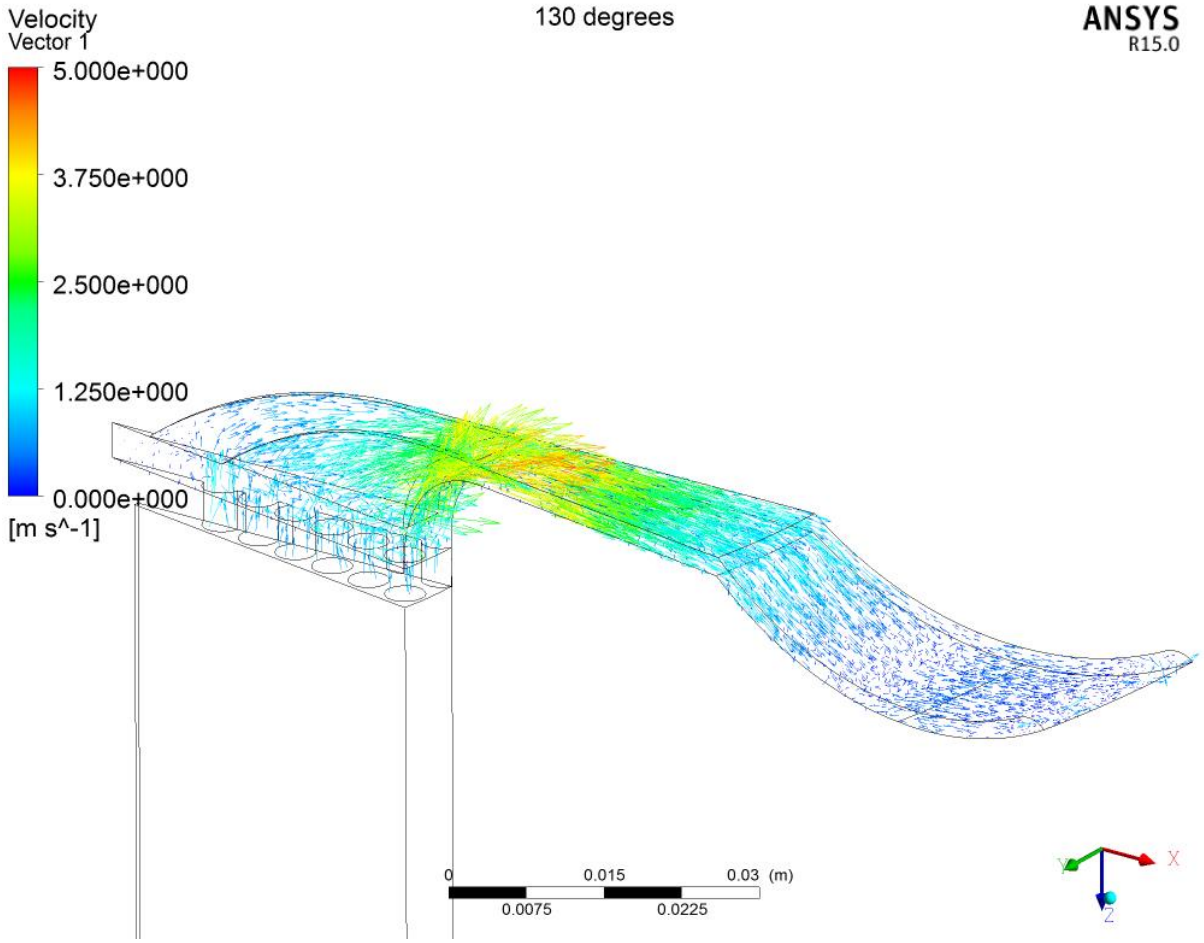

Figure A-13: Velocity vectors for the cold gas at HSE

Figure A-13 shows that although the compression diaphragm is moving downwards, expanding the gas, the flow is still into the cold domain. The displacer movement, which is close to its maximum speed, is increasing the volume of the cold domain and reducing pressure faster than the compression diaphragm. This brings cold gas into the cold domain from the regenerator which further increases the cooling effect. At HSE the gas temperature, Figure A-14, is close to the 77 K wall temperature, resulting in a near-zero wall heat flux. The equivalent of this condition would happen at MSE in a gas spring. A detail to be noted is that the cold gas exiting the regenerator produces some local cold spots and high positive wall heat flux (cooling the walls), which is a desirable effect for a refrigerator.

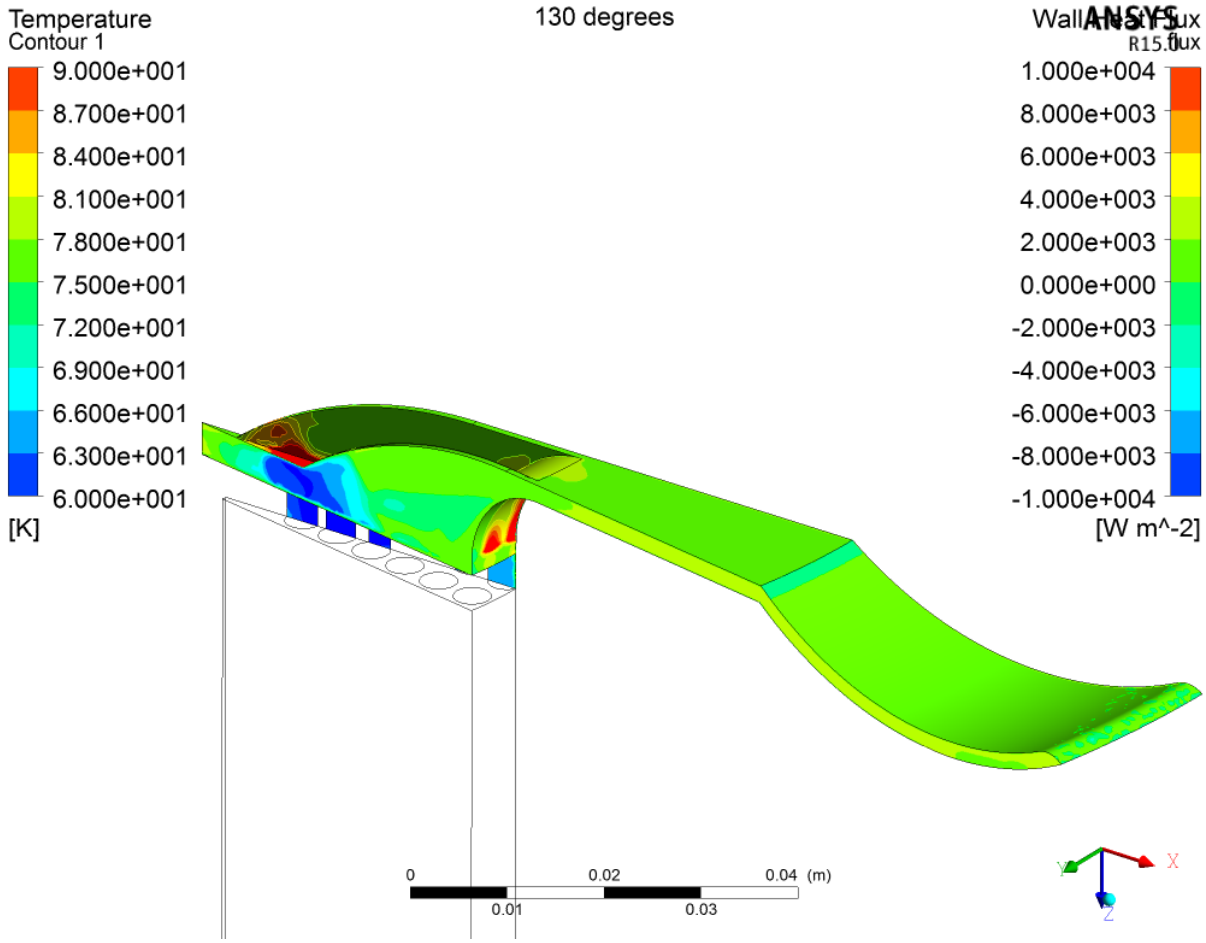

Figure A-14: Gas temperatures (sides) and wall heat flux (surfaces) for the cold domain at HSE

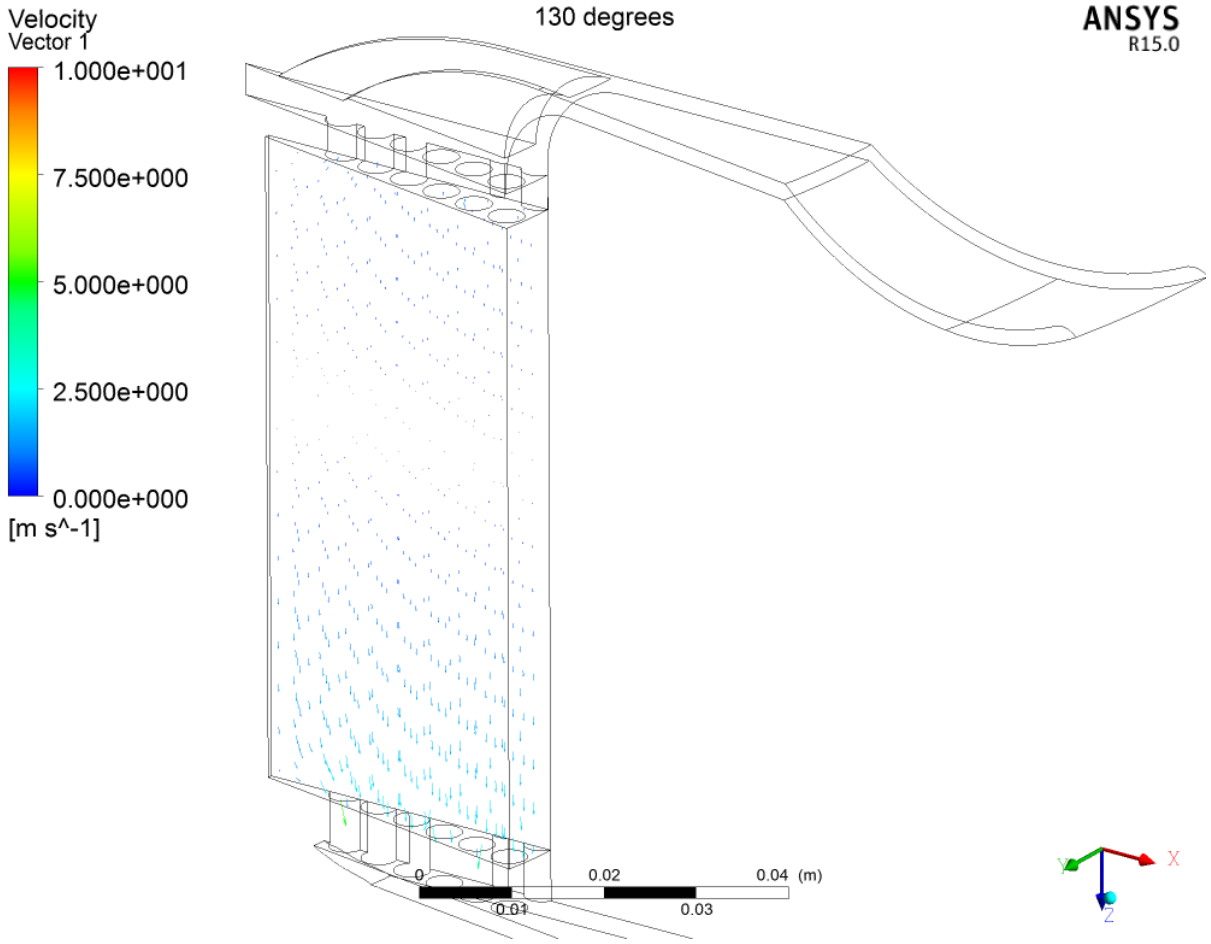

Figure A-15: Gas velocity vectors for the regenerator at HSE

As discussed previously, HSE has an inflection point in the regenerator flow. Figure A-15 shows the gas velocity vectors for the regenerator. The regenerator is being emptied of gas at HSE with the displacer movement sucking gas into the cold domain, and the expanding DPWG diaphragm sucking gas into the warm domain. It is to be noted that the zero velocity point is not static but moves during the cycle.

A.5 Mid Stroke Expanding

Mid-Stroke-Expanding (MSE) is 180° into the cycle. MSE is similar to MSC but with the gas flow from cold to warm. Figure A-16 shows streamlines at MSE, at which point the DPWG diaphragm is descending, expanding the gas throughout the cooler. The displacer is down, with gas in the cold region cooling down due to expansion. Absorption of heat from the walls is high but not at its peak value as the expansion is only half completed. The flux on the warm side of the displacer is, however, near its minimum due to expansion cooling the gas from its high average temperature, which is above the wall temperature.

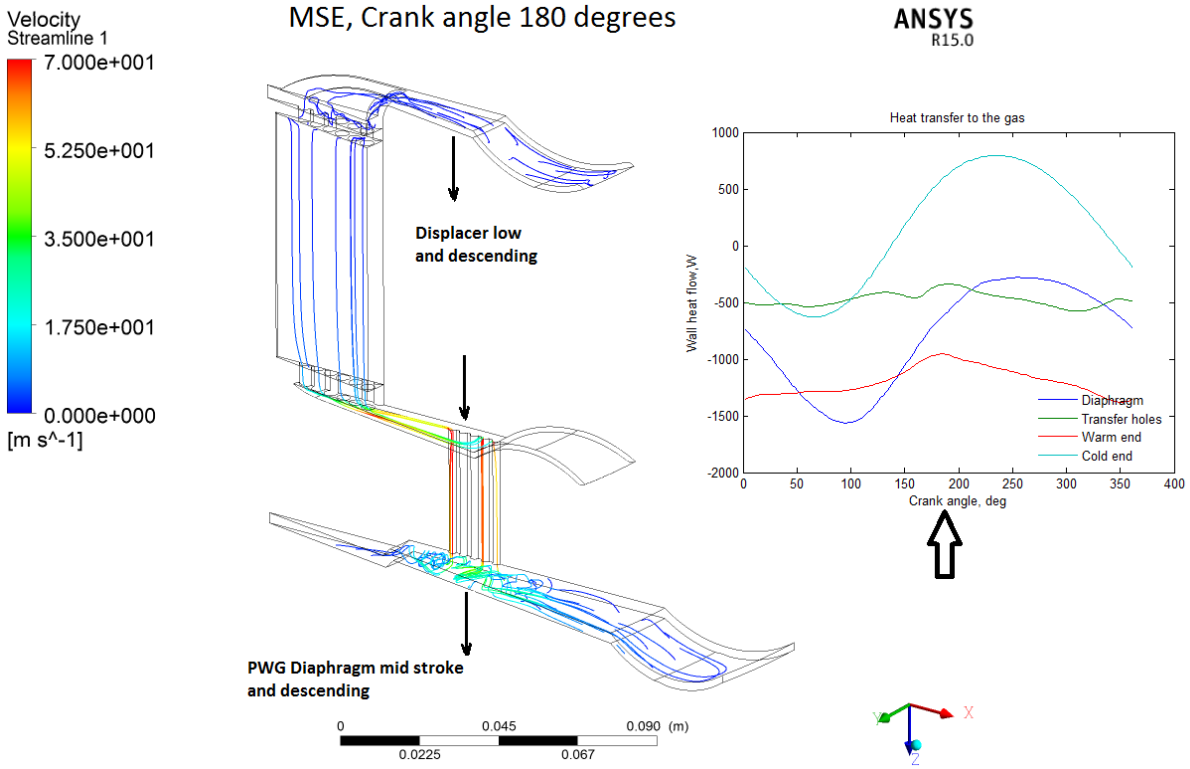

Figure A-16: Mid Stroke Expanding, MSE, streamlines.

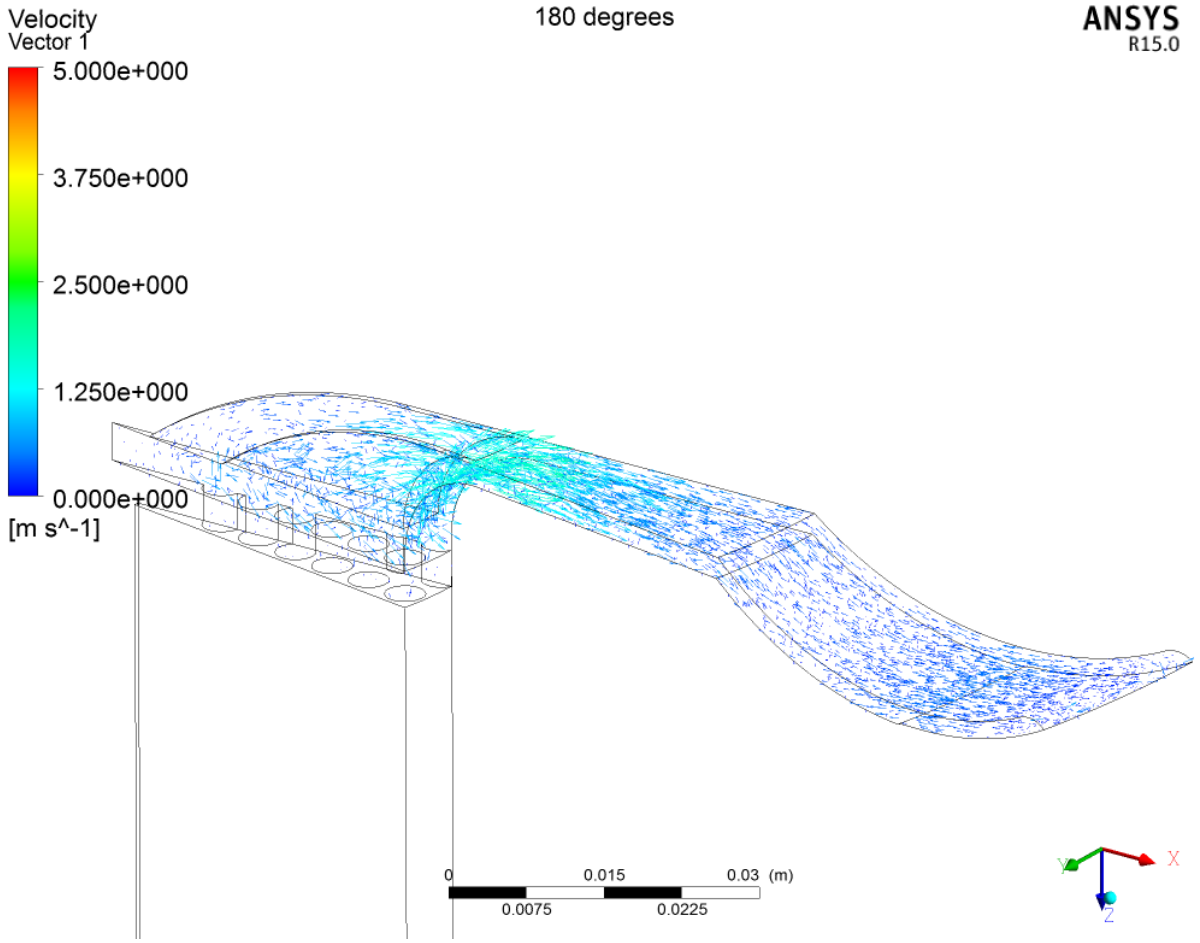

Figure A-17: Cold gas velocity vectors at MSE

Figure A-17 shows the gas velocity vectors for the cold domain at MSE. The radial gas velocity can be seen accelerating (the arrows get longer and lighter blue) towards the centre as the gas exits the cold domain towards the regenerator. The velocity is quite low, at 1.25 m s^{-1}, compared with the 50-70 m s^{-1} seen in the warm domain. It is also evident that a significant amount of gas moves quickly around the corner, short circuiting the slotted heat exchanger in the centre.

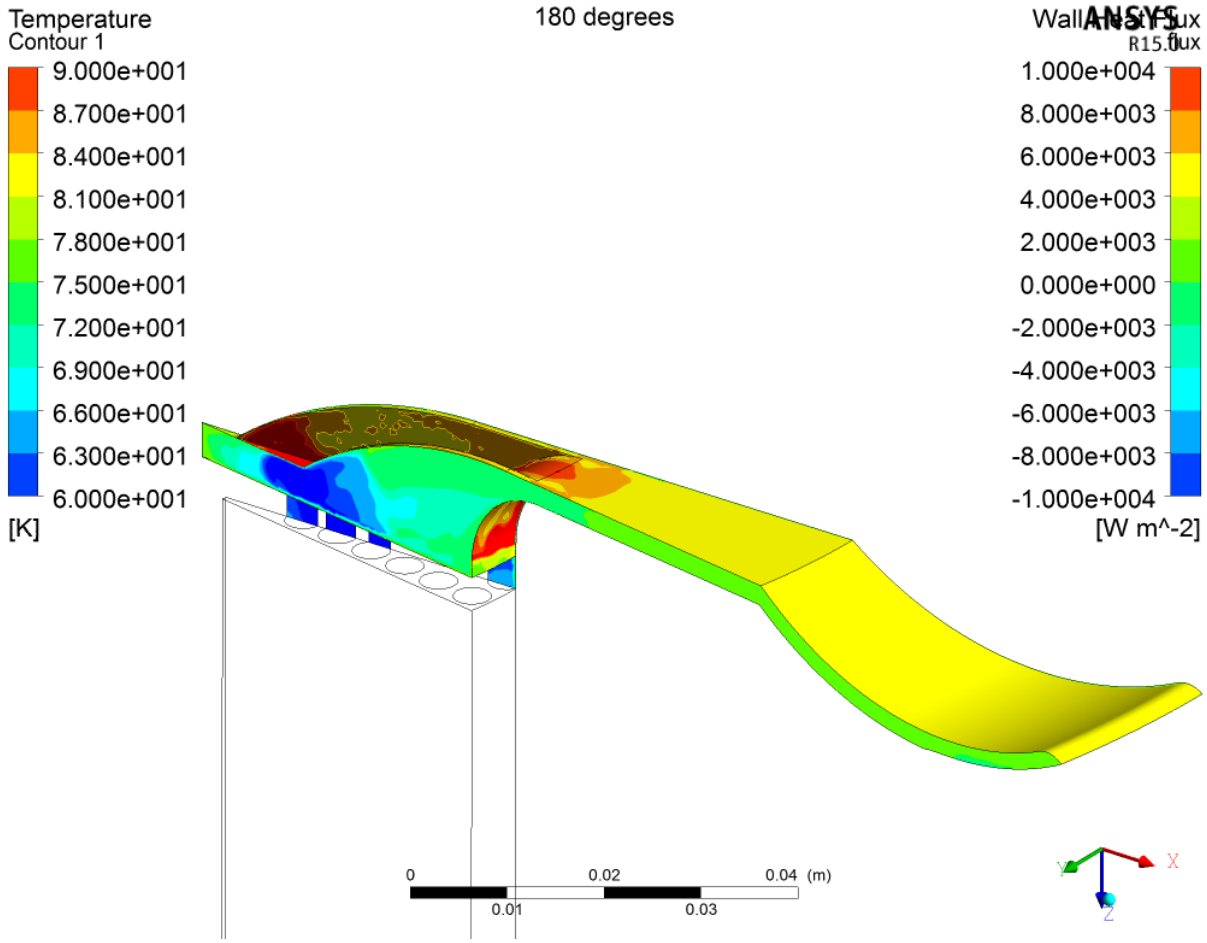

Figure A-18: Cold gas temperatures (sides) and heat flux (faces) at MSE

Figure A-18 shows the gas temperature and heat flux in the cold domain. Expansion cooling has dropped the gas temperature below the 77 K walls which results in a positive heat wall flux. The majority of the outer radial section has a heat flux of 4 to 6 x 10^3 W m^{-2}. The flux increases near the corner where the gas velocities increase and the temperature drops further. The slotted central heat exchanger experiences the highest wall flux, mostly due to cooler gas being present.

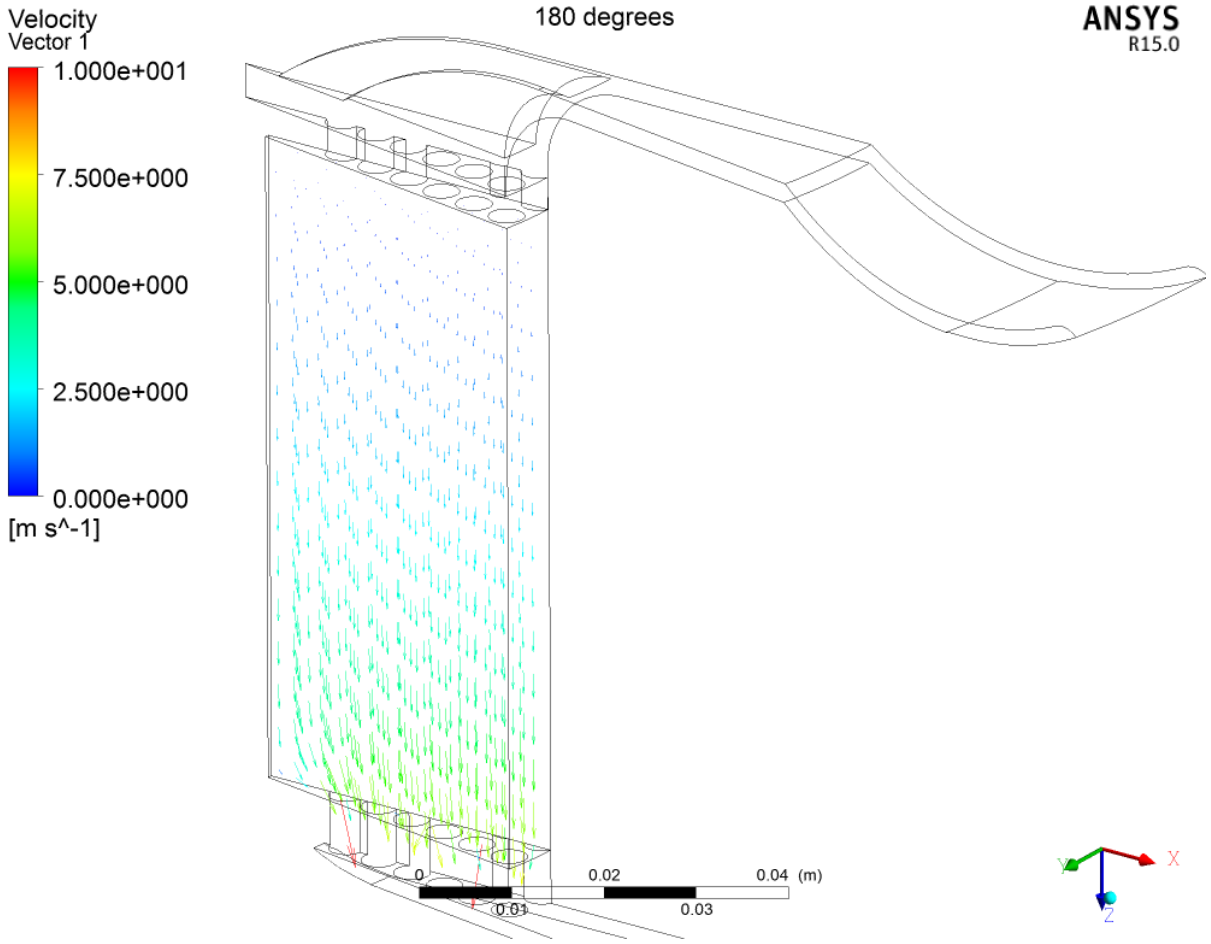

Figure A-19: Regenerator gas velocity vectors at MSE

The gas velocities in the regenerator, Figure A-19, steadily increase down the regenerator due to the warming gas as well as the spring in the gas during expansion. Some asymmetry in velocity is evident at the bottom as the gas finds its way through the holes in the regenerator retaining plate.

The warm gas domain experiences temperatures close to the 300 K walls at MSE which results in a low wall heat flux, Figure A-20 in spite of the gas velocities being relatively high, Figure A-21.

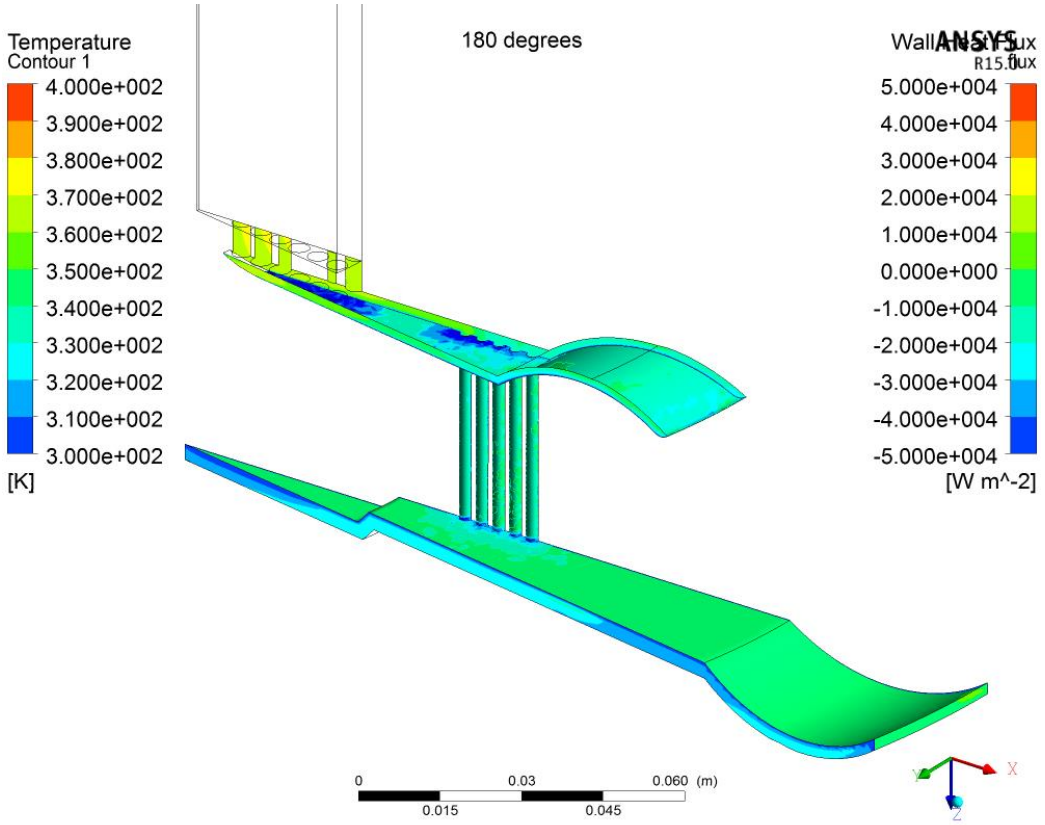

Figure A-20: Warm gas temperatures (sides) and wall heat flux (faces) at MSE

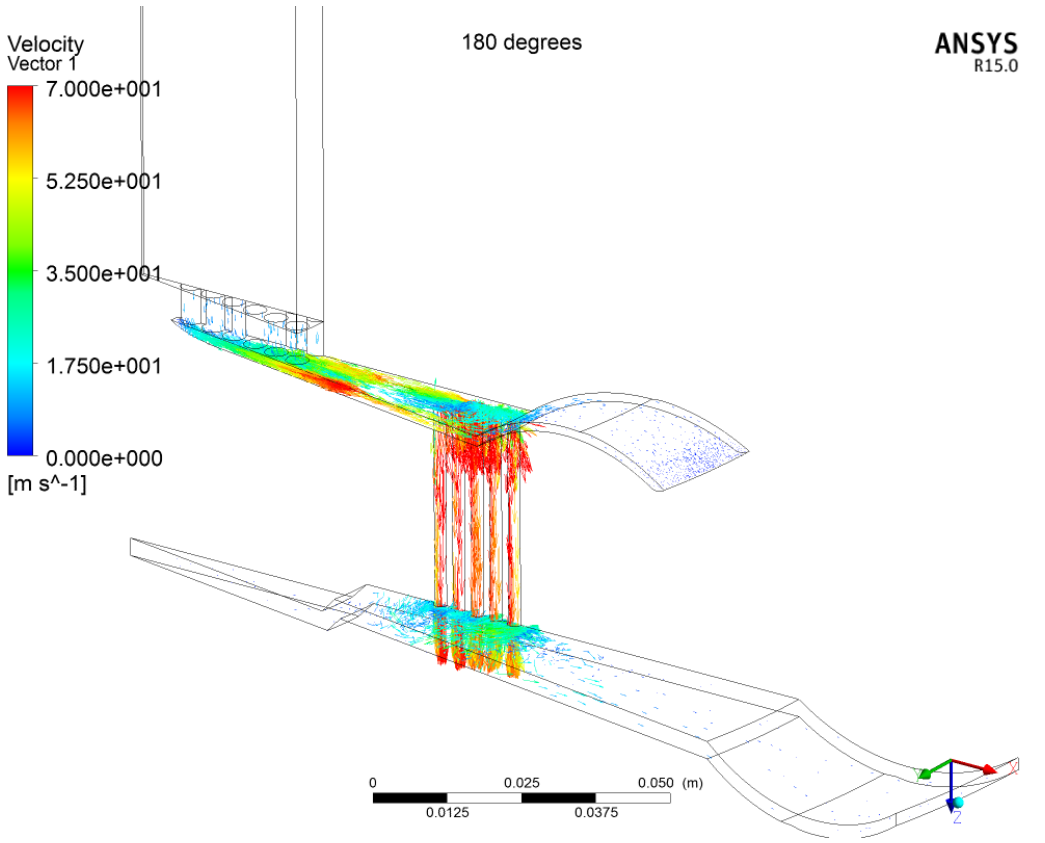

Figure A-21.Warm gas velocity vectors at MSE

A.6 Low Stroke Expanding

Low Stroke Expanding, LSE, is at a crank angle of 230° and is the counter-position to HSC. The compression diaphragm is still moving downwards, creating gas velocity. Temperatures and pressures are low which is good for heat transfer, and the displacer is close to the bottom of its travel, maximising the gas in the cold domain. The heat transfer from walls to the cold gas is at its maximum, which shows the importance of this part of the cycle as the purpose of the cooler is to maximise heat transfer from the cold domain's walls to the gas. The trends in Figure A-23 to Figure A-27 are similar to their equivalents for MSE but are more pronounced with greater velocities, extreme temperatures and higher heat flux figures.

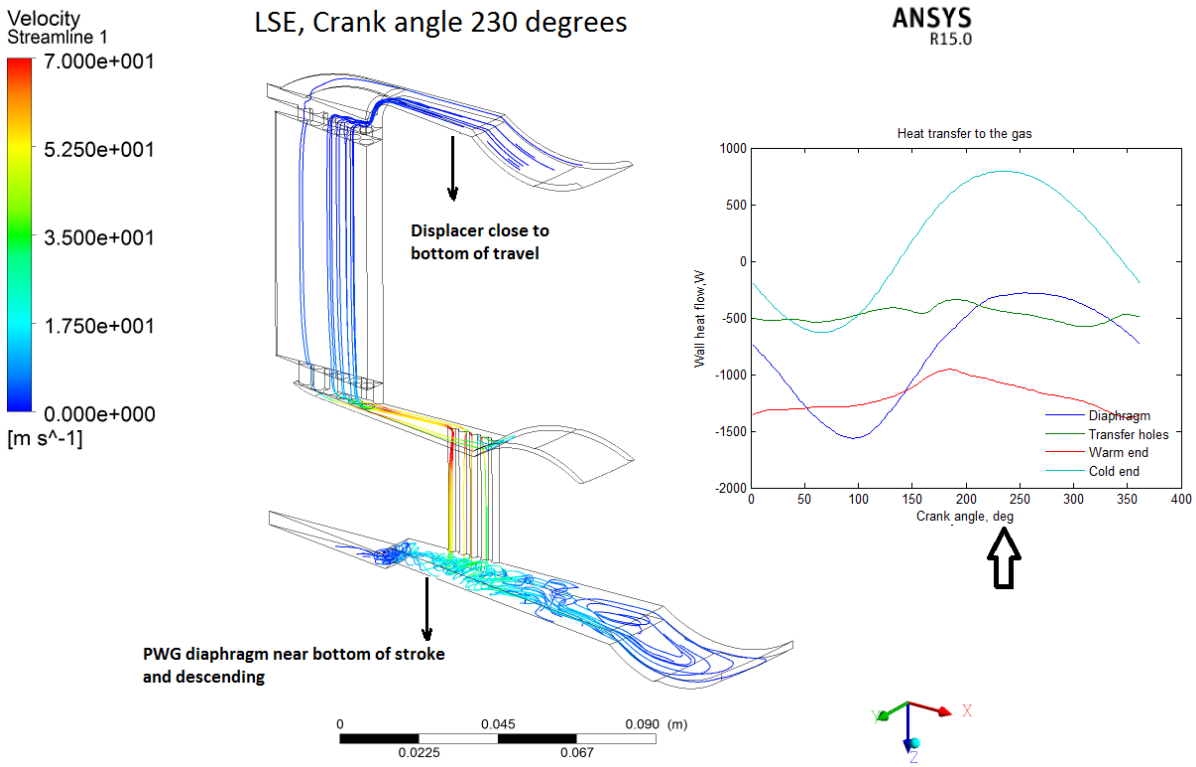

Figure A-22: Low Stroke Expanding, LSE, streamlines

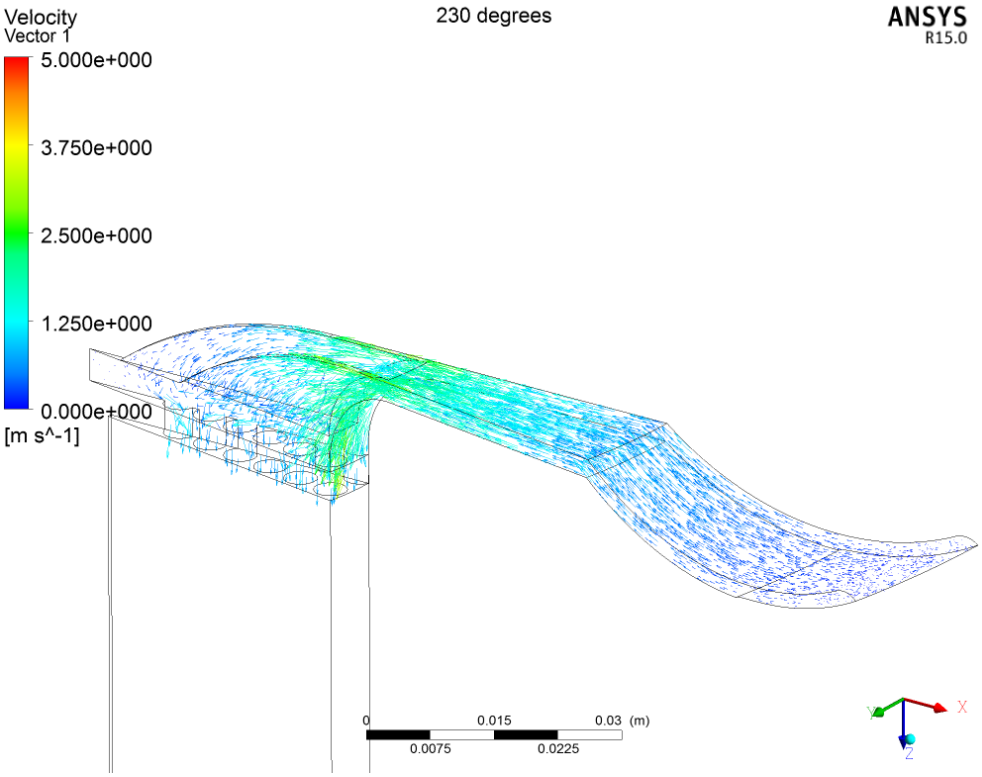

Figure A-23: Cold gas velocity vector at LSE.

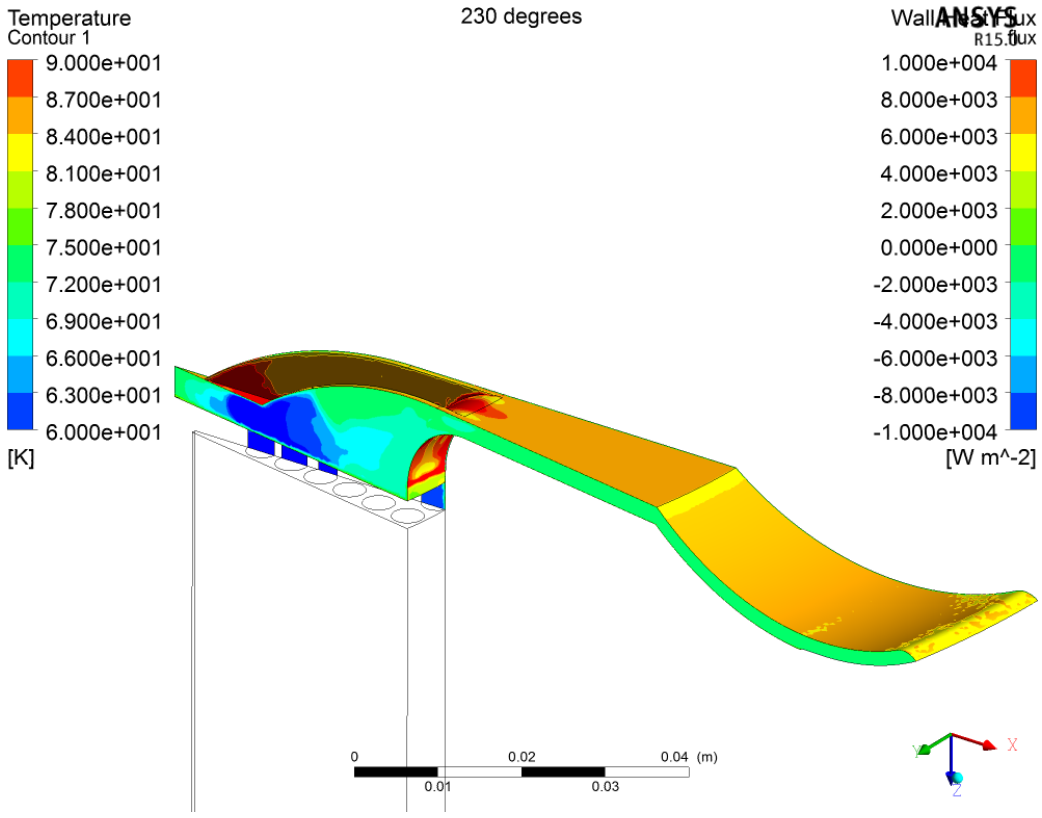

Figure A-24: Cold gas temperatures (sides) and wall heat flux (faces) at LSE

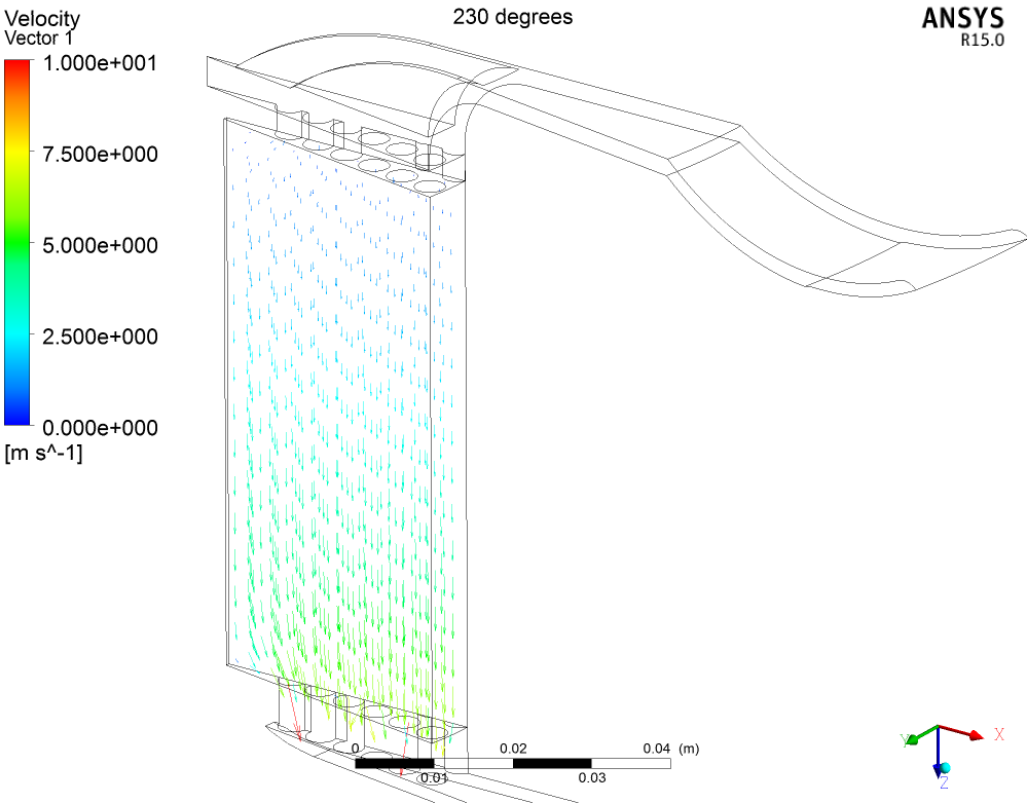

Figure A-25: Gas velocity vectors in the regenerator at LSE

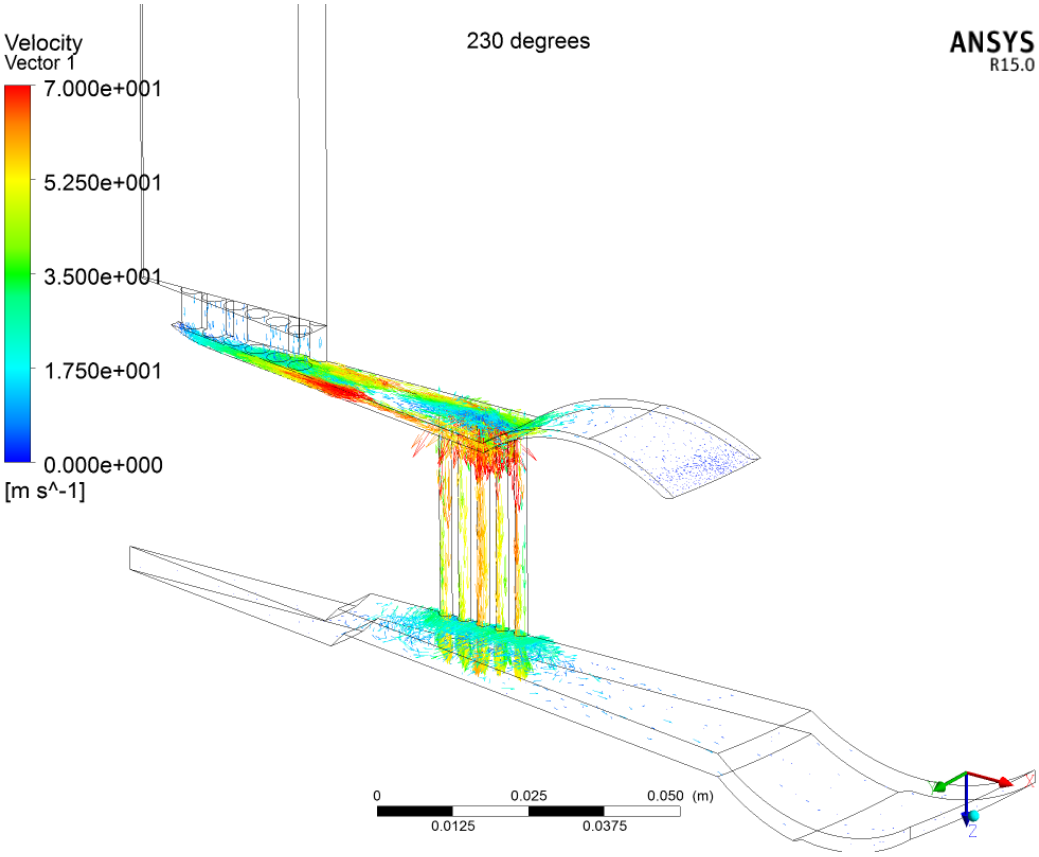

Figure A-26: Gas velocity vectors in the warm domain at LSE.

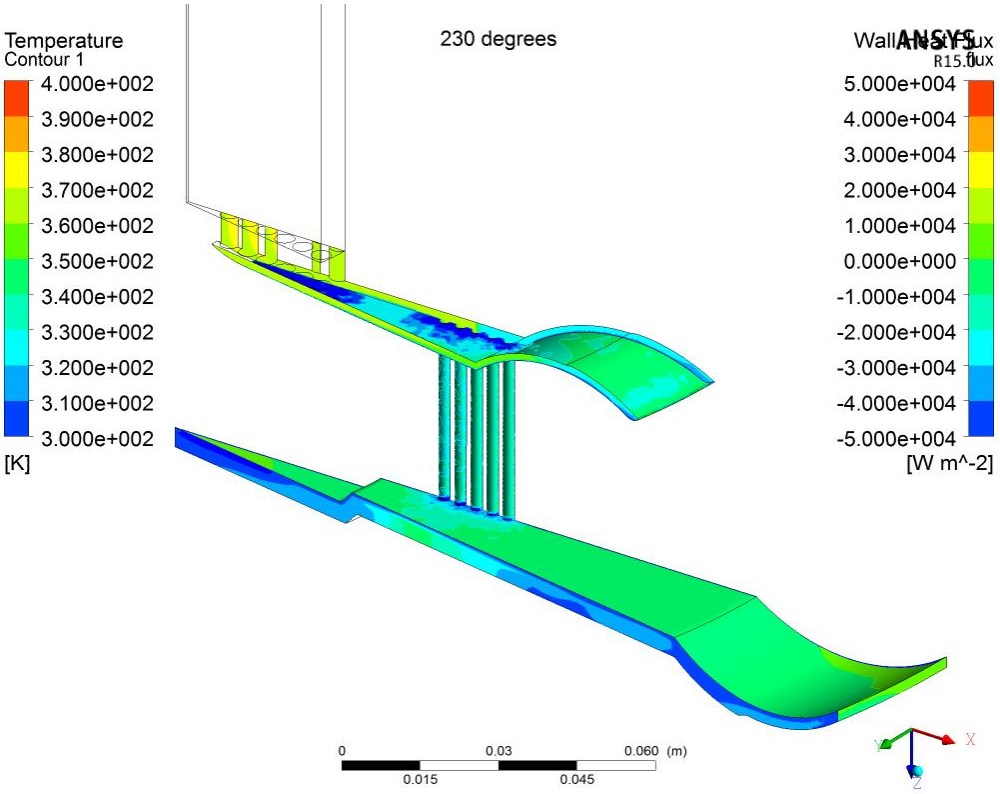

Figure A-27: Gas temperatures (sides) and wall heat flux (faces) in the warm domain at LSE.

A.7 Bottom Dead Centre

Bottom-dead-centre, BDC, is at 270° and is where: the volume is highest; gas velocities are low; and temperatures at their minimum. The displacer has started its movement upwards, transferring cold gas (which has picked up heat from walls) through the regenerator.

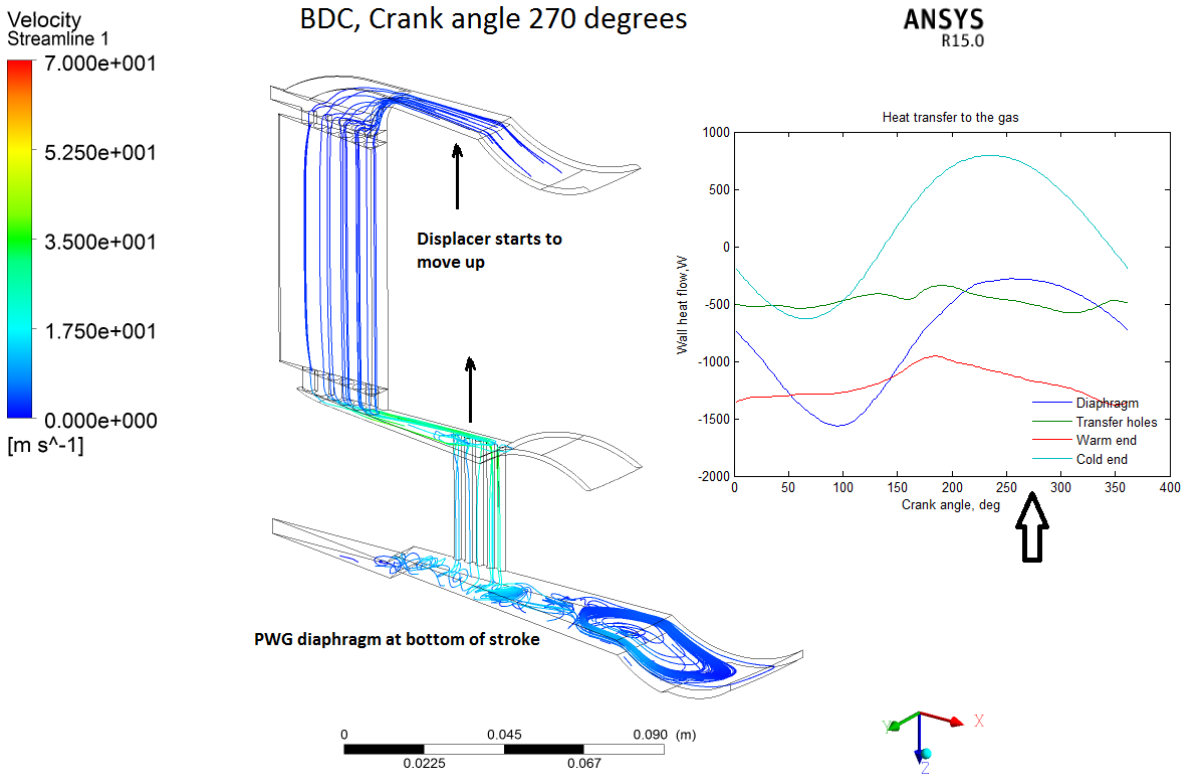

Figure A-28: Streamlines and heat flows at BDC

Figure A-28 shows bottom dead centre, when the pressure is at its minimum and the gas has expanded and cooled to its minimum temperature. Heat flow is highly positive in the cold domain, with energy transferring from the walls into the gas. The gas, with energy gained from the walls, is being pushed into the regenerator by the displacer, cooling the regenerator.

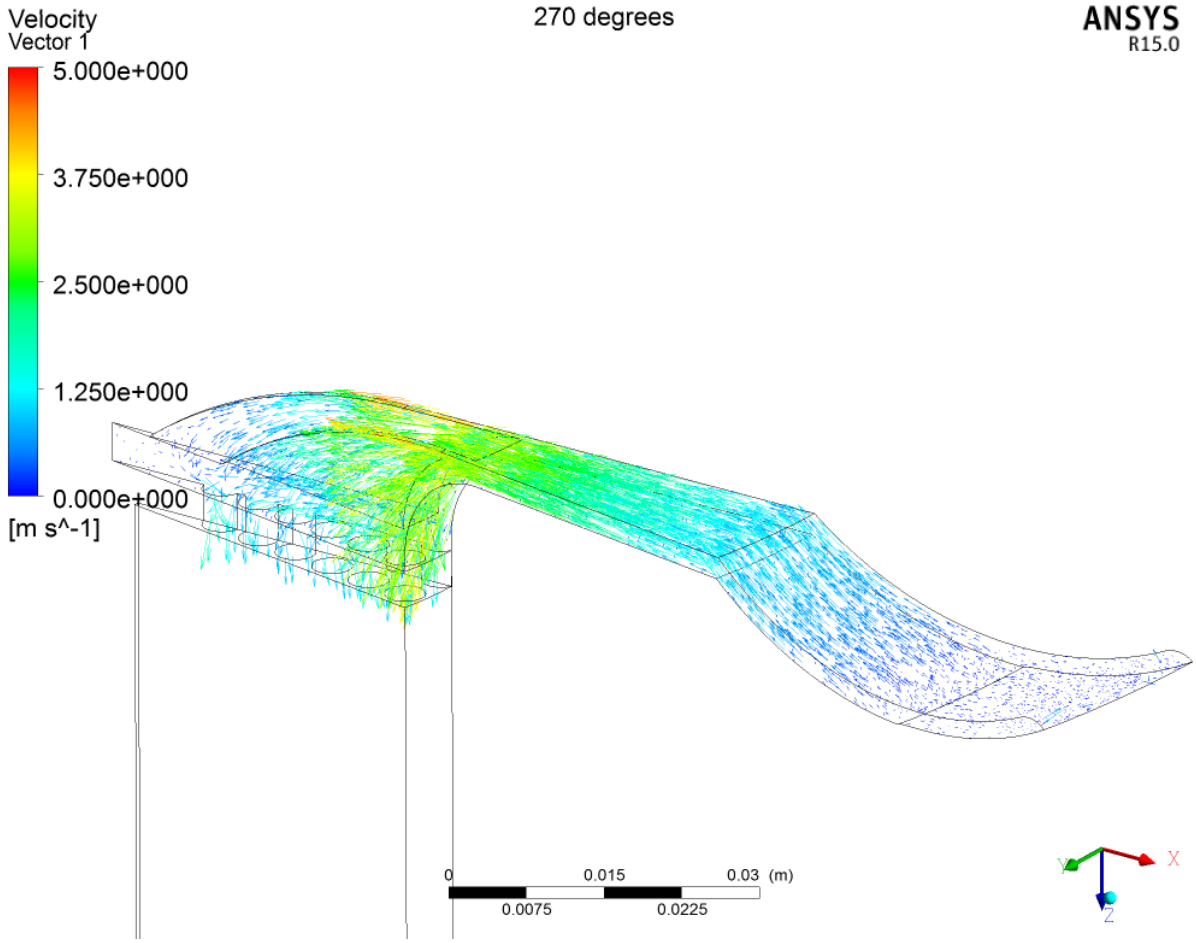

Figure A-29: Cold gas velocity vectors at BDC

Figure A-29 shows the cold gas velocity vectors. Although the DPWG's diaphragm is stationary at the bottom of its travel, the displacer's movement is forcing gas from the cold region into the regenerator. The highest velocity is at the centre of the radial section and, like other parts of the cycle, whilst there is flow in the cold heat exchanger slots, a significant amount of flow is short circuiting the slots at the corner. The gas beyond the membrane half-way point is stationary.

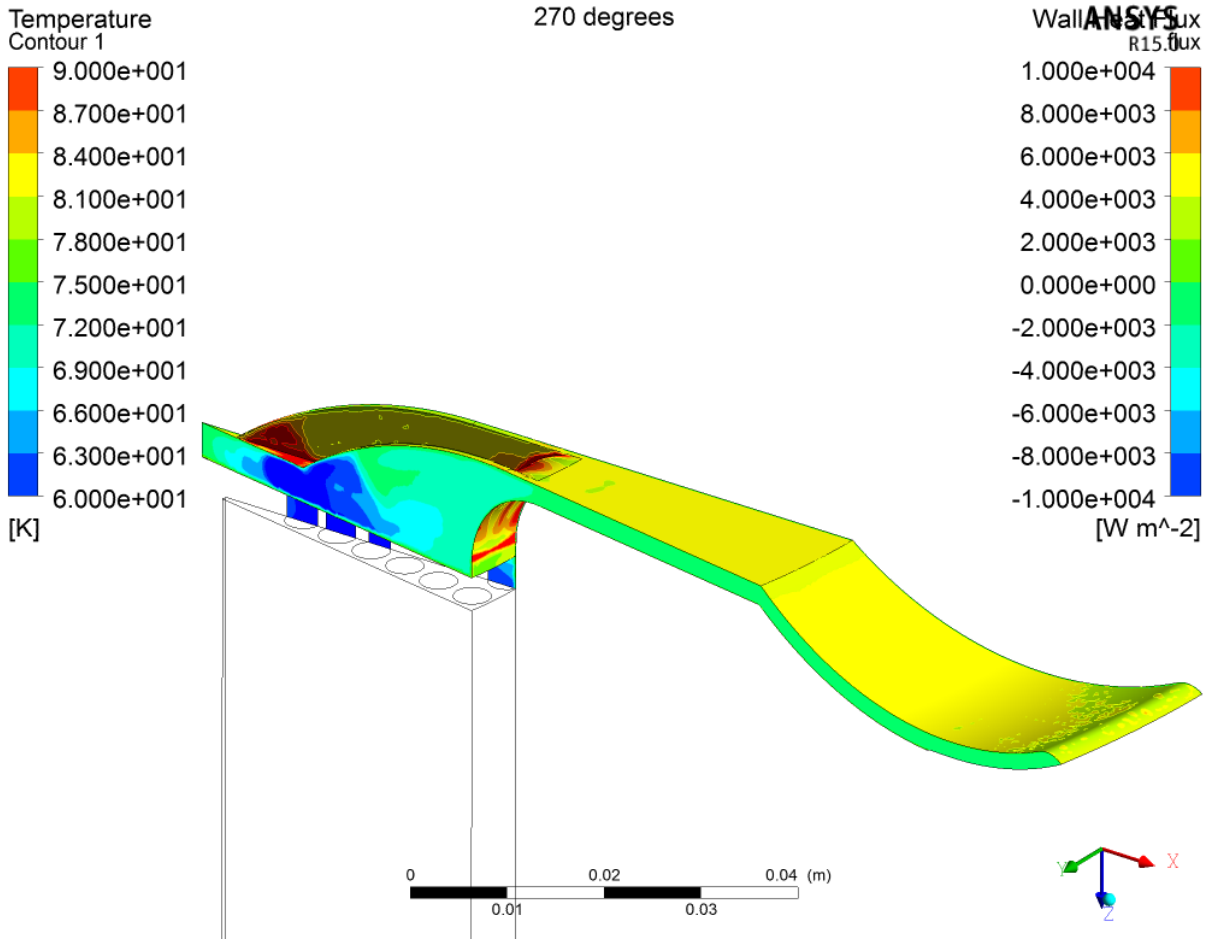

Figure A-30: Cold gas temperature (sides) and wall heat flux (surfaces) at BDC.

Figure A-30 shows the cold gas temperatures and wall heat flux at BDC. The cold gas is generally at its coldest at BDC, the plot showing it being at around 75 K. The uniform heat flux over the majority of the radial section indicates that the gas velocity in the radial section is not significant enough to have a large effect on the heat flux; the magnitude of the flux would therefore be mostly due to the gas temperature and conduction through the gas. Flux is greater in the central slotted heat exchanger part where gas temperatures are lower, evident by colder gas at the centre producing a localised high heat flux.

Figure A-31 shows the velocity vectors, gas temperatures and wall heat flux in the warm region. With gas temperatures at their lowest, but still above that of the walls, and gas velocities generally low, the wall heat flux is low throughout. There are a few areas of higher wall heat flux where velocities increase as the gas passes into and out of the transfer holes but the areas these represent is small so the overall heat transfer out of the gas at BDC is at its lowest in the cycle.

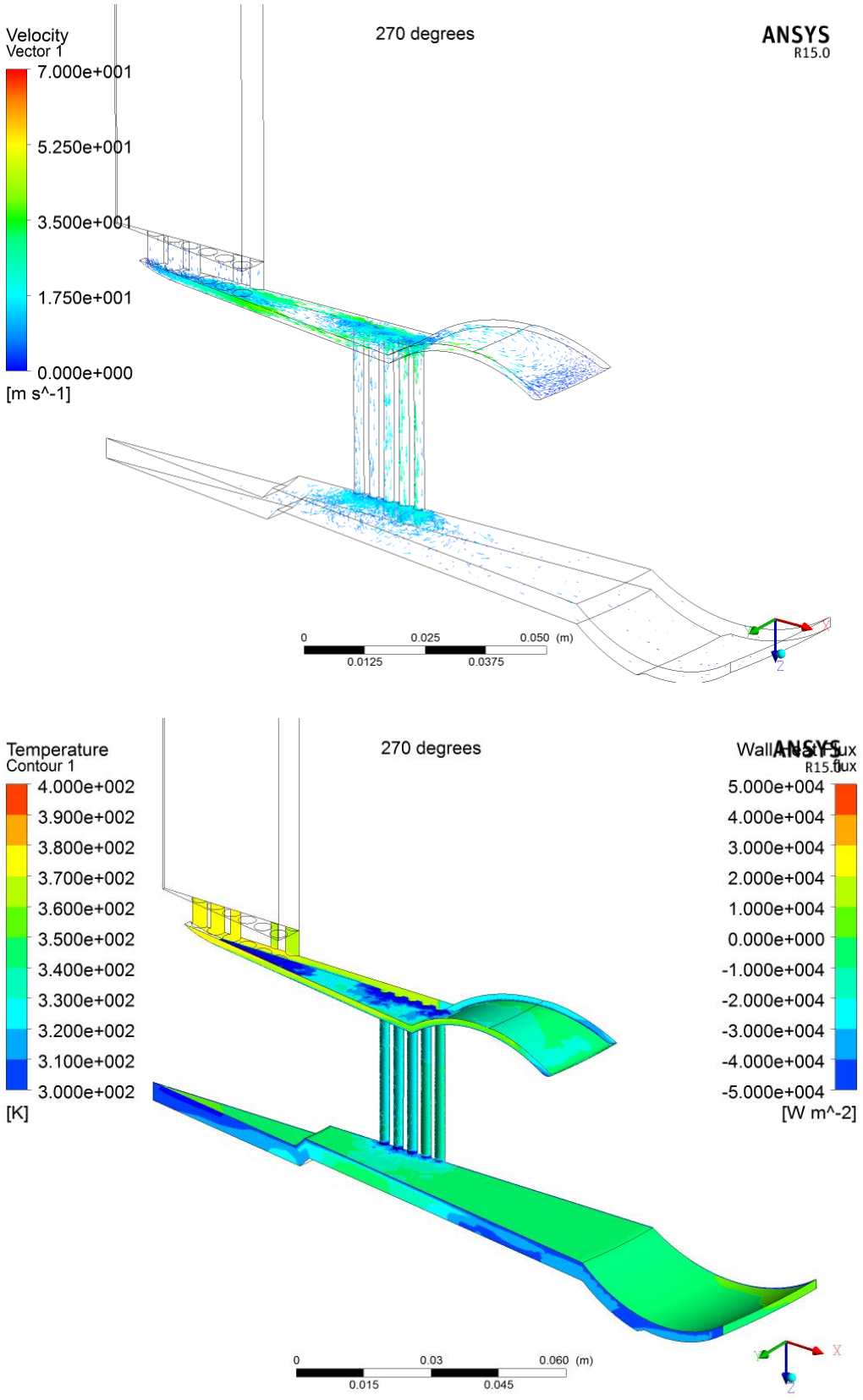

Figure A-31: Top, warm gas velocity vectors. Bottom, warm gas temperature (sides) and wall heat flux (surfaces)

A.8 Low Stroke Compressing

The final position is 310°, Figure A-32, with the compression diaphragm low and compressing, LSC. LSC is characterised by a rising displacer, taking cold gas from the cold domain through the regenerator. Of interest in LSC is that there is an inflection point in the regenerator flow, where the diaphragm is moving up, compressing the gas and moving it upwards whilst the displacer is still moving upwards, moving gas downwards through the regenerator.

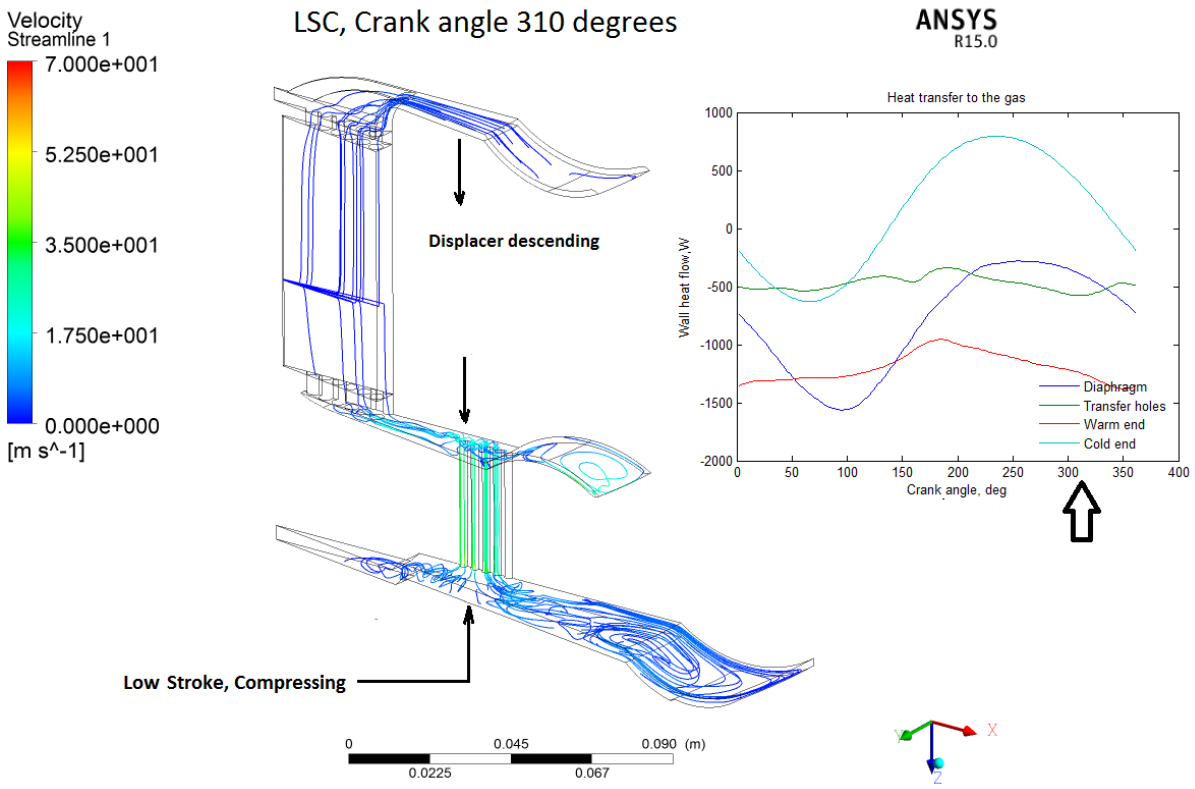

Figure A-32: Streamlines for low stroke compressing, LSC.

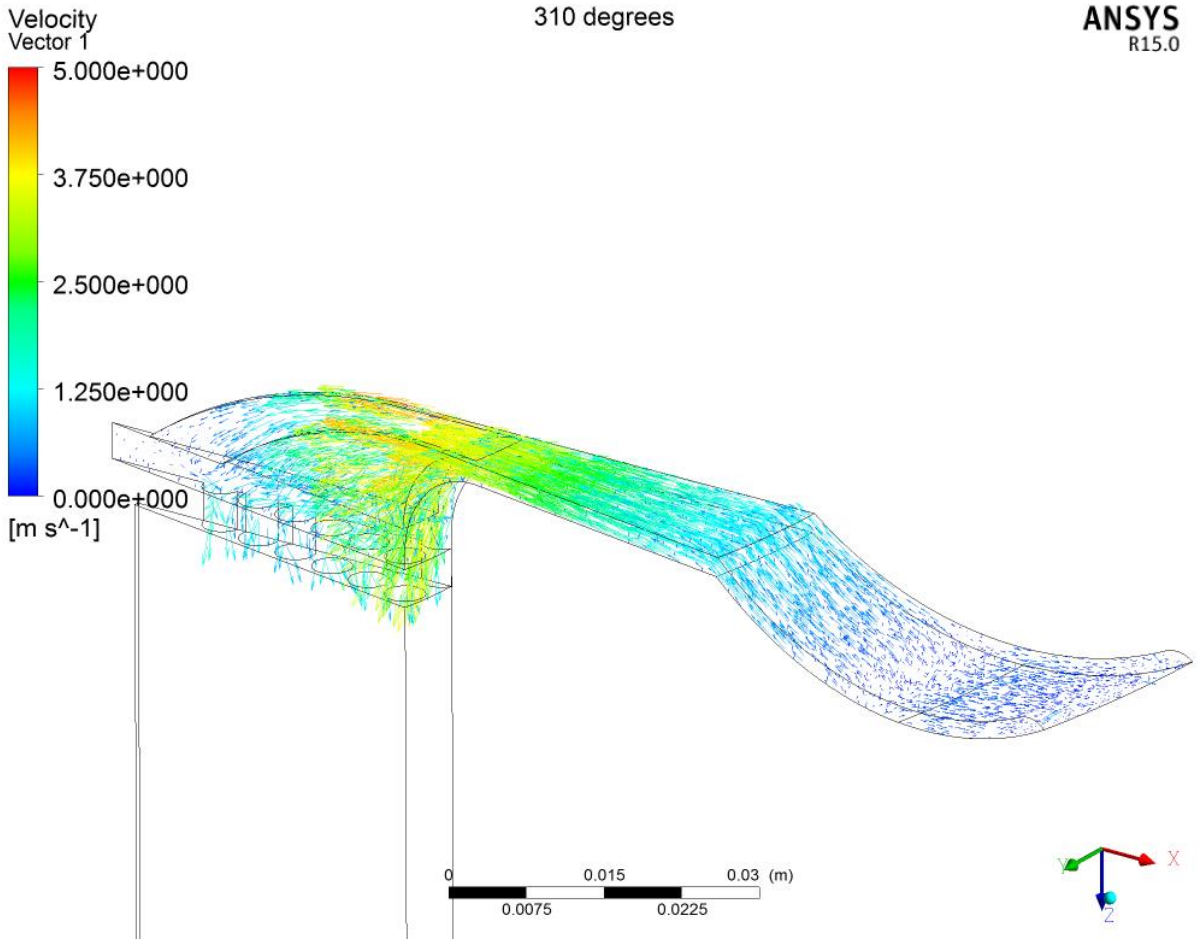

Figure A-33: Cold gas velocity vectors at LSC

Figure A-33 shows the cold gas velocity vectors at LSC. Velocities at the corner from the radial section to the slotted heat exchanger are near their maximum, approaching 4 m s^{-1}. Velocity throughout the radial section is generally high and the displacer compression of the cold gas starts to take effect at the outer radius, as is shown by vectors pointing towards the circumference. The slots in the heat exchanger show good velocity conditions and flow too. All these conditions point to the potential for good heat exchange.

However, Figure A-34 shows a different story. Compression of the gas has warmed it to the point where it is close to the 77 K wall temperatures. The result is a very low wall heat flux in spite of the high gas velocities.

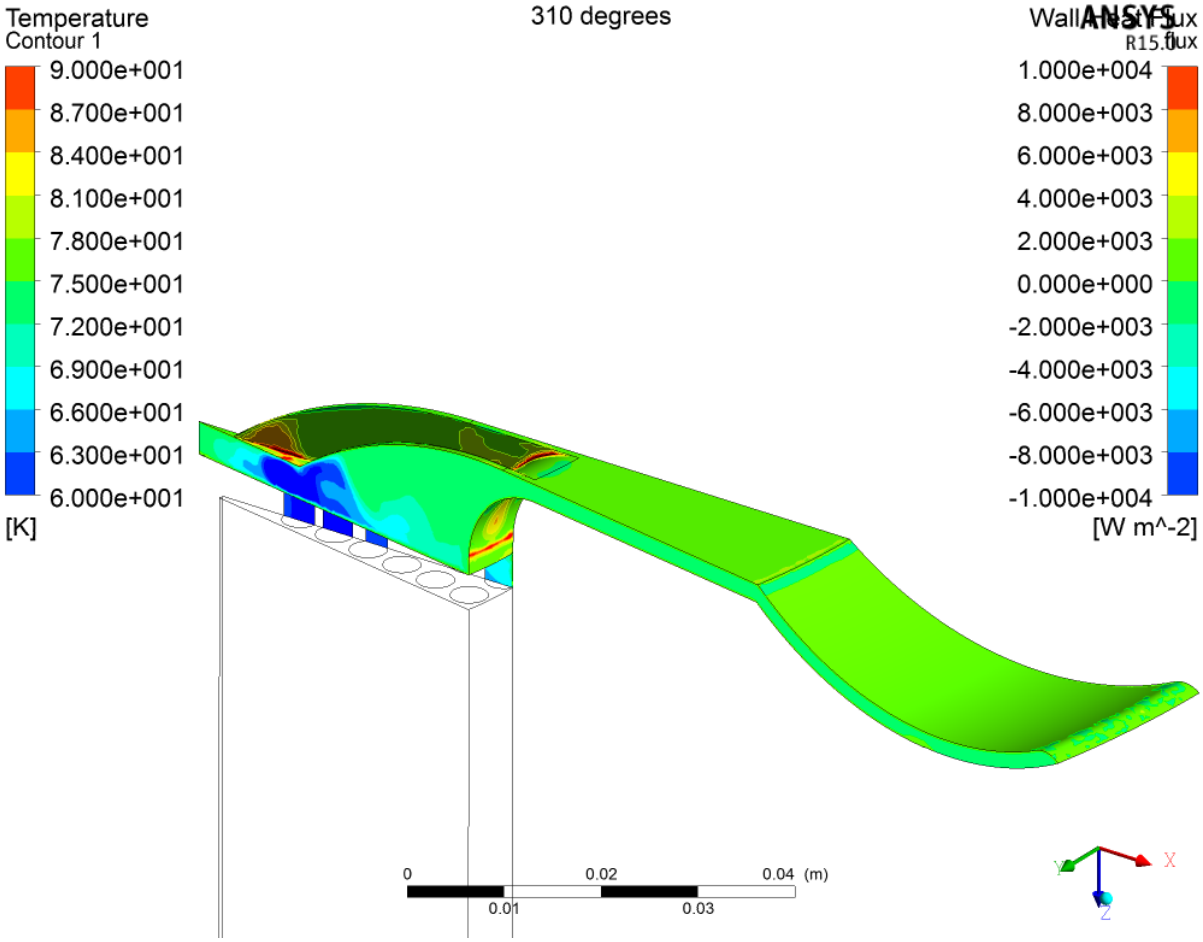

Figure A-34: Temperatures (side) and heat flux (surfaces) for the cold gas at LSC

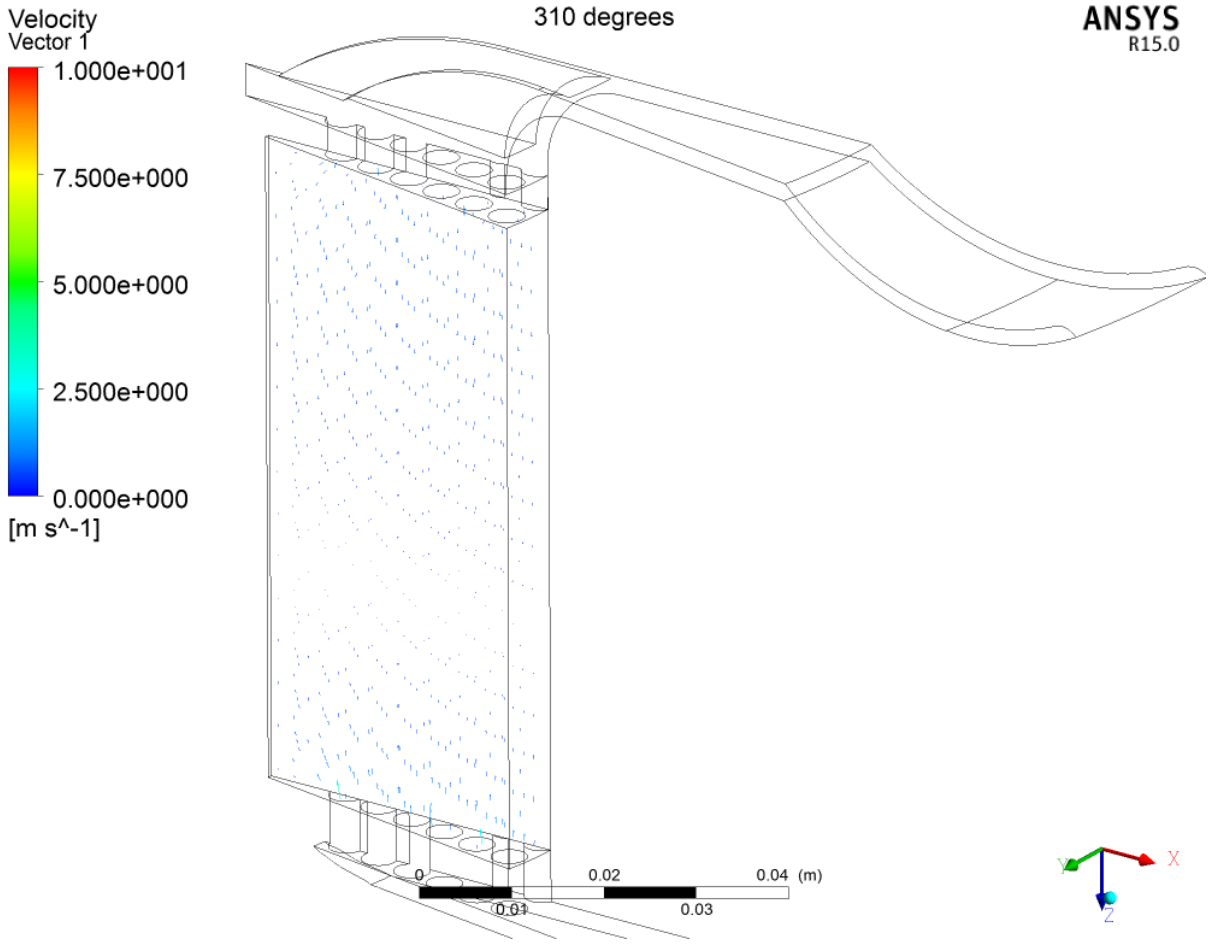

Figure A-35: Gas velocity vectors in the regenerator at LSC.

Figure A-35 shows gas velocity vectors in the regenerator at LSC and it confirms the inflection point in the centre of the regenerator, as shown by the streamlines in Figure A-32. The gas is being compressed towards the centre of the regenerator. This condition results in little heat transfer between the gas and the matrix.

Figure A-36 shows the flow and heat transfer conditions for the warm gas at LSE. Velocities are low and gas is starting to flow from the diaphragm through the transfer holes to the warm side of the displacer before entering the regenerator. The general gas temperature is near the 300 K wall temperature, resulting in little heat transfer with the walls. The exception is the region on the warm side of the displacer close to the regenerator where gas from earlier in the cycle has not had an opportunity to cool fully and re-enters the regenerator at a warm temperature of around 380 K. This situation is not ideal as it keeps the regenerator end at a high temperature, effectively making the thermodynamic cycle eject heat at 380 K.

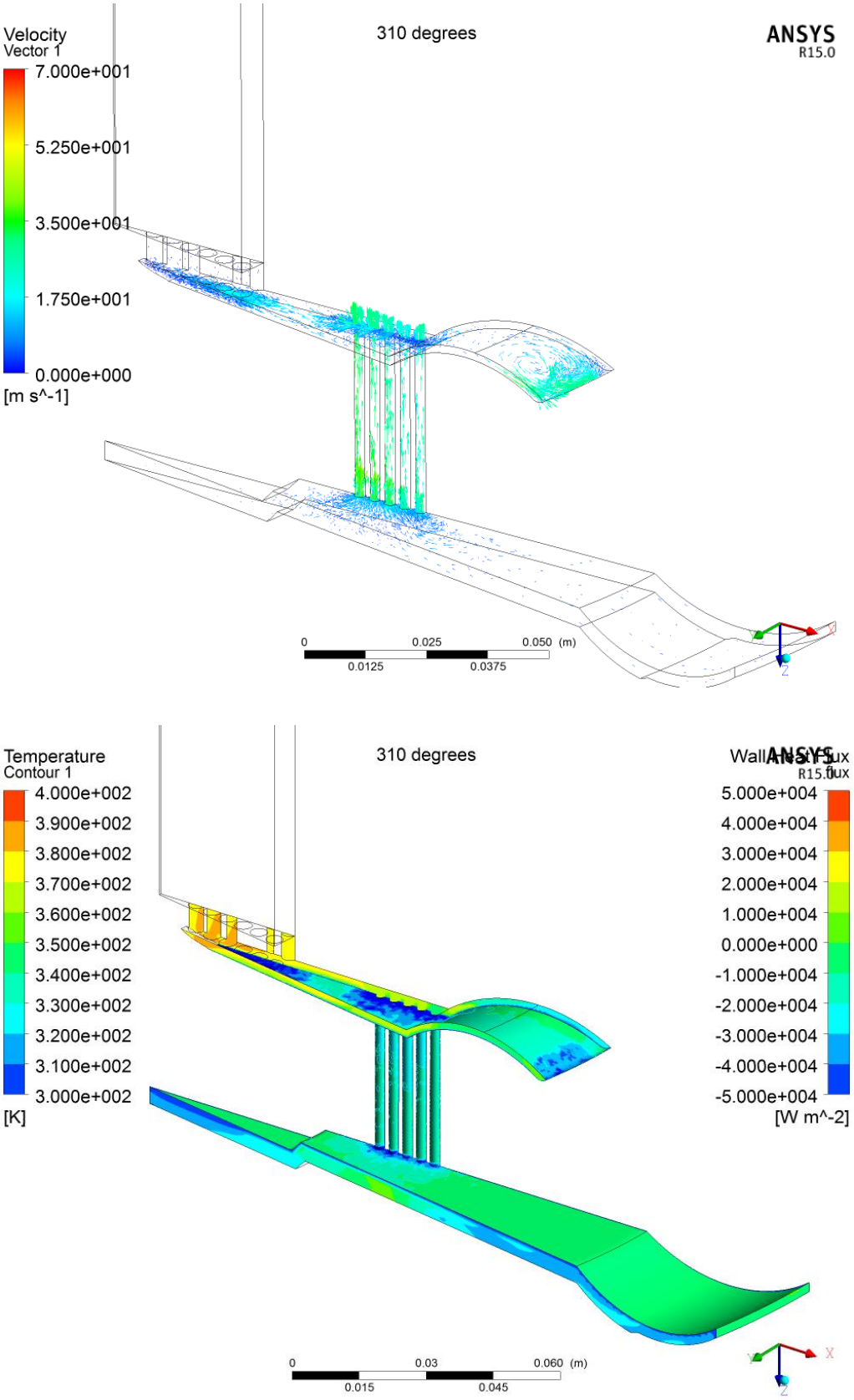

Figure A-36: Above, warm gas velocity vectors at LSC. Below, warm gas temperatures (sides) and wall heat flux (faces) at LSC.